Identified Particle Production in p+p and d+Au Collisions at RHIC Energies

A Dissertation Presented

by

Eftychios Felix Matathias

to

The Graduate School

in Partial Fulfillment of the

Requirements

for the Degree of

Doctor of Philosophy

in

Physics

Stony Brook University

December 2004

Stony Brook University

The Graduate School

Eftychios Felix Matathias

We, the dissertation committee for the above candidate for the Doctor of Philosophy degree, hereby recommend acceptance of this dissertation.

Thomas Hemmick
Relativistic Heavy Ion Group, Stony Brook University
Dissertation Director

George Sterman
C.N. Yang Institute for Theoretical Physics, Stony Brook University
Chairman of Dissertation

John Hobbs
Department of Physics, Stony Brook University

Michael J. Tannenbaum
Department of Physics, Brookhaven National Laboratory
Outside Member

This dissertation is accepted by the Graduate School.

Dean of the Graduate School

Abstract of the Dissertation

Identified Particle Production in p+p and d+Au Collisions at RHIC Energies

by

Eftychios Felix Matathias

Doctor of Philosophy

in

Physics

Stony Brook University

2004

The main goal at the Relativistic Heavy Ion Collider (RHIC) at the Brookhaven National Laboratory in Upton, New York, is to explore the phase structure of the underlying theory of strong interactions, Quantum Chromodynamics (QCD). It is predicted that under extreme temperatures and pressure gradients, nuclear matter undergoes a phase transition where the initially confined quarks and gluons are liberated and their constituent mass disappears, leading to the restoration of chiral symmetry. In nature it is believed that such new states have existed at the very early universe, a few microseconds after the Big Bang, and in the interior of neutron

stars. In order to heat matter in such unprecedented temperatures, RHIC collided Au ions at SQRT(s)=130 A GeV and 200 A GeV in its first and second year of operations.

One of these signatures of the Quark Gluon Plasma (QGP) formed in these collisions is the suppression of high momentum particles that lose a large fraction of their energy inside the dense plasma. This phenomenon was observed at both 130GeV and 200GeV Au+Au collisions, creating a lot of excitement in the experimental and theoretical community. Even more exciting was the discovery of an unusually large production rate of protons and antiprotons compared to pions and kaons, a striking new phenomenon never before predicted or observed at lower energies.

In this thesis we report a measurement of identified pions, kaons, protons and their antiparticles in p+p and d+Au collisions at SQRT(s)=200GeV with the PHENIX experiment at RHIC, and perform a systematic comparison of these baseline spectra with spectra from the Au+Au collisions at the same collision energy. The results of this thesis establish the initial conditions of identified particle production at RHIC energies and measure the properties of the Cronin effect in d+Au collisions. We elaborate on the similarities and differences in all these different collision systems, and finally conclude on the origin of some of the novel effects observed in the hot and dense nuclear matter.

Dedication

to Emily and Effy

...for their unconditional love and support while I was hunting quarks and gluons

Contents

List of Figures

List of Tables

Acknowledgements

First, I would like to say a few words about my adviser, Tom Hemmick. Tom cultivates genius in those around him. A true believer in the human intellect, he shows unconditional trust to all his students, and as he did with me, ignites them for their first steps into the world of science. I have lived nearly all my life in the environment of academic institutions. From my school and the Aristotle University of Thessaloniki in Greece, to Iowa State University for my Master's degree, and then to Stony Brook for my doctoral degree. I have never met an educator that could even come close to his caliber. Tom is a true educator, he defines the term. I will always remember the pen that he carries in his shirt pocket, and how he used to make sketches in napkins, during lunch, of equations, particles going through detectors, or what is the correct way to subtract the background under a mass peak.

When I first joined his group at Stony Brook, among with other fresh graduate students, Tom would always give us long blackboard presentations of how PHENIX (our experiment) was built, how it worked, he was giving us lectures on programming, PHENIX software, everything that was essential for us to start working in the environment of a multi-million dollar, multi-detector, frustratingly intimidating, experimental facility. And he was always lecturing by memory. Never used a single note, a book or manual. Always by memory, to the smallest detail. I considered it natural for a young professor to be so caring and so engaging, and I always thought that his enthusiasm will calm down with time, after lecturing to so many students, so many times.

Five years down the road, I am ready to graduate, the new graduate students became the old guard, and the group has flooded with young blood, fresh minds, ready to start the journey of a doctoral thesis in PHENIX. Until my last days at Stony Brook, Tom was still gathering everyone to his office, lecturing, explaining, defining, educating.

I feel honored and blessed to have worked under his mentorship, and will always cherish the time that I spent with him, working at the frontier of scientific knowledge, pushing me off the cliff, just to teach me that I could fly with my own wings.

There are many people that I would also like to acknowledge. First and foremost Barbara Jacak. Barbara helped me enormously at the last stages of my research, and without her, it would have probably taken me one more year to graduate. She believed in my research, and during times of frustration, she kept pushing me to finish, publish, graduate! I will always be indebted to her for teaching me one of the biggest lessons that I have learned so far in my scientific life: Never leave it to the theorists to interpret your result, always come up with a message yourself. Thank you Barbara for all your help. This thesis would not have been possible without your support.

I would also like to thank Axel Drees and Vlad Pantuev, who along with Tom Hemmick and Barbara Jacak have made the Heavy Ion Group at Stony Brook one of the best groups in the world. I would like to acknowledge the

great support by Ralf Averbeck, who at a crucial stage of this thesis, provided me with invaluable Monte Carlo data, Sasha Milov for his great inquiring spirit, and Mike Reuter, the software guru of the group that taught me how professional programing is really done.

During the hectic months of the east Drift Chamber repair, Rich Hutter helped me enormously at the machine shop, teaching me how to cut metal and how to make professional designs with Auto Cad. Rich Hutter is the Dr.Q of our group. I quote a few lines from Wikipedia.com that describes Q's relationship with Bond:

"The gadgets supplied by Q are almost invariably destroyed as a result of Bond's use of them, and Q is constantly exhorting Bond to take better care of them and to occasionally read the instruction manual."

I could have never expressed in better words my true relationship with Rich.

I would also like to thank the graduate students of the group for providing such a great intellectual environment to work at, in particular Sean Leckey, who beyond a fellow student was also a great friend, Sergey Butsyk, Jiangyong Jia, Anne Sickles, Matt Nguyen, Jamil Egdemir, Dylan Walker, and the rest of the new gang.

From PHENIX, my gratitude goes to Mike Tannenbaum, for teaching me everything I know about cross sections and trigger biases and many many more, directly, or indirectly, through his monumental analysis notes that serve as an invaluable source of information of experimental methods to young scientist in the heavy ion field. Along with Mike Tannenbaum, one of the pillars of the PHENIX experiment is Yasuyuki Akiba, with whom I had the honor to

work closely during the days that I was involved with the electron research. Drs. Akiba and Tannenbaum set the example of scientific ethos and share an insatiable passion for discovery. Along with Tom Hemmick, they were the most influential scientists in my career so far,and for that I wholeheartedly thank them.

This thesis would not have been made possible without the infinite support by Tatsuya Chujo and Julia Velkovska, the pioneers of identified particle analysis with the Phenix Time of Flight in Au+Au collisions. And that is for two reasons. First, for teaching me their techniques in identifying particles with the TOF and providing me with my first code for such an endeavor, and second, because without their Au+Au data, this thesis would not have been as half as interesting as their data make it to be. I thank them for their support, for sharing their data. Tatsuya virtually rescued the p+p part of my analysis, when months of investigating the source of incompatible results had reached a dead end. For his help I will always be grateful.

I would like also to thank Gabor David, for taking the time to organize reading seminars for graduate students, Chris Pinkenburg, for teaching me everything I know about online software, David Morrison, for helping me in my first steps with the offline software, Ron Soltz, for his patience as a convener of my research group, Jamie Nagle for our endless conversations about how to define centrality in d+Au collisions, and last but not least, the neutral pion gang, Henner Bueshing, Stefan Bathe, Saskia Mioduszewski and Sasha Bazilevsky, for sharing their data with me and keeping it cool during the stages where the neutral and charged pions did not agree that well!

My love goes to my wife, Emily. She followed me in the U.S. so that I

could pursue my dream, leaving family and friends, to meet me in a freezing Ames, Iowa, in my second year of graduate studies at Iowa State. She never looked back. From being a jewelery store owner, she became the 2002 Stony Brook valedictorian and now a graduate student in the Comparative Literature Department. She brings the sanity and reason in my chaotic life, and during the last months of finishing this work, she kept things going on in our home. For that, I dedicate this thesis to her. Along with my mother. She is the reason I was able to fulfill my dreams, first supporting me during my undergraduate years in Thessaloniki, and then for making it possible for me to come to the United States. Along with my father, she believed in me and even though she would have liked me to be closer at home, she never stopped encouraging me, in every step of the way. The same goes for my father. His hard work made it all possible for me. Even though he never really understood what I was really doing in the U.S., and even though he never managed to pronounce either "Stony Brook" or "Brookhaven" correctly, not a single time, he was always proud for me. I thank him from the bottom of my heart.

Chapter 1

Introduction and Perspective

1.1 Introduction

The very essence of this thesis is the measurement of 36 particle spectra. Namely, we performed a counting experiment where we recorded, as a function of transverse momentum, the production rates of π^+, π^-, K^+, K^-, p and $\overline{p}$ that emerge from:

- $\sqrt{s} = 200$ GeV proton-proton (p+p) collisions
- $\sqrt{s} = 200$ GeV Minimum Bias Deuteron-Gold (d+Au) collisions
- $\sqrt{s} = 200$ GeV d+Au collisions in 4 centrality bins

whereby centrality bins we mean that we are able to distinguish between central, mid-central, peripheral and ultra-peripheral d+Au collisions and register the particle spectra separately in each case. Obviously the Minimum Bias d+Au measurement is the sum of all centrality bins, but we would like to refer to it as a distinguished item in our menu of spectra, although not independent. The measuring apparatus was the central spectrometer of the Pioneering High Energy Nuclear Interaction Experiment (PHENIX) [1] which detects collisions provided by the Relativistic Heavy Ion Collider (RHIC) [2], [3] at the Brookhaven National Laboratory (BNL) [4] in Upton, New York.

It is evident from the measured quantities that the goal of this thesis is to investigate the properties of identified particle production in elementary nucleon-nucleon (p+p) and nucleon-nucleus (p+A) interactions, and make quantitative statements about the differences and similarities of these two nuclear environments. It is well known since the early 70's that the particle production in p+A collisions does not scale with the number of available p+p collisions. In p+A collisions, at low momentum, there is a suppression of particle production, and at higher momentum there is an excess, as compared to a naive collisional scaling. The former effect is named shadowing and the latter was named "the Cronin effect" after a seminal paper by J.W. Cronin and collaborators [5], [6] who, for the first time, measured and parameterized the A-dependence of the invariant cross section in p+A collisions by:

$$I_i(p_T, A) = I_i(p_T, 1) \cdot A^{a_i(p_T)} \tag{1.1}$$

where I_i denotes the invariant cross section and the index i refers to the particle species produced. Suppression means that $a_i < 1$ while the Cronin effect is the manifestation of $a_i > 1$ above some momentum value, typically around 1 GeV/c.

Put in different words, the Cronin *et al.* measurement at low energies ($\sqrt{s}$ = 19.4, 23.8, 27.4 GeV) and this present thesis at $\sqrt{s}$ = 200 GeV, seek to measure the effect of the propagation and scattering of particles through the color field of a nucleus. Soon after these experimental discoveries, Lev and Petersson [8], and Krzywicki and collaborators [9] tried to give a theoretical interpretation of the Cronin effect at high momentum as the result of multiple scattering of partons inside the nucleus, using the framework of Quantum Chromodynamics (QCD). This original idea still pervades the modern literature although it is inadequate for the most part to give an explanation on the particle species dependence of the effect, with proton and antiproton enhancement in p+A collisions being significantly larger compared to the kaon and pion enhancement.

This short introduction on the importance of p+A collisions for our understanding of the strong nuclear force inside the color field of a nucleus, would have been reason enough to justify the existence of this thesis. But this is only half the story for this work, the other half arising from the third and final nuclear environment that we have not mentioned yet, namely the A+A collision system which experiences its Golden Era with the commissioning of a dedicated collider facility, the Relativistic Heavy Ion Collider and its satellite experiments, built to study these types of nuclear collisions at ultra-relativistic energies.

1.2 p+A Collisions Become the Reference Point

Certainly when the pioneering experimentalists of the 70's were discovering the nuclear effects on particle production in p-nucleus collisions, using as a reference point the properties of p+p collisions, they could not imagine that the p+A system itself would become the reference point for relativistic A+A collisions. But this is indeed the case, and put under this context, the very existence of this present measurement was realized for the sole purpose of excluding -or verifying for that matter- theoretical scenarios that sought to interpret spectacular new phenomena discovered in ultra-relativistic A+A collisions in the first two years of RHIC operations. In other words, p+A became the control experiment.

And justifiably so. At RHIC energies, A+A collisions produce enormous energy densities, well above the critical $\epsilon_c \sim 1$ GeV/fm^3 value, that places the produced hot and dense nuclear matter well within the predicted Quark Gluon Plasma (QGP) phase. The primary goal of the RHIC program is therefore to investigate nuclear matter under extreme conditions of temperature and pressure and advance our understanding of the QCD vacuum, quark confinement, chiral symmetry breaking and of course, new unexpected phenomena in this outer limit of the QCD phase diagram. A brief introduction on the scope of the relativistic heavy ion field is therefore in order here, along with its connection to the p+p and p+A control experiments as was beautifully stated by Miklos Gyulassy in his review of the state of the field [10]. For an experimental review of the field we refer the reader to the monumental PHENIX White Paper that touches upon all experimental aspects of the search for the Quark

Gluon Plasma [11].

1.3 A New Phase of Matter

With the advent of QCD it was soon realized that the reduction of the coupling constant at small distances indicates that the dense nuclear matter at the center of neutron stars would consist of deconfined quarks and gluons [12]. Although this initial treatment focused on the low temperature - high density part of the QCD phase diagram it was realized that similar arguments would apply to the high temperature regime of the theory as Shuryak [13] described extensively in his review [13], where the phrase “Quark Gluon Plasma” first appears.

Shuryak argued that when the energy density ϵ exceeds some typical hadronic values ($\sim$ 1 GeV/fm^3), matter no longer consists of separate hadrons, but as their fundamental constituents, quarks and gluons. This idea of a critical energy density or temperature beyond which a phase transition occurs, and the degrees of freedom describing matter are no longer color-neutral hadron states but rather deconfined quarks and gluons, became the cornerstone of the relativistic heavy ion field and theorists and experimentalists for the next 20 years engaged the formidable task to prove the existence of this new state of matter.

To this day, the most quantitative theoretical support for the hypothesis that hadronic matter undergoes a dramatic transformation in its properties at temperatures of order 170 MeV/c is provided by lattice QCD calculations [14]. In Fig.1.1 the energy density over T^4 is shown for various numbers of species of quarks. Such calculations show that there is a rapid rise of the

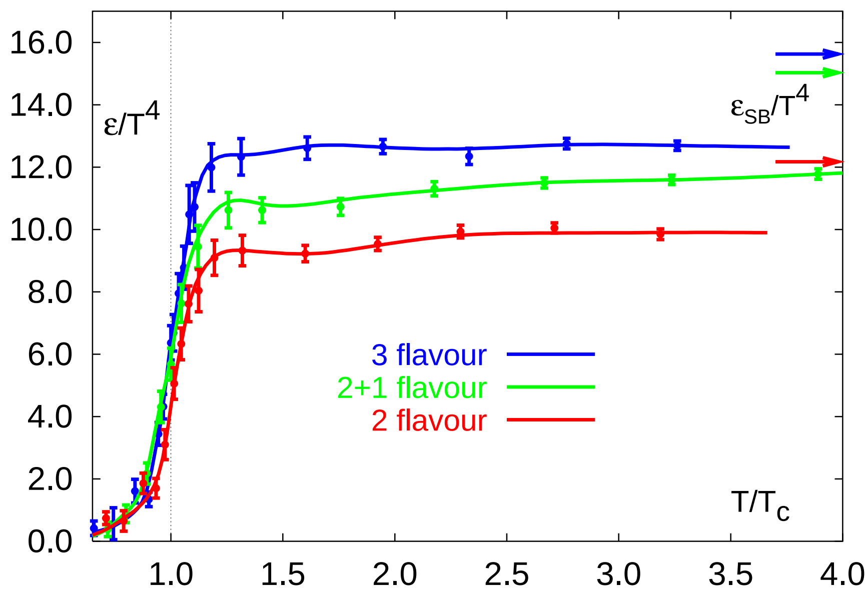

Figure 1.1: Lattice QCD results from [14] for the energy density / T^4 as a function of temperature.

energy density, $\epsilon(T)$, of matter when the temperature reaches T∼160 MeV∼ T_c. The energy density changes by about an order of magnitude in a narrow range of temperatures ΔT∼ 10 - 20 MeV. One can understand this transition as a change in the number of degrees of freedom, where below the critical temperature the active hadronic degrees of freedom are limited to the 3 charged states of pions, while above the critical temperature quark and gluon degrees of freedom become activated.

1.3.1 Plasma Signatures

Since the deconfined degrees of freedom eventually cool down and condense to the ordinary color-neutral hadron states, it is impossible to prove the existence of the QGP by direct measurement of the newly formed degrees of freedom.

A set of experimental observables that would suggest the formation of such a state of matter must be indirect in nature and a number of these observables have been proposed throughout the years and are typically called the QGP signatures. These include [15]:

- Kinematic probes

  These include average transverse momentum, hadron rapidity distribution, transverse energy, flow, and HBT two-particle correlations. These observables are related to the temperature, entropy and energy density of the plasma.

- Electromagnetic probes

  Photons and electrons escape unperturbed from the plasma since they do not participate in strong interactions and therefore can provide information about the earliest and hottest stage of the evolution of the fireball. Due to the smallness of the electromagnetic coupling constant these probes are extremely rare and pose a significant experimental challenge for their measurement. These probes include lepton pairs at low invariant mass where chiral restoration is predicted to alter the mass of hadronic states like the ρ particle, and direct photons where an excess would signify direct radiation from a very hot plasma stage.

- Probes of deconfinement

  The suppression of J/ψ production in a QGP would signify the fact that $c\overline{c}$ pair formation is significantly reduced due to the change of the screening length of the strong force inside the plasma. Strangeness enhancement is another observable that would suggest the creation of a hot plasma. The production of hadrons containing strange quarks relative to those that contain only up and down quarks is normally suppressed in usual hadronic reactions. Inside a plasma though the rapid equilibration of $s\bar{s}$ pairs is expected to saturate the production of hadrons containing strange quarks.

- Hard QCD probes

  The color structure of QCD matter can be probed by its effects on the propagation of fast partons through the dense and hot nuclear matter. Similar to the electromagnetic energy loss of a fast charged particle in matter , energy may be lost inside the plasma either by excitation of the penetrated medium or radiation. The stopping power of a QGP is predicted to be stronger than the stopping power of ordinary nuclear matter and therefore constitutes another experimental signature.

1.3.2 High p_T Suppression and Energy Loss

Of all the QGP signatures mentioned in the previous section, the high p_T suppression and energy loss is the most relevant to this thesis as we will be discussing in the next paragraphs. Partons propagating in colored matter lose energy predominantly through medium-induced emission of gluon radiation [16, 17]. When energetic partons scatter off color charges in the high-parton-density medium they radiate gluon bremsstrahlung. The reduction in the parton energy translates to a reduction in the average momentum of the fragmentation hadrons, which, in turn, produces a suppression in the yield of high-p_T hadrons relative to the corresponding yield in p+p collisions. The suppression of high-p_T hadrons therefore constitutes a direct experimental probe of the density of color charges in the medium through which the parton passes [18–20].

This predicted suppression was one of the first striking observations made at RHIC at $\sqrt{s}$ = 130 GeV [21], [22], and later on at $\sqrt{s}$ = 200 GeV [25], [26] $Au - Au$ collisions. In order to quantify experimentally the suppressed production of particles in ultra-relativistic A+A collisions a few definitions are in order. We closely follow [11] and unpublished notes by Mike Tannenbaum of the PHENIX Collaboration. A detailed proof of these formulae will be presented at a later Chapter.

Since hard scattering is point like, with distance scale $1/p_T \leq 0.1$ fm, the cross section in $p + A$ or $A + B$ collisions, compared to $p + p$, is proportional to the relative number of possible point-like encounters. The number of encounters of point-like constituents of nucleons is then proportional to A (AB), for p+A $(A + B)$ collisions. For $A + B$ collisions at impact parameter b, it is proportional to $T_{AB}(b)$, the nuclear thickness function, which is the integral of the product of nuclear thickness over the geometrical overlap region of the two nuclei.

In detail, the semi-inclusive invariant yield of e.g. high-p_T π^0's for $A + B$ inelastic collisions, with centrality f, is related to the $p + p$ cross section by:

$$\left.\frac{1}{N_{AB}^{\rm evt}}\frac{d^2N_{AB}^{\pi^0}}{dp_T dy}\right|_f = \langle T_{AB}\rangle_f \times \frac{d^2\sigma_{pp}^{\pi^0}}{dp_T dy} \quad . \tag{1.2}$$

Note that

$$\langle T_{AB} \rangle_f = \frac{\int_f T_{AB}(b)\, d^2b}{\int_f (1 - e^{-\sigma_{NN}\, T_{AB}(b)})\, d^2b} = \frac{\langle N_{coll} \rangle_f}{\sigma_{NN}} \quad , \tag{1.3}$$

where $\langle N_{coll} \rangle_f$ is the average number of binary nucleon-nucleon inelastic collisions, with cross section σ_{NN}, in the centrality class f. This leads to the description of the scaling for point-like processes as binary-collision (or N_{coll}) scaling.

Nuclear medium effects, like the above discussed suppression which is a final state effect or for example the Cronin effect which is regarded to be an initial state effect, can modify the expected scaling. These modifications can be quantitatively studied by measurement of the *Nuclear modification factor* R_{AB}, which is defined as

$$R_{AB} = \frac{dN^P_{AB}}{\langle T_{AB} \rangle_f \times d\sigma^P_{NN}} = \frac{dN^P_{AB}}{\langle N_{coll} \rangle_f \times dN^P_{NN}} \tag{1.4}$$

where dN^P_{AB} is the differential yield of a point-like process P in a $A+B$ collision and $d\sigma^P_{NN}$ is the cross section of P in $N+N$ collision. If there are no initial- or final-state effects that modify the yield of P in $A+B$ collisions, the process P scales with $\langle T_{AB} \rangle_f$ and $R_{AB} = 1$. Sometimes, the central to peripheral ratio, R_{CP}, is used as an alternative to R_{AB}. The central to peripheral ratio is defined as

$$R_{CP} = \frac{dN^{Central}/\langle N^{Central}_{coll} \rangle}{dN^{Peripheral}/\langle N^{Peripheral}_{coll} \rangle}, \tag{1.5}$$

where $dN^{Central}$ and $dN^{Peripheral}$ are the differential yield per event of the studied process in a central and peripheral collision, respectively. If the yield of the process scales with the number of binary collisions, $R_{CP} = 1$.

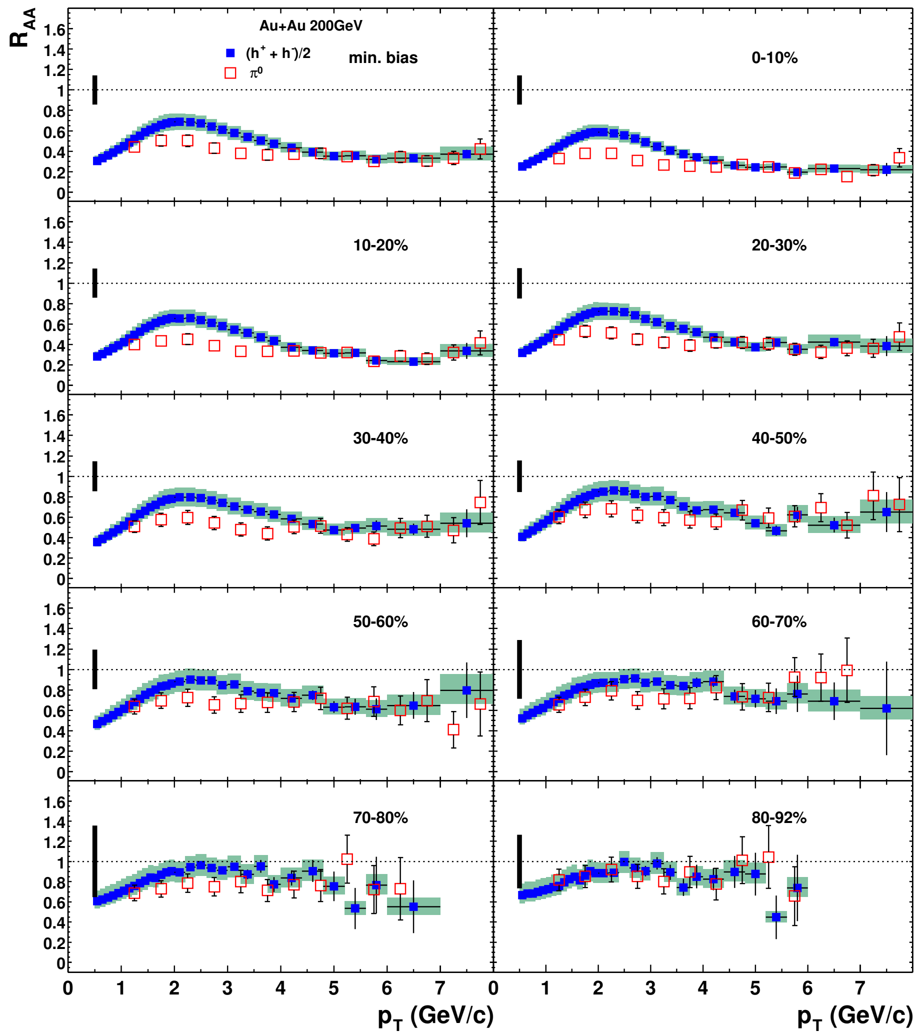

Figure 1.2: Nuclear modification factors in various centrality bins for $\sqrt{s} = 200$ GeV $Au - Au$ collisions from [25], [26].

As mentioned above, the suppression of high-p_T hadrons was one of the first striking results observed at RHIC. In Fig. 1.2 we show the nuclear modification factors, R_{AA}, for inclusive charged hadrons and neutral pions.

R_{AA} is below 1 for the most central collisions, a manifestation of suppressed $Au - Au$ hadron production, while, as the collision centrality evolves to more peripheral collisions R_{AA} approaches 1, as it should if we exclude any additional initial state effects, since in peripheral collisions there is no hot and dense matter produced. The observed suppression of high-p_T particle production at RHIC is a unique phenomenon that has not been previously observed in any hadronic or heavy ion collisions at any energy. The suppression provides direct evidence that $Au-Au$ collisions at RHIC have produced matter at extreme densities, greater than ten times the energy density of normal nuclear matter [11], and the highest energy densities ever achieved in the laboratory. Medium-induced energy loss, predominantly via gluon bremsstrahlung emission, is the only currently known physical mechanism that can fully explain the magnitude and p_T dependence of the observed high-p_T suppression. But there is more to it than meets the eye.

1.4 Surprising Results from Identified Particles in Au+Au Collisions

From Fig. 1.2 the careful reader has already observed the fact that the inclusive charged hadron suppression and the π^0 suppression follow different patterns. Since for the most part the inclusive charged hadrons consist of pions, kaons, protons and antiprotons, we are lead to assume that the suppression pattern of these particles are not the same. Soon after the discovery of suppression in $Au-Au$ collisions, identified hadron analyses signaled a very unusual pattern. Namely an unusually large proton and antiproton production , relative to the much lighter and therefore phase-space favored pion, as compared to elementary hadronic collisions. That by itself is a spectacular result since it is

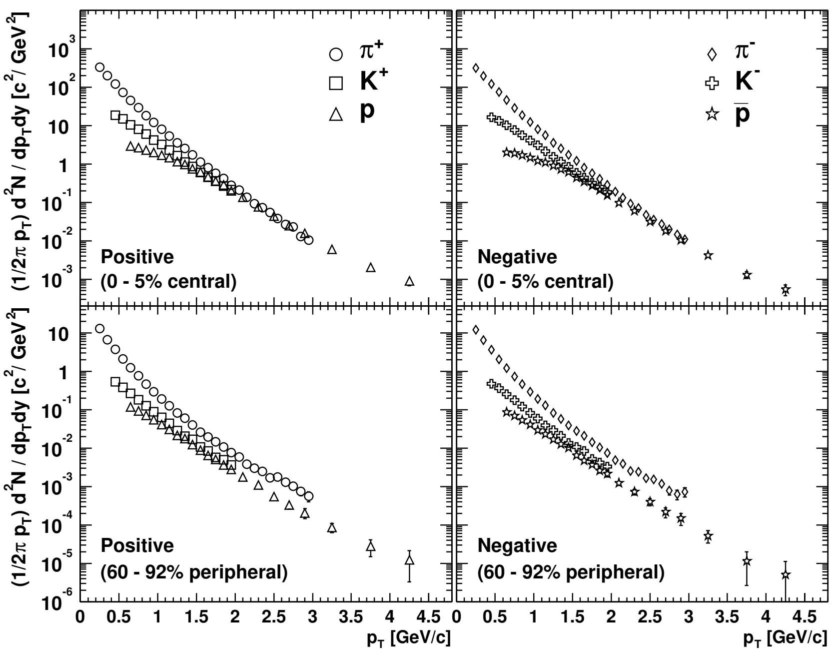

Figure 1.3: Identified spectra for $\sqrt{s} = 200$ GeV $Au - Au$ collisions from [27]. The protons and antiprotons cross the charged pion spectra at around $p_T \sim 1.5$ GeV/c.

in direct contradiction with parton fragmentation expectations.

This phenomenon was first observed in $\sqrt{s} = 130$ GeV collisions [24], [23], but due to the limited statistics of this measurement we will concentrate on the $\sqrt{s} = 200$ GeV results [27], [28], since this also is the center of mass energy that the present p+p and d+Au identified measurements were made. As shown in Fig. 1.3 in the most central $Au - Au$ collisions the protons and antiprotons cross the charged pion spectra at around $p_T \sim 1.5$ GeV/c. That was a discovery that had not been predicted by any theoretical model and it certainly was not in the menu of QGP signatures.

The complementary way of looking at this effect is through the proton to pion , (p/π^+), and antiproton to pion $(\overline{p}/\pi^-)$ ratios as shown in Fig. 1.4. These

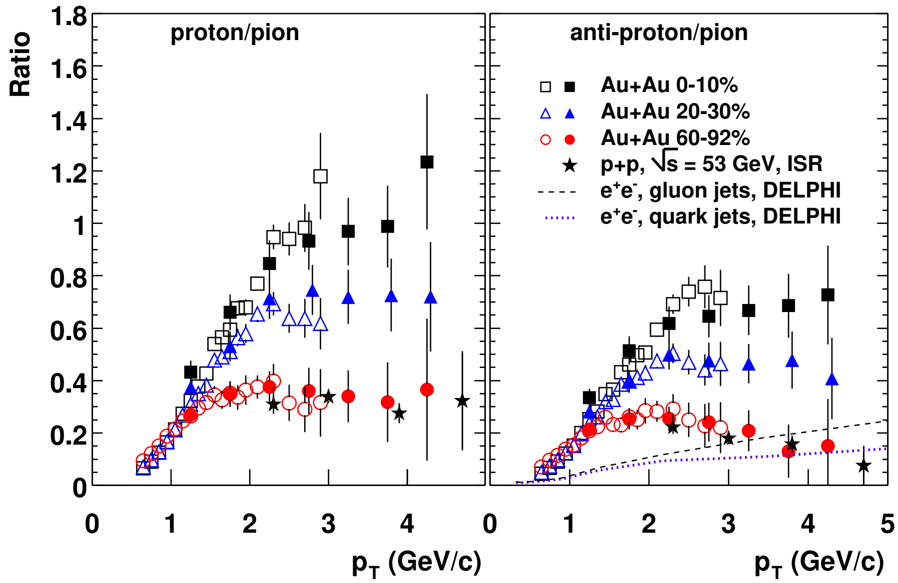

Figure 1.4: Proton to π^+ and antiproton to π^- ratios in $\sqrt{s}$ = 200 GeV $Au-Au$ collisions from [27] in three centrality bins.

unusually large ratios became known as the "anomalous p/π ratios".

In a similar manner, the central to peripheral ratios , R_{CP} (0-10%/60-92%), for the three particle species are shown in Figures 1.5 and 1.6 where in the latter Figure, the π^0 R_{CP}, that reaches much higher in transverse momentum, is also shown for comparison.

It is striking from these Figures that the previous arguments about energy loss in the hot and dense nuclear matter do not seem to apply for protons and antiprotons, while the kaons appear to be in between the pions and the protons. Another unexpected result arising from the identified particle production in $Au-Au$ collisions, is the collisional scaling of the proton and antiproton yields, above a certain p_T, as can be seen in Fig. 1.7. This is indeed an intriguing result since it points to the fact that the competing mechanisms for proton and antiproton production and propagation through the hot matter, like re-

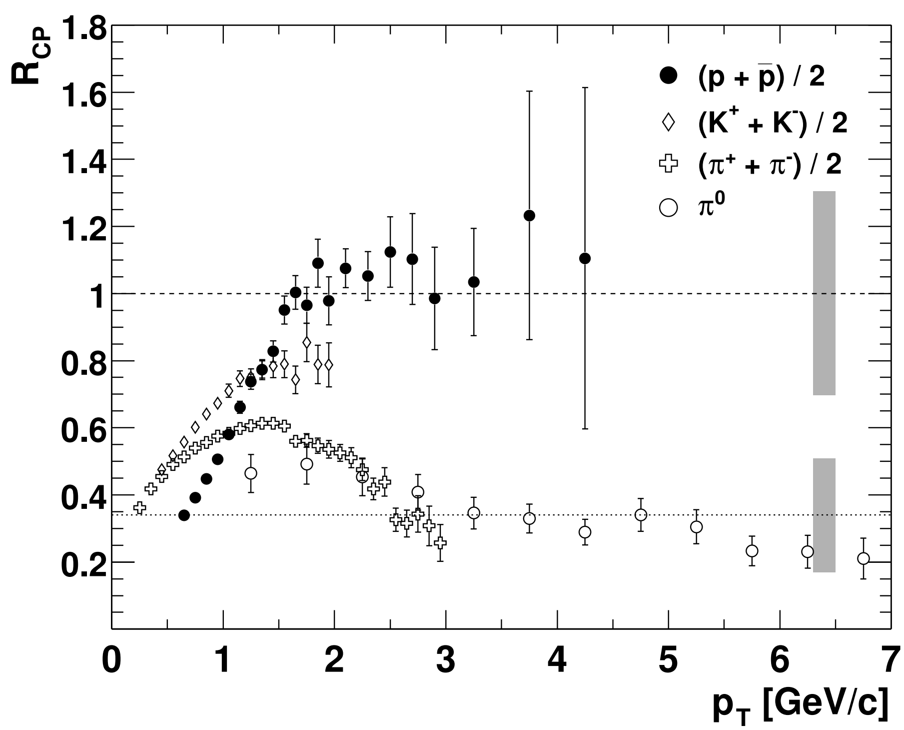

Figure 1.5: Central to peripheral ratios , (0-10%/60-92%), for identified charged hadrons in $\sqrt{s} = 200$ GeV $Au - Au$ collisions from [27].

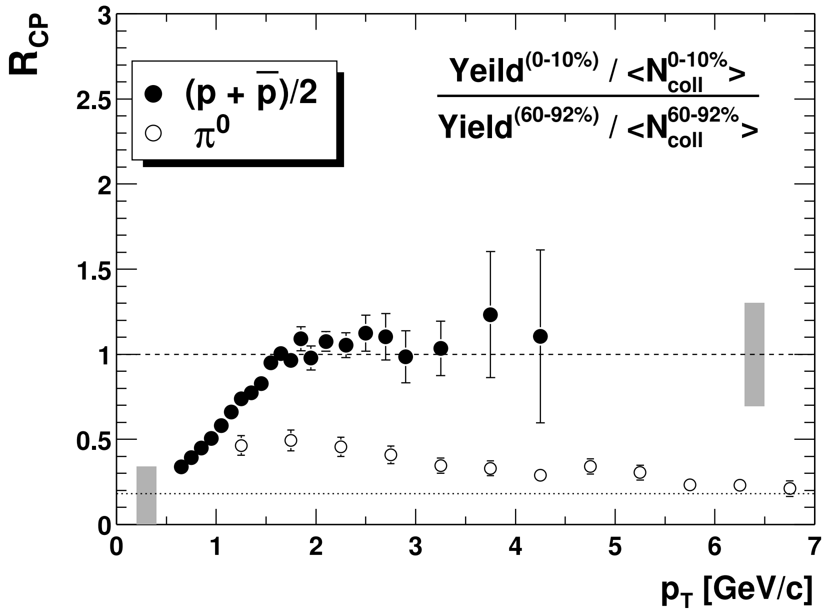

Figure 1.6: Central to peripheral ratios, (0-10%/60-92%), for $(p+\overline{p})/2$ and π^0 in $\sqrt{s} = 200$ GeV $Au - Au$ collisions from [27].

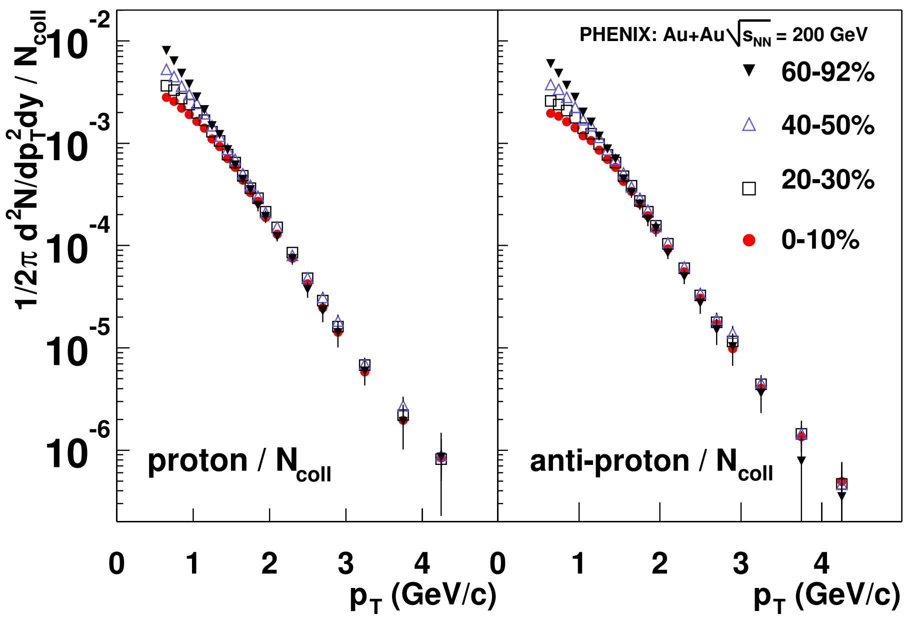

Figure 1.7: Proton and antiproton invariant yields scaled by N_{coll} in various centralities in $\sqrt{s} = 200$ GeV $Au - Au$ collisions from [28]. Error bars are statistical.

combination, radial flow and energy loss, for example, balance themselves out in a detailed way as to produce, at all centralities, N_{coll} scaled spectra. In other words, above $p_T \sim 1.5$ GeV/c, all spectra converge to the same slope and seem to obey N_{coll} scaling as expected for production due to hard processes in the absence of any nuclear effects, at all centralities.

Finally, although someone would expect that the antiproton to proton ratio would be a strong function of centrality in $Au - Au$ collisions, like the proton to pion ratio, as was shown in Fig. 1.4 , on the contrary, it is constant at around 0.73, momentum independent and shows no centrality dependence, within the systematic and statistical errors, as can be seen in Fig. 1.8.

In the following we briefly mention some of the proposed mechanisms that

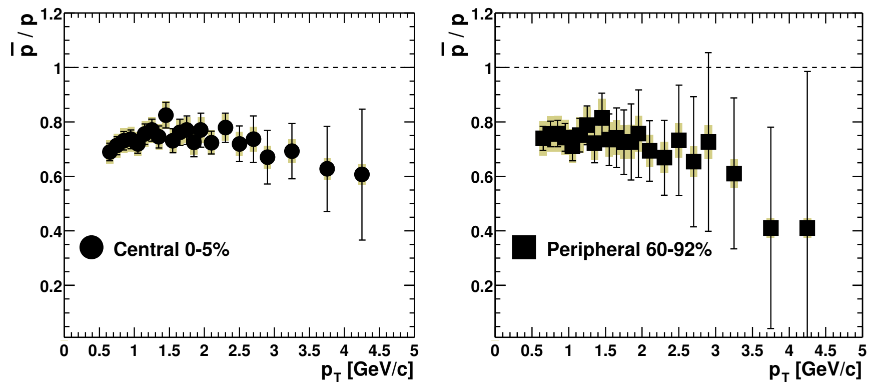

Figure 1.8: Antiproton to proton ratios in central and peripheral $\sqrt{s} = 200$ GeV $Au - Au$ collisions from [27].

can explain various aspects of this remarkable difference in the centrality dependence of pions, kaons, protons and antiprotons.

- Hydrodynamic models offer a natural explanation of the enhanced proton to pion ratio. They have successfully been used to reproduce the pion, kaon and proton spectra, [30], [31], [32], and the large $\overline{p}/\pi^-$ratio is a consequence of the strong radial flow [29]. All particle spectra converge to the same slope if p_T is sufficiently larger than the particle mass $p_T \gg m_0$. The anti-proton-to-pion ratio $\overline{p}/\pi^- \simeq 2\exp(-\mu_b/T_{ch})$ is governed only by the baryon chemical potential μ_b and the chemical freeze-out temperature T_{ch}. Using $T_{ch} = 177\,\mathrm{MeV}$ and $\mu_b = 29\,\mathrm{MeV}$ [33], $\overline{p}/\pi^-$ reaches a limiting value of 1.7.

- Recombination models [34] attempt to describe hadron formation, and were inspired by the increased probability of D meson production at forward rapidities, which is explained by coalescence of a hard scattering created charm quark with a light valence quark from the projectile. In the hot and dense matter created in heavy ion collisions, quark recombination has has been successfully applied to describe a number of features in identified particle production [34]. There have been various scenarios proposed, on what is actually recombining, for example Hwa and collaborators [91] allow hard partons to shower and then recombine with partons of the surrounding thermal background. Within the framework of these models it can be proved that recombination is the dominant hadron production mechanism over fragmentation, at intermediate p_T, while fragmentation dominates at higher p_T. The baryon excess is naturally explained by the quark content of hadrons.

1.5 Statement of Purpose

It is certainly not within the scope of this thesis to discuss the theoretical interpretation of all the surprising new phenomena discovered by the $Au-Au$ identified analysis. What is in the scope of this thesis though, is the detailed examination of identified particle production at the same center of mass energy, $\sqrt{s} = 200$ GeV, in elementary p+p and d+Au collisions, where hot and dense nuclear matter is not expected to be produced. The goal of this thesis is to state which of these new phenomena are already at work in elementary hadronic collisions, and can, therefore, be attributed to the initial conditions of the colliding systems, as opposed to effects that are present only during the production of matter at extreme conditions.

The identified production in p+p collisions accomplishes the first step of establishing the properties of the collision of 2 nucleons at RHIC energies. The d+Au analysis then will probe any effects arising from the wave-function of the Au nucleus, for example the Cronin effect, shadowing, or parton saturation. In particular, since we are able to select between central and peripheral d+Au collisions, we can measure the centrality dependence of various observables in the cold nuclear matter. The p+p and d+Au identified analyses serves therefore as the final link for a comprehensive study of identified charged particle production in p+p, d+Au, and $Au-Au$ collisions that will disentangle the cold from the hot nuclear matter effects, and will hopefully give a handle to present and future theoretical works, to construct a framework that can consistently describe particle production under any conditions and nuclear environments.

More specifically, the target of this thesis will be to:

- Measure identified particle spectra in elementary p+p collisions at $\sqrt{s} = 200$ GeV

- Provide the identified p+p spectra that will be used to calculate, for the first time at RHIC, identified nuclear modification factors , R_{AuAu}, in $Au-Au$ collisions, as opposed to Central to Peripheral ratios , R_{CP}, that are currently available, and therefore quantify the different suppression or absence of suppression, in an absolute scale, for all three particle species

- Measure particle spectra and nuclear modification factors, R_{dAu}, in d+Au collisions at $\sqrt{s} = 200$ GeV which will establish the initial conditions of the $Au - Au$ colliding system, without any further space for theoretical speculation for all three particle species. More specifically, measure the magnitude and species-dependence of the Cronin effect at these energies. As a consequence, this work, will be able to answer the fundamental question, if an enhanced Cronin effect for the protons and antiprotons, in d+Au collisions, is enough to explain the absence of suppression for protons and antiprotons in $Au - Au$ collisions.

- Measure the centrality dependence of the Cronin effect in d+Au collisions. Make a comparison to the magnitude of the effect observed at lower energies.

- Measure antiparticle to particle ratios in p+p and d+Au collisions and compare them to the corresponding $Au - Au$ ratios in order to make a quantitative statement about the origin of these ratios, and the apparent lack of any centrality or momentum dependence in $Au - Au$ collisions.

- Measure inter-particle ratios, p/π, K/π, p/K, in p+p and d+Au collisions and make a comparison to the corresponding $Au - Au$ ratios, as a function of centrality and momentum.

- Measure dN/dy and average transverse momentum, $< pt >$, for the three particle species in p+p and d+Au collisions and compare them to the corresponding quantities, as a function of centrality, in $Au - Au$ collisions. Examine if the smooth transition that they follow in $Au - Au$ collisions as a function of centrality continues to the more elementary colliding systems.

Chapter 2

The Phenix Experiment

2.1 PHENIX Detector

PHENIX [1], [35] is a sophisticated multi-detector system composed of 11 subsystems, which allows the measurement of hadrons, leptons and photons with excellent momentum and energy resolution. It is designed to perform a broad study of A-A, p-A and p-p collisions to investigate nuclear matter under extreme conditions. Since a large part of the spectrometer was designed to study the properties of excited matter through electromagnetic probes, which are rare due to the smallness of the E/M coupling constant, it uses Level-1 and Level-2 triggers in conjunction with the most sophisticated and fastest Data Acquisition system at RHIC, and can routinely reach recording rates of many KHz.

The PHENIX subsystems are grouped into four spectrometer arms – two around mid-rapidity (the central arms) and two at forward rapidity (the muon arms) – and a set of global detectors. The east and west central arms are cen-

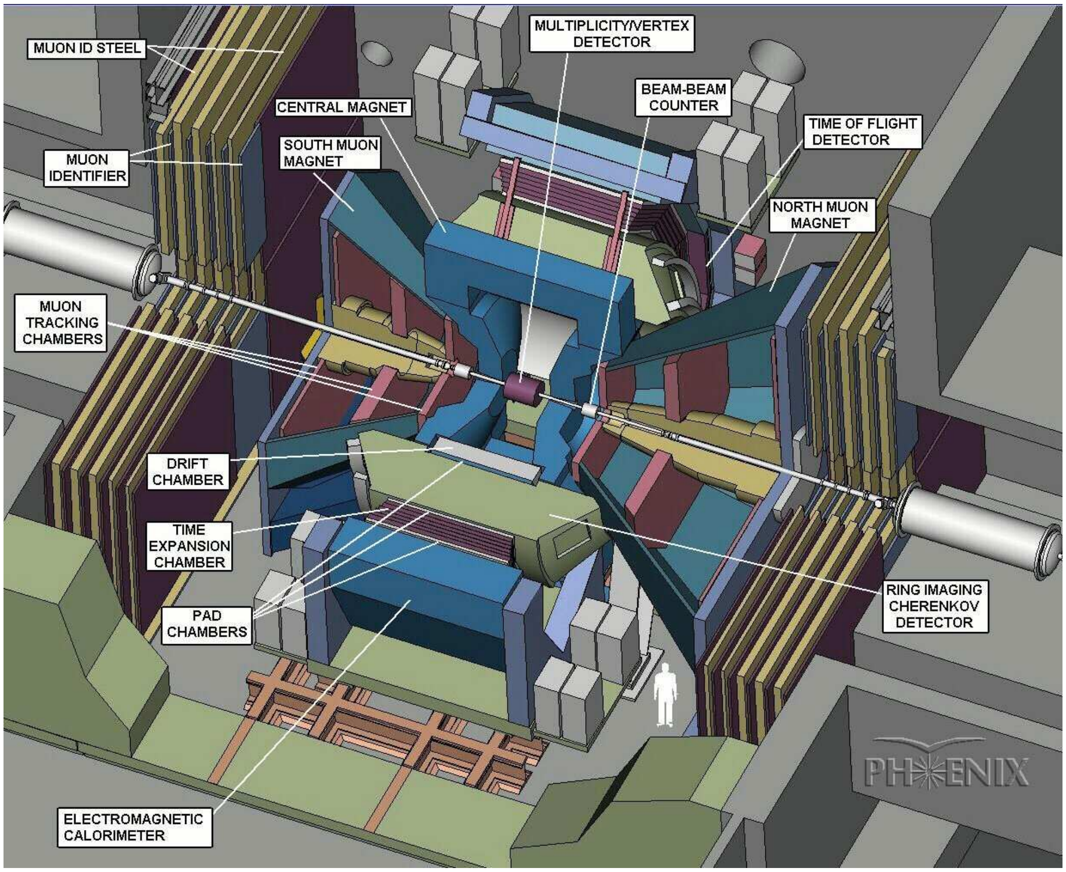

Figure 2.1: The Phenix Experiment.

tered around rapidity zero and are instrumented to detect electrons, photons, and charged hadrons. The north and south forward arms have full azimuthal coverage and are instrumented to detect muons. The global detectors measure the time and the position of the interactions, and the multiplicity of produced particles. The layout of the PHENIX detector is shown in Fig. 2.1. A beam view of the central spectrometer and a side view of the muon arms is shown in Fig. 2.2 A summary of the geometrical acceptance of each PHENIX subsystem along with its purpose is presented in Table 2.1.

The PHENIX coordinates are defined relative to the beam axis. The ori-

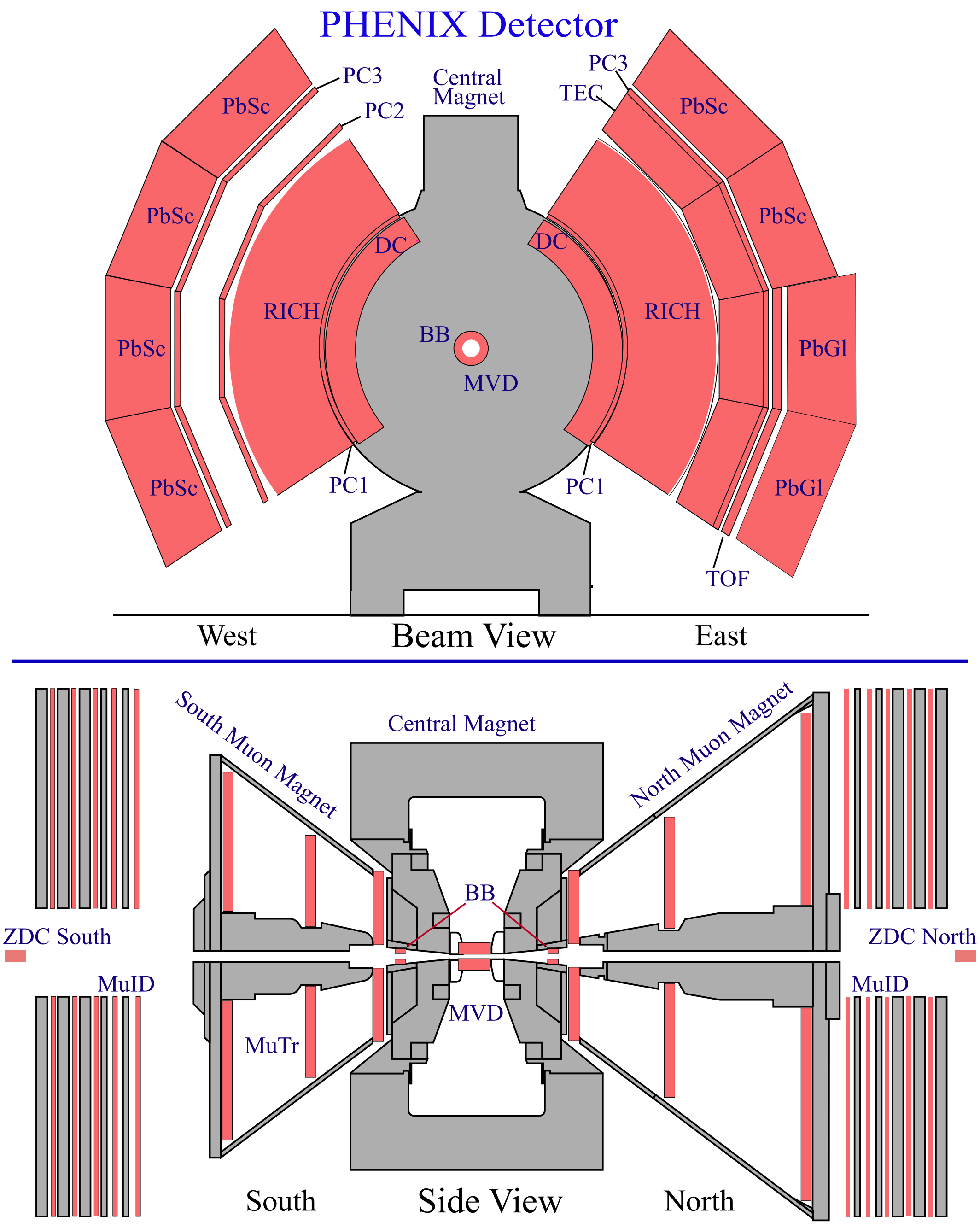

Figure 2.2: Beam view of the central arms and side view of the muon arms.

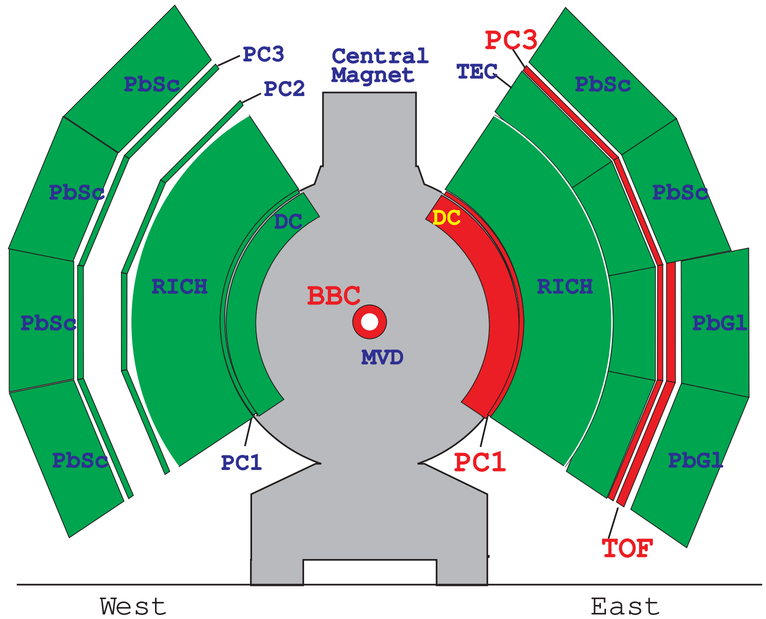

Figure 2.3: Subset of detectors used for identified hadron analysis.

gin is located at the middle of the beam axis, between the two Beam Beam Counters. In Cartesian coordinates, the z axis is along the beam axis pointing to the north muon arm, the x axis is pointing horizontally to the west arm and the y axis points up-wards.

The identified hadron analysis discussed in the present work uses a subset of the global detectors and a subset of the central arm detectors shown in Fig. 2.3 as will be described in the following.

2.2 Global Detectors

The global properties of the collision used in this analysis, including the collision vertex along the beam direction, the trigger and timing information, the impact parameter $\vec{b}$, and the charged particle multiplicity are measured

Table 2.1: Summary of the PHENIX Detector Subsystems [35].

Element	$\Delta\eta$	$\Delta\phi$	Purpose and Special Features
Magnet: central (CM)	± 0.35	360°	Up to 1.15 T·m.
muon (MMS)	-1.1 to -2.2	360°	0.72 T·m for $\eta = 2$
muon (MMN)	1.1 to 2.4	360°	0.72 T·m for $\eta = 2$
Silicon (MVD)	± 2.6	360°	$d^2N/d\eta d\phi$, precise vertex, reaction plane determination
Beam-beam (BBC)	$\pm$(3.1 to 3.9)	360°	Start timing, fast vertex.
NTC	$\pm$(1 to 2)	320°	Extend coverage of BBC for p-p and p-A.
ZDC	± 2 mrad	360°	Minimum bias trigger.
Drift chambers (DC)	± 0.35	90°×2	Good momentum and mass resolution, $\Delta m/m = 0.4\%$ at $m = 1$GeV.
Pad chambers (PC)	± 0.35	90°×2	Pattern recognition, tracking for nonbend direction.
TEC	± 0.35	90°	Pattern recognition, dE/dx.
RICH	± 0.35	90°×2	Electron identification.
ToF	± 0.35	45°	Good hadron identification, σ <100 ps.
T0	± 0.35	45°	Improve ToF timing for p-p and p-A.
PbSc EMCal	± 0.35	90°+45°	For both calorimeters, photon and electron detection.
PbGl EMCal	± 0.35	45°	Good $e^{\pm}/\pi^{\pm}$ separation at $p > 1$ GeV/c by EM shower and $p < 0.35$ GeV/c by ToF. $K^{\pm}/\pi^{\pm}$ separation up to 1 GeV/c by ToF.
μ tracker: (μTS)	-1.15 to -2.25	360°	Tracking for muons.
(μTN)	1.15 to 2.44	360°	Muon tracker north installed for year-3
μ identifier: (μIDS)	-1.15 to -2.25	360°	Steel absorbers and Iarocci tubes for
(μIDN)	1.15 to 2.44	360°	muon/hadron separation.

by the Beam Beam Counters (BBC). In the Au+Au analysis the Zero Degree Calorimeters (ZDC) are also used for centrality determination along and the Multiplicity Vertex Detector (MVD) measures the reaction plane of the collision. For our present analysis of the p+p and d+Au data set from RUN03 the ZDC and the MVD are not used. Other analyses of the d+Au data use the ZDC to tag a subset of peripheral d+Au events where the neutron of the deuteron nucleus does not interact in the collision and is detected by the ZDC -these events are usually called neutron-tagged events- but we don't separate these events from the rest of the Minimum Bias events in the present work.

The PHENIX beam-beam counters (BBC) are arrays of quartz Cerenkov detectors which measure relativistic charged particles produced in cones around each beam ($3.0 \leq \eta \leq 3.9$, with 2π azimuthal coverage). There are two identical Beam-Beam counters each positioned 1.4 m from the interaction point, just behind the central magnet poles around the beam axis. The inner(outer) radius of the BBC is 5cm(30cm), leaving about 1cm space from the beam-pipe. Each counter consists of 64 photomultiplier tubes equipped with quartz Cerenkov radiators in front. The BBC is designed to operate under various collision species (dynamic range 1-30 MIP), high radiation and large magnetic field (0.3 T). The main role of the BBC is to provide the start time for the TOF measurement, to serve as a crucial component for PHENIX Level-1 trigger, and to measure the collision vertex point (z_{vtx}).

The time and vertex position are determined by the BBCs using the measured time difference between the north and the south detectors and the known distance between the two detectors. The start time (T_0) and the vertex position along the beam axis (z_{vtx}) are calculated as

$$\begin{aligned} T_0 &= (T_1 + T_2)/2 \\ z_{vtx} &= (T_1 - T_2)/2c \end{aligned} \tag{2.1}$$

where T_1 and T_2 are the average timing of particles in each counter and c is the speed of light.

The BBCs also provide the trigger conditions for both the p+p and d+Au data set. A coincidence of the two BBCs and a vertex position along the beam axis within $|z| < 30$ cm constitute the Minimum Bias Level-1 trigger requirement used in this analysis. The Minimum Bias d+Au trigger accepts (88$\pm$4%) of all inelastic d+Au collisions that satisfy the vertex condition. In the p+p case, as we will discuss later on, the BBC trigger accepts approximately 50% of the total inelastic p+p cross section at $\sqrt{s} = 200$ GeV.

In d+Au collisions, the particle multiplicity measured by the South BBC (Au direction) is correlated with the collision geometry and can also be used to measure the collision centrality (impact parameter $|\vec{b}|$). The BBCs are sensitive to charged particles produced in the collisions (produced by participating nucleons) and can provide information on the impact parameter of the nuclear interaction. This observable, combined with a Glauber model for the collision geometry, allow us to determine different centrality classes. The details on a Glauber simulation in PHENIX are discussed in Chapter 4.

2.3 The Central Arm Detectors

Each of the west and the east central arm spectrometers covers the pseudo-rapidity range $|\eta| < 0.35$ and 90 degrees in azimuthal angle ϕ. As shown on Fig. 2.3, each of the spectrometers consists of layers of tracking and particle identification subdetectors. Viewed from the inner radius outward, the west arm spectrometer is composed of Drift Chamber (DC) at 2-2.4m, Pixel Pad Chambers (PC1) at 2.45m, Ring Image Cerenkov Counters (RICH) at 2.6-4.0m, Pixel Pad Chambers (PC2) at 4.2m, Pixel Pad Chambers (PC3) at 4.9m, and Lead Scintillator electromagnetic calorimeters (PbSc) at 5.07-6m. The east arm spectrometer consists of similar detectors as the west arm at the same radial locations, but it does not have PC2, and in addition, it has

2 sectors of a Time-of-Flight Scintillator Wall (TOF) at 5.06m, four layers of Time Expansion Chambers (TEC) at 4.1-4.8m between TOF and PC3, two sectors of PbSc and 2 sectors of Lead Glass electromagnetic calorimeters (PbGl) at 5.07m and 5.4 m, respectively.

In what follows we will discuss the subsystems of the East Central Arm used in this analysis for identifying pions, kaons, protons and antiprotons. These systems are: the magnet, DC, PC1 and TOF.

2.3.1 The Central Arm Magnet

The PHENIX magnet system [40] is composed of three spectrometer magnets, the Central Magnet (CM) and the north and south Muon Magnets (MMN and MMS). The Central Magnet is energized by two pairs of concentric coils and provides an axially symmetric field parallel to the beam and around the beam axis. Charged particles bend in a plane perpendicular to the beam axis. The bending angles are accurately measured by the DCs, from which the charged particle momenta can be accurately determined.

Fig. 2.4a shows the cutaway drawing of the PHENIX magnets showing the CM and MM field lines. The magnetic field for the central spectrometer is axially symmetric around the beam axis. Its component parallel to the beam axis has an approximately Gaussian dependence on the radial distance from the beam axis. At the center close to beam axis, the field line uniformly points along the beam direction. However, the residual field at the DC distance (2-2.4m radially) is highly non-uniform, the field line is parallel to the beam near $z = 0$, but has a significant r component at large z. The z dependence of the field is better illustrated in Fig. 2.4b, where B_z as function of radius r along the lines connecting origin and different z at the DC radius is shown. The field strength is about 0.48 T at the beam line ($r = 0$), and decreases as r increases. The field is almost uniform for different z at $r < 2m$. But in the drift chamber region, the residual field strength strongly varies with z. At around $z = 0$, the field is about 0.096 T (0.048 T) at the inner (outer) radius of the DC. At large z ($80cm$), the field changes direction and is much weaker(0.04 T(0.02 T) at the inner (outer) radius of the DC).

2.3.2 The Drift Chamber

The main goal of the DC [41] is to accurately measure charged particle trajectories in the r-ϕ direction to determine their transverse momentum (p_T), and the invariant mass of pairs of particles. Together with the hits measured by the PC1 detectors (mounted on the back of each DC) and the collision z_{vtx} measured by the BBC, the DC also determines the track polar angle θ. Finally the DC participates in the pattern recognition [43] by providing tracking information that is used to link together tracks and hits in various PHENIX central detector subsystems.

In order to achieve these functionalities, the DC performance has to satisfy the following main requirements:

- Single wire resolution better than 150 um in r-ϕ direction
- Single track reconstruction efficiency better than 99%
- Two track resolution better than 1.5 mm.

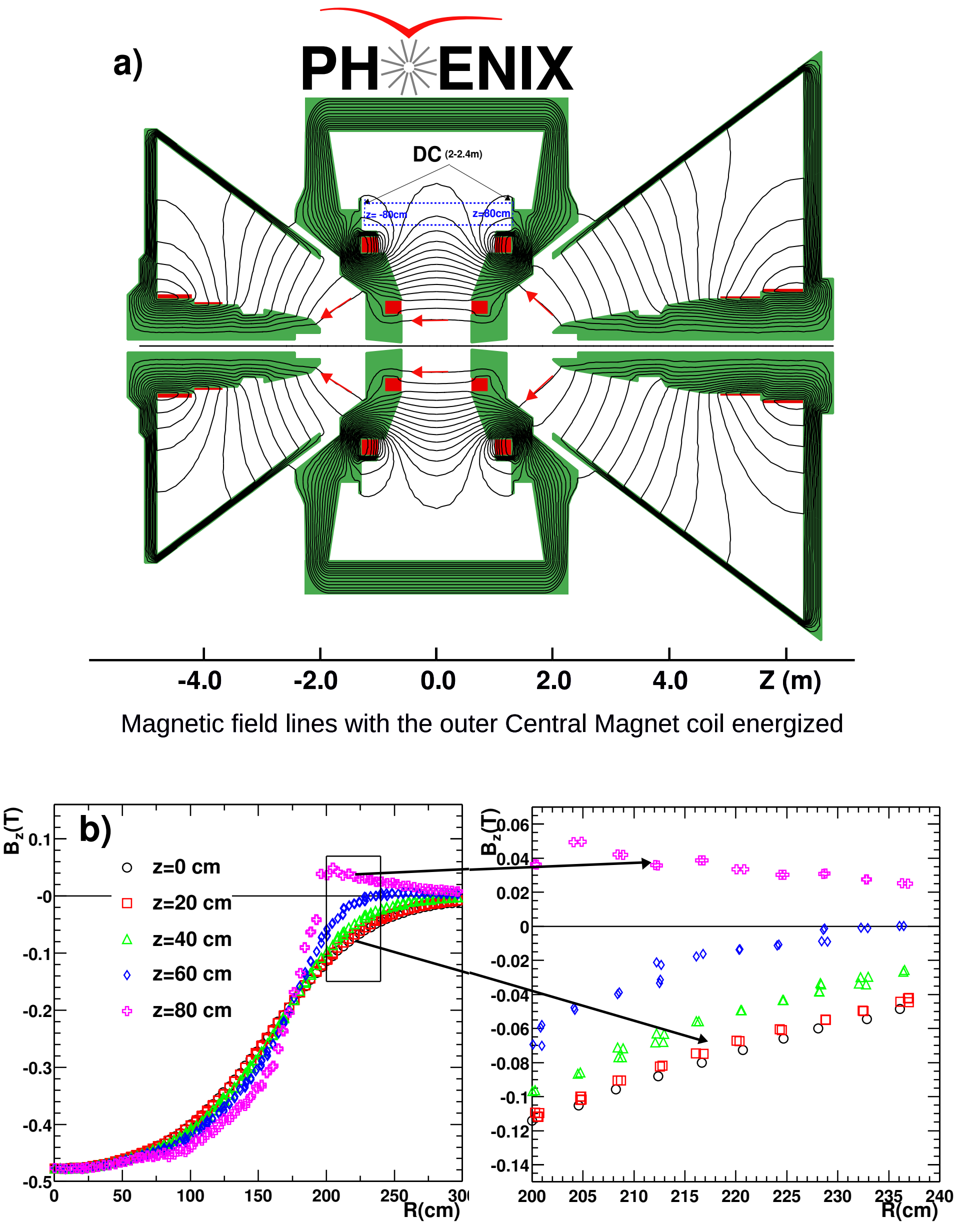

Figure 2.4: a) CM and MM field lines shown on a cutaway drawing of the PHENIX magnets. The beams travel along the z axis in this figure and collide at $z = 0$. b) z component of the magnetic field, B_z, as a function of, R, the radial distance along the line connecting origin and different z locations at the DC (it is the z component of the magnetic field that bends the track).

- Spacial resolution in the z direction better than 2 mm.

The PHENIX Drift Chamber system consists of two independent gas volumes located in the west and east arm, respectively. The east arm detector is the mirror image of the west arm. Each volume is defined by a cylindrical Titanium frame defining the azimuthal and beam-axis limits of the detector as shown on Fig. 2.5 which shows the east DC during construction phase. The detectors are located in the region from 2–2.4 m in radial direction from the beam axis. Their length is 1.8 m along the beam direction. Each DC covers $90°$ in azimuthal angle ϕ and consists of 40 planes of sensing wires subdivided into 80 drift cells, each cell spanning $1.125°$ in azimuth. The wire planes are arranged in six types of wire modules stacked radially in the following order, X1, U1, V1, X2, U2, V2. Each of the X and U,V modules contains 12 and 4 sense wires, respectively. The X, U, V wire orientations are shown in Fig. 2.6. The X1 and X2 wire modules run in parallel to the beam to perform precise track measurements in r-ϕ. U1,V1 and U2,V2 wire modules are placed after X1 and X2, respectively. They have stereo angles about $\pm 5°$ relative to the X wires and measure the z coordinate of the track. The stereo angle is selected to match with the z resolution of the pad chambers and minimize tracking ambiguities.

In typical central $Au - Au$ collisions, there are as many as 200 tracks in each DC. In order to reduce the occupancy and keep good track reconstruction efficiency, each sensing wire is separated electrically in the center by a low mass kapton strip ($100 \mu m$ thickness) and are read out separately as shown on Fig. 2.7. This way, the number of DC readout channels is doubled with little

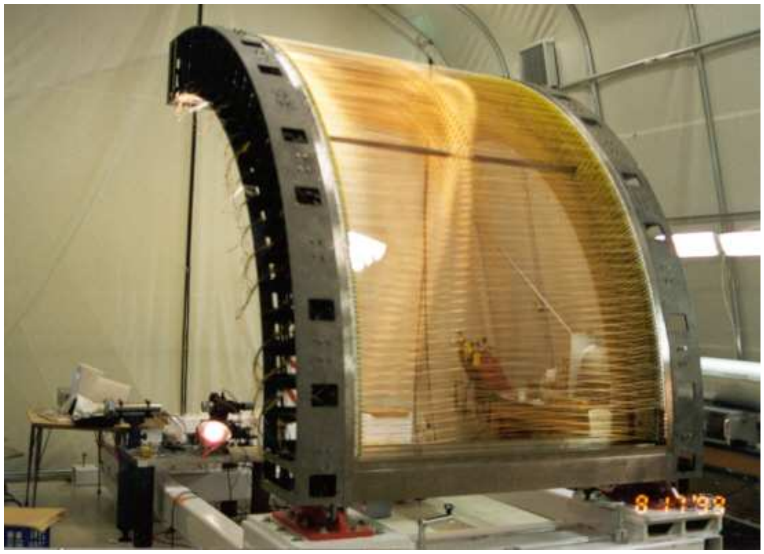

Figure 2.5: The DC Titanium frame being populated with FR4 cards that hold the high voltage and sense wires during production.

additional material in the fiducial volume of the chamber. In total, each DC contains roughly 3200 anode wires and ,therefore, there are about 6400 readout channels in total. The measured occupancy in central $Au-Au$ collisions is about 2 hits per wire.

In the third year of operation, RUN03, the momentum resolution was $\delta p/p = 0.7\% \bigoplus 1.1\% p(\mathrm{GeV/c})$. The momentum scale is known to 0.7%, from the reconstructed proton mass using the Time of Flight detector.

2.3.3 The Pad Chambers

The primary functions of the PCs [41] are [35]:

- Measurement of non-projective three dimensional spatial points, which are used for both momentum determination (p_z) and pattern recognition.

- Reject decays and photon conversion background at high p_T by tight

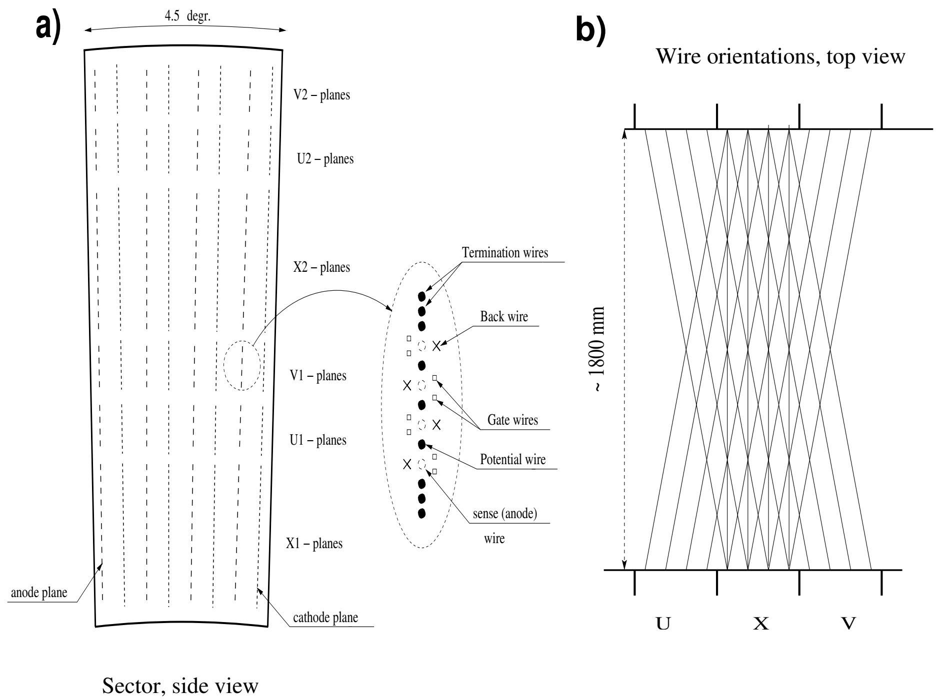

Figure 2.6: a) Layout of the wire position for 4 cells and a blow up drawing of the wire arrangement for a V1 net (the arrangement are similar for other wire nets). b) Top view of a schematic diagram of the stereo wire orientation.

matching requirement to the track measured by the DC.

- Distinguish electrons from other particles by accurate pointing of charged track to the RICH and EMCal.
- Charged particle veto in front of EMCal.
- Providing seed for tracks in charged high p_T Level-2 triggers and electron Level-2 triggers.

In this present work we implicitly use the east PC1 for momentum determination (p_z) and pattern recognition through the pattern recognition software.

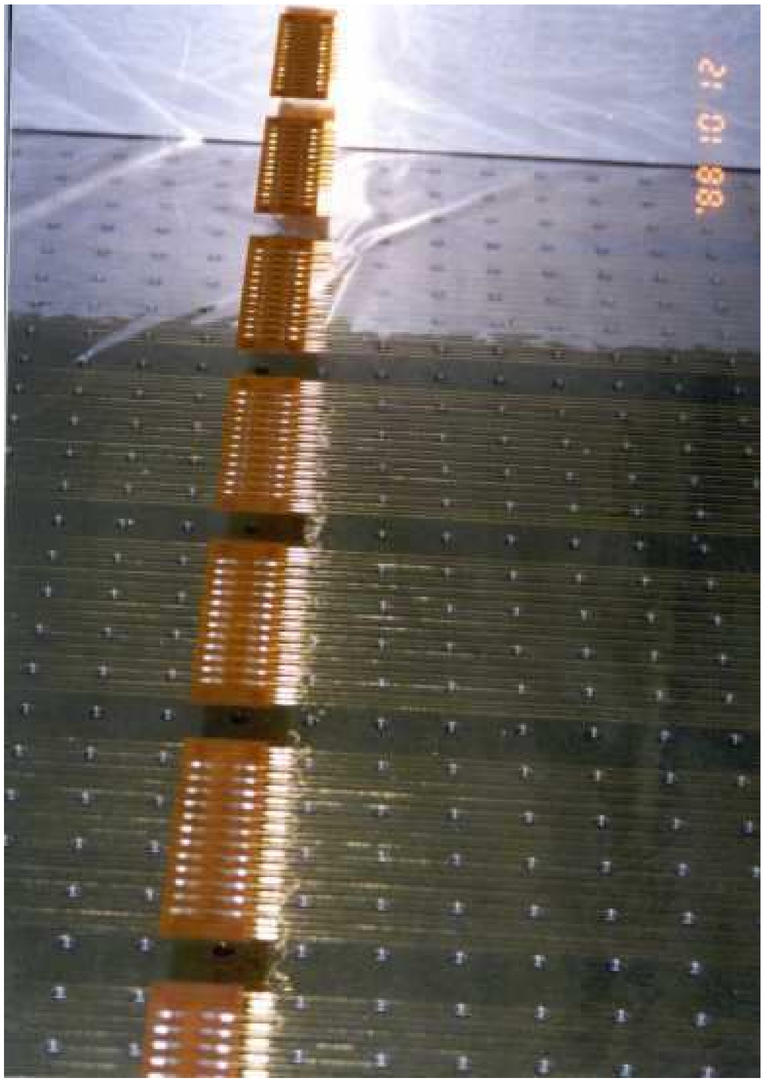

Figure 2.7: The anode wires from the north and south part of the DC terminate at a thin kapton film in the middle of the wire nets therefore doubling the number of DC readout channels. Each anode wire is first soldered in the kapton and then glued for additional strength.

Although in the high density Au+Au environment some identified analyses use the east PC3 for background reduction, by matching the PC3 hit information with each projected track from the track model, in the d+Au and p+p analysis the benefits of such matching cuts are virtually negligible due to the low occupancy of the detectors. In addition the inclusion of another detector in the analysis requires further efforts for the accurate determination of its efficiency and dead areas during the running period. For these reasons the PC3 detector is not used in the identified analysis of the p+p and d+Au data.

The design of the pad chambers is driven by the following considerations [36]

- Very high efficiency ($> 99\%$) and low occupancy(few % in most central $Au - Au$ collisions).
- Good spatial resolution.
- Low mass, in order to minimize secondary particle production and multiple scattering.

The PCs are multi-wire proportional chambers that form three separate layers of the PHENIX central tracking system. Each detector contains a single plane of wires inside a gas volume bounded by two cathode planes. One cathode is finely segmented into an array of pixels. The charged induced on a number of pixels when a charged particle starts an avalanche on an anode wire is read out through specially designed readout electronics.

The 3D view of the pad chamber system is shown in Fig. 2.8. The important PC specifications achieved in RUN-2 are listed in Table 2.2. The pad size for

PC1 is 0.84 $cm\times$ 0.845 cm to achieve less than 8% occupancy in most central $Au-Au$ collisions. This gives a position resolution of 1.7 mm along z and 2.5 mm in r-ϕ. The pad size for PC2 and PC3 is chosen such that they have similar angular resolution compared to PC1. The use of a frameless wire chamber held by honeycomb sandwich minimize the amount of material in the PC [36].

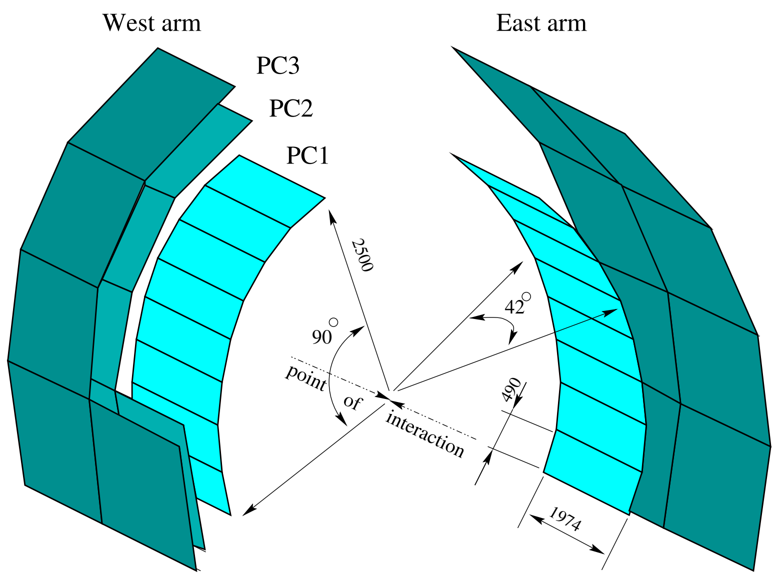

Figure 2.8: The Pad Chamber system in PHENIX. Several sectors of PC2 and PC3 in the west arm are removed for clarity of the picture. Figure from Ref. [36].

Table 2.2: Performance of Pad Chambers in RUN-2 [37, 36].

Parameters	PC1	PC2	PC3
Pad Size (r-$\phi\times z$)(cm^2)	0.84×0.845	1.355×1.425	1.6×1.67
Single hit resolution (r-ϕ, z) in mm	(2.5,1.7)	(3.9,3.1)	(4.6,3.6)
Double hit resolution (r-ϕ, z) in cm	(2.9,2.4)	(4.6,4.0)	(5.3,5.0)
Radiation Length (% X_0)	1.2	2.4	2.4
Efficiency	>99%	>99%	>99%

2.3.4 The Time Of Flight

The PHENIX Time of Flight (TOF) detector [42] is the most important device for identifying charged hadrons in a wide range of p_T and along with the east DC plays a key role in this analysis.

Particle identification with the TOF, DC and BBC is achieved by by comparing the particle time of flight to the measured momentum of the particle:

$$m^2 = (\frac{t_{TOF}^2}{L^2} - 1) \cdot p^2 \tag{2.2}$$

where t_{TOF} is the time of flight measured by the TOF, p is the momentum of the particle as measured by the DC, and L is the path length of the particle trajectory as measured by the track model. The start time of the collision is determined by the BBC. A track is reconstructed from hits in the DC and PC1 that point to the TOF detector. In this reconstruction we use a window for TOF association adjusted so that the residuals between the projection point and the reconstructed TOF hit position is within 3.0 standard deviations as will be shown in greater detail on the Data Analysis Chapter. The flight-path length of the track from the event vertex to the TOF detector as calculated by the track model is used to correct the time-of-flight value measured by the TOF detector.

The widths of the Particle Identification (PID) cuts used to select pions, kaons, protons and antiprotons are determined by the angular resolution of the DC, the timing resolution of the TOF and the multiple scattering term, through the following equation:

$$\sigma_{m^2}^2 = \frac{\sigma_\alpha^2}{K_1^2}(4m^4p^2) + \frac{\sigma_{ms}^2}{K_1^2}\left[4m^4\left(1+\frac{m^2}{p^2}\right)\right] + \frac{\sigma_{TOF}^2 c^2}{L^2}\left[4p^2\left(m^2+p^2\right)\right] \quad (2.3)$$

where p is momentum, m is particle mass, σ_α is the DC angular resolution in [mrad], σ_{ms} is the multiple scattering term, σ_{TOF} is the overall TOF resolution and K_1 is the field integral value (87.0).

The TOF detector contains 960 scintillator slats and 1920 channels of PMTs, oriented along the r-ϕ direction, covering $\pi/4$ in azimuthal direction in the lower part of the east arm, between the PC3 and the Electromagnetic Calorimeter. It consists of 10 panels of TOF walls as shown on Fig. 2.9. The upper 8 panels are named sector 1 of the TOF detector while the 2 lower panels are named sector 0 of the detector. In this analysis we use only the upper 8 panels (sector 1) of the TOF since the lower 2 panels were not fully calibrated at the time of this work.

One TOF panel consists of 96 segments, each equipped with a plastic scintillator slat and photomultiplier tubes which are read out on both ends. Fig. 2.11 shows a schematic view of one panel of the TOF detector. Each end of the scintillator slat is attached with optical glue to a 180° bent light guide as shown on Fig. 2.10. Scintillators with two different lengths (637.7 and 433.9mm) are assembled in an alternating fashion in order to avoid geometrical conflicts between the PMTs of neighboring slats. In each panel there are 64 long slats and 32 short slats. The slats provide time and longitudinal position information of particles that hit the slat. The hit position in the vertical direction (along the slats) is derived from the time difference observed in

Figure 2.9: The TOF system during installation in the east arm of PHENIX. All 10 panels of the detector are shown.

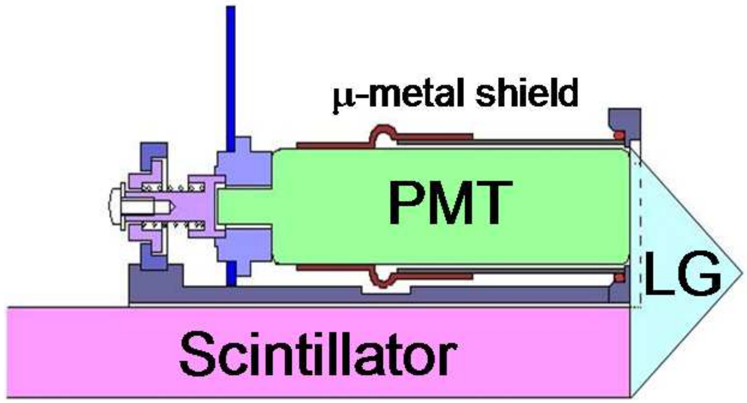

Figure 2.10: Close up view of the geometrical construction of one side of a TOF element, consisting of the plastic scintillation counter, the photomultiplier tube, the light guide and μ-metal shielding.

the signals, read out at the two ends of the slat.

The TOF system uses Hamamatsu R3478S PMT's. The length of the tube is about 6.7cm. The signal timing from the PMT is determined by a leading edge discriminator followed by a Time-to-Voltage Converter (TVC). The charge information is converted to a voltage by a Charge-to-Voltage Converter (QVC). The charge information at each slat can be fitted with a Landau distribution as shown in Fig. 2.12 and a channel-to-GeV conversion is calculated providing information on the energy loss of the particles hitting the TOF. The energy deposit at the TOF scintillators is then used to apply an energy loss cut that reduces noise hits on the detector.

After slewing corrections, shown on Fig 2.14, velocity of light on the scintillator calibrations, shown on Fig 2.13, and slat-by-slat and run-by-run timing offset corrections, as presented in detail in the Data Analysis Chapter, the TOF timing resolution in Au+Au collisions is about 100 ps [38]. In the RUN03 p+p and d+Au run the timing resolution is about 130ps due to the lower resolu-

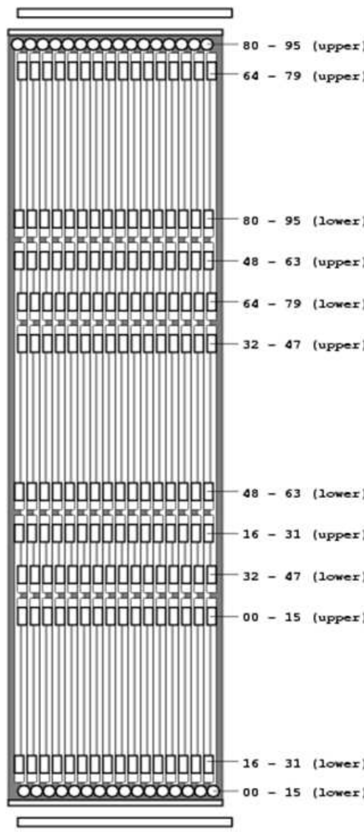

Figure 2.11: Schematic diagram of the composition of a single TOF panel, which consists of 96 plastic scintillation counters with photomultiplier tubes at both ends, light guides and supports.

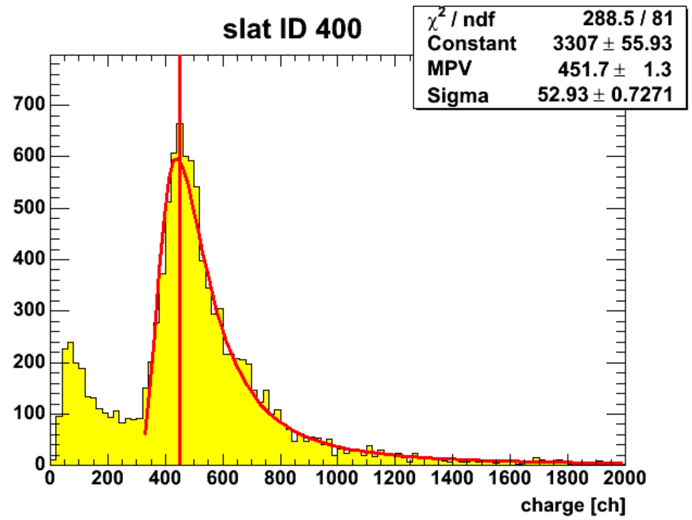

Figure 2.12: Landau fit to the charge distribution of an individual TOF slat. The MIP peak is at around 3 MeV.

tion in the start time signal of the BBC (lower hit multiplicities). With these excellent time resolutions the TOF detector can provide clear particle separation in the high momentum region, i.e. π/K separation up to 2.5 GeV/c and K/p separation up to 4.0 GeV/c. In addition the TOF is used in PHENIX to determine the DC momentum resolution and momentum scale, based on the width and mean location of m^2 for identified particles as function of p_T.

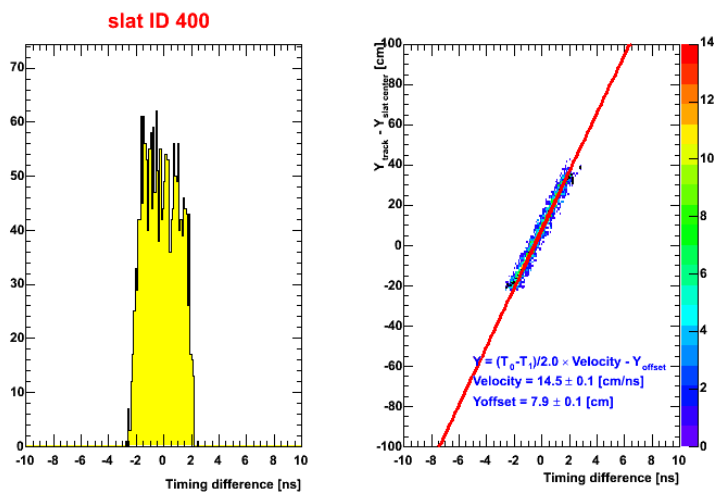

Figure 2.13: Left panel: Time difference of the times registered by the two PMTs reading slat ID 400. Right panel: Time difference versus position difference being fit by a straight line. The fitting parameters determine the velocity of light in each scintillator and the position offset that is then used in determining the hit position in the vertical direction.

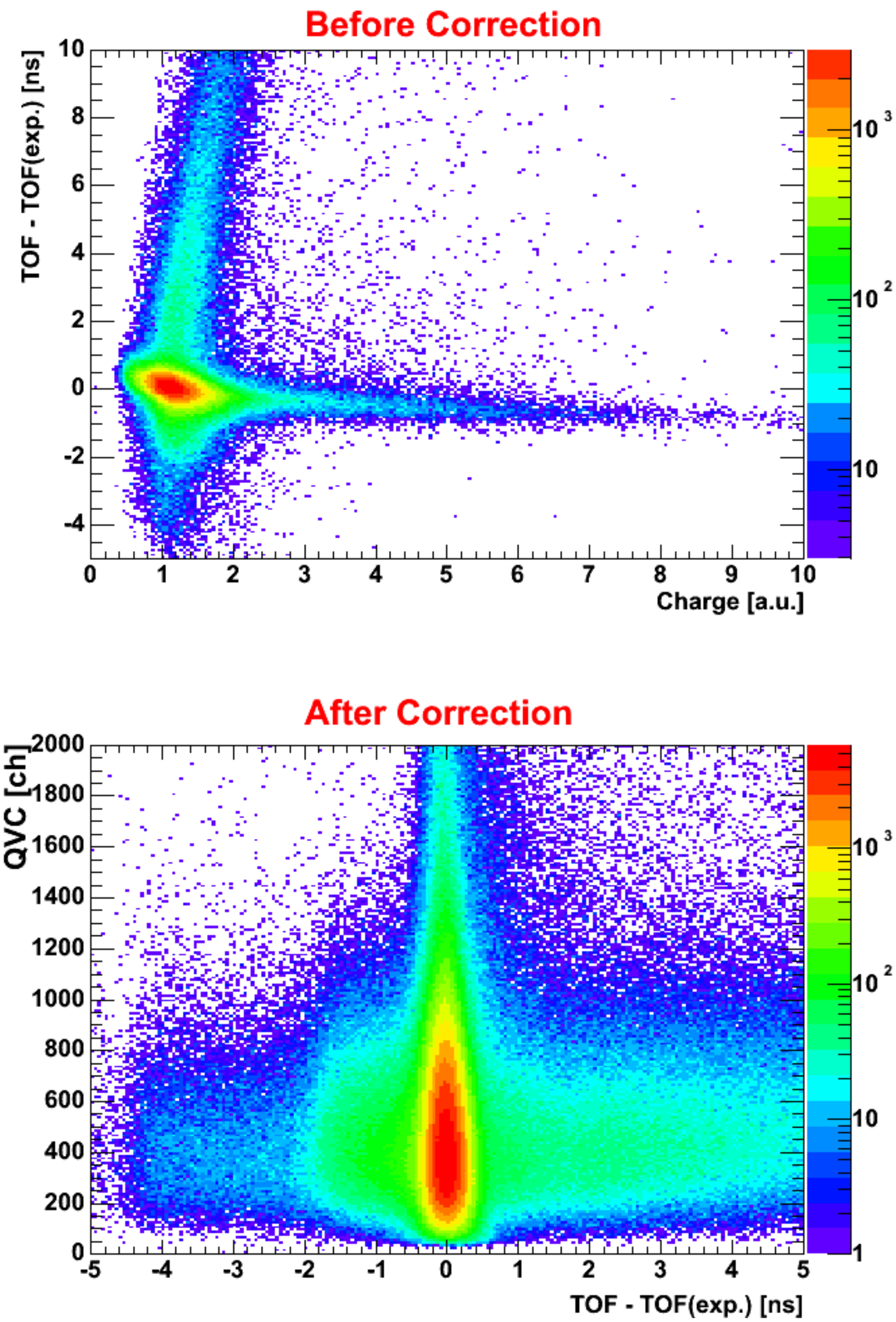

Figure 2.14: TOF slewing corrections. The expected time of flight of a pion, minus the measured time of flight measured by the TOF as a function of charge. Left panel is before the correction, the right panel shows the result of the slewing correction.

Chapter 3

"dear Boris , . . ."

3.1 Introduction

In this chapter[1] we describe the process of calculating physical cross sections from the measured particle yields and luminosity calibrations with the PHENIX experiment in p+p collisions. In the case of d+Au collisions PHENIX does not measure directly the inelastic d+Au cross section but rather particle yields per inelastic d+Au event. The repercussions of the inability to directly measure cross sections in the d+Au case are explained. We also review the concept of trigger bias in p+p and d+Au collisions and techniques for accurately determining it. Glauber model calculations and point-like scaling for hard processes are also discussed along with the definition and various formats of the nuclear modification factor. Finally, centrality determination is described in d+Au collisions, along with centrality selected nuclear modification factors.

[1]The title of this chapter was inspired by a letter written by Mike Tannenbaum to Boris Kopeliovich explaining a subtle point in the definition of the Deuteron-Gold nuclear modification factor used in the first d+Au PHENIX publication.

3.2 p+p collisions: A Complete and Robust Measurement of Particle Production Cross Sections

3.2.1 Cross Sections and Luminosity

The cross section of a process is a quantity that is intrinsic to the colliding particles, and therefore allows comparisons of two different experiments with different beam sizes and intensities [44]. Consider a target at rest consisting of particles of type B with density ρ_B [particles per unit volume], length L_B and cross-sectional area A. We aim another bunch of particles of type A with density ρ_A, length L_A and the same cross-sectional area, moving with velocity v, Figure 3.1. We expect the the number of scattering events (of any type) to be proportional to ρ_A, ρ_B, L_A, L_B and the common cross-sectional area A of the two bunches.

We define the cross section, denoted by σ, to be the total number of events (of whatever type) divided by all these quantities, Equation 3.1:

$$\sigma \equiv \frac{\text{Number of Scattering Events}}{\rho_A \cdot \rho_B \cdot L_A \cdot L_B \cdot A} \tag{3.1}$$

From this definition the cross section has the dimensions of area. Typically the size of cross sections in high energy and nuclear interactions is measured in barns, where:

$$1 \text{ barn } \equiv 10^{-28} m^2 = 10^{-24} cm^2 \tag{3.2}$$

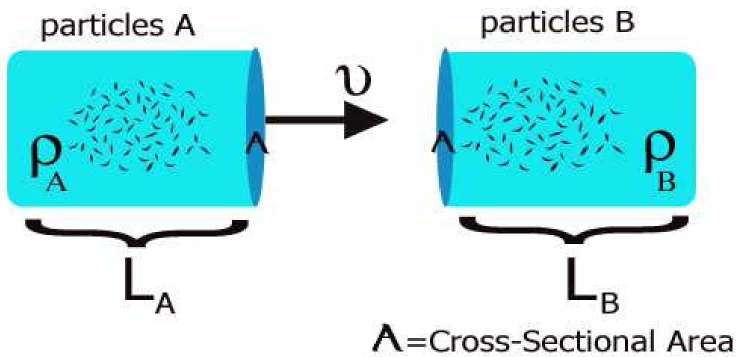

Figure 3.1: Two bunches of particles colliding.

As we shall see later on, at collision energies at $\sqrt{s} = 200$ GeV the nucleon-nucleon inelastic cross section is $(42.2 \pm 1.9)\ mb$ [45] [46] [50] , the d+Au cross section is $(2130 \pm 100)\ mb$ [47], and the Au+Au cross section is $(6847 \pm 542)\ mb$ [48].

Carrying on with the definition of cross sections, from Equation 3.1, we can rewrite the denominator as

$$\sigma = \frac{\text{Number of Scattering Events}}{\eta_A \cdot \eta_B \,/\, A} \tag{3.3}$$

where we used the fact that the total number of particles inside the colliding bunch can be written as

$$\eta_A = \rho_A \cdot L_A \cdot A \tag{3.4}$$

In the case of a storage ring where the frequency of the machine is f and assuming k bunches in each beam, we can write equation 3.3 as

$$\sigma = \frac{\text{Number of Scattering Events} \cdot f}{k \cdot f \cdot \eta_A \cdot \eta_B \,/\, A} \tag{3.5}$$

and writing $f = 1/T$ we have

$$\frac{\text{Number of Scattering Events}}{T} = \sigma \cdot [\frac{k \cdot f \cdot \eta_A \cdot \eta_B}{A}] \tag{3.6}$$

The left-hand side of Equation 3.6 is just the rate, R, of scattering events while on the right-hand side the quantity inside the brackets is defined to be the luminosity of the machine, a quantity that is solely determined by the characteristics of the machine

$$\mathcal{L} \equiv \frac{k \cdot f \cdot \eta_A \cdot \eta_B}{A} = \frac{k \cdot f \cdot \eta_A \cdot \eta_B}{4\pi \cdot \alpha_h \cdot \alpha_v} \tag{3.7}$$

where A is the effective cross-sectional area of the beam overlap and in the case of Gaussian beam profiles is proportional to the RMS horizontal and vertical dimensions of the beam, α_h and α_v accordingly. From the definition of luminosity we see that its dimensions are $[\frac{1}{area \cdot time}] = [cm^{-2} sec^{-1}]$. At RHIC the machine luminosity is expressed as [50]

$$\mathcal{L}_{machine} = \frac{f_{beam}}{2\pi \sigma_x^v \sigma_y^v} \cdot \sum_{crossings} (N_b \cdot N_y)_i \tag{3.8}$$

where f_{beam} is the revolution frequency for one bunch in the beam (78 KHz), σ_x^v is the horizontal width of the beam overlap as measured by vernier scans, σ_y^v is the vertical width of the beam overlap as measured by vernier scans, and $(N_b \cdot N_y)$ is the product of the number of protons in the blue (N_b)

and the yellow (N_y) bunches for the i^{th} beam crossing. In this expression there is no dependence on the longitudinal extent of the beam since at RHIC the two beams collide head-on, i.e. with zero crossing angle [50].

Integrating Equation 3.6 over the period of time that the machine is running and the experiment is collecting events we end up with the fundamental relation for scattering experiments in storage rings:

$$N^{Total\,Events}_{for\,process\,X} = \sigma^X \cdot \widehat{\mathcal{L}} \tag{3.9}$$

where $\widehat{\mathcal{L}}$ stands for integrated luminosity in units of cm^{-2}.

3.2.2 Lorentz Invariant Differential Cross Sections

In scattering experiments we are usually interested in measuring the particle production cross section for a particular process, for example pion production, as a function of the transverse momentum of the produced pions. In that case what we want to measure is the differential cross section which can be written in a Lorentz-invariant form in terms of rapidity and momentum p_T transverse to the beam direction (in the center-of-mass frame) [45]

$$E\frac{d^3\sigma}{d^3p} = \frac{d^3\sigma}{d\phi dy p_T dp_T} \tag{3.10}$$

where

$$y = \frac{1}{2}\ln(\frac{p_0 + p_z}{p_0 - p_z}) \tag{3.11}$$

is the rapidity of the particle and p_0 and p_z are the components of the 4-

momentum of the particle $p^{\mu} = (p_0, p_x, p_y, p_z)$. Assuming azimuthal symmetry for the process that we are interested in and integrating out the azimuthal angle ϕ we end up with the basic formula for invariant differential cross sections

$$E\frac{d^3\sigma}{d^3p} = \frac{1}{2\pi} \cdot \frac{1}{p_T} \cdot \frac{d^2\sigma}{dp_T dy} \tag{3.12}$$

3.2.3 The Ideal Measurement

Counting experiments measure the number of particles produced in a particular physical process of interest, which we will call the yield of the process from now on. Since the yield is a time dependent quantity that depends on how many events have been collected by the experiment, what is typically measured is the yield per event for the process of interest. To be more precise we measure the yield per event for the events that trigger the experimental apparatus. For example, for pion production in p+p collisions we measure the yield per BBC-triggered event for the process $p + p \rightarrow \pi + X$, where X means any other product, i.e. we are interested in inclusive pion production.

Differentiating Equation 3.9 with respect to momentum and rapidity of the detected particle we have

$$\frac{d^2\sigma^X}{dp_T dy} = \frac{1}{\widehat{\mathcal{L}}} \cdot \frac{d^2 N^{Total\,Events}_{for\,process\,X}}{dp_T dy} \tag{3.13}$$

and using equation 3.12 we have

$$E\frac{d^3\sigma^X}{d^3p} = \frac{1}{\widehat{\mathcal{L}}} \cdot \frac{1}{2\pi} \cdot \frac{1}{p_T} \frac{d^2 N^{Total\,Events}_{for\,process\,X}}{dp_T dy} \tag{3.14}$$

For an experiment that utilizes the full integrated luminosity offered by the machine -we are of course always referring to integrated luminosity corresponding to the live time of the experiment- which means that all events that are produced are triggered upon and registered by the detector and represent an unbiased sample of the physical phase space of the process of interest, Equation 3.14 is more accurately written as

$$E\frac{d^3\sigma_X^{Unbiased}}{d^3p} = \frac{1}{\widehat{\mathcal{L}}_{machine}} \cdot \frac{1}{2\pi} \cdot \frac{1}{p_T}\frac{d^2N_X^{Total\,Unbiased}}{dp_T dy} \tag{3.15}$$

where by unbiased we mean that the experimental trigger is not biased, i.e. all bunch crossings that produce an event that belongs to the complete set of events of process X , S_X, are triggered on by the detector and recorded to form the total unbiased yield of process X, $N_X^{Unbiased}$.

The luminosity of the machine, according to Equation 3.9 , can be expressed as

$$\widehat{\mathcal{L}}_{machine} = \frac{1}{\sigma_X^{Unbiased}} \cdot N_X^{Total\,Unbiased} \tag{3.16}$$

In this case we can use the experimental apparatus, or more specifically the triggering apparatus, as a luminosity counter, assuming that the physical (unbiased) cross section of process X is a priori known. Then we can write Equation 3.15 as

$$E\frac{d^3\sigma_X^{Unbiased}}{d^3p} = \sigma_X^{Unbiased} \cdot \frac{1}{2\pi} \cdot \frac{1}{p_T} \cdot \frac{1}{N_X^{Total\,Unbiased}}\frac{d^2N_X^{Unbiased}}{dp_T dy} \tag{3.17}$$

This is the idealized form of the famous “yield per event” equation. The problem with this equation is that it violates the principle of "there is no free lunch" since it implies that we can use the detectors for measuring the yield of the physical process X and also as luminosity counters at the same time. But, ...

3.2.4 Counting Luminosity Spoils the Counting of Pions

Although the "yield per event equation" is a beautiful idealized equation, there is nothing ideal about our measuring devices. It is extremely difficult to measure unbiased yields because of the limited nature of our triggering capabilities and the limited acceptance of the triggering detectors. The ideal solution would of course be to not trigger at all and record events at every bunch crossing but this is not practical. Nevertheless PHENIX has operated in this mode as will be discussed later on [54], albeit for very limited time, for the exact purpose of measuring bias effects. These triggers are called clock triggers since the detectors are triggering on each bunch crossing which is determined by the RHIC clock.

Equation 3.16 implied that the triggering detectors of an experiment can serve as luminosity counters. It was further implied that the process X used to normalize the luminosity counters should be a physical process. Of course all processes are physical processes but not all of them are meaningful. In the PHENIX case for example someone could use as the process X the subset of events in p+p collisions that trigger the BBC counters with no additional requirements. Obviously this is a physical process albeit not a meaningful one in the sense that it is irreproducible by other experiments. Someone should use the same detectors with the same efficiency at the same geometrical location to reproduce this measurement. Nevertheless any process is legitimate for normalizing the luminosity measurement and the subset of events in p+p collisions that trigger the BBC counters -without any further requirements from the central detectors- is exactly what PHENIX uses. Clearly this is a set favoring forward rapidity events, let us call it S_{BBC}, which is a subset of the total set of events that comprise the total inelastic p+p cross section, which we call S_{inel}.

We will see later on that although this process is sufficient to normalize the luminosity counters it creates a bias in the measurement of inclusive particle production in the mid-rapidity region where the PID detectors are located. In simple words, using the BBC as luminosity counters spoils the counting of pions. The reason is that the events that belong to S_{BBC} are not an unbiased subset of events of the total inelastic p+p cross section set, S_{inel}. To be more accurate, the problem is not that S_{BBC} is a biased set of events but rather the fact that we don't know apriori what fraction of the total mid-rapidity pionic events is contained in this biased subset as shown in Figure 3.2. In the most extreme case we could have the situation where S_{BBC} contains no mid-rapidity pions at all, something totally improbable but it drives the point. The requirement for measuring an unbiased pionic yield can be expressed as

$$\frac{Y^{\pi}_{BBC}}{Y_{BBC}} = \frac{Y^{\pi}_{total\,inel}}{Y_{total\,inel}} \tag{3.18}$$

which is not true as we will see later on (Y stands for yield in Equation 3.18). All is not lost of course since there is a way to calculate this bias but before we

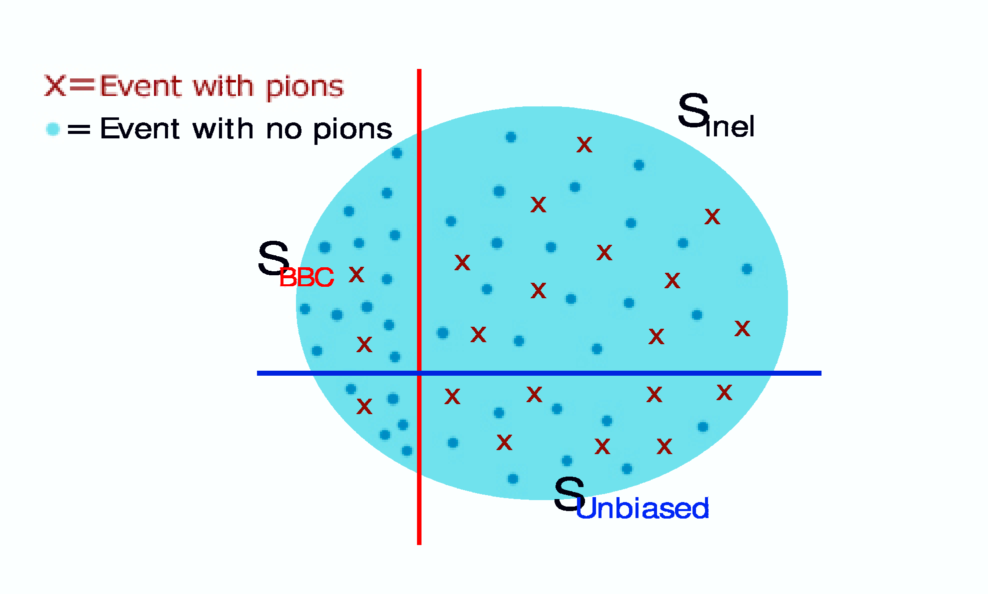

Figure 3.2: Set theory for group of events.

do that lets discuss briefly the procedure of using the Beam Beam Counters as luminosity counters. Along the way we will see the terms of the ideal "yield per event" Equation 3.17 being substituted, one after another, by effective terms which are relevant in a real life measurement with PHENIX.

3.2.5 PHENIX Beam Beam Counters as Luminosity Counters

PHENIX has a vertex region ($\pm$75 cm for the trigger and $\pm$30 cm in the offline analysis) which is small compared to the longitudinal length of the beams (FWHM $\sim$ 5-10 ns), and therefore the machine luminosity is not the relevant luminosity for PHENIX. In other words, not all of the machine luminosity is available to the experiment because the acceptance of the detectors restrict the vertex distribution. That means that Equation 3.15 should be written as

$$E\frac{d^3\sigma_X^{Unbiased}}{d^3p} = \frac{1}{\widehat{\mathcal{L}}_{effective}} \cdot \frac{1}{2\pi} \cdot \frac{1}{p_T}\frac{d^2N_X^{Total\,Unbiased}}{dp_T dy} \tag{3.19}$$

where $\mathcal{L}_{effective}$ is the effective luminosity seen by PHENIX and can be calculated by the following expression

$$\mathcal{L}_{effective} = \mathcal{L}_{machine} \cdot \epsilon_{vertex} = \mathcal{L}_{machine} \cdot \int Z_{vtx}(z)dz \tag{3.20}$$

where $\mathcal{L}_{machine}$ is the machine luminosity calculated with vernier scans from Equation 3.8 and $Z_{vtx}(z)$ is the vertex distribution normalized such that its integral over all z is 1.0 and the integral is done over the range of vertex positions viewed by the experiment, or to be more precise, the range of vertex positions used by the experimentalists in offline analysis. This range is $z = \pm 30$ cm since all PHENIX offline analyses use a 30 cm vertex cut. For further details on the estimation of the integral above see [50]. The factor ϵ_{vertex} is equal to the fraction of the vertex distribution in the $z = \pm 30$ cm window.

During the vernier scan that determines the beam widths, the count rates of the trigger counters are also measured and at the same time the machine luminosity can be computed from the measured beam parameters (Equation 3.8). Therefore the cross section for the trigger counter can be computed starting from the rate Equation 3.9 (notice that we have now returned to rates and instantaneous luminosity instead of integrated)

$$\sigma_{BBC} = \frac{R_{BBC\,max}}{\mathcal{L}_{effective}} \tag{3.21}$$

$$= \frac{R^{\pm 30\,cm}_{BBC\,max}}{\mathcal{L}_{machine} \cdot \epsilon^{\pm 30\,cm}_{vertex}} \tag{3.22}$$

and finally using the luminosity equation we have

$$\sigma_{BBC} = \frac{R^{\pm 30\,cm}_{BBC\,max}}{\int_{\pm 30\,cm} Z_{vtx}(z)dz} \cdot \frac{2\pi\sigma^v_x\sigma^v_y}{f_{beam} \cdot \sum_{crossings}(N_b \cdot N_y)_i} \tag{3.23}$$

where $R^{\pm 30\,cm}_{BBC\,max}$ is the BBCLL1 rate when the beams are overlapping maximally and has also been corrected for the fraction of events with reconstructed vertices within ±30 cm of the interaction point.

The final result for the BBC cross section from [50] is

$$\sigma_{BBC} = 21.8 \pm 2.1(9.6\%)\ mb \quad at\ 2 - sigma \tag{3.24}$$

The total inelastic p+p cross section from world data is $\sigma_{BBC} = 42.2 \pm 1.9(4.5\%)$ mb and therefore the BBC efficiency is $0.516 \pm 0.051\,(9.8\%)$. This is a beatifull result because first it tells us directly what fraction of the total inelastic p+p cross section PHENIX actually sees and triggers on, and second, it absolutely normalizes the Beam Beam Counters as luminosity counters.

3.2.6 Towards an Unbiased p+p Cross Section: Calculating the BBC Trigger Bias

The laborious work described in [50] and briefly touched upon in the previous section cuts the umbilical cord of PHENIX with the collider machine in terms of luminosity counting. From now on $\widehat{\mathcal{L}}_{effective}$ will really mean:

$$\frac{1}{\widehat{\mathcal{L}}_{effective}} = \frac{\sigma_{BBC}}{N_{BBC}^{Total}} \tag{3.25}$$

and we rewrite Equation 3.15 as

$$E\frac{d^3\sigma_X^{Unbiased}}{d^3p} = \frac{\sigma_{BBC}}{N_{BBC}^{Total}} \cdot \frac{1}{2\pi} \cdot \frac{1}{p_T} \frac{d^2N_X^{Total\,Unbiased}}{dp_T dy} \tag{3.26}$$

From the discussion in section 3.2.4 we know that the subset of events that BBC triggers on is a biased set as far as mid-rapidity pion production is concerned. We therefore define the bias correction $C_{p+p}^{BBC\,bias}(pt, y)$ to be

$$\frac{d^2N_X^{Total\,Unbiased}}{dp_T dy} = C_{p+p}^{BBC\,bias}(pt, y) \cdot \frac{d^2N_X^{Total\,Biased}}{dp_T dy} \tag{3.27}$$

which also prescribes the way to calculate it:

$$C_{p+p}^{BBC\,bias}(pt, y) = \frac{\frac{d^2N_X^{Total\,Unbiased}}{dp_T dy}}{\frac{d^2N_X^{Total\,Biased}}{dp_T dy}} \tag{3.28}$$

We need to note here that the rapidity distribution of particles near mid-rapidity is assumed to be a flat distribution and therefore the bias correction is not a function of y. It remains to be seen if it is a function of transverse momentum. Equation 3.28 implies that all that is needed to calculate the trigger

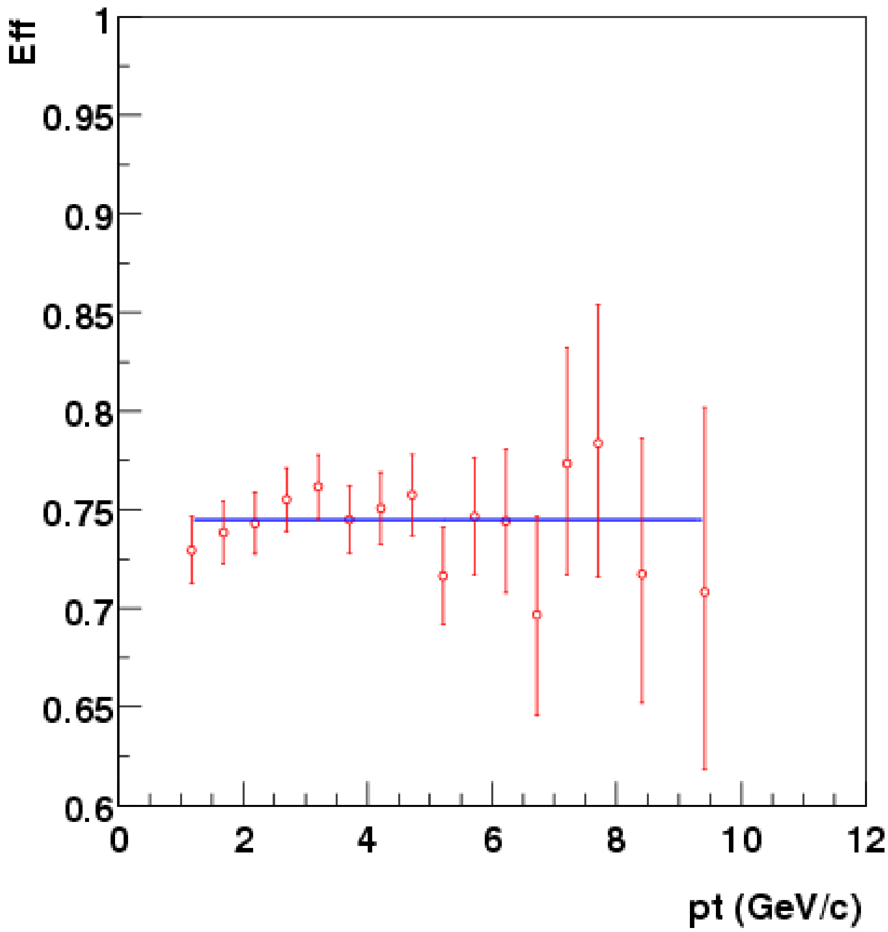

Figure 3.3: Inverse trigger bias for neutral pions as a function of transverse momentum measured with the PbSc EMCal.

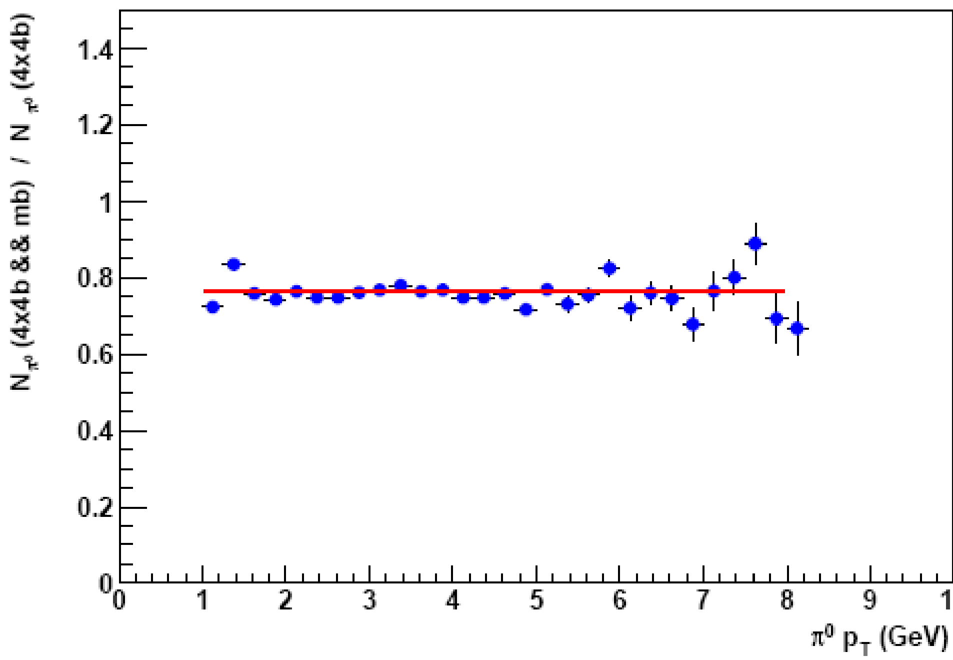

Figure 3.4: Inverse trigger bias for neutral pions as a function of transverse momentum measured with the PbGl EMCal.

bias correction is to define (trigger on) an unbiased set of events, $S_{Unbiased}$, as shown on Figure 3.2, and then calculate the fractional yield of pions in this unbiased sample that in addition satisfies the BBCLL1 trigger (and therefore makes it biased).

Clearly $S_{Unbiased}$ should be a subset of events that is completely decoupled from the BBC trigger requirement, i.e. this subset should arise from an independent unbiased mid-rapidity trigger. PHENIX used two different types of triggers that satisfy this requirement. The first one was a 4x4B ERT trigger [55] [56] (where ERT stands for EMCal-RICH-Trigger), while the second one was the mother of all unbiased triggers, namely, a clock trigger [54] (see definition in section 3.2.4).

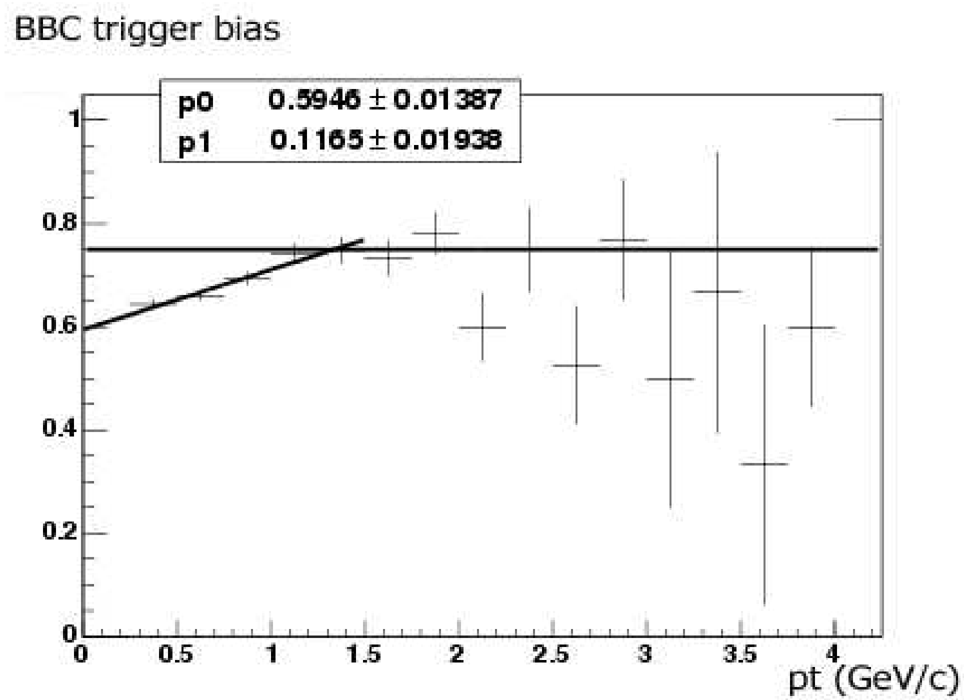

Figure 3.5: Inverse BBC trigger bias for charged particles from clock triggers.

The 4x4B ERT trigger is basically an EMCal trigger with a high enough energy threshold to reduce its raw trigger rate so that it can all be recorded without having to be in coincidence with the BBCLL1 trigger. It fires when a particle with energy above the trigger threshold hits the central arm electromagnetic calorimeter with no further requirements from any other subsystem or triggering device. Notice that this is a true unbiased trigger since it fires on any particle hitting the calorimeter, not just photons, as long as the energy threshold is high enough for a 4x4 tower to fire. The trigger bias correction is then calculated by the ratio of the total pion yield from this set of 4x4B ERT events divided by the pion yield from the subset of those 4x4B ERT events for which the BBC trigger also fired, those events that belong to the intersection of the S_{BBC} subset and the $S_{Unbiased}$ subset shown in Figure 3.2. The inverse of this ratio, namely $1/C_{p+p}^{BBC\,bias}(pt)$ is shown in Figure 3.3 from [55] as measured by the PbSc calorimeter, in excellent agreement with a PYTHIA calculation of this effect shown as the blue line. The same ratio was measured independently with the PbGl calorimeter and the result from [56] is shown in Figure 3.4 in excellent agreement with the PbSc measurement. Notice that the red line in Figure 3.4 is a fit to the points not a PYTHIA simulation.

The average of these measurements is $1/C_{p+p}^{BBC\,bias}(pt) = 1/C_{p+p}^{BBC\,bias} = 0.7478$ with a systematic error of 3% and independent of the transverse momentum of the pions down to the lowest p_T value that we can reconstruct neutral pions, about 1GeV.

This is almost the end of the road as far as biases are concerned. The trigger bias correction for $p_T > 1.0\,GeV$ is $C_{p+p}^{BBC\,bias} = 1.337$ which is a large correction and had it been overlooked it would have resulted in a lower pion spectrum by more than 30%.

For the second trigger used to calculate the BBC trigger bias, the clock trigger, we follow [54]. This analysis is notoriously difficult since in clock triggered events there is no vertex information and no starting time for the collision and hence no momentum reconstruction. In this case a new method for reconstructing particle tracks was used where the Pad Chamber and EM-Cal hits were combined in order to reconstruct particle tracks and then the momentum vector of the particles.

Again the bias correction is obtained by the ratio of the total charged particle yield from this set of clock triggered events divided by the charged particle yield from the subset of those clock triggered events for which the BBC trigger also fired and is shown in Figure 3.5 along with a fit for the low momentum points. From the fit we obtain

$$\frac{1}{C_{p+p}^{BBC\,bias}(pt)} = 0.59 + 0.12 \cdot pt \quad for\, p_T < 1.33\, GeV \tag{3.29}$$

In this momentum region the BBC bias becomes momentum dependent. For $p_T = 1.33\, GeV$ the inverse bias correction becomes 0.7496 in excellent agreement with the correction obtained from the calorimeter triggers. At the lowest $p_T = 300\, MeV$ reached by charged analyses in PHENIX the ratio reaches the value of 0.626 which means that at the lowest p_T bin $C_{p+p}^{BBC\,bias} = 1.6$.

3.2.7 The Golden Formula

Now we can put everything together and derive the final formula that makes the connection between what PHENIX measures and the physical observable. Using Equations 3.26 and 3.27 we get

$$E\frac{d^3\sigma_X^{Unbiased}}{d^3p} = \frac{\sigma_{BBC}}{N_{BBC}^{Total}} \cdot \frac{1}{2\pi} \cdot \frac{1}{p_T} \cdot C_{p+p}^{BBC\,bias}(pt) \cdot \frac{d^2N_X^{Total\,Biased}}{dp_T dy} \tag{3.30}$$

As a final ingredient we also include the efficiency and geometrical acceptance correction factor $C_{eff}^{geo}(pt)$ that has to be used to upscale the PHENIX yield measurements to 2π in azimuthal angle and 1 unit of rapidity. It is derived from simulating the PHENIX aperture and detector efficiencies and assuming flat azimuthal and rapidity distributions for the phase space of the measurement which is outside the PHENIX acceptance. We finally have

$$E\frac{d^3\sigma_X^{Unbiased}}{d^3p} = \frac{\sigma_{BBC}}{N_{BBC}^{Total}} \cdot \frac{1}{2\pi} \cdot \frac{1}{p_T} \cdot C_{eff}^{geo}(pt) \cdot C_{p+p}^{BBC\,bias}(pt) \cdot \frac{d^2N_X^{Total\,PHENIX}}{dp_T dy} \tag{3.31}$$

This is how PHENIX calculates particle production cross sections in p+p collisions. There are no assumptions whatsoever in any step of the way for any effect, bias or cross sections. Everything is a result of a direct measurement by the PHENIX experiment.

3.2.8 Yield per Event in p+p Collisions

It is obvious from the previous discussions that someone must be very careful when comparing p+p "yield per event" particle spectra between different experiments, even among the RHIC experiments. Even when the trigger bias has been included in the calculation, the number of inelastic collisions is an extremely pure way of normalizing p+p yields since the efficiency of triggering on p+p inelastic collisions can widely vary among different experiments. In other words, if we choose to trigger on a process $p + p \to Y$, where Y means inclusive p+p inelastic collisions in the PHENIX case, we have

$$\frac{Yield^{p+p\to\pi+X}}{Event} = \frac{N^{p+p\to\pi+X}}{N^{p+p\to Y}} = \frac{N^{p+p\to\pi+X}}{N^{triggers}_{BBC}} \tag{3.32}$$

It is only when an appropriate multiplier (cross section) is used, where appropriate means

$$\frac{\sigma^{Y}}{N^{p+p\to Y}} = \frac{\sigma^{BBC}}{N^{BBC}} = \frac{1}{\widehat{\mathcal{L}}_{effective}} \tag{3.33}$$

that we end up with the correct normalization and a meaningful physical quantity that can be directly compared to other experiments. As trivial as this may sound it is not uncommon to see yield/event p+p spectra from different experiments being plotted and compared at the same plot without any further corrections or clear statement of the cross section seen by the experiments. The author is guilty of such faulty comparisons in the past.

The STAR collaboration uses a similar procedure with PHENIX to measure luminosity with their Beam Beam Counters and reports that their BBC cross section for p+p collisions is $\sigma^{BBC}_{STAR} = 26.1 \pm 0.2(stat) \pm 1.8(syst)\, mb$ [61] (STAR triggers on the coincidence of 2 BBCs similar to PHENIX). STAR simulates the BBC trigger with a PYTHIA-HERWIG-GEANT simulation and finds the PYTHIA trigger cross section to be 27 mb of which 0.7 mb results from singly diffractive events. That means that PYTHIA predicts that single diffractive events contribute only 2.6% to the triggered cross section by the BBCs and therefore call their measured BBC cross section to be entirely a Non Single Diffractive (NSD) cross section. At $\sqrt{s} = 200\ GeV$ they quote in the same paper the NSD p+p cross section to be $30 \pm 3.5\, mb$ which makes their BBC counters to be 87% efficient in measuring the NSD cross section. Kopeliovich in [62] also calculates the NSD inelastic cross section at $\sqrt{s} = 200\ GeV$ to be 30 mb. As a reminder the total p+p cross section can be written as

$$\sigma_{tot} = \sigma_{elastic} + \sigma_{inelastic} = \sigma_{elastic} + \sigma_{single-diffractive} + \sigma_{double-diffractive} + \sigma_{non-diffractive} \tag{3.34}$$

The elastic, single diffractive and double diffractive processes give rise to low multiplicity events with particles emitted in the very forward and very backward regions in the c.m. system. The single diffractive cross-section seems to increase slowly from 6 mb to about 9 mb in the range 20-1800 GeV . The non-diffractive cross-section is the main part of the inelastic cross-section; the non-diffractive processes give rise to high multiplicity events and to particles emitted at all angles. Most of the non-diffractive cross-section concerns particles emitted with low transverse momentum with properties which change slowly with c.m. energy. A relatively small part of the non-diffractive cross-section is due to central collisions among the colliding particles and gives rise to high pt jets of particles emitted at relatively large angles. The contribution of jet physics increases with c.m. energy.

For the trigger bias STAR uses a PYTHIA and HERWIG simulation and finds that the trigger accepts 87±8% of all NSD events containing a TPC track, with negligible track p_T dependence. The fact that the STAR trigger bias is smaller than PHENIX is a result of the larger pseudo-rapidity acceptance of the STAR TPC ($|\eta| = 0.5$) and the different location of the BBCs at STAR ($3.3 < |\eta| < 5.0$) at ±3.5 m from the interaction region.

Why do we get away comparing Yield per Event spectra among different experiments in d+Au and Au+Au collisions ? It is simply a matter of cross section size. The d+Au cross section is approximately 50 times larger than the p+p inelastic cross section while the Au+Au geometrical cross section is approximately 160 times larger. This results in large triggering efficiencies in d+Au ($\epsilon^{BBC} = 88.5\%$) and Au+Au ($\epsilon^{BBC} = 92\%$) with similar efficiencies in other experiments, resulting in << 10% differences, which are well within the systematic errors of the measured spectra. Still though, as we shall see in the following section, the lack of a measured cross section for d+Au and Au+Au collisions, will require the use of a Glauber model for the definition of some important physical quantities.

3.3 d+Au Collisions

There is a fundamental difference between the p+p and d+Au measurements in PHENIX. For reasons unknown to the author, in the d+Au case (and in the Au+Au case) , we do not perform scans to measure, in absolute scale, the total d+Au cross section seen by the Beam-Beam Counters (σ_{BBC}^{dAu}), as was done for p+p collisions. Therefore, in d+Au and Au+Au, we never quote cross sections for particle production, but rather invariant yields, i.e. yield of a process per inelastic d+Au interaction. This has some implications in the way that we quote our results and the way we calculate our nuclear modification factors. As we shall see, the most important implication for this thesis, is the fact that our nuclear modification factors will need input from a Glauber model [57] calculation in order to be complete.

In the following we will revisit the concept of point-like scaling in p+A and A+A collisions, redefine the nuclear modification factors introduced in the first Chapter in a more rigorous manner, and finally, present the process used in PHENIX, to categorize d+Au collisions according to their centrality, or in other words, the impact parameter between the Deuteron and Gold nuclei, in order to systematically study the cold nuclear effects as a function of the nuclear matter present in the collision. The impact parameter $\vec{b}$ is the vector defined by the center of the two colliding nuclei, being a d+Au or Au+Au collision, and therefore defines the geometry (centrality) of the collision. Large impact parameters imply peripheral collisions, while small impact parameters imply more central collisions. When $\vec{b} = \vec{0}$ the two nuclei collide head-on.

3.3.1 Point-like Scaling in p+A and A+A collisions

Following the formalism in [58] and [51], the inelastic cross section of a p+A reaction, σ_{pA}, can be derived in the eikonal limit (straight line trajectories of colliding nucleons) from the corresponding inelastic nucleon-nucleon NN cross section, σ_{NN}, and the geometry of the pA collision, simply determined by the impact parameter b of the reaction. In the Glauber model, such a cross section reads

$$\sigma_{pA} = \int d^2b \, [1 - e^{-\sigma_{NN} T_A(\vec{b})}] \tag{3.35}$$

where $T_A(\vec{b})$ is the nuclear thickness function of the nucleus A at impact parameter $\vec{b}$,

$$T_A(\vec{b}) = \int dz \, \rho_A(\vec{b}, z) \tag{3.36}$$

$T_A(\vec{b})$ gives the number of nucleons in the nucleus A, per unit area, along a direction z separated from the center of the nucleus by an impact parameter $\vec{b}$. The nuclear density is usually parameterized by a Woods-Saxon distribution and is normalized so that

$$\int d^2b \, T_A(\vec{b}) = A \tag{3.37}$$

If instead of the total inelastic cross section given in Equation 3.35 we are interested in an inclusive $p + A \rightarrow h + X$ process, where σ^h_{NN} is very small, like in a hard process for example, one can expand Equation 3.35 in orders of $\sigma_{NN} T_A(b)$ and then get to first approximation

$$\sigma_{pA}^{hard} \sim \int d^2b\, \sigma_{NN}^{hard}\, T_A(\vec{b}) \tag{3.38}$$

where upon integration becomes

$$(\sigma_{pA}^{hard})_{MB} = \sigma_{NN}^{hard} \cdot \int d^2b\, T_A(\vec{b}) \tag{3.39}$$

and using Equation 3.37

$$(\sigma_{pA}^{hard})_{MB} = A \cdot \sigma_{NN}^{hard} \tag{3.40}$$

Equation 3.40 defines the notion of point-like scaling for hard processes, which simply states that hard processes in p+A collisions, in the absence of any nuclear effects, scale with the number of possible point-like encounters, which , of course, is proportional to the number of nucleons in the nucleus, A.

For A+B collisions at impact parameter $\vec{b}$, the nuclear overlap integral $T_{AB}(\vec{b})$ is defined as the convolution of the corresponding thickness functions of the nuclei, over their overlapping area:

$$T_{AB}(\vec{b}) = \int d^2s\, T_A(\vec{s})\, T_B(\vec{b} - \vec{s}) \tag{3.41}$$

where $d^2s = 2\pi s ds$. We will come back to the meaning of this equation at a later point. $T_{AB}(\vec{b})$ is normalized so that

$$\int d^2b\, T_{AB}(\vec{b}) = AB \tag{3.42}$$

The total cross section for an AB collision can be written in a Glauber model as

$$\sigma_{AB} = \int d^2b\,[1 - e^{-\sigma_{NN}T_{AB}(\vec{b})}] \tag{3.43}$$

where, as in the p+A case, for a hard process, the exponential can be approximated by

$$\sigma_{AB}^{hard} \sim \int d^2b\,\sigma_{NN}^{hard}\,T_{AB}(\vec{b}) \tag{3.44}$$

Upon integration, and using Equation 3.42, we have

$$(\sigma_{AB}^{hard})_{MB} = A \cdot B \cdot \sigma_{NN}^{hard} \tag{3.45}$$

Equation 3.45 is the definition of point-like scaling for hard processes in A+B collisions, which of course, has the same meaning as Equation 3.40 for p+A collisions.

3.3.2 Nuclear Modification Factors

Inspired by Equations 3.40 and 3.45 that define the notion of point-like scaling, we define the Minimum Bias nuclear modification factor R_{pA} for p+A collisions as:

$$R_{pA} \equiv \frac{(\sigma_{pA}^{hard})_{MB}}{A \cdot \sigma_{NN}^{hard}} \tag{3.46}$$

and the Minimum Bias nuclear modification factorR_{AB} for A+B collisions as:

$$R_{AB} \equiv \frac{(\sigma_{AB}^{hard})_{MB}}{A \cdot B \cdot \sigma_{NN}^{hard}} \tag{3.47}$$

In the absence of any nuclear effects, the two nuclear modification factors should obey point-like scaling exactly, and therefore both should be equal to 1. From these two definitions we can also see that if an experiment can measure p+A and A+A cross sections, then there is no additional need for a Glauber model to define the nuclear modification factors. As we have said already though, in PHENIX we do not measure cross sections for p+A and A+A collisions, but rather differential yields. In the following we rewrite the nuclear modification factors in a way more suitable for our measurement.

We start by defining differential nuclear modification factors, as functions of transverse momentum:

$$R_{pA}(p_T) = \frac{\dfrac{d^2(\sigma_{pA}^{hard})_{MB}}{dp_T dy}}{A \cdot \dfrac{d^2\sigma_{NN}^{hard}}{dp_T dy}} \tag{3.48}$$

and

$$R_{AB}(p_T) = \frac{\dfrac{d^2(\sigma_{AB}^{hard})_{MB}}{dp_T dy}}{A \cdot B \cdot \dfrac{d^2\sigma_{NN}^{hard}}{dp_T dy}} \tag{3.49}$$

We now convert the numerators of the above equations from cross sections to differential yields per event, which is what we really measure. We proceed with the nuclear modification factor for A+B collisions. The p+A case is identical and we will show the final result at the end.

Using the fundamental equation that relates cross sections and yields, Equation 3.9, for the hard scattering process of interest, we have:

$$N_{AB}^{hard} = \sigma_{AB}^{hard} \cdot \widehat{\mathcal{L}} \tag{3.50}$$

and Equation 3.49 becomes

$$R_{AB}(p_T) = \frac{\frac{1}{\widehat{\mathcal{L}}} \cdot \frac{d^2(N_{AB}^{hard})_{MB}}{dp_T dy}}{A \cdot B \cdot \frac{d^2\sigma_{NN}^{hard}}{dp_T dy}} \tag{3.51}$$

We use Equation 3.9 once more, this time for the total geometric cross section of A+B collisions (this is the same cross section that appears in Equation 3.43), which, when multiplied by the integrated luminosity, yields the total number of inelastic A+B events:

$$N_{inelastic,AB}^{Total\,Events} = \sigma_{AB}^{geo} \cdot \widehat{\mathcal{L}} \tag{3.52}$$

We use this relation to substitute for the integrated luminosity in Equation 3.51, since we do not measure it in the A+B case:

$$R_{AB}(p_T) = \frac{\frac{1}{N_{inelastic,AB}^{Total\,Events}} \cdot \frac{d^2(N_{AB}^{hard})_{MB}}{dp_T dy}}{\frac{A \cdot B}{\sigma_{AB}^{geo}} \cdot \frac{d^2\sigma_{NN}^{hard}}{dp_T dy}} \tag{3.53}$$

The nuclear modification factor R_{AB} that appears in Equation 3.53 is now in a from that can be directly calculated. The numerator is the differential invariant yield for the hard process that we measure, and in the denominator the p+p cross section is also directly measured by PHENIX. The only term that we do not directly measure is the geometrical cross section for A+B collisions. This term is typically calculated by a Glauber model calculation as shown in Equation 3.43.

For completeness we also quote the nuclear modification factor for p+A collisions:

$$R_{pA}(p_T) = \frac{\frac{1}{N^{Total\ Events}_{inelastic,pA}} \cdot \frac{d^2(N^{hard}_{pA})_{MB}}{dp_T dy}}{\frac{A}{\sigma^{geo}_{pA}} \cdot \frac{d^2\sigma^{hard}_{NN}}{dp_T dy}} \tag{3.54}$$

where again, the only term not directly measured experimentally is the geometrical cross section which is also calculated by a Glauber model as shown in Equation 3.35.

3.3.3 The Golden Formula of the Glauber Model: Nuclear Luminosity

We now return to the interpretation of Equation 3.41, [51]. If we consider a nucleon in nucleus A at $(z_A, \vec{s})$, the expected number of binary inelastic collisions with the nucleons from nucleus B at the same 2-d position ($\vec{b} - \vec{s}$ in coordinates from the center of B) is given by:

$$N_{coll}(z_A, \vec{b} - \vec{s}) = \sigma_{NN} \cdot \int dz_B\, \rho_B(z_B, \vec{b} - \vec{s}) = \sigma_{NN} \cdot T_B(\vec{b} - \vec{s}) \tag{3.55}$$

Notice the correct dimension of the result. The cross section has dimensions of inverse area, while the nuclear density has dimensions of number of nucleons per volume. Integrating over all the nucleons in A yields

$$
\begin{aligned}
N_{coll}(\vec{b}) &= \int d^2s \int dz_A\ \rho_A(z_A,\vec{s}) \cdot N_{coll}(\vec{b}-\vec{s}) && (3.56)\\
&= \sigma_{NN} \cdot \int d^2s \int dz_A\ \rho_A(z_A,\vec{s})\, T_B(\vec{b}-\vec{s}) && (3.57)\\
&= \sigma_{NN} \cdot \int d^2s \int dz_A \int dz_B\ \rho_A(z_A,\vec{s})\, \rho_B(z_B,\vec{b}-\vec{s}) && (3.58)\\
&= \sigma_{NN} \cdot \int d^2s\, T_A(\vec{s})\, T_B(\vec{b}-\vec{s}) && (3.59)
\end{aligned}
$$

and finally we have

$$
N_{coll}(\vec{b}) = \sigma_{NN} \cdot T_{AB}(\vec{b}) \tag{3.60}
$$

This equation is the unintegrated form of the Golden Formula of the Glauber model (our definition). It shows that the mean (or expected) number of binary collisions when two nuclei collide at impact parameter $\vec{b}$, is given by the product of the nuclear overlap integral, $T_{AB}(\vec{b})$ (typically calculated by a Glauber model) , with the nucleon-nucleon cross section. The similarity of this equation with Equation 3.9 (which we reproduce here for completeness)

$$
N^{Total\,Events}_{for\,process\,X} = \sigma^X \cdot \widehat{\mathcal{L}} \tag{3.61}
$$

has inspired many authors to think of the nuclear overlap integral, $T_{AB}(\vec{b})$, as a nuclear luminosity per AB collision. In this picture, the two particle beams are the overlapping nucleons in the two nuclei, that cross each other at impact parameter $\vec{b}$, in the same way as two bunches of particles cross each other, Fig.3.1. For the p+A case we have an equivalent relation:

$$N_{coll}(\vec{b}) = \sigma_{NN} \cdot T_A(\vec{b}) \tag{3.62}$$

and if we want to stretch the idea of nuclear luminosity, in this case one of the bunches always consists of one particle.

We proceed now to the integrated form of Equation 3.60. Upon integration over the impact parameter $\vec{b}$, and using the normalization of the nuclear overlap integral, we have:

$$\int d^2b\, N_{coll}(\vec{b}) = \sigma_{NN} \cdot \int d^2b\, T_{AB}(\vec{b}) = \sigma_{NN} \cdot A \cdot B \tag{3.63}$$

Using the definition for Minimum Bias averages over the entire impact parameter range, we have:

$$< N_{coll} >_{MB} \equiv \frac{\int d^2b\, N_{coll}(\vec{b})}{\int d^2b} \tag{3.64}$$

and similarly for the nuclear overlap integral (or any other quantity of interest):

$$< T_{AB} >_{MB} \equiv \frac{\int d^2b\, T_{AB}(\vec{b})}{\int d^2b} \tag{3.65}$$

where of course $\int d^2b = \sigma_{AB}^{geo}$. Equation 3.63 then becomes,

$$< N_{coll} >_{MB} \cdot \sigma_{AB}^{geo} = \sigma_{NN} \cdot A \cdot B \tag{3.66}$$

or, if we use the middle part of Equation 3.63 and Equation 3.65 we get the mean nuclear overlap integral in Minimum Bias collisions

$$< T_{AB} >_{MB} \cdot \sigma_{AB}^{geo} = A \cdot B \tag{3.67}$$

Equations 3.66 and 3.67 constitute the integrated forms of the Golden Formula of the Glauber model. Combining them we have

$$< N_{coll} >_{MB} = < T_{AB} >_{MB} \cdot \sigma_{NN} \tag{3.68}$$

which clearly shows that T_{AB} corresponds to the Glauber estimate of the number of collisions calculated with the σ_{NN} cross section [51].

3.3.4 Centrality Slices

Similar to the previous section, for any fraction, f, of the geometrical cross section, or equivalently, for any range of impact parameters $b_1 < b < b_2$:

$$\int_{b1}^{b2} d^2b \equiv f \cdot \sigma_{AB}^{geo} \tag{3.69}$$

we can define the average number of collisions in this centrality slice:

$$< N_{coll} >_f \equiv \frac{\int_{b1}^{b2} d^2b\, N_{coll}(\vec{b})}{\int_{b1}^{b2} d^2b} \tag{3.70}$$

and similarly for the average nuclear overlap integral in this range:

$$< T_{AB} >_f \equiv \frac{\int_{b1}^{b2} d^2b\, T_{AB}(\vec{b})}{\int_{b1}^{b2} d^2b} \tag{3.71}$$

and finally

$$< N_{coll} >_f = < T_{AB} >_f \cdot \sigma_{NN} \tag{3.72}$$

3.3.5 Nuclear Modification Factors Reloaded

The golden Formulae that we derived in the previous sections are now used to rewrite the Minimum Bias A+B nuclear modification factor from Equation 3.53 as

$$R_{AB}(p_T) = \frac{\dfrac{1}{N^{Total\,Events}_{inelastic,AB}} \cdot \dfrac{d^2(N^{hard}_{AB})_{MB}}{dp_T dy}}{\dfrac{< N_{coll} >_{MB}}{\sigma_{NN}} \cdot \dfrac{d^2\sigma^{hard}_{NN}}{dp_T dy}} \tag{3.73}$$

This is the most intuitive form of the nuclear modification factor. We also note that the only model dependent part of this equation is the mean number of Minimum Bias collisions, which we take from a Glauber model. Equivalently, using the nuclear overlap integral, we can rewrite the nuclear modification factor as

$$R_{AB}(p_T) = \frac{\dfrac{1}{N^{Total\,Events}_{inelastic,AB}} \cdot \dfrac{d^2(N^{hard}_{AB})_{MB}}{dp_T dy}}{< T_{AB} >_{MB} \cdot \dfrac{d^2\sigma^{hard}_{NN}}{dp_T dy}} \tag{3.74}$$

For p+A collisions the nuclear modification factors are rewritten as

$$R_{pA}(p_T) = \frac{\dfrac{1}{N^{Total\,Events}_{inelastic,pA}} \cdot \dfrac{d^2(N^{hard}_{pA})_{MB}}{dp_T dy}}{\dfrac{< N_{coll} >_{MB}}{\sigma_{NN}} \cdot \dfrac{d^2\sigma^{hard}_{NN}}{dp_T dy}} \tag{3.75}$$

or, using the nuclear thickness function, as

$$R_{pA}(p_T) = \frac{\frac{1}{N_{inelastic,pA}^{Total\ Events}} \cdot \frac{d^2(N_{pA}^{hard})_{MB}}{dp_T dy}}{< T_A >_{MB} \cdot \frac{d^2\sigma_{NN}^{hard}}{dp_T dy}} \quad (3.76)$$

The nuclear modification factors for centrality slices are trivially calculated from the above equations, by substituting the Minimum Bias quantities with their corresponding averages over the impact parameter range of interest, for example, $< N_{coll} >_{MB} \rightarrow < N_{coll} >_f$.

We conclude this section by noting the fact that our nuclear modification factors are model-dependent since they depend on a Glauber model calculation of $< N_{coll} >$ for example. In the d+Au case, objections have been raised [62] on the validity of the Glauber model used, since it does not take into account Gribov's inelastic corrections that make the nucleus appear more transparent than a simplified Glauber model. There are two options for the experimentalists here. Either use more realistic Glauber model calculations, or measure directly the d+Au cross section. The latter is of course preferable.

3.4 PHENIX d+Au Glauber Model

The Glauber mode implemented by PHENIX calculates the number of participants (N_{part}) and the number of binary nucleon-nucleon collisions (N_{coll}) in a nucleus-nucleus collision. The Glauber model is based on a purely geometric picture of a heavy ion reaction: for each trial, the two nuclei are distributed in space by sampling the appropriate nucleon density profile. Then, an impact parameter, b, of the nucleus-nucleus collision is chosen randomly, and then the

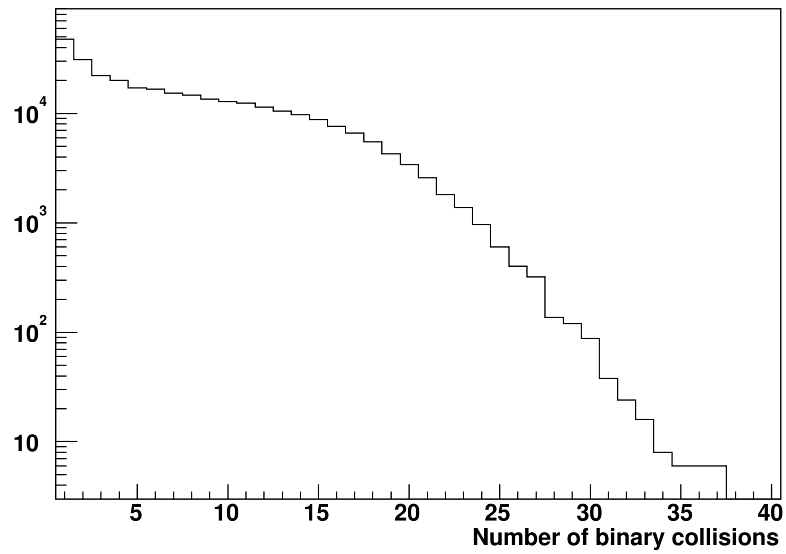

Figure 3.6: Distribution of number of collisions in Minimum Bias d+Au events calculated with the PHENIX d+Au Glauber model from [64].

nucleons travel on straight-line trajectories. A collision between two nucleons takes place if their distance, d, in the transverse plane is smaller than a certain value given by the inelastic nucleon-nucleon cross section:

$$d < \sqrt{\frac{\sigma_{NN}}{\pi}} \tag{3.77}$$

We used $\sigma_{NN} = 42mb$ at $\sqrt{s} = 200$ GeV.

The deuteron nucleus is modeled after a wave function due to Hulthèn [63]

$$\phi_{\mathrm{d}}(\mathbf{r}_{\mathrm{pn}}) = \left(\frac{\alpha\beta(\alpha+\beta)}{2\pi(\alpha-\beta)^2}\right)^{\frac{1}{2}} (\mathrm{e}^{-\alpha r_{\mathrm{pn}}} - \mathrm{e}^{-\beta r_{\mathrm{pn}}})/r_{\mathrm{pn}} \tag{3.78}$$

where $\alpha = 0.228\,\mathrm{fm}^{-1}$ and $\beta = 1.18\,\mathrm{fm}^{-1}$ and $\mathbf{r}_{\mathrm{np}}$ refers to the separation between the proton and the neutron.

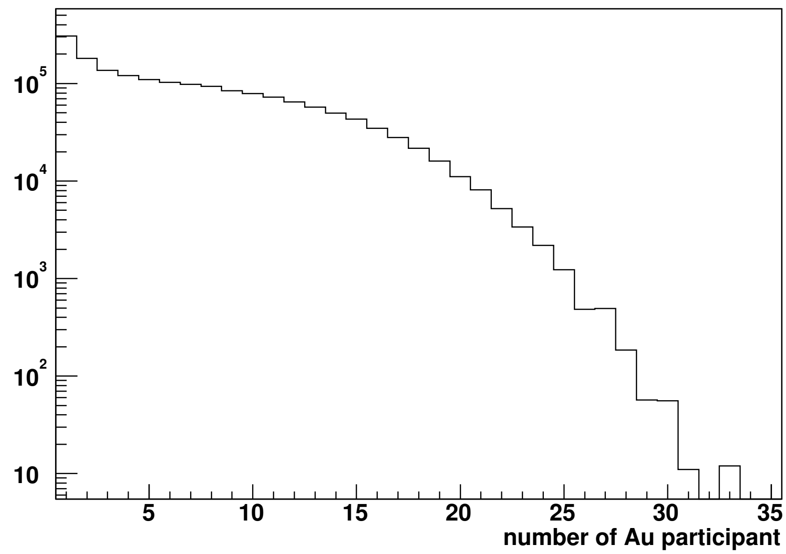

Figure 3.7: Distribution of the number of participating nucleons in Minimum Bias d+Au collisions calculated with the PHENIX d+Au Glauber model from [64].

From $\phi_{\mathrm{d}}(\mathbf{r}_{\mathrm{pn}})$ one obtains the following probability distribution for $\mathbf{r}_{\mathrm{np}}$

$$P_{\mathrm{d}}(\mathbf{r}_{\mathrm{pn}}) = \frac{2\alpha\beta(\alpha+\beta)}{(\alpha-\beta)^2}(\mathrm{e}^{-2\alpha r_{\mathrm{pn}}} + \mathrm{e}^{-2\beta r_{\mathrm{pn}}} - 2\mathrm{e}^{-(\alpha+\beta)r_{\mathrm{pn}}}). \tag{3.79}$$

by multiplying by a 3-space measure, $r^2 \sin\theta dr d\theta d\phi$, and integrating over the angular coordinates.

The Au nucleus is modeled using a Woods-Saxon density distribution

$$\rho(r) = \frac{\rho_0}{1 + \exp\left(\frac{r-c}{a}\right)} \tag{3.80}$$

where $a = 0.54\,\mathrm{fm}$ and $c = 1.12 \times A^{1/3} - 0.86 \times A^{-1/3} = 6.40\,\mathrm{fm}$, a value which agrees well with the measured charge radius of 6.38 fm for gold.

In Fig. 3.6 we show the distribution of the number of collisions obtained with the PHENIX d+Au Glauber model, and in Fig. 3.7 we show the distribution of the number of participants.

Another Glauber model approach [47] is a based on a hybrid of a discrete nucleon Monte Carlo for the Deuteron and a numerically integrated Glauber model for the Gold nucleus. The hybrid approach repeatedly constructs deuterons according to the Hulthèn wave function and then samples the thickness function of a Gold nucleus. The Gold nucleus is described as a continuous Woods-Saxon charge distribution. Both approaches yield consistent results within the systematic errors.

After including the BBC efficiency, the mean number of binary collisions in Minimum Bias d+Au collisions is: $N_{coll} = 8.5 \pm 0.4$. We describe the centrality selection in d+Au and the corresponding number of binary collisions in each centrality category in the following sections.

3.5 Centrality Determination in d+Au

The detector used for determining the centrality of d+Au collisions is the south BBC (BBCS). This is the BBC that faces in the direction of the Au beam. It is expected that the number of produced charged particles in the backward rapidity (Au-direction) should be proportional to the number of participating nucleons in the Au nucleus . We therefore have a direct relation of proportionality between the charge seen by BBCS and N_{part}^{Au} which we will further exploit to categorize d+Au events in various centrality classes.

The choice of definition of centrality classes in d+Au collisions has been a subject of intense research and often debate among the collaboration. This is a testament of the difficulty to define, in a reliable way, impact parameter distributions in p+A experiments in general. This is not so difficult to understand. In Au+Au collisions, we know from Glauber model calculations [48] that the number of participating nucleons ranges from approximately 6 to 350, while the number of collisions ranges from 5 to approximately 1000. Such a wide range of nuclear geometry can be easily categorized by the BBC and ZDC detectors. In the d+Au case, as we will soon see, the average number of collisions in Minimum bias events, is approximately 8. In this case the intrinsic resolutions of the detectors are stretched to the maximum in order to be able to discriminate between a small range of nuclear collisions. In addition, correlations between particular event types, for example, events with at least one hard scattering, and the BBC response start to play non-trivial roles, in particular in the most peripheral d+Au centrality bin.

In this work we follow the approach by Nagle and Chun [64]. The most important aspect of this study is its unique definition of what constitutes a centrality bin.

- The true event category is defined in terms of a true distribution of binary collisions (N_{coll}), with a given $< N_{coll} >$ and width.

The measured yield of particles and the measured number of events in each event category that define the measured invariant yield of the process we are interested in , (Yield/Event), is corrected in such a manner as to correspond to the "true" distribution of N_{coll} of the particular centrality bin. Of course the N_{coll} distributions used to define the event categories are not chosen randomly, but are rather driven from the detectors that are used in the centrality definition, namely, the number of hits registered by the BBCS. In that way the correction factors to the invariant yields will be minimal.

By defining our event categories in this manner it becomes straightforward to communicate them to the community, to theorists and to other experiments, since the only thing needed to be communicated are well defined N_{coll} distributions, with no further need of any other PHENIX-dependent quantities, like for example a simulation of the BBCS response, geometrical acceptance of the BBCS etc.

3.5.1 Modeling the BBCS Response

At the core of our method is the modeling of the BBCS response in d+Au collisions. This is done as follows:

- We use a Glauber Monte Carlo model with the same parameters as for the Minimum Bias case.
- We assume that the number of charged particles firing the BBCS is proportional to the number of participating nucleons in the Au nucleus.
- The real BBCS response from p+p collisions is used to account for the BBCS response for individual nucleon-nucleon collisions in Monte Carlo d+Au events.
- The modeled BBCS response for each event therefore arises from sampling the p+p BBCS distribution N_{part}^{Au}-times, where N_{part}^{Au} is determined by the Glauber model.

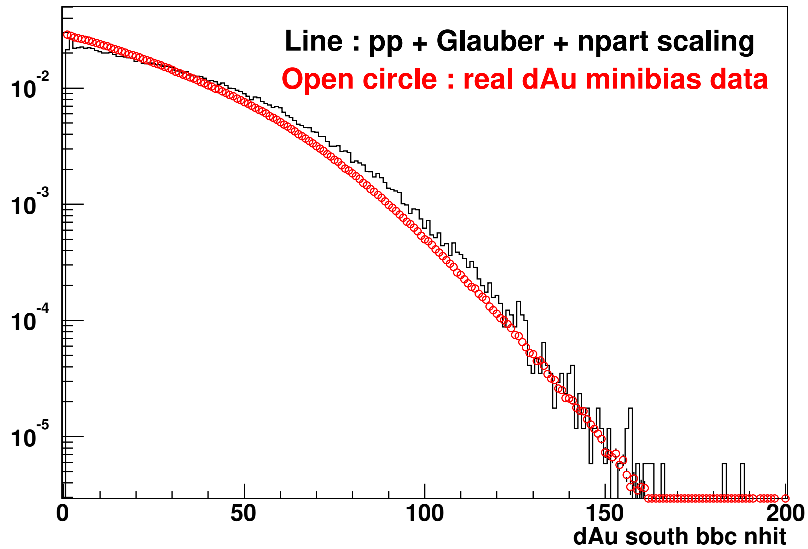

Figure 3.8: Comparison between the modeled [64] and real BBCS response. Although the agreement is certainly not perfect it follows the general features of the data distribution in a log scale.

- We require that at least one of the nucleon-nucleon reactions fired the BBCLL1[2] trigger.

The resulting modeled BBCS distribution, along with the real BBCS distribution from the d+Au data is shown in Fig. 3.8.

A subtle point must be explained at this point. The p+p BBCS distribution that we sample from, in each of the N_{part}^{Au} nucleon-nucleon collisions, is the unbiased, inclusive BBCS response ($BBC_{inclusive}^{pp,unbiased}$) from real p+p collisions, with no BBCLL1 trigger fire condition (hence the name "unbiased"). This unbiased distribution is determined by clock triggers since they have no BBCLL1 trigger fire requirement. The decision of whether a Glauber Monte

[2]BBCLL1 is the name of the Minimum Bias d+Au trigger which requires that there is at least one hit in both BBC North and BBC South

Carlo event fires the BBCLL1 trigger or not is done as follows. For each nucleon-nucleon collision, after a BBCS nhit (number of hits) is sampled from $BBC^{pp,unbiased}_{inclusive}$, the ratio between the content of the nhit bin in the BBCLL1 BBCS distribution, $BBC^{pp,biased}_{inclusive}$ (we call this distribution "biased"), and the content of the same bin in the unbiased distribution is compared with a random number uniformly distributed from 0 to 1. If the ratio is larger than the random number then the this nucleon-nucleon collision fires the trigger. As long as one nucleon-nucleon collision fires the trigger, the Monte Carlo d+Au event fires the trigger.

3.5.2 Definition of Centrality Classes

We divide the modeled BBCS distribution, shown in Fig. 3.8, into four centrality bins, 00-20%, 20-40%, 40-60%, and 60-88%. The 88% upper limit comes from previous studies that showed that the BBCLL1 trigger fires on 88% of the total inelastic d+Au cross section. These percentages refer to fractions of the modeled BBCS distribution within a specified range of BBCS cut values, as shown in Fig. 3.9.

These BBCS cuts now are mapped to 4 N_{coll} distributions that will serve as the definition of our centrality bins. The mapping is done trivially, since, in the Glauber calculation, for each event, we know the the N^{Au}_{part} and the N_{coll}. Thus we can perfectly calculate the N_{coll} distribution that is associated with each of the 4 BBCS centrality selections. These distributions are shown in Fig.3.10 and serve from now on as the definition of our centrality bins.

The mean number of collisions $< N_{coll} >_f$ for our 4 centrality bins are

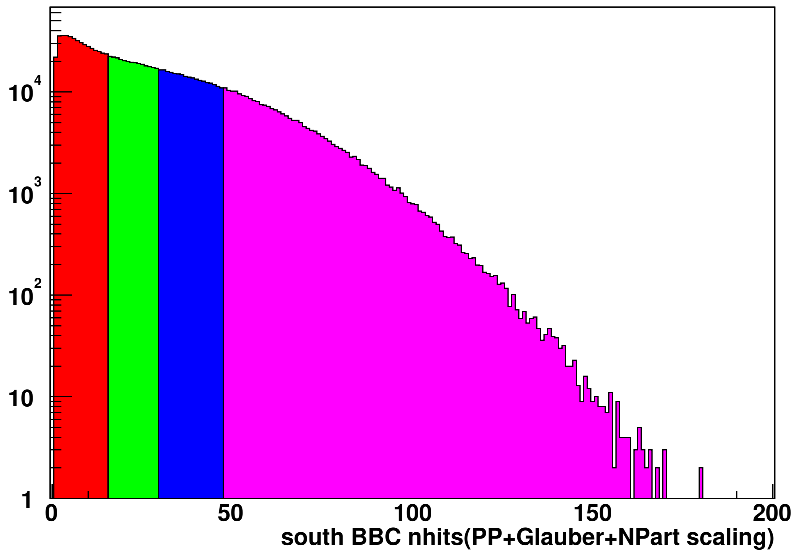

Figure 3.9: The modeled biased (since it satisfied the BBCLL1 trigger), inclusive BBCS nhit distribution, sliced into centrality bins according to percentages described in the text.

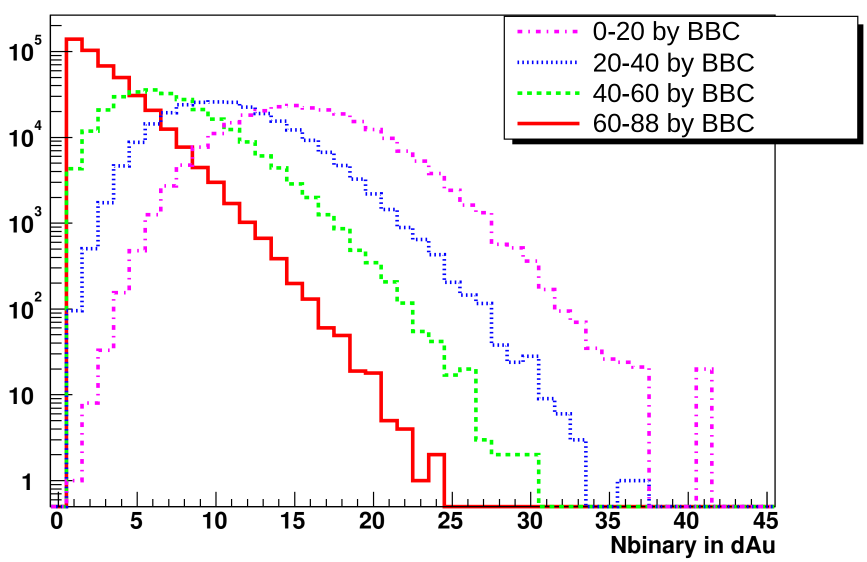

Figure 3.10: The N_{coll} distributions that correspond to the BBCS cut distributions. These distributions can be viewed as the definition of each centrality bin.

shown in Table 3.1.

Table 3.1: Mean number of collisions from [64]

correction	00-20%	20-40%	40-60%	60-88%
	15.64	10.86	7.0	2.94

In this analysis we use as the number of collisions the average of the values shown in Table 3.1, which are based on [64], and the values determined by Milov et al. [65], using Negative Binomial Distributions instead of measured p+p BBCS distributions. Both results are consistent within the systematic errors. The final numbers used in this work are shown in Table 3.2.

Table 3.2: Number of collisions from averaging [64] and [65]

correction	00-20%	20-40%	40-60%	60-88%
	15.37±1.0	10.63±0.7	6.95±0.6	3.07±0.3

3.5.3 Trigger Bias and Centrality Bin Shifting Corrections for d+Au

There are two effects that must be taken into account in d+Au collisions, that also depend on the centrality selection process. The first is the trigger bias, that is already present in p+p collisions and was extensively discussed in the previous sections of this chapter. The same effect is at work in d+Au collisions too, and, as expected, is only important in the most peripheral d+Au centrality bin.

The second effect is an artifact of the way we categorize reactions into different centralities, using the BBCS distribution, as explained in the previous section. We call this effect "the bin shifting effect" [64] , and in the following we discuss its origin. The true invariant yield , lets us say the number of pions per d+Au reaction, in each category is:

$$Y_{\pi}^{true}(i) = \frac{N_{\pi}^{true}(i)}{N_{reactions}^{true}(i)} \tag{3.81}$$

where i is the index over 1, 2, 3, 4, for the centrality categories. What we measure experimentally though , is:

$$Y_{\pi}^{meas}(j) = \frac{N_{\pi}^{meas}(i)}{N_{reactions}^{meas}(i)} \tag{3.82}$$

where j is the index over 1, 2, 3, 4, for the measured centrality categories. However, during the analysis of real data, the "measurement" case, where, for each measured event, the centrality is defined by the registered number of BBCS hits for that particular event, the centrality category is not guaranteed to be correct, since it is based on the real BBCS detector.

As an example of this bias, an interaction with N_{coll}=3, may normally fall into the most peripheral centrality category. However, it is known that, if this particular event includes one hard scattering, the charged particle multiplicity is increased, and therefore there is an enhanced probability that this event will have a larger than usual nhit distribution in the BBCS. It follows that during the determination of the centrality category for this event, using the BBCS cuts that were defined previously, this event may land into the next higher centrality bin. Therefore, more measured pions are shifting out of the

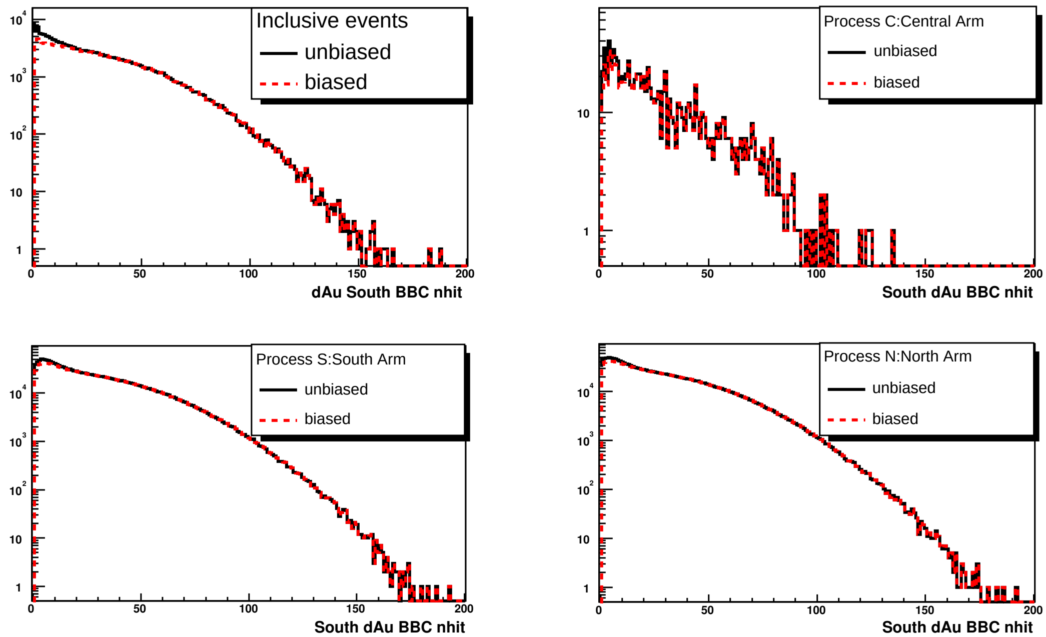

Figure 3.11: BBCS nhit distributions for different classes of events from [64]. Starting from the upper left corner and going clockwise, these p+p BBCS distributions are from inclusive, hard scattering in central arm, hard scattering in the north muon arm, and, hard scattering in the south muon arm, p+p events. The unbiased distributions are derived from clock trigger events.

peripheral bin relative to regular events. This bin shifting effect therefore reduces the invariant yield, $Y_{\pi}^{meas}(j = 1)$, relative to the true yield, $Y_{\pi}^{true}(i = 1)$. For the most central bin we expect the opposite effect, namely more pions shifting in that category from the mid-central bin and therefore artificially enhancing the measured yield, relative to the true yield.

We correct for both effects, by determining correction factors using our Glauber Monte Carlo simulation. In addition to the $BBC_{inclusive}^{pp,unbiased}$ and $BBC_{inclusive}^{pp,biased}$ distributions that we used previously to define our event categories, we will now need two more BBCS distributions. These are the $BBC_{hard}^{pp,unbiased}$ and $BBC_{hard}^{pp,biased}$ distributions, where hard means that these distributions have been registered with the additional requirement of a hard scattering detected in the central arm (biased and unbiased continue to be associated with the firing or not of the BBCLL1 trigger, respectively). This hard scattering requirement is basically the requirement of a hard pion (p_T>1.5GeV) detected in the central arm. These additional distributions are shown in Fig.3.11. For comparison we also show the inclusive p+p distributions, along with the distributions in which the hard scattering is detected in the south or north muon arm.

It is the hard scattering requirement in the central arm that causes both the BBC trigger bias and the centrality bin shifting effect, and that is why we need the corresponding BBCS distributions to calculate the correction factors for both of these effects. We calculate the correction factor for both of these effects simultaneously. We use the same Glauber Monte Carlo, as above, to calculate the following 4 quantities (numerators and denominators from Equations 3.81 and 3.82) for each centrality bin: $N_{reactions}^{true}(i)$, $N_{reactions}^{meas}(i)$, $N_{\pi}^{true}(i)$, $N_{\pi}^{meas}(i)$. The correction factors are then defined by the following equation:

$$Y_{\pi}^{true}(i) = CorrectionFactor(i) \cdot Y_{\pi}^{meas}(i) \tag{3.83}$$

For each centrality category we keep 4 counters that correspond to the 4 quantities mentioned above. The problem then reduces in determining, for each event, the "true" and "measured" centrality category for each of the counters, as follows:

- $N_{reactions}^{true}(i)$

  Centrality category determined from the N_{coll}, given by the Glauber model for each event.

- $N^{meas}_{reactions}(i)$

  Centrality category determined by modeling the BBCS response summing N^{Au}_{part} samplings of the $BBC^{pp,unbiased}_{inclusive}$ distribution. Counter is updated only if the BBCLL1 is fired (by any of the N^{Au}_{part} nucleon-nucleon collisions) as explained previously.

- $N^{true}_{\pi}(i)$

  Centrality category determined from the N_{coll}, given by the Glauber model for each event. The counter is advanced by N_{coll} since we assume N_{coll}-scaling for hard processes.

- $N^{meas}_{\pi}(i)$

  Centrality category determined by modeling the BBCS response as follows: We assume that there is 1 hard scattering and for that we sample the $BBC^{pp,unbiased}_{hard}$ distribution. The rest of the (N_{coll}-1) nucleon-nucleon interactions are sampled from the $BBC^{pp,unbiased}_{inclusive}$ distribution. For each nucleon-nucleon collision we examine whether the BBCLL1 fires and if that is the case we advance the counter by N_{coll}.

The correction factors thus determined, for each centrality, are listed in Table 3.3.

Table 3.3: Centrality bias corrections

correction	00-20%	20-40%	40-60%	60-88%
	0.95±0.029	0.99±0.007	1.03±0.009	1.04±0.027

These corrections conclude our discussion on the centrality selection in d+Au collisions.

Chapter 4

Data Analysis

4.1 Timing Calibrations of the Time of Flight Detector

The first step to-wards an identified particle analysis is the fine tuning of the timing distributions at the TOF.

We apply two kinds of corrections:

Slat by Slat corrections Using a single run we calculate the expected time of flight of a pion, minus the time of flight reported by the TOF, for each slat, fit the distributions, and use the mean of the fits of these slat-by-slat distributions to shift each individual slat timing distribution so that they are all centered at zero time. There is no particle identification cut applied to identify pions but all particles are treated as pions, an assumption that is mostly correct due to the large abundance of pions at these energies.

Run by Run global offsets After applying the slat by slat corrections to all runs, we use the corrected expected time of flight of a pion minus the TOF time, now for all slats combined, and calculate the resulting global time offset run by run.

The reason for a run-by-run global offset calibration is due to timing shifts that may occur during the months of data collection and potential changes in cable lengths.

For each track that hits the TOF we calculate the expected time of flight of a pion (Eq. 4.1)

$$FlightTime_{\pi} = \frac{PathLength_{TOF}}{c * \beta_{\pi}} \tag{4.1}$$

where

$$\beta_{\pi} = \frac{p}{\sqrt{p^2 + m_{\pi}^2}} \tag{4.2}$$

and then subtract from it the TOF measured and plot it as a function of slat number, Figure 4.1.

It is clear from Figure 4.1 that some slats have large timing offsets and furthermore, there is a systematic trend of larger offsets as the slat number increases as can be seen in Figure 4.2. For that reason we fit each time distribution, for each slat, and use the resulting means of these distributions to shift them as to have zero offsets. A typical fit for two different TOF slats is shown in Figure 4.3 for a particular template run number that was chosen for its stability.

The larger deviations as the slat number grows (Figures 4.2 and 4.3) is

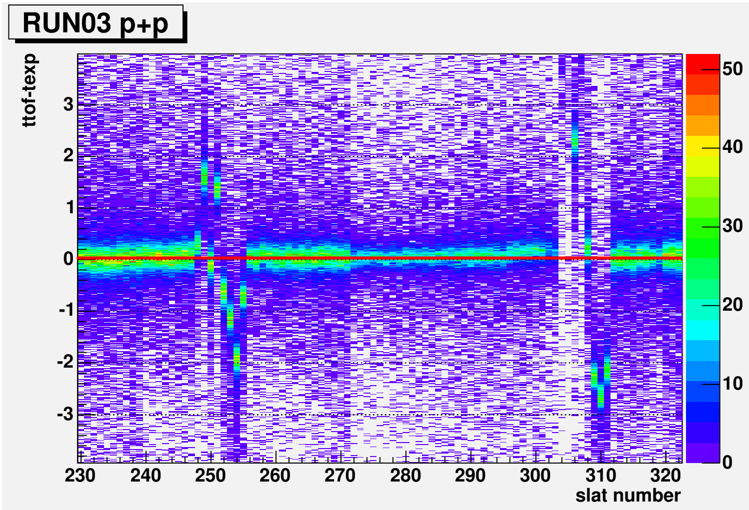

Figure 4.1: Time measured by TOF minus the expected time of flight of a pion (in nanoseconds) for a group of slats.

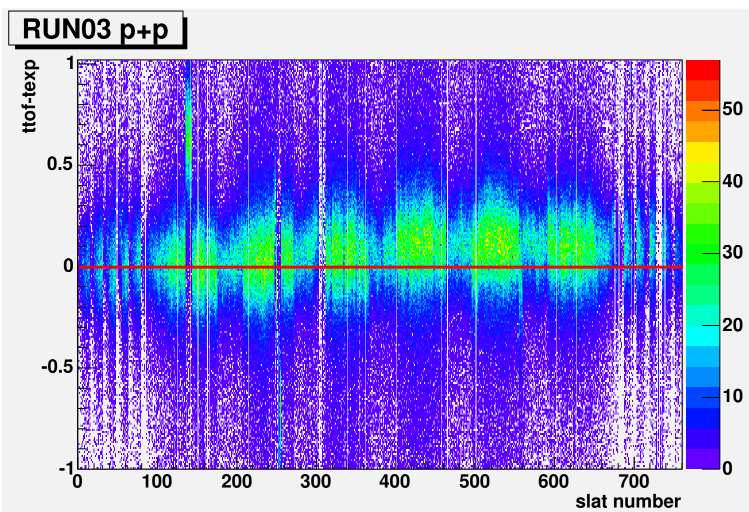

Figure 4.2: Time measured by TOF minus the expected time of flight of a pion (in nanoseconds).

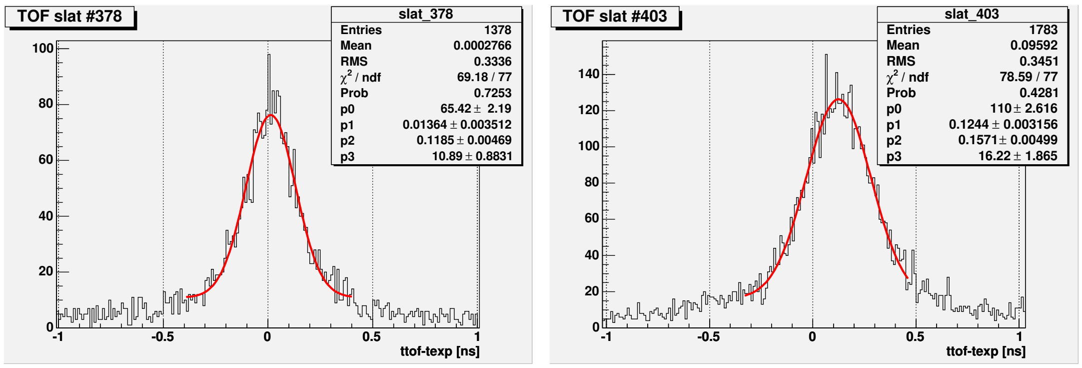

(a) TOF slat number 378.

(b) TOF slat number 403.

Figure 4.3: Individual slat fits of timing distributions. The means of the fits are used as offsets to calibrate the timing distributions.

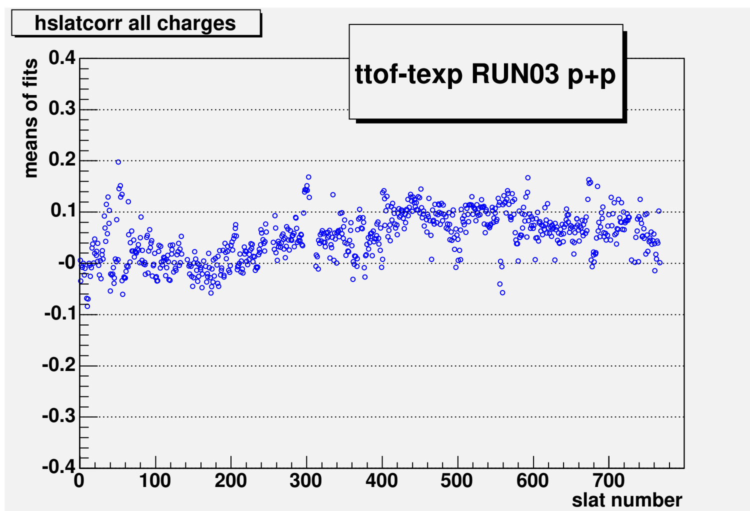

Figure 4.4: Slat by slat corrections as a function of slat number (in ns).

calculated and corrected for. The results of the slat by slat corrections for all slats is shown in Figure 4.4.

Furthermore, it was observed (Fig. 4.5) that slats with very large timing offsets, although they are corrected for time, they still report the wrong *phi* location at the TOF and typically fail the standard matching cuts of 2 or

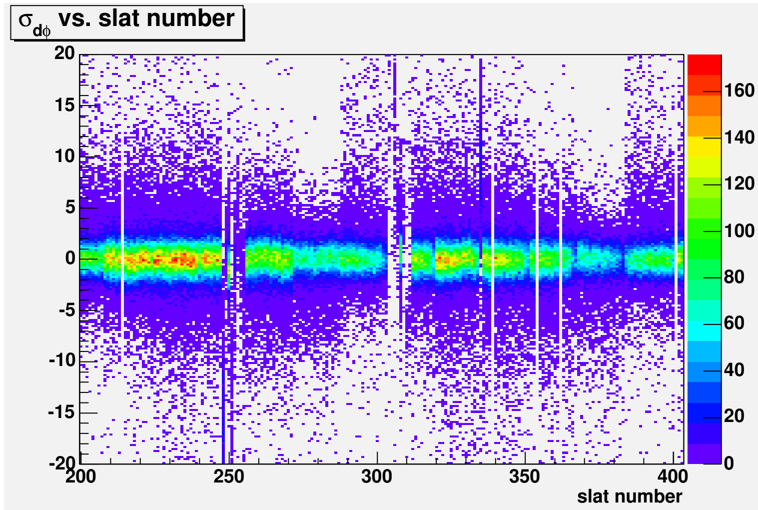

Figure 4.5: Normalized in σ residual matching distributions in the ϕ direction as a function of slat number. The slat timing corrections cannot correct for the phi coordinate reported by the TOF.

3 standard deviations that are applied later on this analysis. We did not correct the *phi* distributions slat by slat but instead chose to remove these pathological slats from both the in the real data and Monte Carlo. There are 21 slats removed in total.

4.1.1 Run by Run Global Offsets

The slat by slat corrections were applied to each run. On top of these corrections, there is a global timing offset that is run dependent. We used the expected time of flight for a pion technique once more, but now combining all slats together to form a global timing distribution for each run. We fit these distributions and derive a global timing offset for each run that is finally applied as an after-burner to the real data. A typical fit for global timing and slat-by-slat timing can be seen in Figure 4.6.

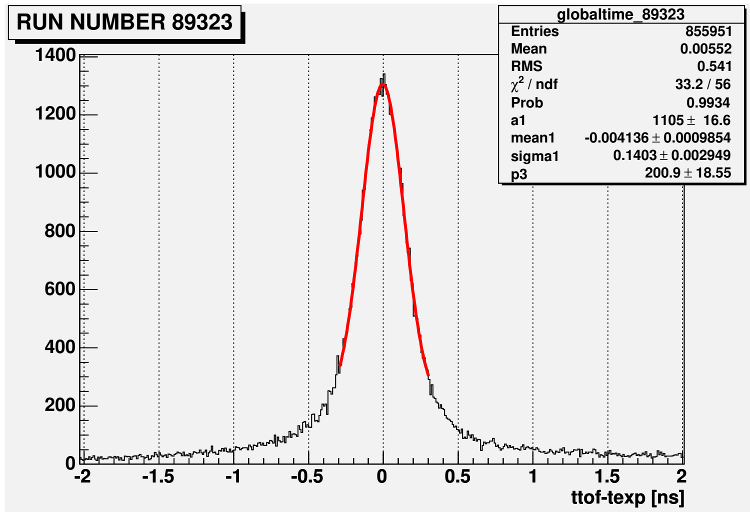

Figure 4.6: Fit for global timing distribution for run 89323.

The global timing offsets calculated for all runs are shown in Figure 4.7. An example of the effect of the timing calibrations is shown in Figure 4.8. In this plot we have combined slat-by-slat and global timing offset corrections to the entire data set and compare it with the corresponding distribution before applying the corrections.

As a final cross check for these corrections we plot all the corrected timing distributions for all runs combined Figure 4.9. All slats are centered around zero and there is no global offset or any slats with large timing offsets. That concludes the TOF calibrations applied to the real data.

In Figure 4.10 we plot the charge/momentum versus time of flight distribution for the d+Au data set, and in Figure 4.11 we plot the same distribution for the p+p data set.

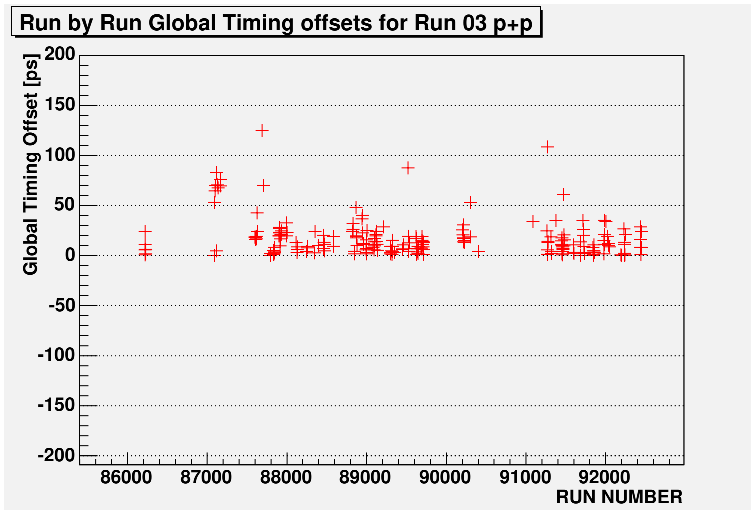

Figure 4.7: Global timing offsets as a function of run number for all runs in the p+p data sample.

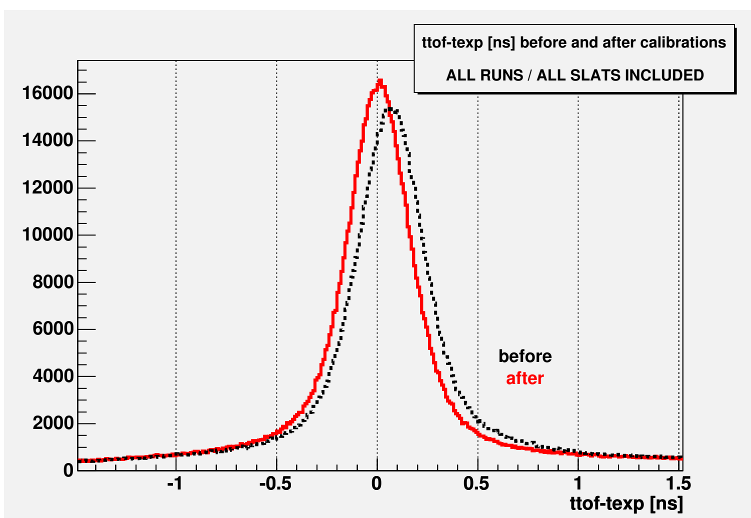

Figure 4.8: Timing distributions before and after the application of the corrections.

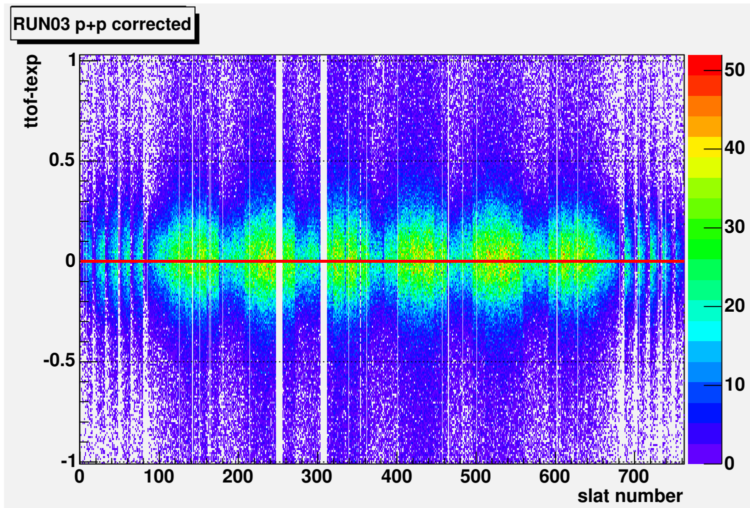

Figure 4.9: TOF time - expected in nanoseconds for all runs combined after all timing calibrations applied to the data.

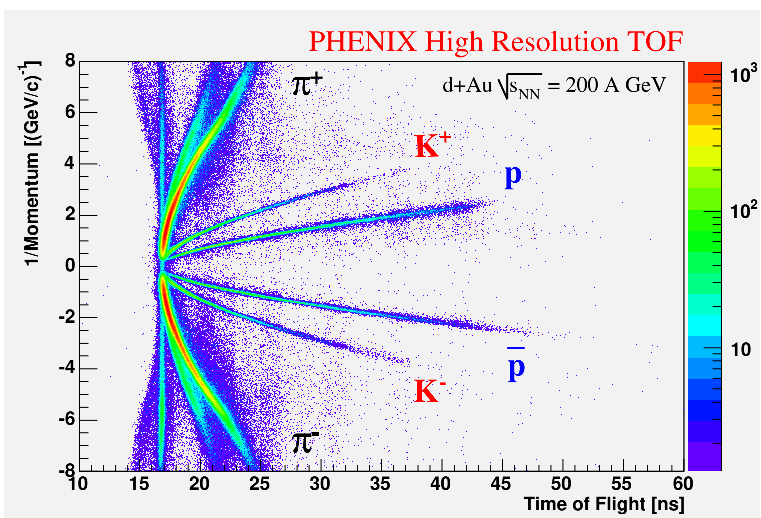

Figure 4.10: Charge/momentum versus time of flight after all calibrations for d+Au.

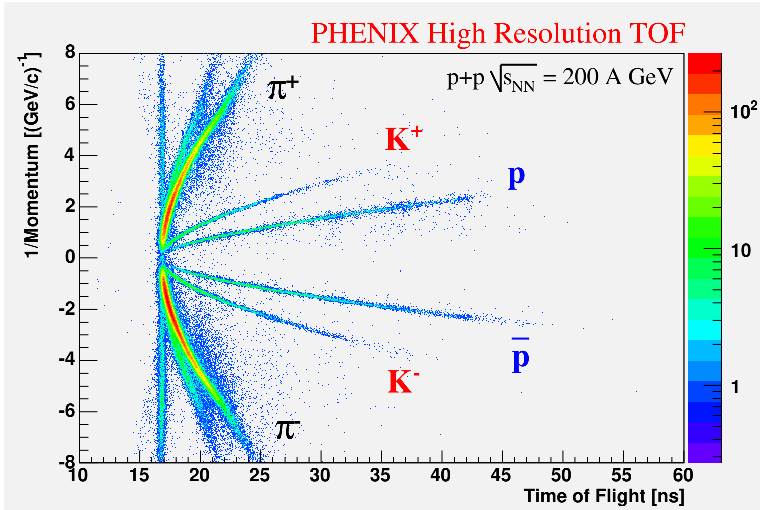

Figure 4.11: Charge/momentum versus time of flight after all calibrations for p+p.

4.2 Particle Identification with the DCH and TOF

The particle identification method used in this analysis is identical to the method used for the Au+Au data. Central role on this method plays the functional form of the resolution on the squared mass of the particles which can be derived analytically through error propagation on the standard formula that determines the squared mass of a particle, given its arrival time, its path length at the TOF and the momentum measured by the Drift Chamber:

$$m^2 = (\frac{1}{\beta^2} - 1)p^2 \tag{4.3}$$

The mass resolution then is given by Eq. 4.4 :

$$\sigma_{m^2}^2 = \frac{\sigma_\alpha^2}{K_1^2}(4m^4p^2) + \frac{\sigma_{ms}^2}{K_1^2}\left[4m^4\left(1+\frac{m^2}{p^2}\right)\right] + \frac{\sigma_{TOF}^2 c^2}{L^2}\left[4p^2\left(m^2+p^2\right)\right] \tag{4.4}$$

where p is momentum, m is particle mass, σ_α is the angular resolution in [mrad], σ_{ms} is the multiple scattering term, σ_{TOF} is the overall TOF resolution and K_1 is the field integral value (87.0).

Given the above functions, the steps that comprise the Particle Identification (PID) method are the following:

1. Determination of the means and widths of m^2 for each particle species in increasing p_t bins.

2. Simultaneous fit of the particle widths as a function of p_t with Eq. 4.4, using as free parameters:

   (a) σ_{ms} : the multiple scattering term,

   (b) σ_α : the angular resolution term and

   (c) σ_{TOF} : the TOF resolution.

3. Using the fitted values of the three parameters and the centroids of the particle $mass^2$ distributions we form the variables isPi, isK and isP for each species, where:

   - $$isXXX = \frac{mass^2_{measured} - mass^2_{centroid}}{\sigma_{m^2}} \tag{4.5}$$

   - The resulting isXXX variables, if correctly parameterized, should be Gaussians with zero mean and $\sigma = 1$.

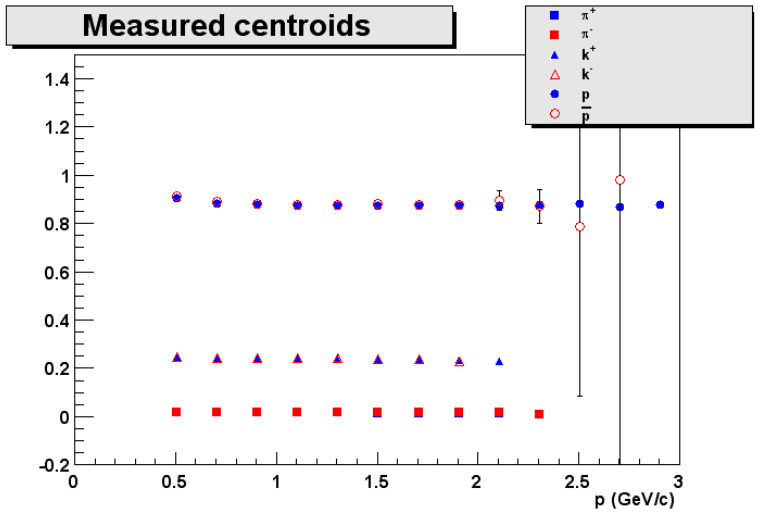

Figure 4.12: Measured centroids for each species and charge as a function of momentum.

- Use these variables to form PID bands that will be used for the cuts.

4.2.1 Particle Identification Cuts

In Fig. 4.12 we show the centroids of the $mass^2$ distributions for all species and charges as a function of momentum. For these calculations we use all triggers contained in the CNT files, not just Minimum Bias, to increase the statistics of the measurements and fits. The particle masses are constant and at the right values as a function of momentum.

For the widths of the particle masses and the simultaneous fit to derive the angular, multiple scattering and TOF resolutions we average over two different methods. In Fig. 4.13 all particle widths as a function of momentum are fitted simultaneously while in Fig. 4.14 only the protons are fitted with the TOF resolution constant at $130ps$. Both methods yield consistent results, within

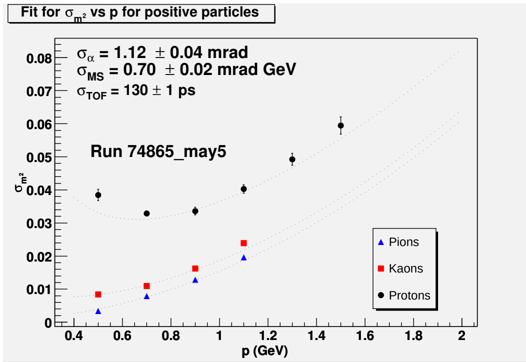

(a) Simultaneous fits to the widths of all positive particles.

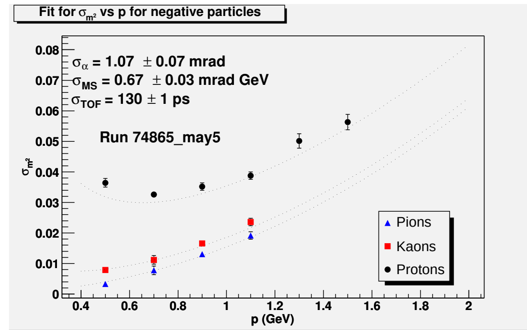

(b) Simultaneous fits to the widths of all negative particles.

Figure 4.13: Particle widths with simultaneous fits. All three parameters are free.

the error bars, and for this analysis we used the averaged values of the three parameters, over these two methods (for both positive and negative particles):

- $\sigma_\alpha = 1.095$ [mrad]
- $\sigma_{ms} = 0.7272$ [mrad GeV]
- $\sigma_{TOF} = 130$ [ps]

Using the above values for the resolution parameters in the mass resolution formula (Eq. 4.4), we form the PID cuts for pions, kaons and protons. The 2σ PID cuts are shown with red lines in Fig. 4.15 and Fig. 4.16 for each particle species as a function of momentum. There is a clear separation between kaons and pions up to $2.0 GeV/c$ while above that the two particles start to merge. For that reason we stop the kaon identification at $1.8 GeV/c$ in momentum while the pions are extended up to $2.5 GeV/c$ by requiring a 2σ veto on the kaon PID. The fractional loss under the pion peak due to the veto in real and

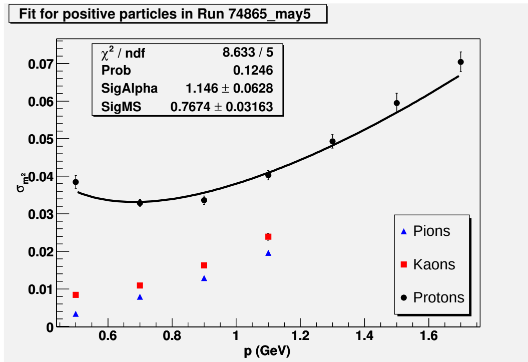

(a) Independent fit to proton widths.

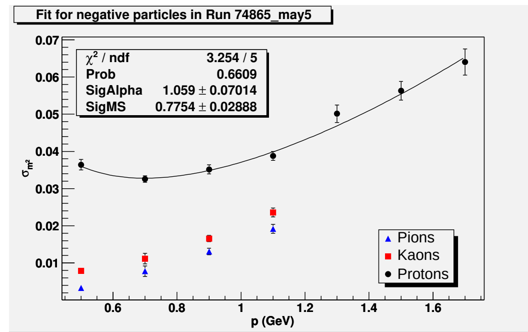

(b) Independent fit to antiproton widths.

Figure 4.14: Particle widths with independent fits to (anti)protons. TOF resolution is held constant at $130ps$.

Monte Carlo data is shown in Figures 4.17 and 4.18. The pion identification stops at the point where the veto removes up to 50% of the pion peak and that happens at around $2.5GeV/c$ in momentum. Due to differences in the veto correction in real data and Monte Carlo we calculate the relative difference in the loss of pions between real data and Monte Carlo as shown on Fig. 4.19 and correct the real data for this difference. The maximum difference is $\sim 15\%$ at $p_T = 2.5GeV/c$.

For the protons, as shown in Fig. 4.15, there is a clear separation from kaons and pions at low momentum and the 2σ upper kaon PID band starts merging at $p \sim 3.5GeV/c$, after constraining the lower accepted $mass^2$ for the protons and antiprotons to be $0.6GeV/c$. Therefore the PID for protons and antiprotons stops at $p_T = 3.6GeV/c$ without any additional kaon veto.

In Fig. 4.20 we show the application of the above mentioned PID cuts to the real d+Au data from all the Minimum Bias events used in this analysis, while in Fig. 4.21 we show the corresponding PID accepted particles for the

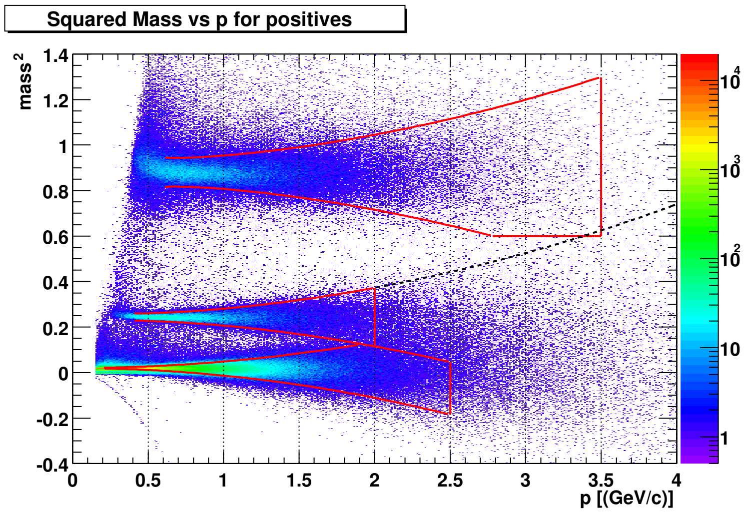

Figure 4.15: PID cuts at 2σ for positive pions, kaons and protons. The red lines represent the actual cuts applied to the data. The black dashed line demonstrates the point of impact between the kaons and the protons.

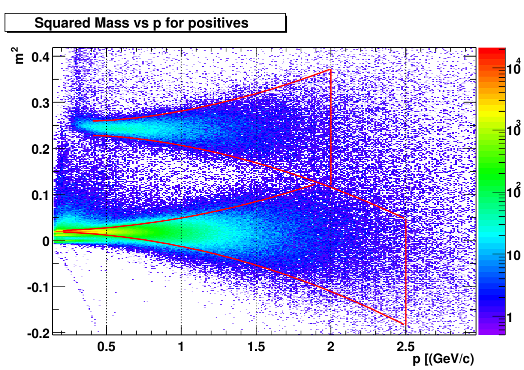

(a) Zoomed in PID cut for positive pions and kaons.

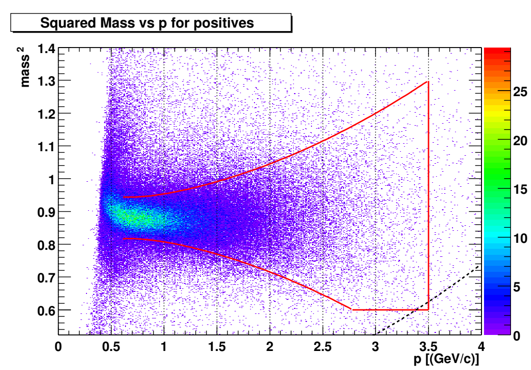

(b) Zoomed in PID cut for protons.

Figure 4.16: PID cuts at 2σ.

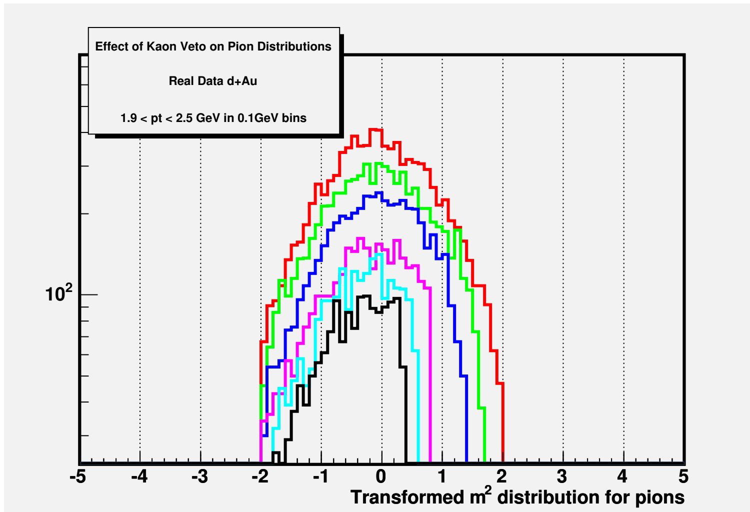

Figure 4.17: Effect of kaon veto PID in the pion peak in 6 successive momentum bins for real data.

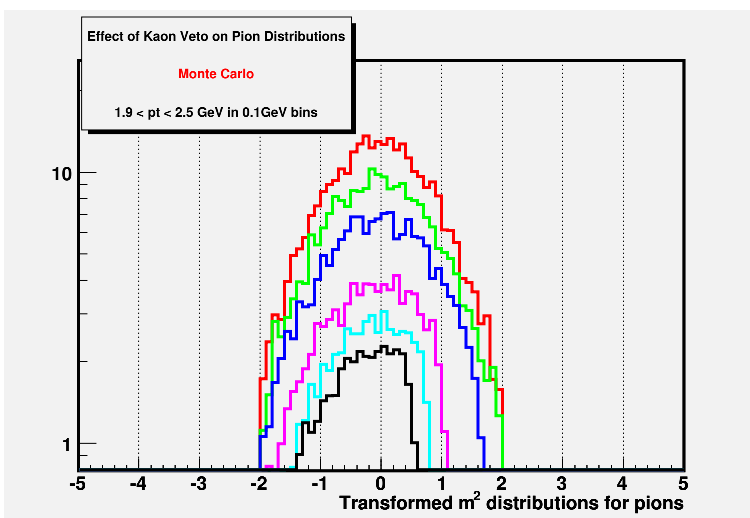

Figure 4.18: Effect of kaon veto PID in the pion peak in 6 successive momentum bins for Monte Carlo.

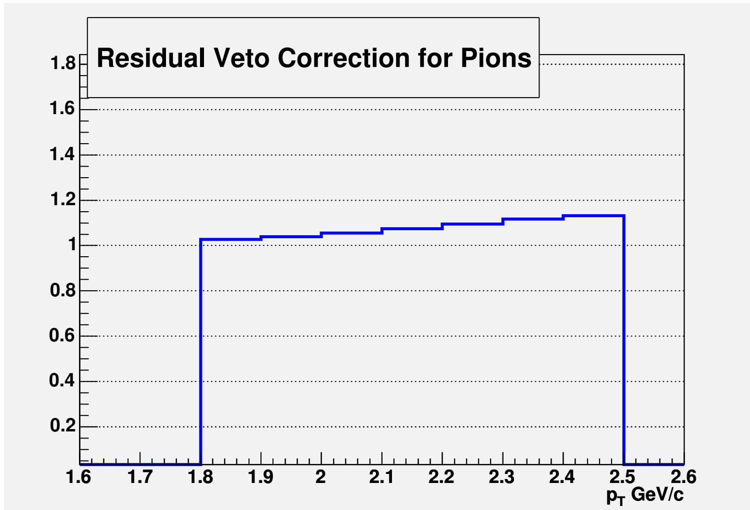

Figure 4.19: Additional correction to the pion yield above $2.0 GeV$ due to the difference in the veto cut in real data and Monte Carlo.

p+p data set.

For a closer look at the PID bands and their evolution with momentum we show the actual mass distributions along with the PID bands in three different momentum windows as shown in Figures 4.22, 4.23 and 4.24 for d+Au. For the p+p case the corresponding distributions are shown in Figures 4.25, 4.26 and 4.27. In all cases the PID cuts are well centered and symmetric under the mass peaks of all particles.

As a final cross-check, we perform a very stringent test on the PID efficiency of the cuts, namely we perform the entire analysis of the data again, but this time choosing a narrow 1σ PID cut. We also apply the same cut to the Monte Carlo and derive corrected spectra for all species. We then divide the 1σ spectra with the 2σ spectra and since we divide corrected spectra we expect the ratio to be at 1. In Figures 4.28(a), 4.28(b) and 4.28(c), we show the ratio of the corrected spectra. Despite the fact that a PID cut of one standard

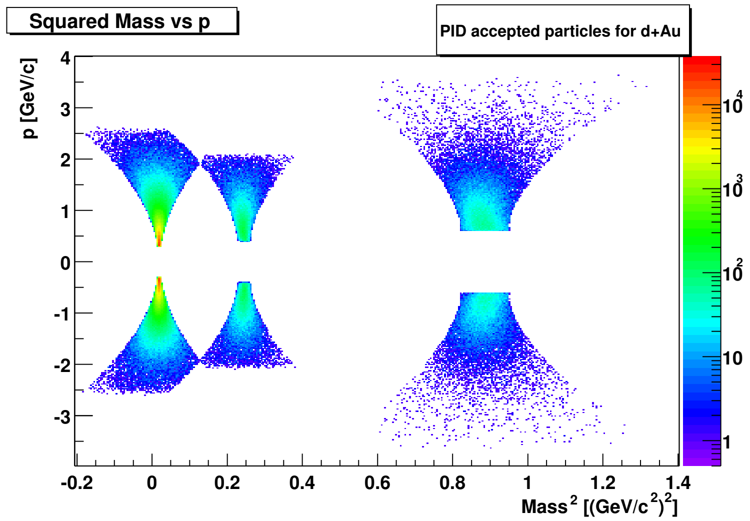

Figure 4.20: Accepted particles after application of PID cuts in d+Au. This plot contains the actual Minimum Bias tracks involved in the analysis

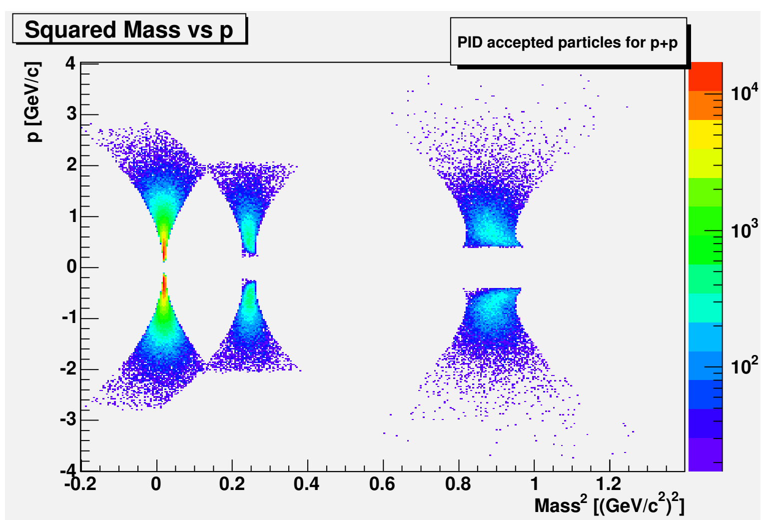

Figure 4.21: Accepted particles after application of PID cuts in p+p. This plot contains the actual tracks involved in the analysis.

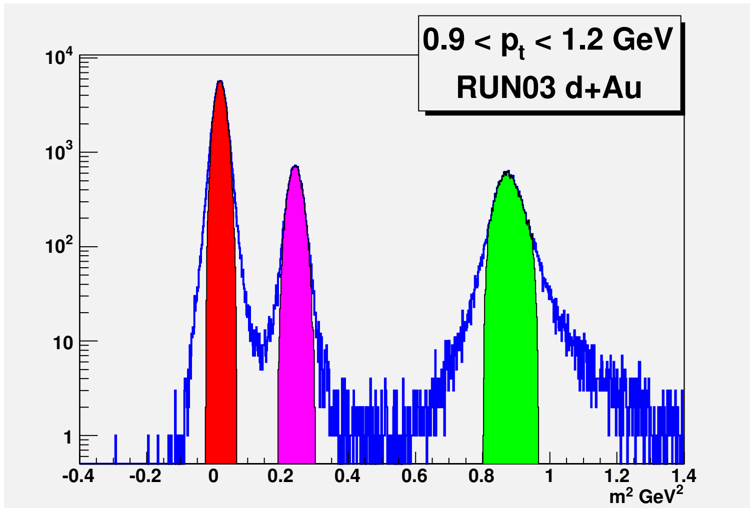

Figure 4.22: Accepted particles after application of PID cuts. This plot contains the actual Minimum Bias tracks involved in the analysis

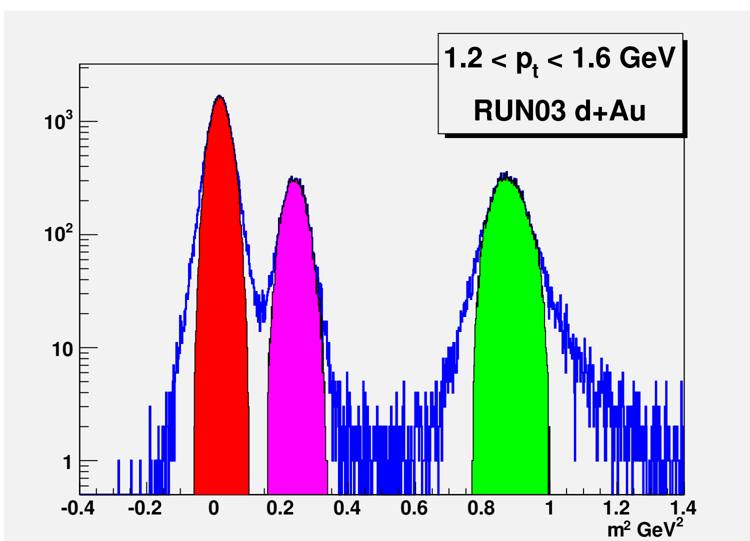

Figure 4.23: Accepted particles after application of PID cuts. This plot contains the actual Minimum Bias tracks involved in the analysis

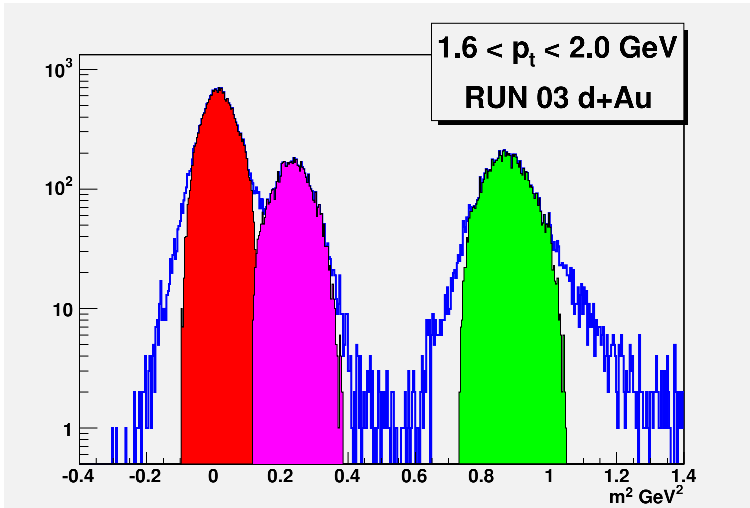

Figure 4.24: Accepted particles after application of PID cuts. This plot contains the actual Minimum Bias tracks involved in the analysis

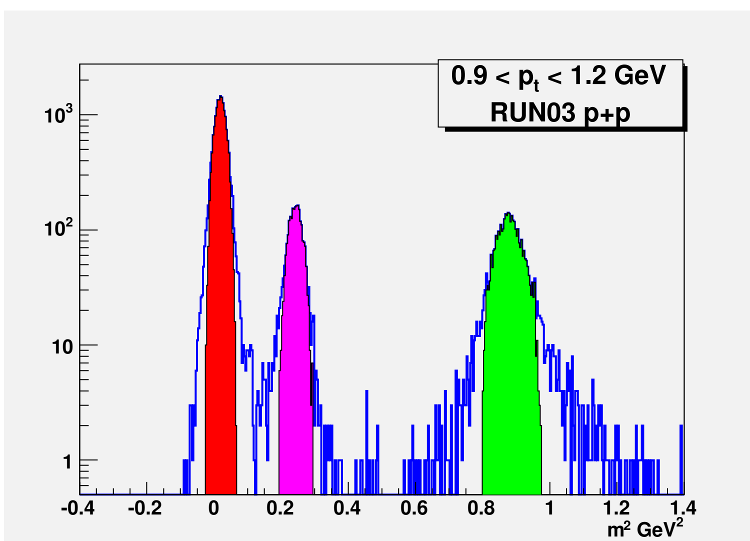

Figure 4.25: Accepted particles after application of PID cuts. This plot contains the actual Minimum Bias tracks involved in the analysis

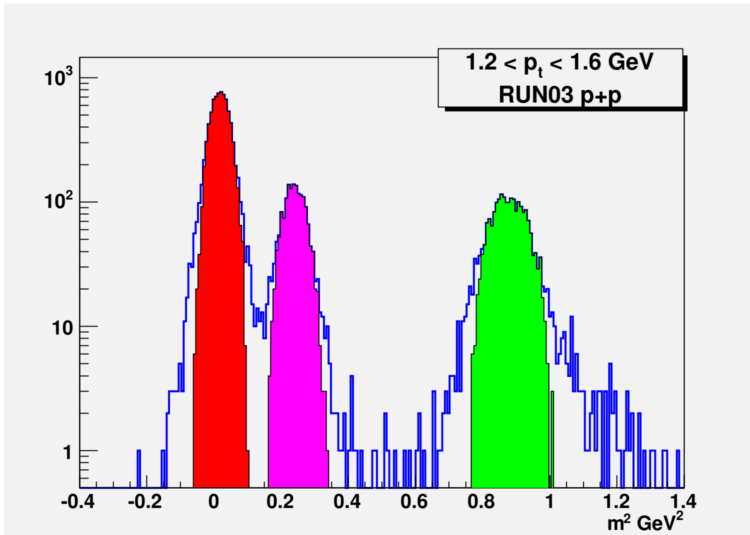

Figure 4.26: Accepted particles after application of PID cuts. This plot contains the actual Minimum Bias tracks involved in the analysis

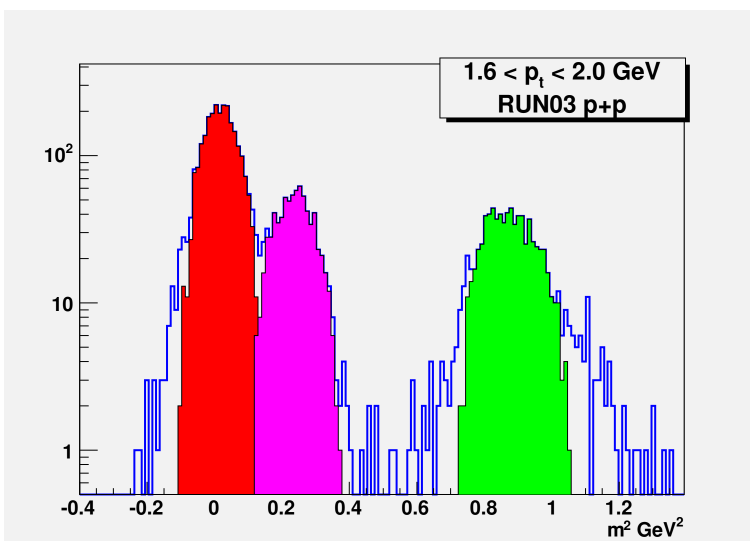

Figure 4.27: Accepted particles after application of PID cuts. This plot contains the actual Minimum Bias tracks involved in the analysis

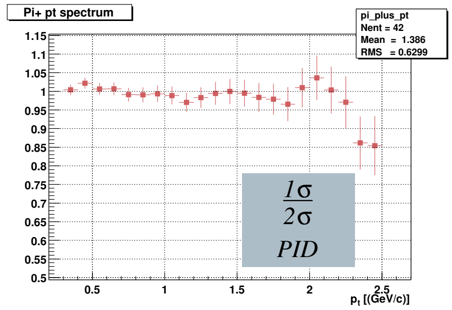

(a) Ratio for Pions.

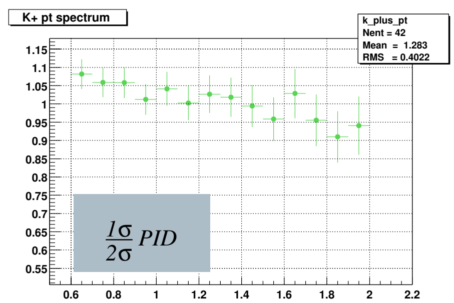

(b) Ratio for Kaons.

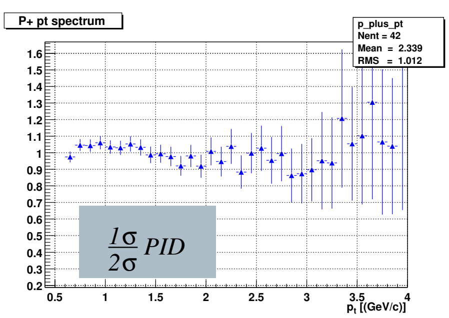

(c) Ratio for Protons.

Figure 4.28: Ratio of 1σ over 2σ corrected spectra for positive pions, kaons and protons as a function of momentum.

deviation is very narrow, we see that the performance of the cut is under control with small fluctuations, about 5% maximum for pions and kaons and about 10% for protons. The same method will be re-applied in the following, for the determination of the systematic uncertainty of the PID cuts.

4.3 Matching Cuts at the TOF

A powerful cut for removing background tracks and tracks that do not originate at the collision point or are artifacts of the reconstruction software is the residual or matching cuts applied at the TOF detector. The relevant residual distributions that are calculated on a track by track basis are the difference between the track model projection in outer detectors like the TOF and the actual point registered by the corresponding detector. We apply these matching cuts in real data and Monte Carlo.

The first step in applying these cuts is to normalize them in a way that the normalized variables describing these distributions can be applied in the same way in real and Monte Carlo data. We apply this normalization as a function of momentum so that a 1σ cut in low momentum or at a higher momentum always covers 1σ of the raw distribution, irrespective of the fact that the means and widths of these distributions change as a function of momentum.

In Figure 4.29 the residual *phi* distribution at a particular p_T bin is fitted with a Gaussian function. After we determine the fit parameters (means and widths) for all $p_T$bins we use them to convert the raw Gaussian distributions into Gaussians of zero mean and unit sigma for all p_T bins. In Figure 4.30 we show a typical fit for the *zed* coordinate at the TOF for $1.1GeV < p_T <$

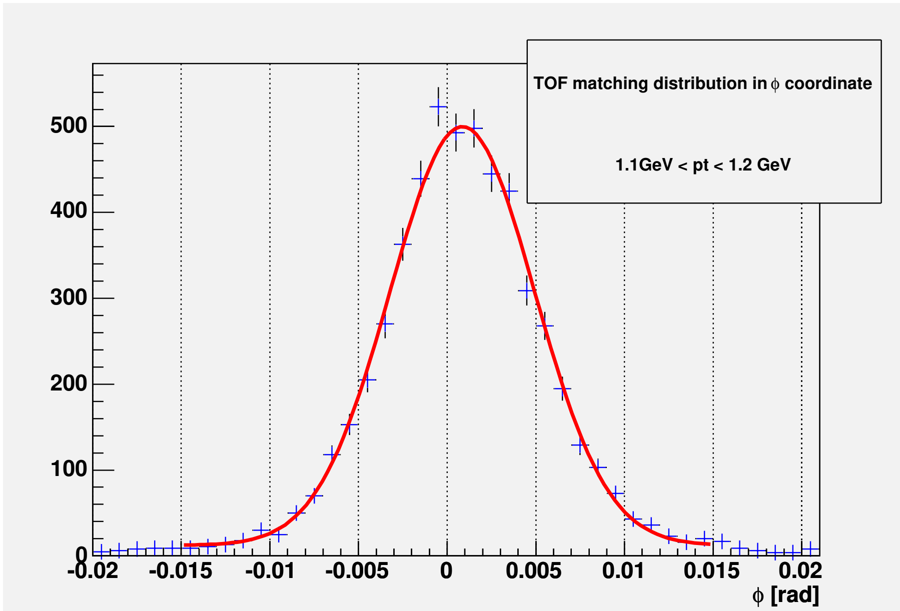

Figure 4.29: Residual distribution of the ϕ coordinate for positive particles at the north side of the TOF.

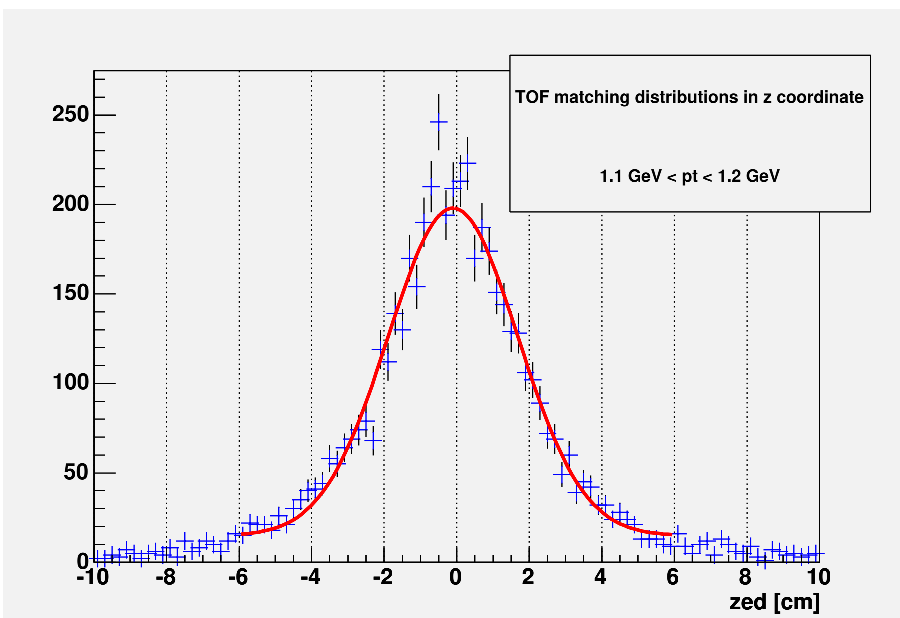

Figure 4.30: Residual distribution of the *zed* coordinate for positive particles at the north side of the TOF.

$1.2GeV$.

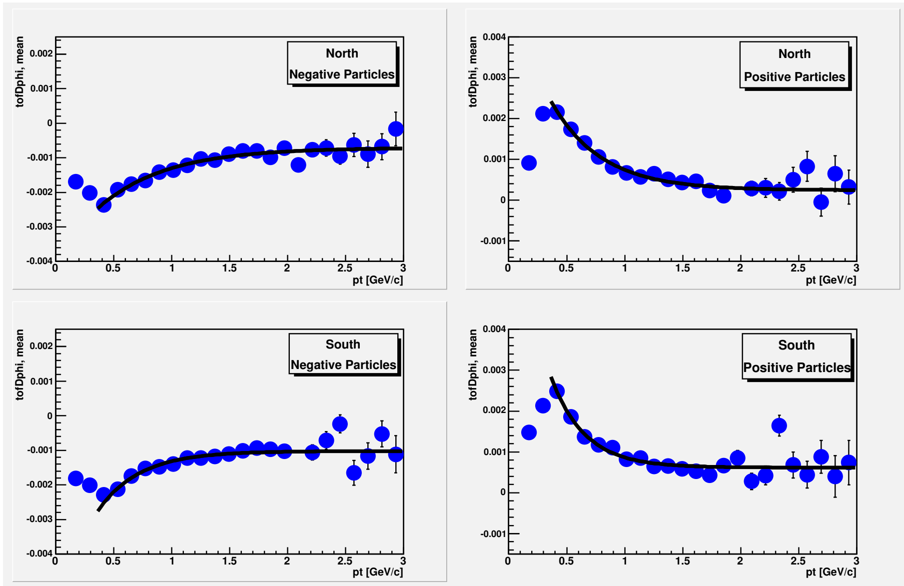

Figure 4.31: Momentum dependence of the parameterization of the means of the ϕ residual distributions in radians.

In order to account for potential differences in the magnetic field configuration in the north and south part of the detector, that may affect the matching quality, and also, in order to study any effects arising from the fact that positive and negative particles bend in opposite directions inside the PHENIX magnetic field, we parameterize the residual distributions as a function of the north and south side of PHENIX, and also separately for positive and negative particles, for both the ϕ and *zed* distributions. In Figure 4.31 we show the momentum dependence of the means for the ϕ coordinate, and in Figure 4.32, the momentum dependence of the widths for the same distributions.

The corresponding parameterizations for the *zed* coordinate are shown in Figure 4.33 and Figure 4.34.

The accuracy of the parameterization of the residual distributions can be checked -as a function of p_T- by examining the new transformed variables (that

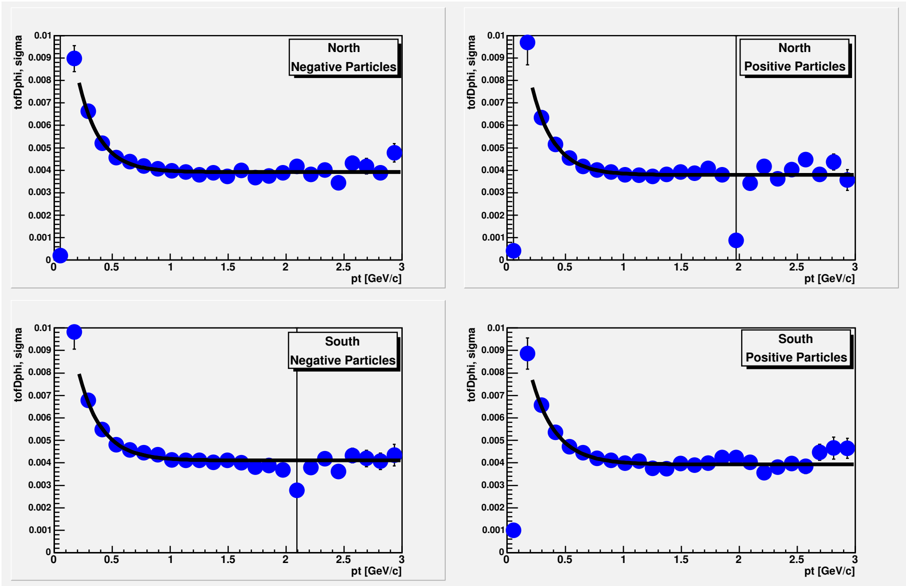

Figure 4.32: Momentum dependence of the parameterization of the widths of the ϕ residual distributions in radians.

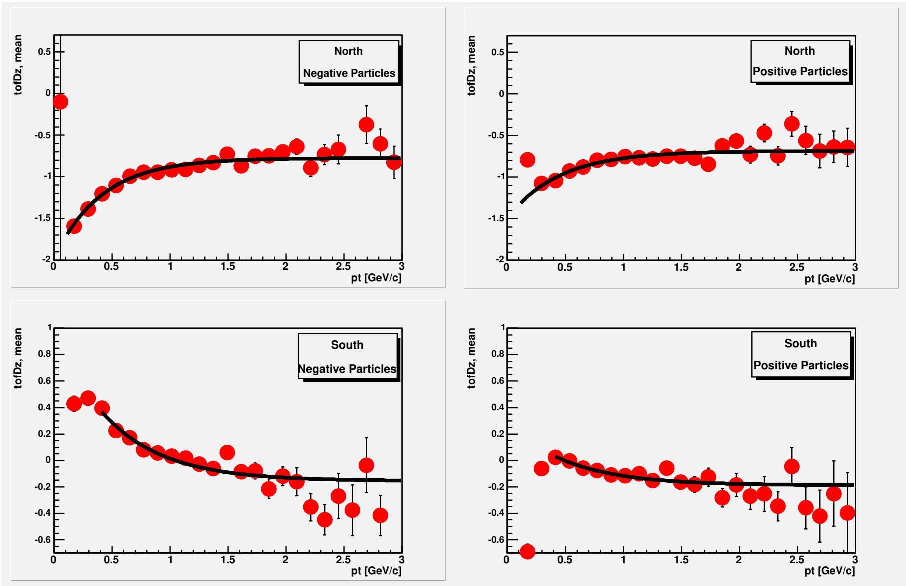

Figure 4.33: Momentum dependence of the parameterization of the means of the *zed* residual distributions in cm.

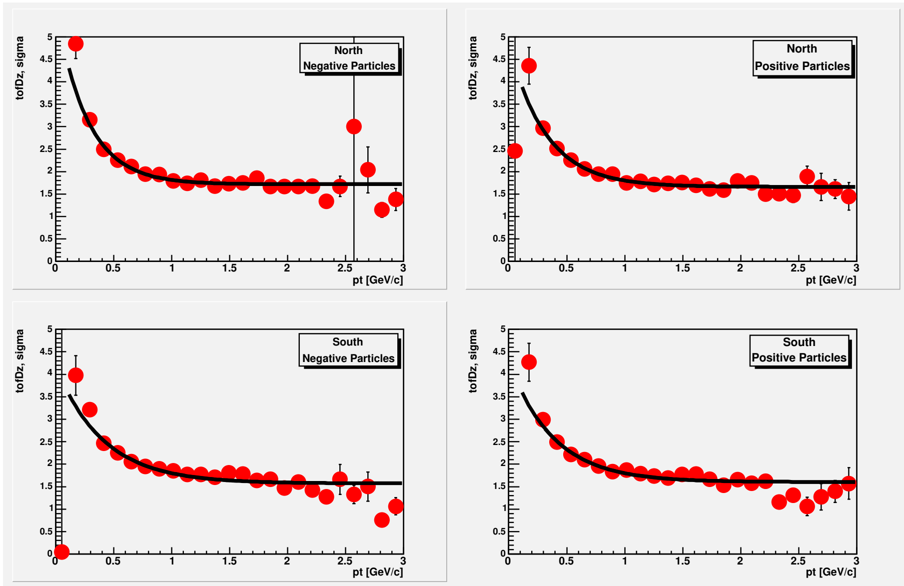

Figure 4.34: Momentum dependence of the parameterization of the widths of the *zed* residual distributions in cm.

we collectively call X):

$$\Delta\bar{X} = \frac{X - \mu_X(p_T)}{\sigma_X(p_T)} \tag{4.6}$$

where $\mu_X(p_T)$ is the momentum dependent means of the fits, while $\sigma_X(p_T)$ are the widths of the fits.

In Figures 4.35 and 4.36 we show the normalized means and widths of the ϕ residual distributions as a function of p_T. The means are stable at zero and the widths at 1, proving that we have achieved a quantitative description of the matching cuts for all ranges of momenta used in the analysis.

The corresponding plots for the transformed *zed* residual distributions are shown in Figures 4.37 and 4.38.

In addition to the momentum dependence of the matching cuts, as a final crosscheck, we examine the zed-dependence of the normalized matching dis-

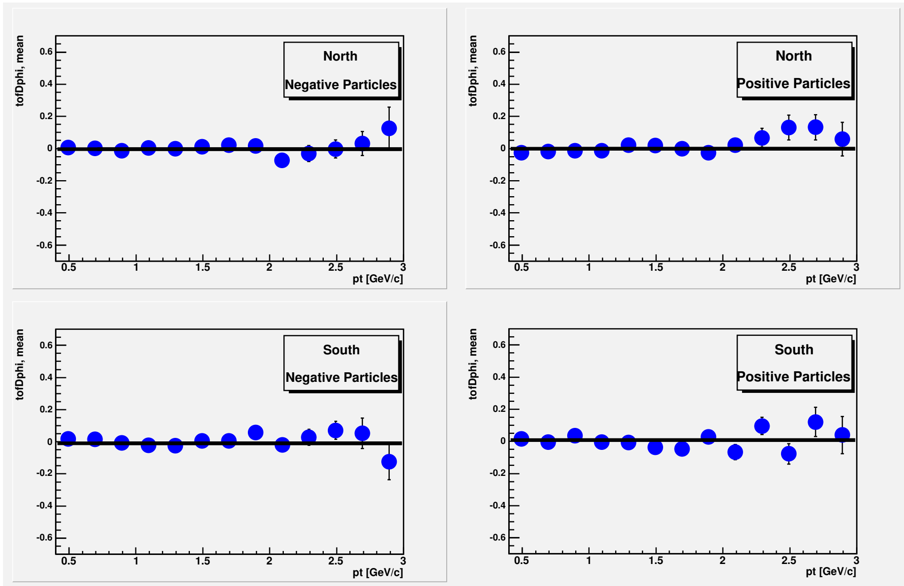

Figure 4.35: Momentum dependence of the transformed means of the ϕ residual distributions.

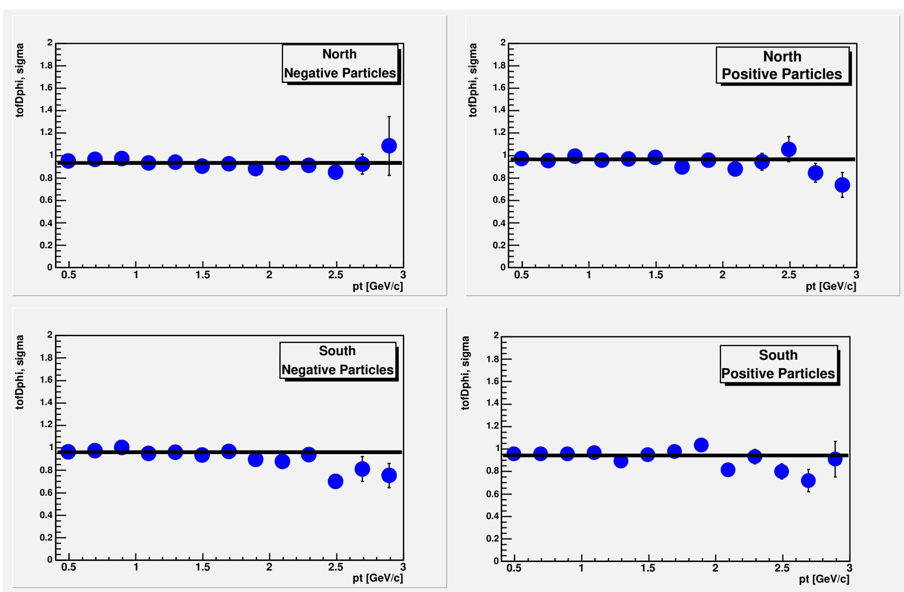

Figure 4.36: Momentum dependence of the transformed widths of the ϕ residual distributions in units of sigma.

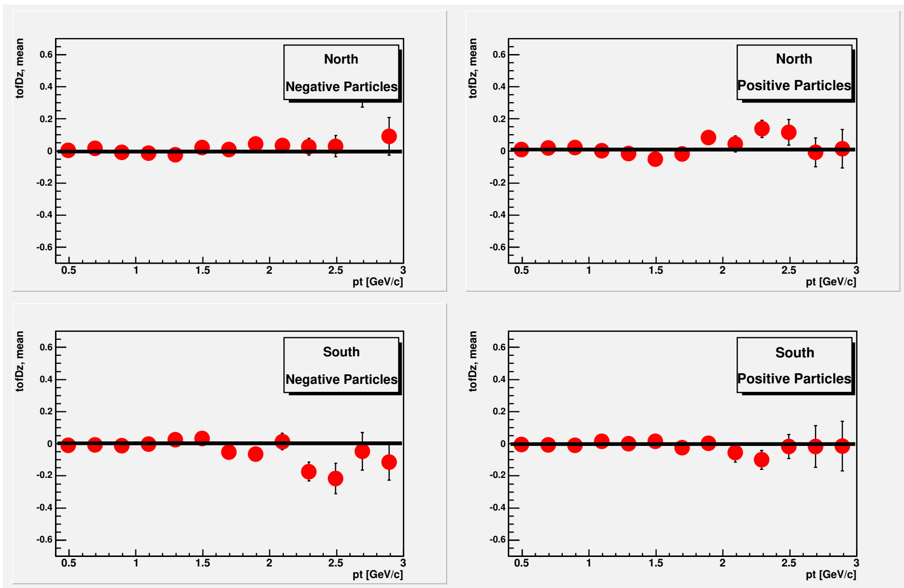

Figure 4.37: Momentum dependence of the transformed means of the *zed* residual distributions.

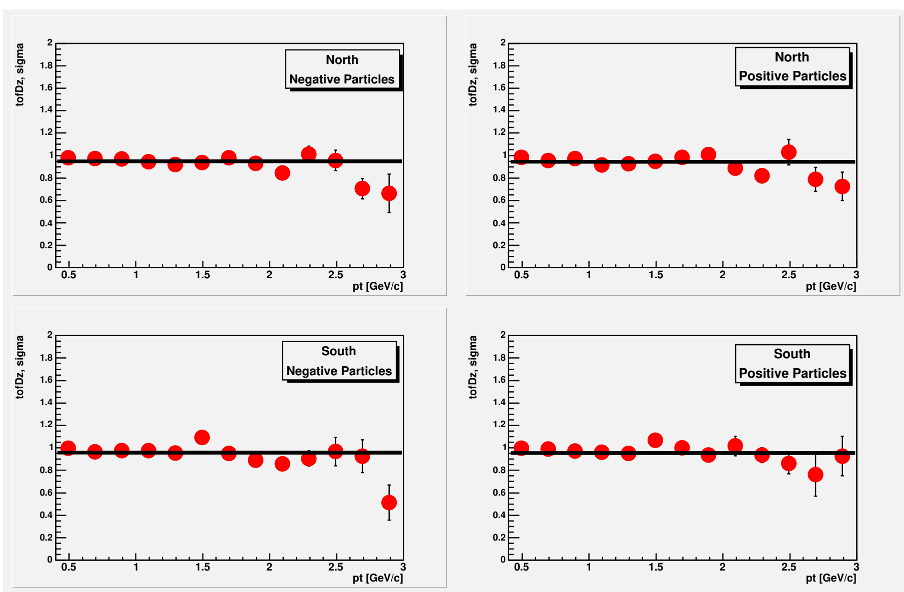

Figure 4.38: Momentum dependence of the transformed widths of the *zed* residual distributions in units of sigma.

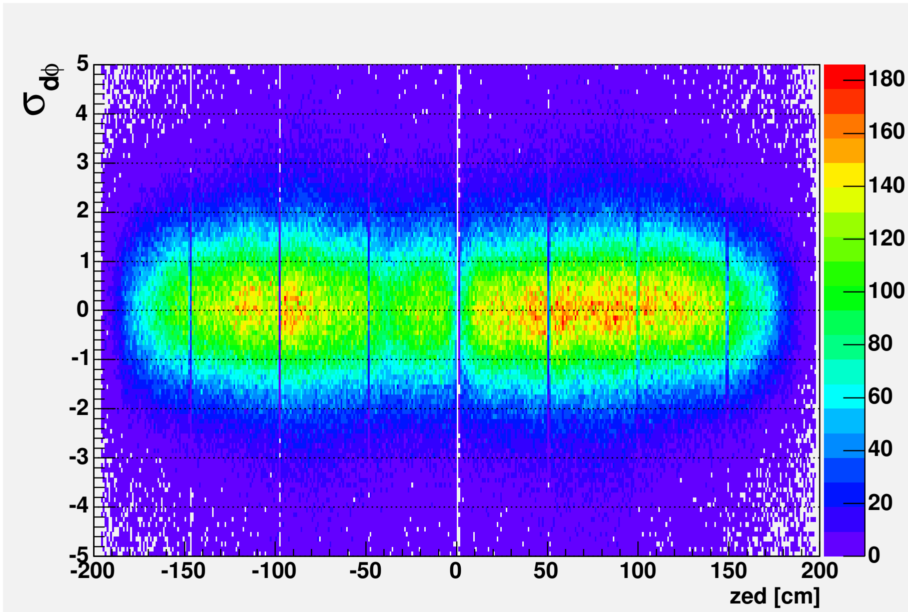

Figure 4.39: Zed dependence of the transformed sigmas of the ϕ residual distributions.

tributions. These are shown in Figures 4.39 and 4.40. There is no additional zed-dependence that must be accounted for. This is due to the fact that the north and south part of the detectors were tuned independently and also as a function of the particle charges.

4.4 Energy Loss

As was mentioned in the Experimental Setup Chapter, the TOF detector has the capability of measuring the charge information of particles hitting its slats. As was shown in Fig. 2.12, the charge information at each slat can be fitted with a Landau distribution and a channel-to-GeV conversion is calculated providing information on the energy loss of the particles hitting the TOF. The energy deposit at the TOF scintillators is then used to apply an energy loss

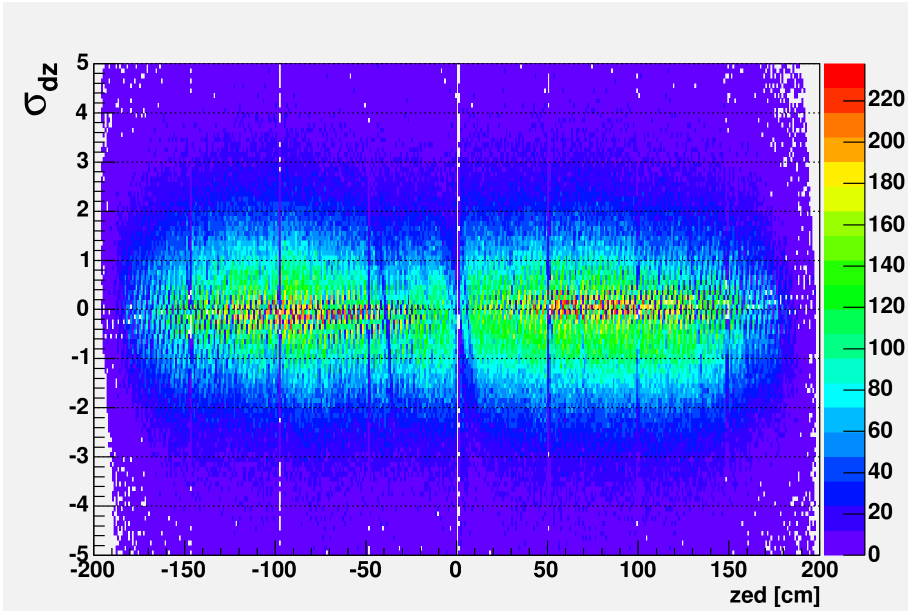

Figure 4.40: Zed dependence of the transformed sigmas of the *zed* residual distributions.

cut that reduces noise hits on the detector. Such a cut is shown in Fig. 4.41 which shows the distribution of β vs. energy loss. The cut is parameterized as follows:

$$Eloss(cut) = a \cdot \beta^b, \tag{4.7}$$

where $a = 0.0014$ and $b = -1.66$.

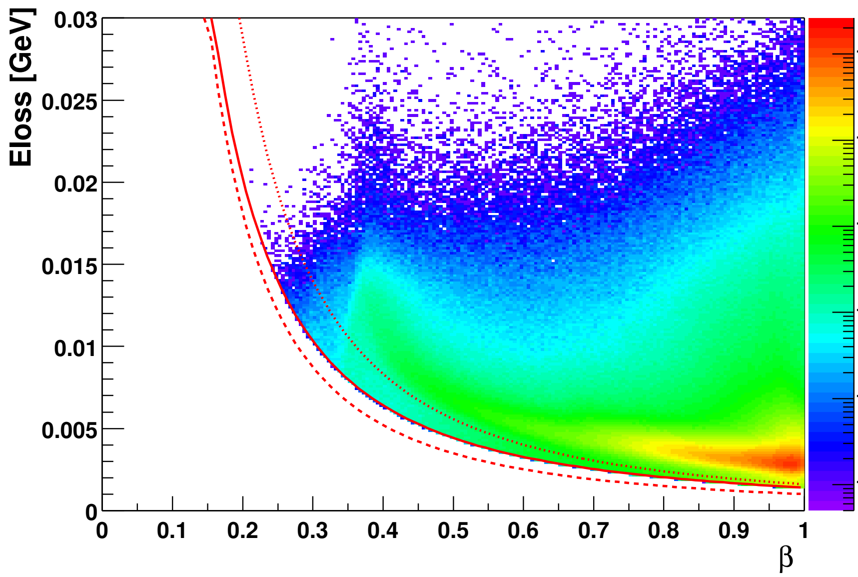

Figure 4.41: β vs. Eloss distributions with eloss cut boundary (solid red line in the middle). The dashed lines above and below the solid line are only used for systematic error estimation.

4.5 Acceptance, Stability, Monte Carlo and Efficiency

4.5.1 Acceptance Cuts and Stability

At the lowest level, the measurement of a particle spectrum consists of counting the number of particles produced in the collision, and, registered by the detectors, as a function of p_T. This initial raw spectrum has to be corrected for acceptance and detector efficiencies since the physical measurable is a probability distribution normalized to 2π in azimuth and 1 unit of rapidity. The PHENIX detector does not cover the entire geometrical area of the physical quantity we want to measure and, in addition to that, the active area of the detectors change as a function of time while the data are being recorded. For that reason we must correct for acceptance and also for efficiencies of the detectors and stability as a function of time.

The primary tool used for these corrections is a Monte Carlo simulation of the relevant detectors which can provide a measurement of the number of particles actually missing the detector due to limited acceptance and also can simulate the effects of dead areas in the acceptance. One of the first inputs needed for the Monte Carlo study is a stable dead channel map that reflects the condition of the detectors during data taking. Since this map needs to be consistent throughout the time of data taking the first thing that must be done is a Quality Analysis (QA) as a function of time -or run number- of the detector acceptance and efficiency so that a representative map is selected to serve as a reference.

The QA in the case of the DCH+TOF analysis is comprised of a run-by-run test of the active area and efficiency of the detectors. For the active area test we measure the angular distributions of the particles hitting the detectors as a function of inverse momentum times the charge of the particle as shown in Figure 4.42.

The dead areas must be parameterized at a later stage but before that we must examine if the maps are constant with time. For the RUN03 p+p data sample we identified four periods of time that the acceptance significantly changed in the detectors as shown in Figure 4.43.

The 3 sets of run numbers that diverged from the chosen template were rejected. We did not attempt to apply a different set of corrections for each set of different run groups because the gains in statistics would be limited, but

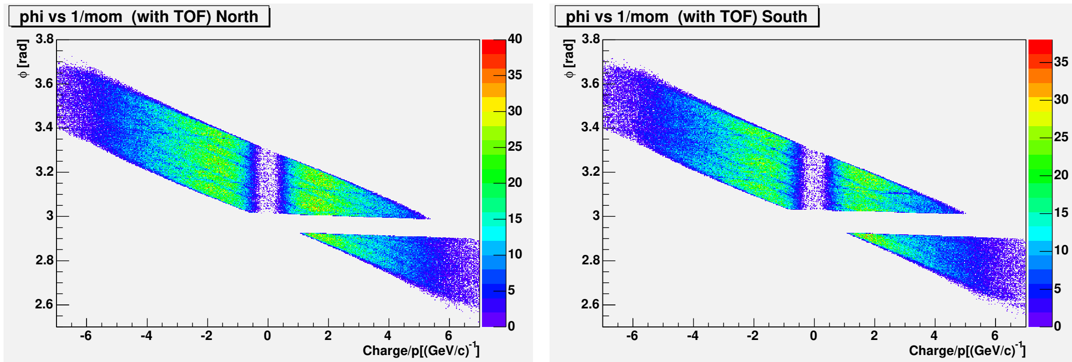

(a) North Side.

(b) South Side.

Figure 4.42: Fiducial acceptance of particles hitting the TOF and DCH.

rather decided to reject the bad runs.

After the Quality Analysis of the data, the fiducial cuts that best map the dead areas in the real data are shown as lines in Figure 4.44. These acceptance cuts will be applied in both real and Monte Carlo data. In this plot, the black lines represent the actual cut applied, while the wider red lines will be used for a systematic evaluation of the cuts.

In order to check the bulk efficiency of the detectors in the chosen good set of runs (from now on simply mentioned simply as runs), the number of TOF+DCH tracks per minimum bias events as a function of run number was examined, Figure 4.45 . Two additional runs were eliminated from the good set of runs and can be seen in Figure 4.45 lying outside the two red lines. The deviation in the number of tracks/minimum bias events in the total set of runs is shown in Figure 4.46, which is the projection in the Y-axis of Figure 4.45. The distribution of Figure 4.45 is fitted with a Gaussian and a 5% uncertainty in the run by run accepted will be included as a systematic error later on

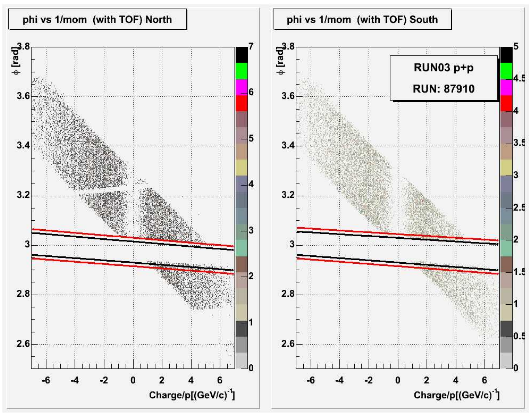

(a) RUN 87910, rejected, problem at North, $\phi < 2.8deg$.

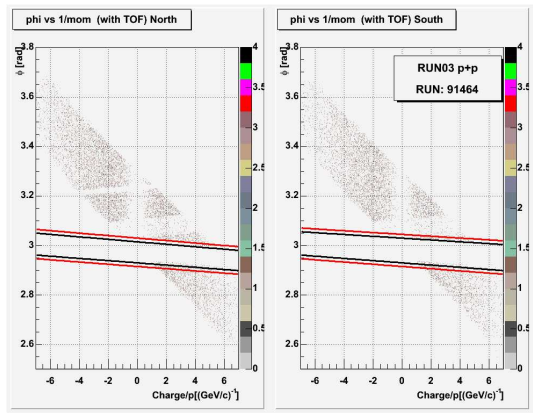

(b) RUN 91464, rejected, problem at North and South , $\phi = 3.1deg$.

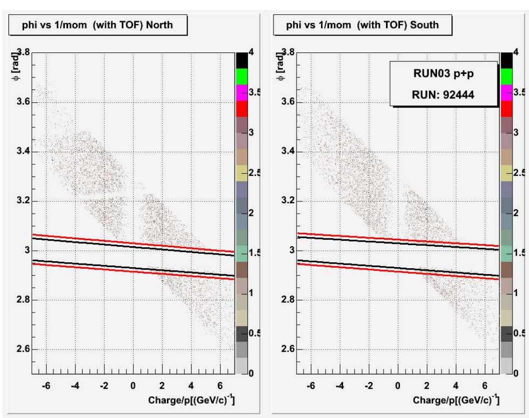

(c) RUN 92444, rejected, problem at North, $\phi > 3.4deg$.

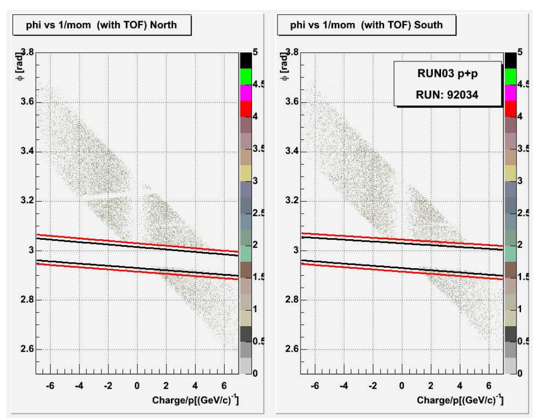

(d) RUN 92034, accepted, used as a template run.

Figure 4.43: Fiducial acceptance of particles hitting the TOF and DCH for different run numbers.

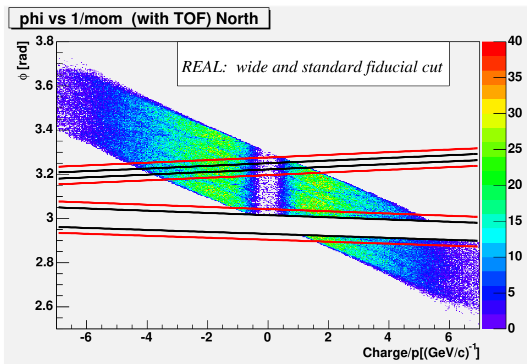

(a) Real data, North side

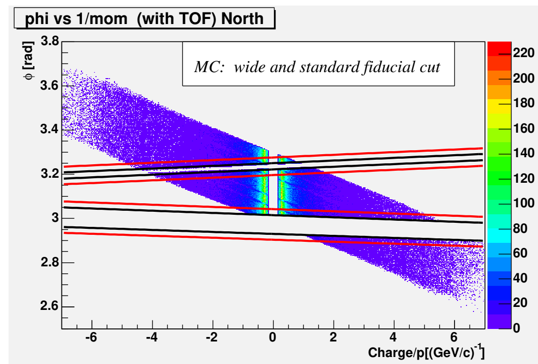

(b) Monte Carlo, North side

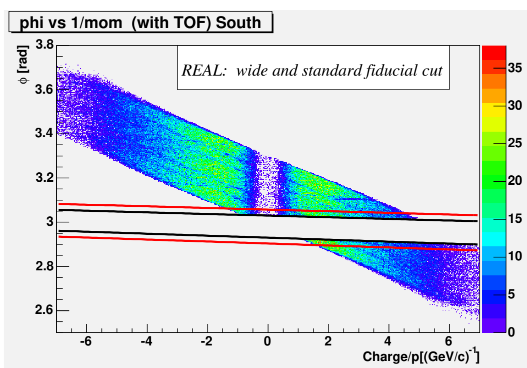

(c) Real data, South side

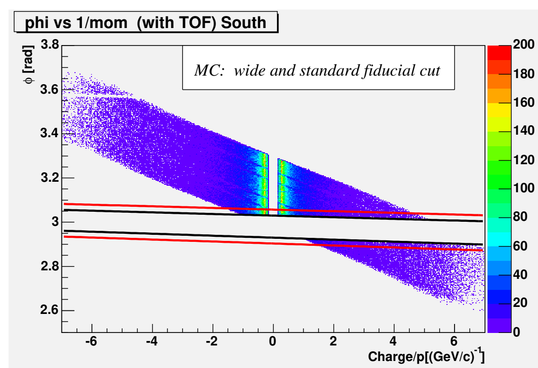

(d) Monte Carlo, South Side

Figure 4.44: Fiducial cuts that best map the dead areas of the detectors after the run-by-run Quality Analysis. Black lines represent actual cut, while red lines are used for systematic evaluations.

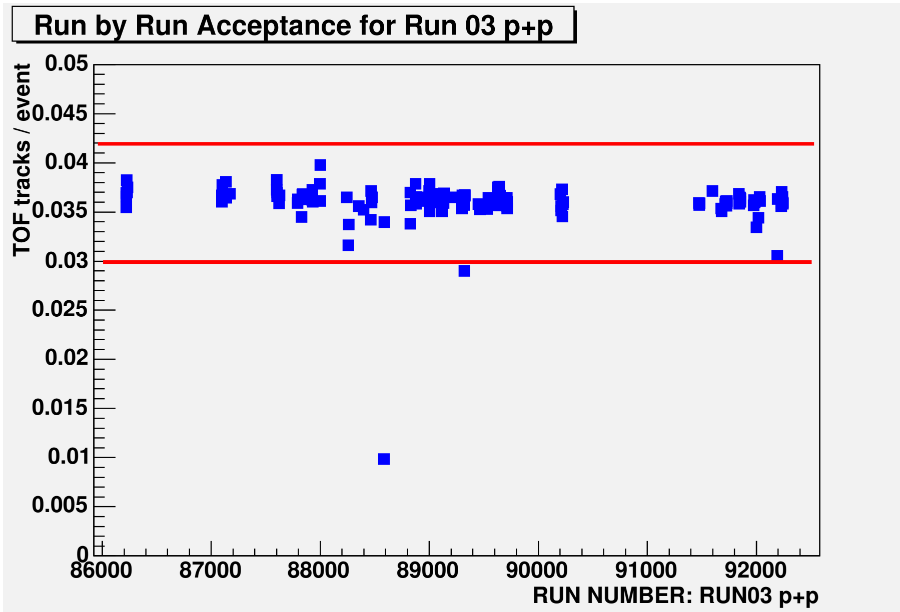

Figure 4.45: Number of DCH+TOF tracks per minimum bias events as a function of run number.

this analysis. The stability of the detectors for the final chosen group of runs is satisfactory and no further rejections are applied to the data set. For the tracks/event plots, the tracks that are registered have been applied the full set of cuts as applied in the final analysis.

As a next step, a more detailed study of the acceptance and efficiency of the TOF+DCH detectors has been performed by comparing the active areas of the DCH and TOF in the real data with that in Monte Carlo. In Figure 4.47 and Figure 4.48 we compare the phi versus zed distributions of the particles hitting the Drift Chamber with an additional tag by the TOF. These plots are usually called "radiographs" and we examine these radiographs for positive and negative particles separately, since due to the opposite bending of the low momentum positive and negative particles in the magnetic field of PHENIX, different parts of the low acceptance TOF are being hit depending on the

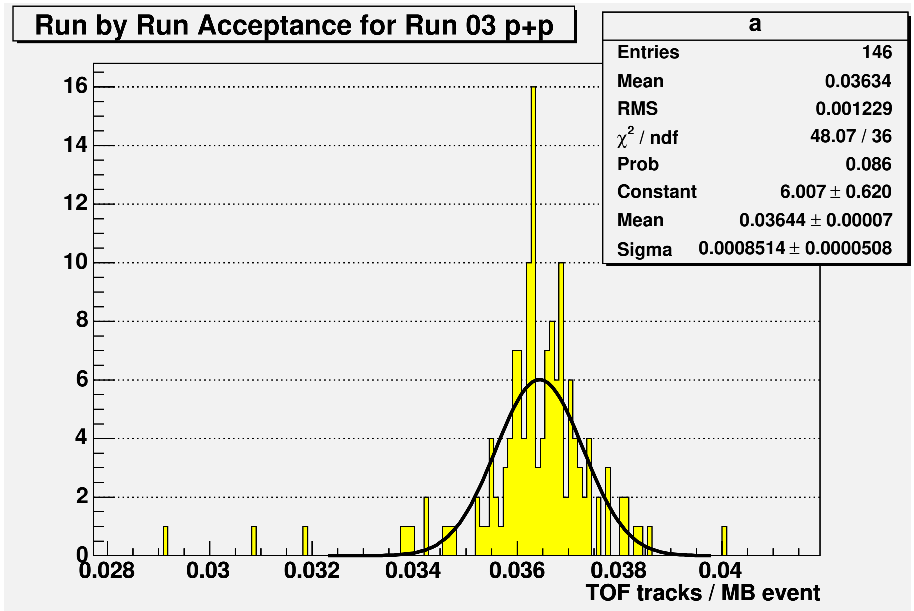

Figure 4.46: Distribution of the number of DCH+TOF tracks per minimum bias events.

charge of the particle. Due to the low momentum bending effect we must be sure that the input momentum distribution in the Monte Carlo is similar with the physical momentum distribution of the real data and for that reason the Monte Carlo tracks are weighted by a realistic momentum distribution as measured by the corrected real data momentum distribution.

In Figure 4.49 the radiograph for negative particles is presented in the DCH while in Figure 4.50 the corresponding TOF radiograph for negative particles is shown. From this acceptance and efficiency study we conclude that the real and Monte Carlo distributions are in very good agreement. This is a result of the fiducial cuts applied that remove dead areas in the detectors. An example is the removal of a PC1 dead area as can be seen in Figure 4.47 at around $zed = -70cm$ and $\phi = 175deg$. Since these acceptance cuts are applied in real and Monte Carlo, a good reproduction of the active geometry of the detector is

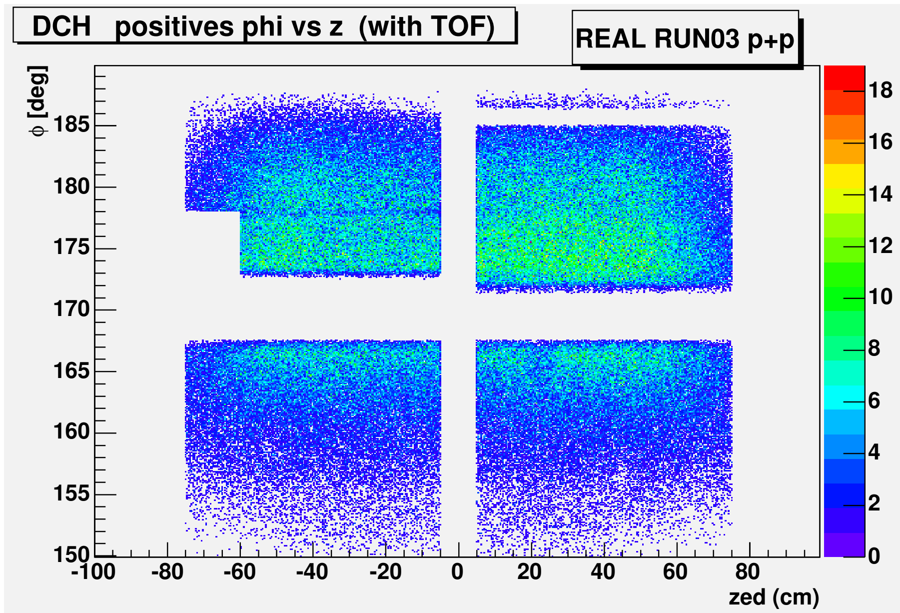

Figure 4.47: DCH radiographs for positive particles in real data.

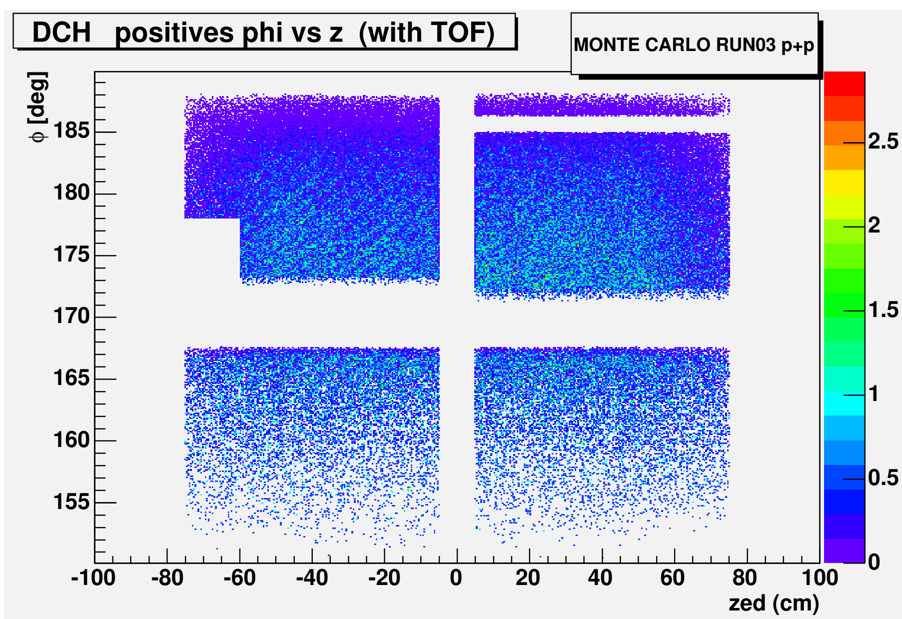

Figure 4.48: DCH radiographer for positive particles in Monte Carlo.

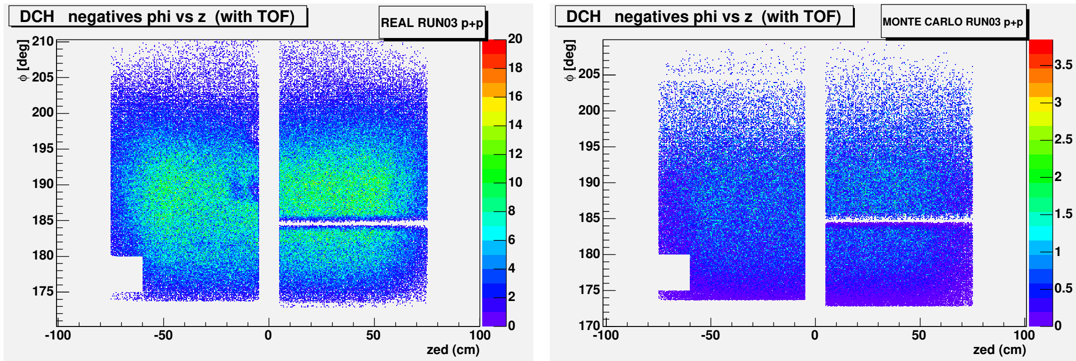

(a) Real data.

(b) Monte Carlo.

Figure 4.49: DCH radiographs for negative particles in Monte Carlo.

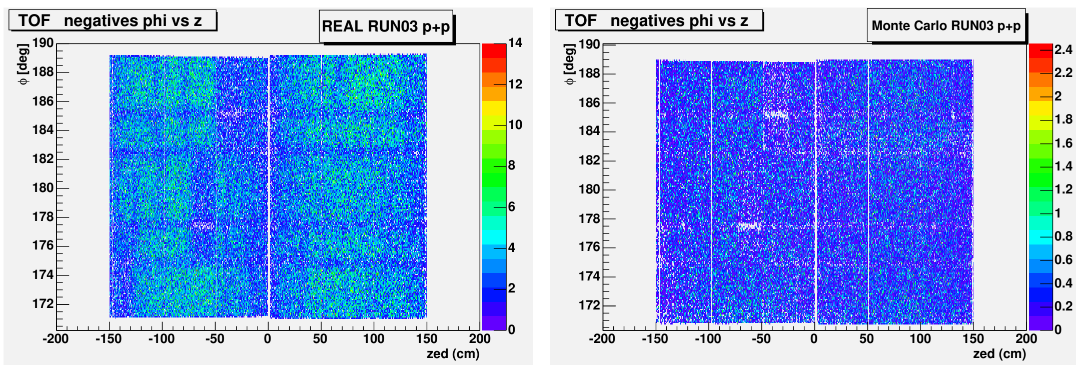

(a) Real data.

(b) Monte Carlo.

Figure 4.50: TOF radiographs for negative particles in Monte Carlo.

achieved, which is crucial later on when we calculate the correction factors that are applied to the data to upscale the measured cross sections in 2π azimuthal and 1 unit of rapidity acceptance.

Moving on to the next level of detail we will examine the ϕ and *zed* acceptance of the TOF+DCH individually by projecting the corresponding radiographs in the ϕ and *zed* directions in order to calculate the final efficiency corrections to the data, but before this final step we will study the effect of the efficiency of the quality cuts as will be explained in the next section.

4.5.2 Efficiency Study of Quality Cuts

In the high multiplicity events of central $Au+Au$ collisions where a large number of particles emerge from each collision and the detectors are experiencing high occupancy factors, a set of tracking quality cuts has been established. The most stringent of the quality cuts require that a track is reconstructed in both the X1 and X2 layers of the DCH and there is also a unique association of the track with a hit in the PC1, right behind the DCH. We study the efficiency of these cuts in p+p collisions by plotting the phi distributions of positive and negative particles in the north and south part of the detector once requiring a high quality tracking cut and once with no application of the cut, always in the real data. In Figure 4.51 the two distributions for positive particles in the south part of the detector are shown with and without any quality cuts along with the ratio of these distributions. Figure 4.52 shows the corresponding distributions for the north part of the detector for positive particles.

In these Figures the distributions with and without the cut have not been normalized externally so that any resulting differences are a direct consequence of the quality cuts. It is clear from Figures 4.51 and 4.52 that there is an overall efficiency loss of the order of $5\% - 10\%$ due to the tracking cuts that most probably arise from a low efficiency region of the PC1 detector, required for a unique association of the track. In other regions where the PC1 operates in maximum efficiency these plots prove that there is no overall gain from the

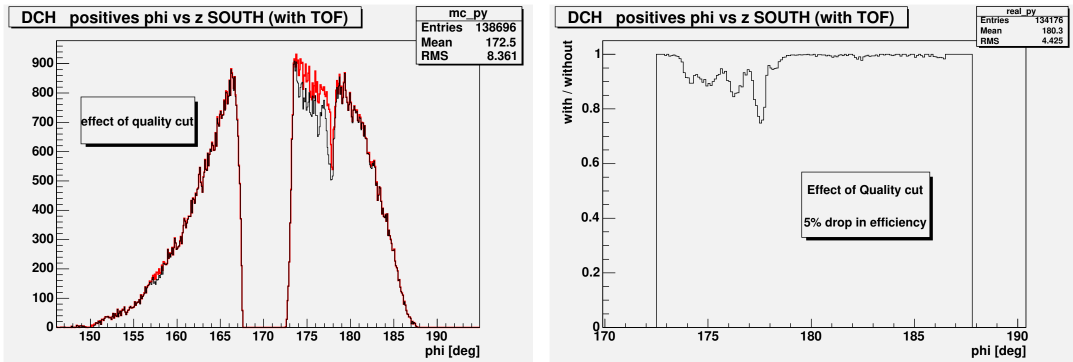

(a) ϕ distributions at the DCH+TOF with (black) and without (red) a quality cut.

(b) Ratio of the distributions.

Figure 4.51: Effect of quality cut for positive particles in the south part of the detector.

cut since the ratio of these distributions is a constant at 1. In Figures 4.53 and 4.54 the same effect is observed for negative particles although it is much smaller due to the difference in acceptance.

The conclusion of this study is that, in the very low multiplicity environment of p+p and d+Au collisions, and, furthermore, in an analysis that requires the DCH tracks to registers a hit at the TOF, which is almost 3 meters downstream from the DCH, and with the additional constraint of matching cuts at the TOF, the requirement for an additional tracking cut just exploits the inefficiencies of the PC1 detector in a certain region and does not offer any additional selection of good tracks. Instead of correcting these inefficiencies which are different for positive and negative particles, the quality cut was dropped in the analysis and will not be applied in the following.

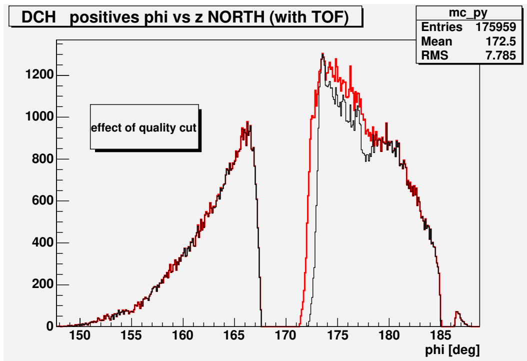

(a) ϕ distributions at the DCH+TOF with (black) and without (red) a quality cut.

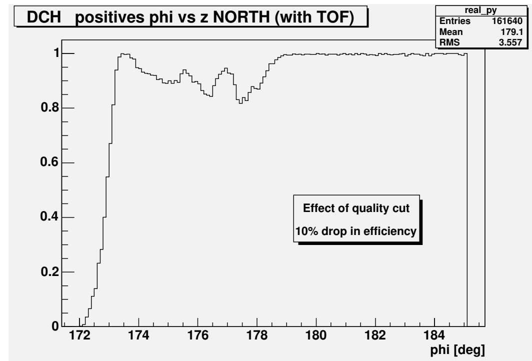

(b) Ratio of the distributions.

Figure 4.52: Effect of quality cut for positive particles in the north part of the detector.

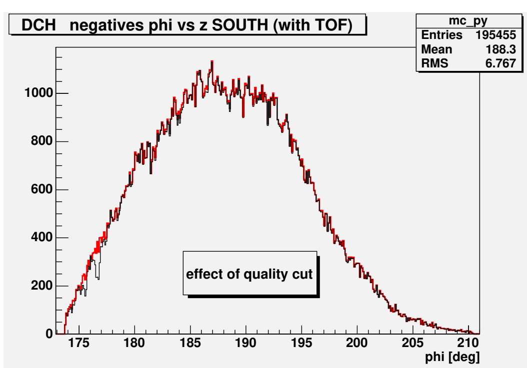

(a) ϕ distributions at the DCH+TOF with (black) and without (red) a quality cut.

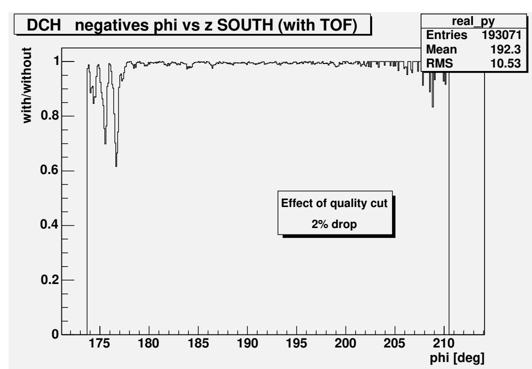

(b) Ratio of the distributions.

Figure 4.53: Effect of quality cut for negative particles in the south part of the detector.

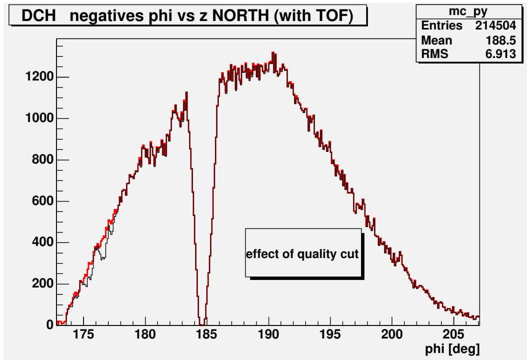

(a) ϕ distributions at the DCH+TOF with (black) and without (red) a quality cut.

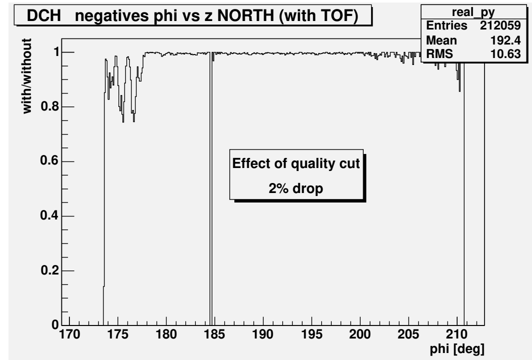

(b) Ratio of the distributions.

Figure 4.54: Effect of quality cut for negative particles in the north part of the detector.

4.5.3 Final Efficiency Corrections

The radiographs are good for eyeball determinations of holes in the detectors and regions of low efficiency but the quantitative comparison is done by projecting the distributions in the ϕ and zed axes and comparing them with the corresponding weighted Monte Carlo distributions. The method that we apply begins by identifying a region in the real distribution were we assume 100% efficiency for the detectors. We calculate the integral under this region and use it to normalize the corresponding region in the Monte Carlo distribution. After the two distributions (Real and Monte Carlo) have been normalized at the maximum efficiency region of the detector we calculate the ratio of the two distributions for all the active areas. This ratio determines the final efficiency correction. The same procedure is applied in the ϕ and zed distributions and the final efficiency correction is the product of the two.

We show the positive particle ϕ distributions in the north and south part of

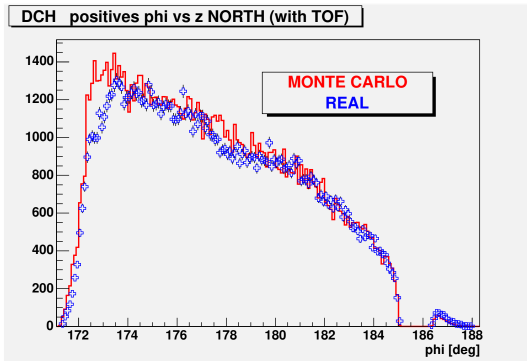

(a) North.

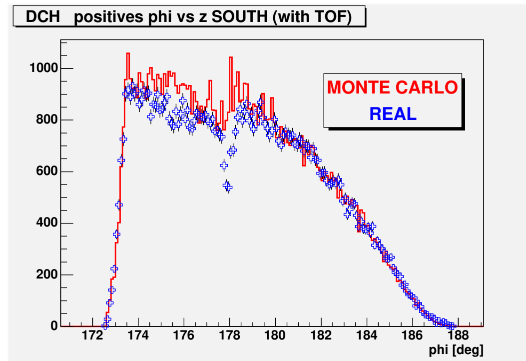

(b) South.

Figure 4.55: ϕ distribution of positive tracks at the DCH with a TOF hit.

the detector in Figure 4.55 and the corresponding ratios of the real and Monte Carlo after the normalization in Figure 4.56. The *zed* distributions for positive particles in north and south are shown in Figure 4.57. The corresponding distributions in ϕ and *zed* coordinates for negative particles in the north and south part of the detector are shown in Figures 4.58 and 4.59.

The final corrections factors that are applied in the data are on the order of 3%.

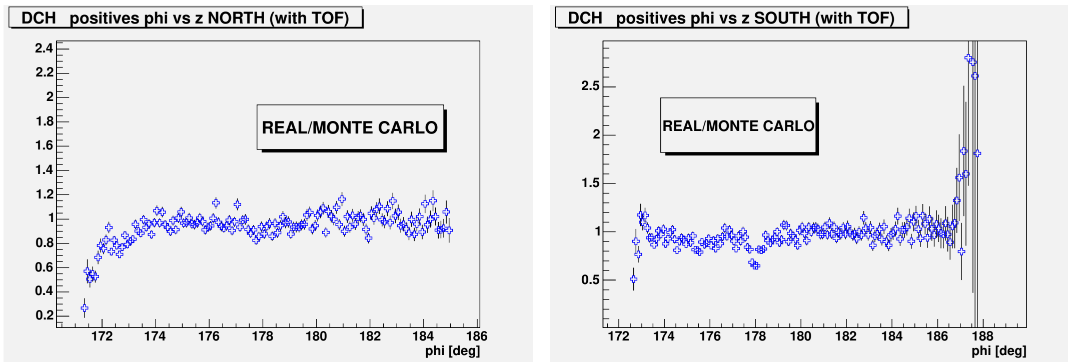

(a) North.

(b) South.

Figure 4.56: Ratio of ϕ distribution for data and Monte Carlo of positive tracks at the DCH with a TOF hit.

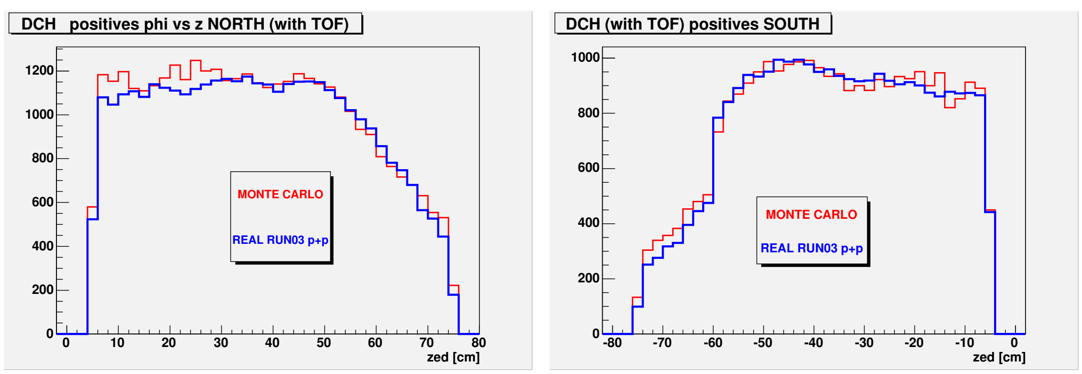

(a) North.

(b) South.

Figure 4.57: *Zed* distribution of positive tracks at the DCH with a TOF hit.

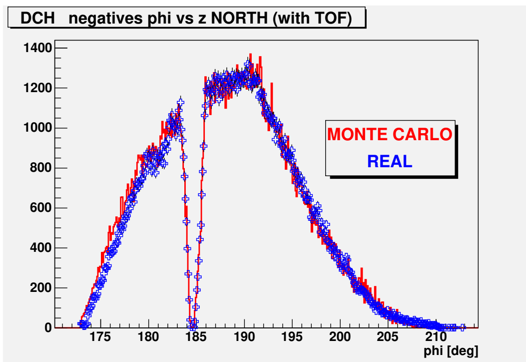

(a) North.

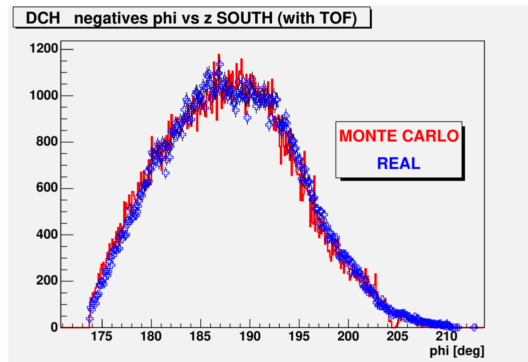

(b) South.

Figure 4.58: ϕ distribution of negative tracks at the DCH with a TOF hit.

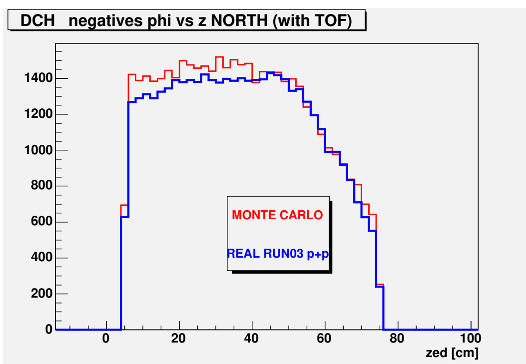

(a) North.

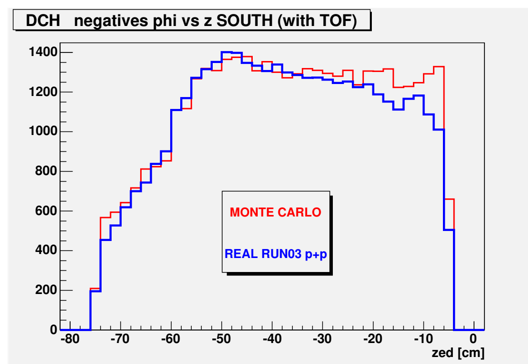

(b) South.

Figure 4.59: *Zed* distribution of negative tracks at the DCH with a TOF hit.

Chapter 5

Correction Functions from Single Particle Monte Carlo

5.0.4 Generation and Tuning of Monte Carlo

The inclusive p_T spectra for each particle species that are measured with the PHENIX spectrometer must be corrected for acceptance since the TOF detector covers 0.7 units in rapidity and $\pi/8$ radians in azimuth. Since these distributions are PHENIX acceptance dependent we must provide a physical normalization of the data. In order to normalize the spectra in full azimuth and one unit of rapidity we use a single particle Monte Carlo simulation that accurately describes the geometry and characteristics of the detector. A simple geometrical scaling would not be accurate enough since, due to the magnetic field, particles at low momentum curve significantly before they reach the spectrometer, and make the geometrical scaling non trivial. Also dead areas in the detector and areas of low efficiency must be corrected for using the Monte

Carlo simulation.

We apply the same procedure for all particle species and charges which is summarized in the following table:

- Single Particle Event Generation with the EXODUS event generator.
- Simulate PHENIX detector Response with PISA and Reconstruction (PISA is the GEANT based simulation of the PHENIX spectrometer)
- Calculation of Correction Factors

A single particle generator called EXODUS was developed by Ralf Averbeck of Stony Brook to generate input distributions for the Monte Carlo. The statistics used for this simulation project are described in Table 5.1.

Table 5.1: Statistics of single particle Monte Carlo

particle species	run number	N_{file}	processed N_{evt}	Available N_{evt}
π^+	24000–24199	200	10M	9,900,000
π^-	24200–24399	200	10M	9,900,000
K^+	24400–24599	200	10M	9,750,000
K^-	24600–24799	200	10M	9,650,000
proton	24800–24999	200	10M	9,750,000
$\bar{p}$	25000–25199	200	10M	9,900,000

The generation of particles in momentum and coordinate space was chosen so that it covers a wide area that fully contains the TOF detector allowing also for the large bending of low momentum tracks. The p_T distributions generated were enhanced at low momentum in order to produce a high statistics correction function at that momentum region, where statistics typically suffers due

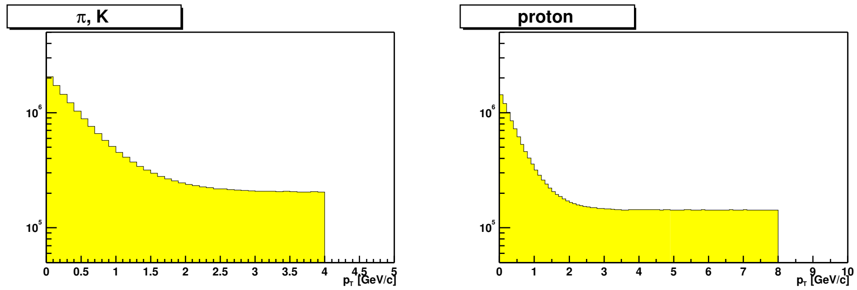

Figure 5.1: Transverse momentum distribution generated for Monte Carlo.

to the fact that most particles miss the detector in this region. The particle generation parameters are the following:

- Event type: single particle $\pi^{\pm}, K^{\pm}, p, \bar{p}$
- Event quantity: 10 million
- vertex: $-30 < vertex < +30$ cm (continuous, uniform)
- rapidity: $-0.6 < y < +0.6$ (flat)
- azimuthal range: TOF acceptance ($100^o < \phi < 260^o$)
- transverse momentum (p_T)
  - 0.0 to 4.0 GeV/c for pions (low p_T enhancement)
  - 0.0 to 4.0 GeV/c for kaons (low p_T enhancement)
  - 0.0 to 8.0 GeV/c for protons (low p_T enhancement)

Figures 5.1 and 5.2 show the momentum and space distributions generated by the single particle Monte Carlo generator.

The single particle distributions generated by EXODUS are then used as an input for PISA, the PHENIX detector response software, and then we perform

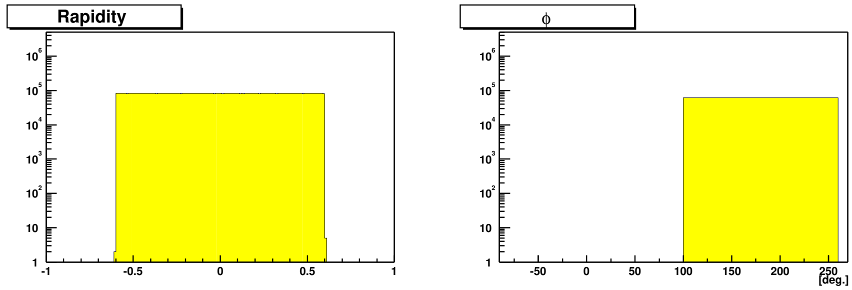

Figure 5.2: Azimuthal and rapidity distributions generated for Monte Carlo.

a full reconstruction pass that generates output files identical to the data files used in the analysis. The various parameters in the Monte Carlo are tuned in the same way as in the data. The track matching residual on TOF for Monte Carlo are shown in Figure 5.3 for both the ϕ and *zed* coordinate.

The normalized residual distributions that are used in the analysis are shown in Figure 5.4. As in the real data, we normalize the residual distributions in Gaussian σ's so that we can quantify the magnitude of cuts in real data and Monte Carlo in terms of momentum-independent standard deviations. In Figure 5.4 we show the effect of the tuning since the values that come out of the Monte Carlo reconstruction are not well parameterized. We present the distributions before and after the application of the tuning as a function of momentum.

The particle identification cuts used in Monte Carlo have been tuned with the same procedure as the real data and are shown in Figure 5.5.

5.0.5 Correction Functions

After the Monte Carlo data go through the Phenix detector response they pass through the PHENIX reconstruction software in a similar manner to the

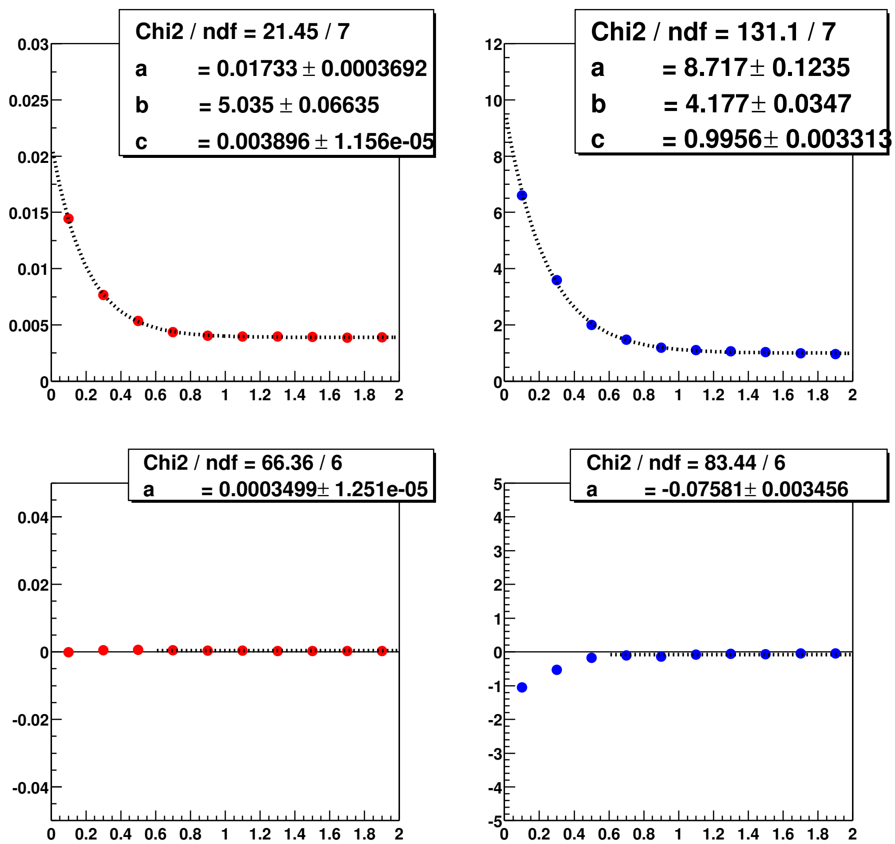

Figure 5.3: Track matching residual on TOF for Monte Carlo. Upper panel are width residuals of ϕ (left) and Z (right) as a function of momentum. Lower panel are mean residuals of ϕ (left) and Z (right) as a function of momentum.

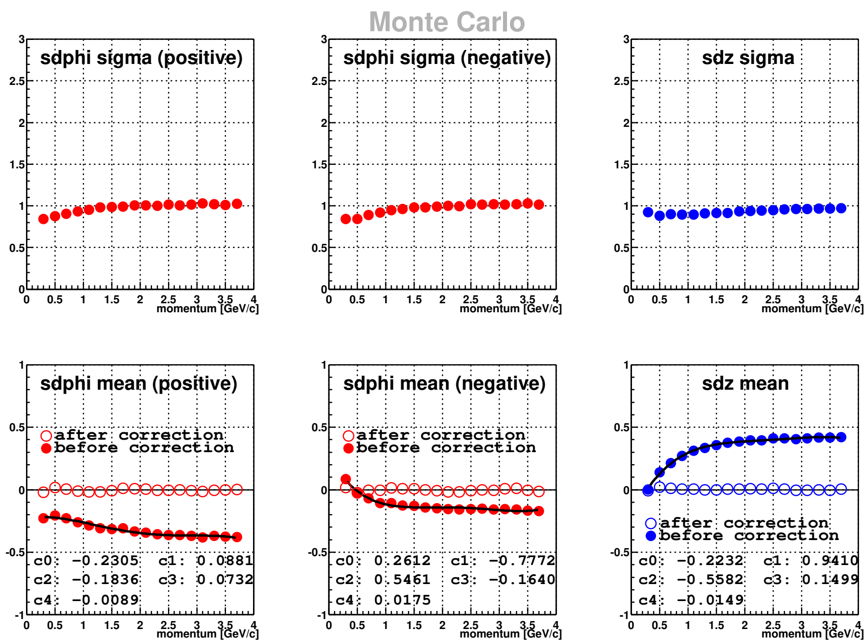

Figure 5.4: Track matching residual on TOF for Monte Carlo. Upper panel are sigmas in the ϕ coordinate (left-positive, middle-negative) and in *zed* (right) as a function of momentum. Lower panel are the means in ϕ (left-positive, middle-negative) and *zed* (right) as a function of momentum. Open circles are corrected value.

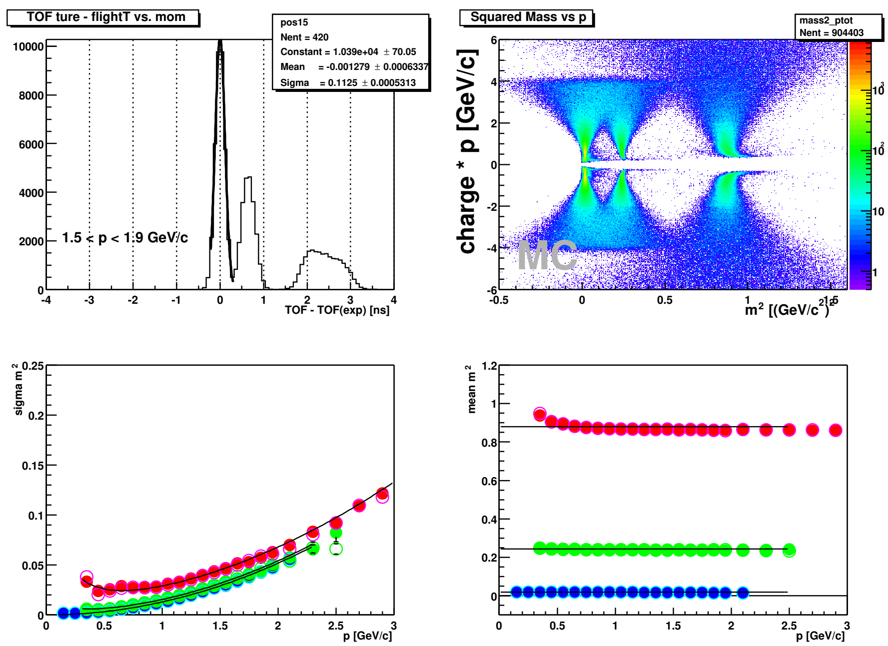

Figure 5.5: Upper left: TOF-TOF(expected) for Monte Carlo data. Upper right: Charge/momentum vs mass squared for Monte Carlo data. Lower left: Widths of particle masses as a function of momentum. Lower right: mean values of particle masses as a function of momentum.

real data. The cuts applied in the real data, including matching cuts, particle identification cuts, energy loss and fiducial cuts are also applied in exactly the same manner in Monte Carlo, through the same analysis software.

The correction functions are then determined by the ratio of the input over the output Monte Carlo distributions. Since the Monte Carlo distributions were generated in 1.2 units of rapidity and $100^o < \phi < 260^o$, the Monte Carlo correction functions must be weighted appropriately in order to upscale the real data in full azimuth and 1 unit of rapidity. The weighting factors are:

- $\Delta\eta = 1.2$
- $\Delta\phi = 160^o/360^o$

The input and output transverse momentum distributions that are used in the *in/out* ratio that determines the correction functions is shown in Figure 5.6 for positive particles and in Figure 5.7 for negative particles.

The final correction functions for each species and charge that are applied to the data are shown in Figures 5.8 and 5.9. The correction functions for the p+p and d+Au are very similar since the cuts that are applied in real and Monte Carlo are almost identical. The correction functions become very large at low momentum since most of the particles miss the spectrometer due to the large bending. Also, corrections for in-flight decays are incorporated in the Monte Carlo.

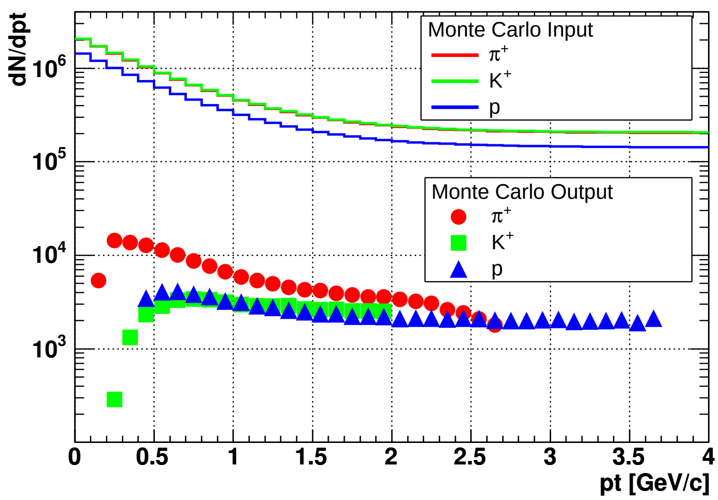

Figure 5.6: Input and output (after detector response and reconstruction) transverse momentum Monte Carlo distributions for positive particles.

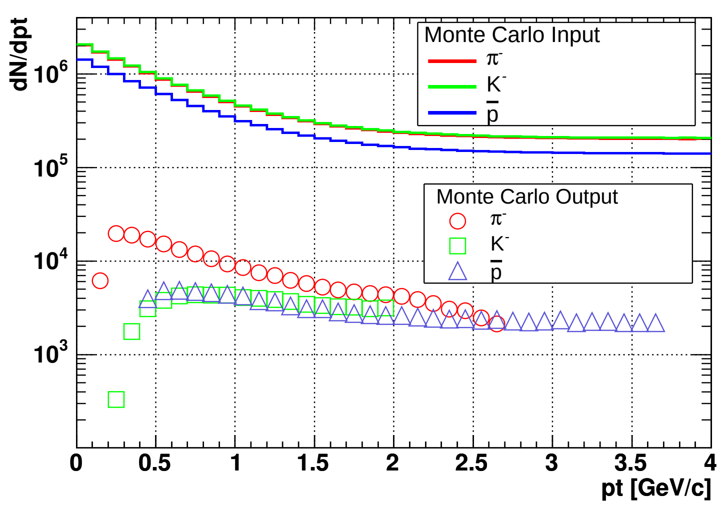

Figure 5.7: Input and output (after detector response and reconstruction) transverse momentum Monte Carlo distributions for negative particles.

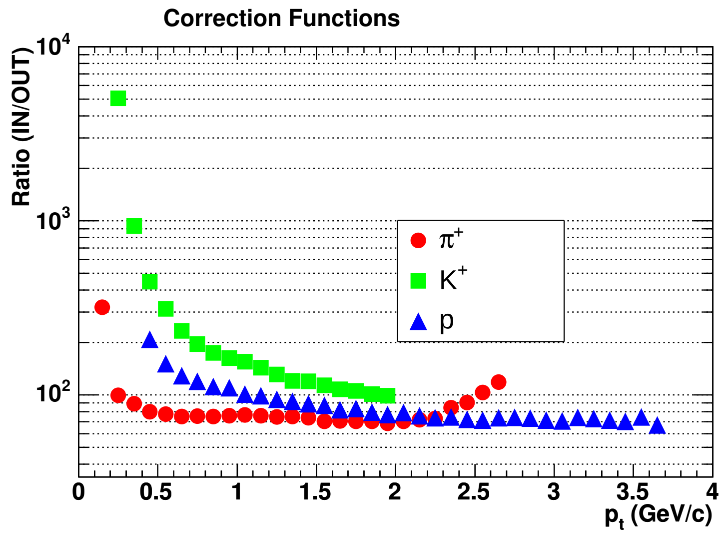

Figure 5.8: Final correction functions for p+p data as a function of transverse momentum for positive particles.

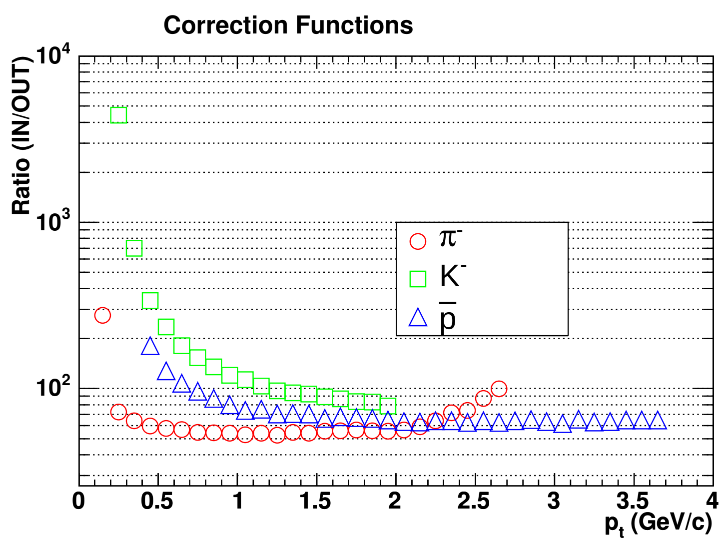

Figure 5.9: Final correction functions for p+p data as a function of transverse momentum for negative particles.

Chapter 6

Systematic Error Calculations

6.1 Definition of Systematic Errors

The systematic errors on spectra have been traditionally broken down in PHENIX publications in three categories:

1. **TYPE A: point-to-point error uncorrelated between p_T-bins**
2. **TYPE B: p_T-correlated, all points move in the same direction but not by the same factor.**
3. **TYPE C: all points move by the same factor independent of p_T.**

Type A errors are usually quoted in $\pi^0 \to \gamma\gamma$ spectra and arise from peak extraction systematic errors that are point-to-point but uncorrelated between p_T-bins. This type of error is not used in this analysis. Type B errors arise in this analysis in the error determination of the PID cuts and errors from the feed-down correction procedure, as will be described in the corresponding chapter. For the PID systematic, at low-p_T kaons and protons and their antiparticles experience energy loss in the detectors and the widening of the m^2 distributions introduces pt-dependent errors with all points moving at the same direction. For pions at high-p_T there is also a TYPE B error that arises from kaon contamination under the pion m^2 peak. Finally, TYPE C errors are from systematic trends in the analysis due to cut conditions like the matching cuts, acceptance, energy loss, run-by-run and efficiency corrections that can move all points by the same factor independent of p_T.

In this analysis we also quote one more type of error for the p+p data, that we call Normalization Error that is introduced by the BBC trigger-bias and cross section determination. These normalization errors would fall under the TYPE-C category but we quote them independently because their nature is external to this analysis and also because these errors cancel out when different spectra from different analyses, within the PHENIX experiment, are compared with each other.

The determination of systematic effects on the spectra, particle ratios and Nuclear Modification Functions as a function of p_T is done by varying the cut conditions that were applied during the analysis and comparing the effect of these variations to the canonical cuts. The variation of the cut parameters is done simultaneously in the real data and in Monte Carlo. Therefore, someone expects, in the absence of any systematic effect, that the ratio of two spectra, or particle ratios, derived with two different cut conditions, should oscillate around $\simeq 1$. Any significant deviations from unity will be counted for as a systematic error. In the following we present the cuts that were changed for this study.

The cuts that were varied are as follows:

1. Fiducial cut (wider and narrower acceptance cut applied)

2. Energy loss cut (different parameterizations of the energy loss curve applied)

3. PID cut (a tight 1 σ_m^2 was applied instead of the standard 2 σ_m^2 cut)

4. Matching cut at the TOF (a tighter 2σ cut was applied instead of the standard 3 σ cut)

6.1.1 Fiducial Cut Error Estimation

The fiducial cuts were varied in order to calculate potential trends in the application of this cut. A wider cut was parameterized and applied and then compared with the standard cut used in the analysis as shown in Figures 6.1.

The effect of this variation is shown in Figure 6.2 for positive pions and Figure 6.3 for negative pions. In these figures we plot the ratio of the corrected pion spectra with the two different sets of cuts. We apply the different set of cuts in both real and Monte Carlo data in this and following studies of systematic effects.

We determine a systematic error of 5% that brackets the variation for both positive and negative particles.

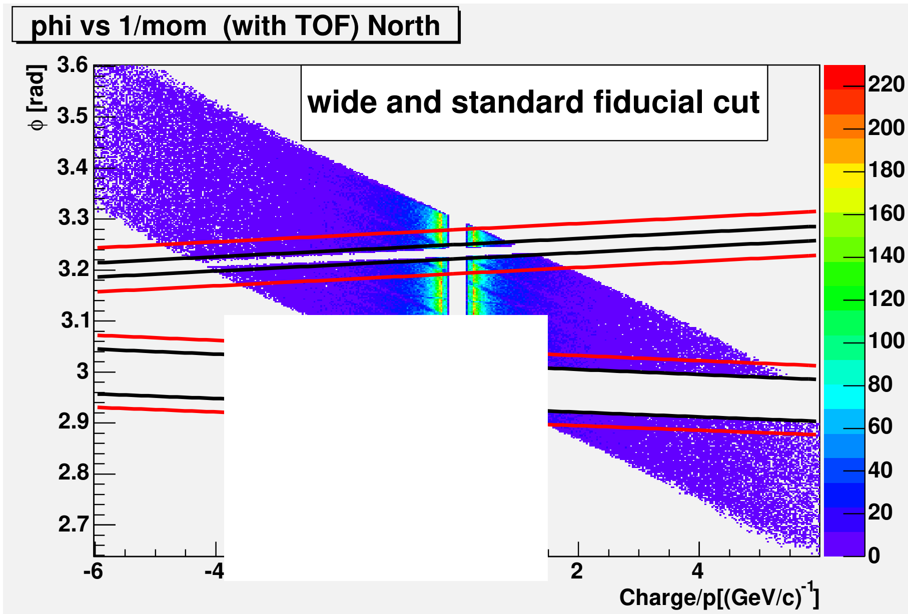

Figure 6.1: Wide(red) and standard(black) fiducial cut used to determine systematic effect of acceptance.

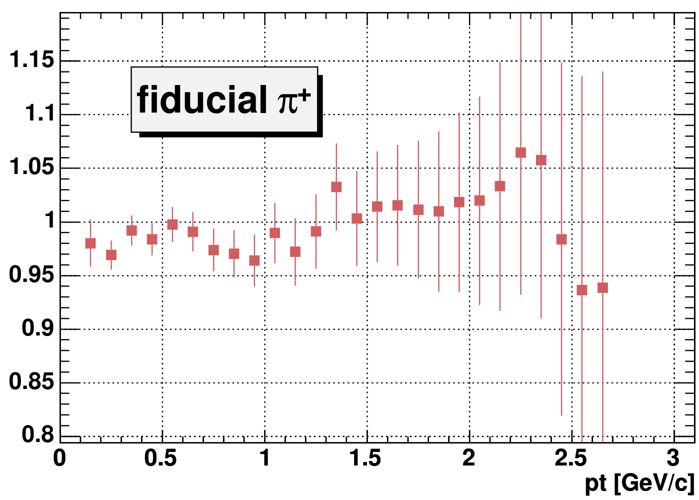

Figure 6.2: Ratio of corrected positive pion spectra for two different sets of fiducial cuts.

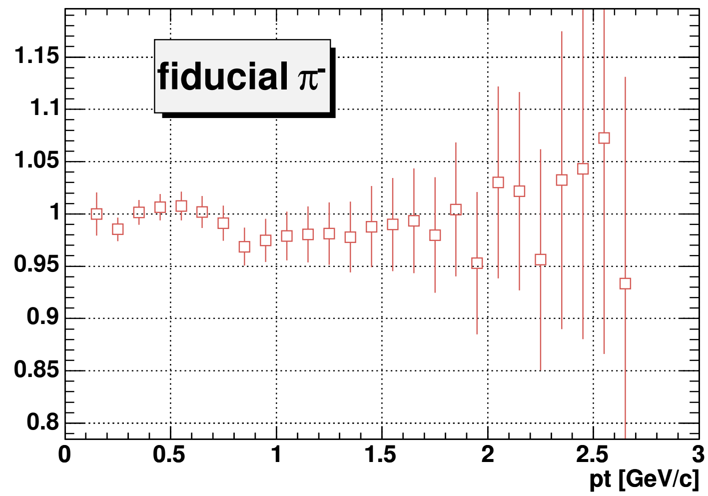

Figure 6.3: Ratio of corrected negative pion spectra for two different sets of fiducial cuts.

6.1.2 Energy Loss

We apply two different parameterizations of the energy loss cut as shown in Figure 6.4 and described in the Energy Loss section.

The effect of this variation is small and is shown in Figures 6.5, 6.6 and 6.7 for negative pions, kaons and antiprotons. We determine a systematic error of 2% on the energy loss cut for all particles and charges.

6.1.3 Systematic Error on Particle Identification

For the calculation of systematic effects on the particle identification cuts we perform a very stringent test in the data, narrowing the PID cuts for all particle species at 1σ. This very narrow cut is very sensitive on the PID parameterization since small errors on the means or widths of the m^2 distributions of each

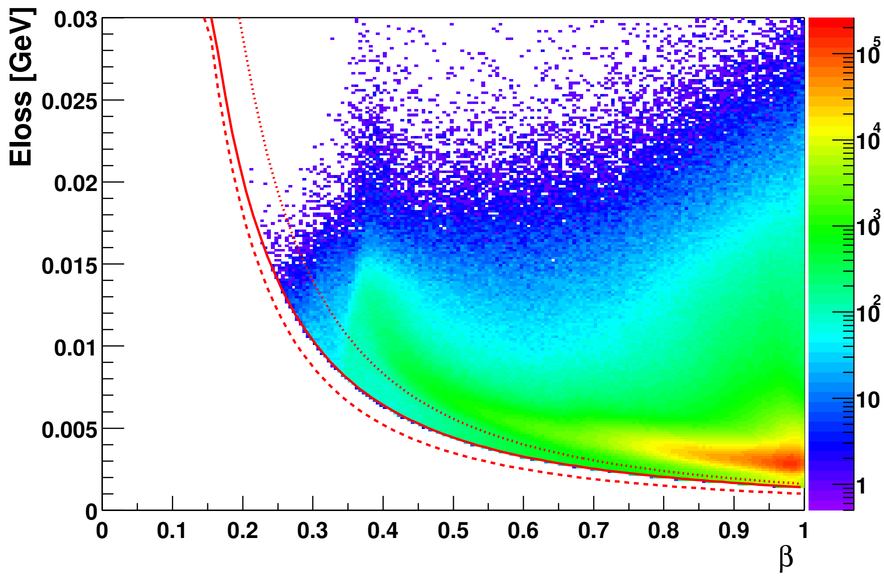

Figure 6.4: Variation of parameterizations for the study of systematic error on energy loss.

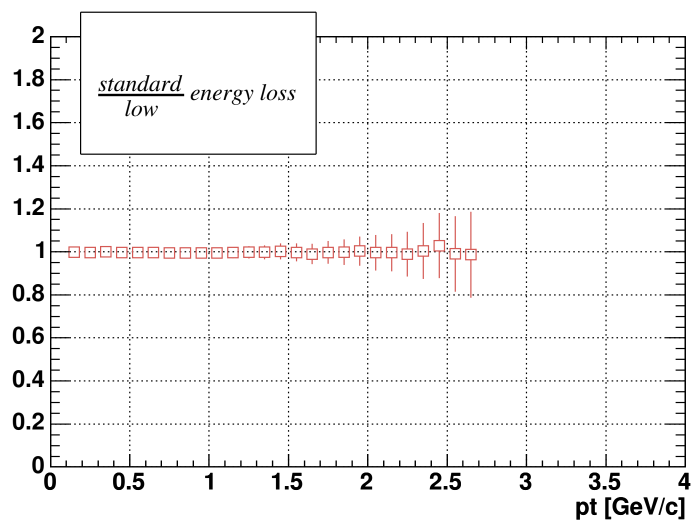

Figure 6.5: Ratio of corrected negative pion spectra for two different sets of energy loss cuts.

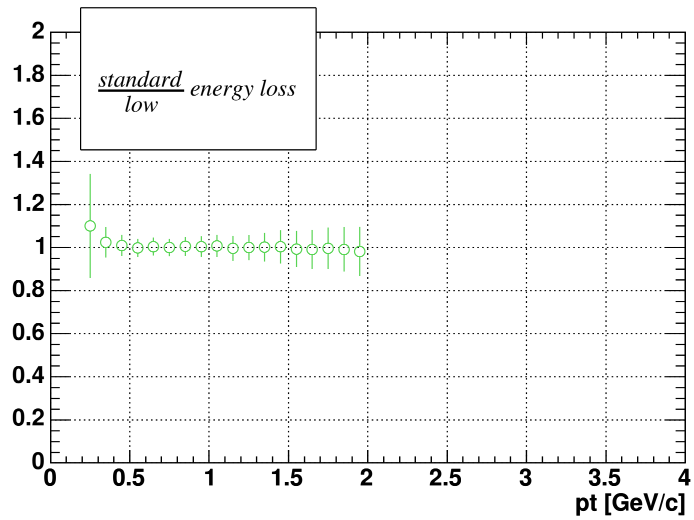

Figure 6.6: Ratio of corrected negative kaon spectra for two different sets of energy loss cuts.

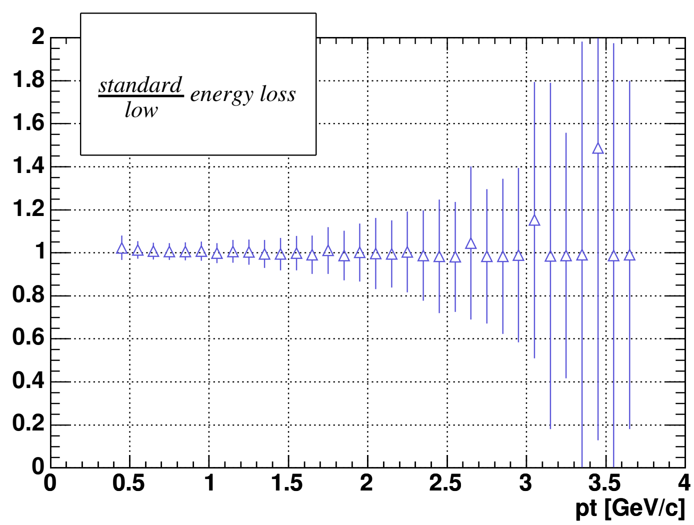

Figure 6.7: Ratio of corrected antiproton spectra for two different sets of energy loss cuts.

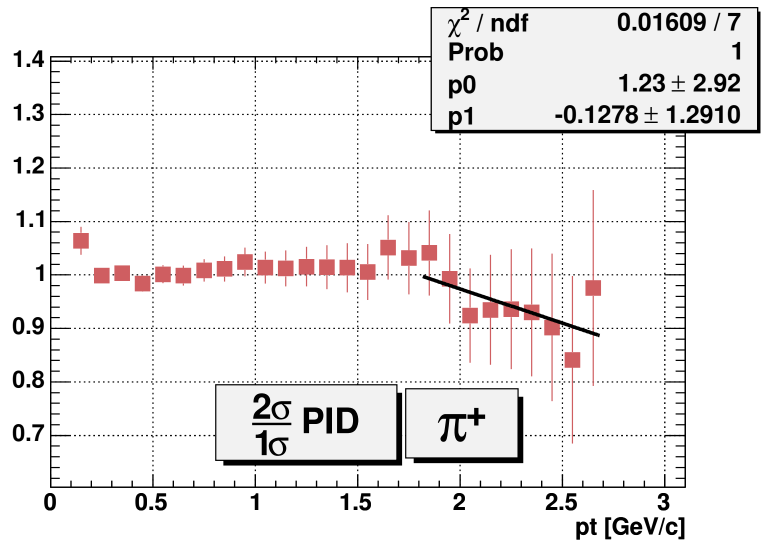

Figure 6.8: Ratio of corrected positive pions for 1σ and 2σ PID cuts.

particle as a function of momentum, can cause large systematic deviations in the final yields.

In Figures 6.8 and 6.9 we present the ratio of corrected spectra for positive and negative pions respectively for 1σ and 2σ PID cuts.

For $p_T < 2.0GeV/c$ the pion PID cuts are stable as a function of momentum and close at 1, verifying the accuracy of the PID parameterization. For $p_T > 2.0GeV/c$ we observe a drop in the ratio that reaches up to 10% at the highest p_T where pions are identified. This is attributed to the kaon contamination under the m^2 pion peak and the effect is parameterized and accounted for in the systematic error determination. For the parameterization of this error at high p_T we refer the reader to the Summary section of this chapter.

The corresponding plots for kaons are shown in Figures 6.10 and 6.11.

For low momentum we parameterize the increasing ratio with an exponen-

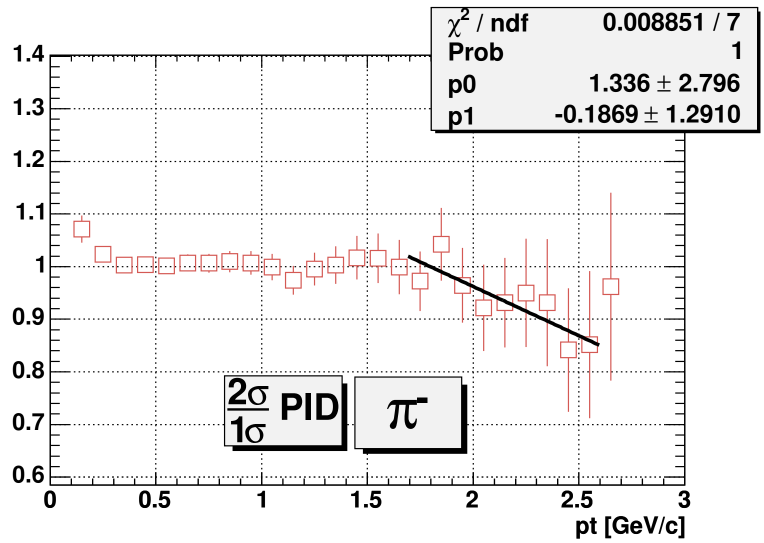

Figure 6.9: Ratio of corrected negative pions for 1σ and 2σ PID cuts.

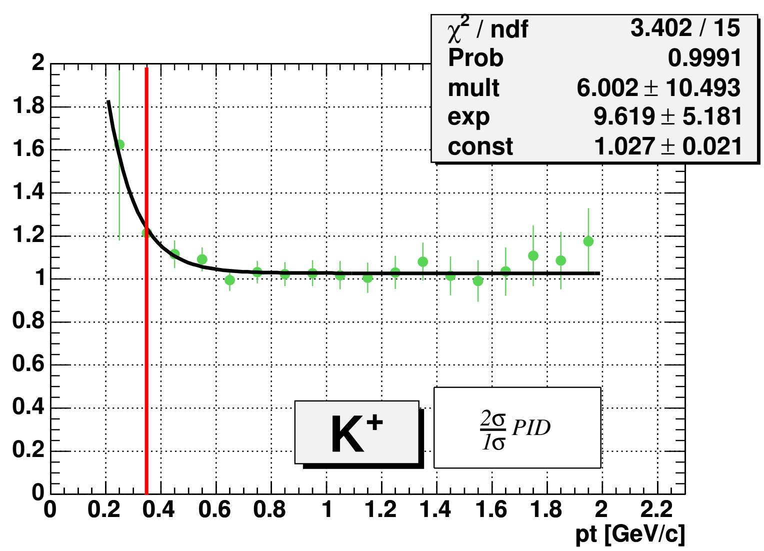

Figure 6.10: Ratio of corrected positive kaons for 1σ and 2σ PID cuts.

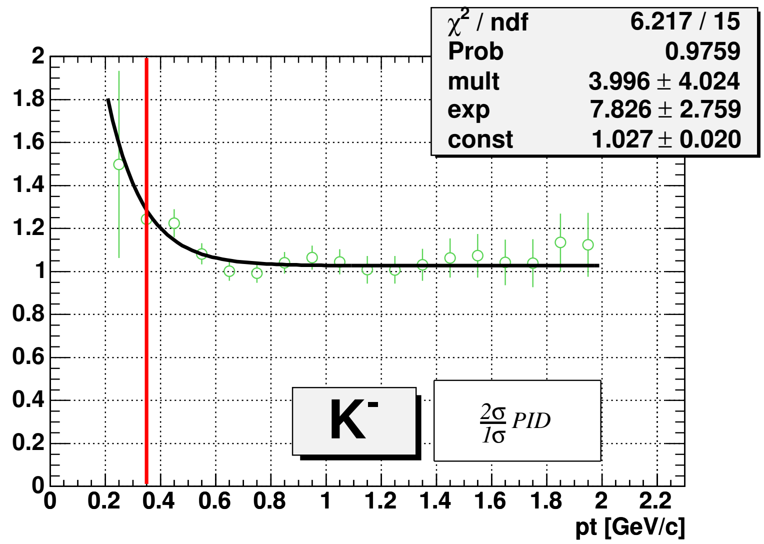

Figure 6.11: Ratio of corrected negative kaons for 1σ and 2σ PID cuts.

tial distribution that saturates into a constant value at $p_T > 0.5 GeV$. We fit the ratio of corrected spectra separately for positive and negative kaons. The red lines in the figures represent the lowest p_T-bin included in the kaon spectra. The systematic effect observed at low momentum for the kaons is attributed to a shift in the mean of the kaon distributions due to energy loss in the detectors.

For protons and antiprotons the PID ratios are presented in Figures 6.12 and 6.13. The red lines in the figures represent the lowest p_T-bin included in the proton and antiproton spectra.

A similar effect as for the kaons appears at low momentum which is parameterized with an exponential distribution and is accounted for in the final calculation of systematic errors. For both kaons and (anti)protons this is a momentum dependent point-to-point systematic error of type B. For the pa-

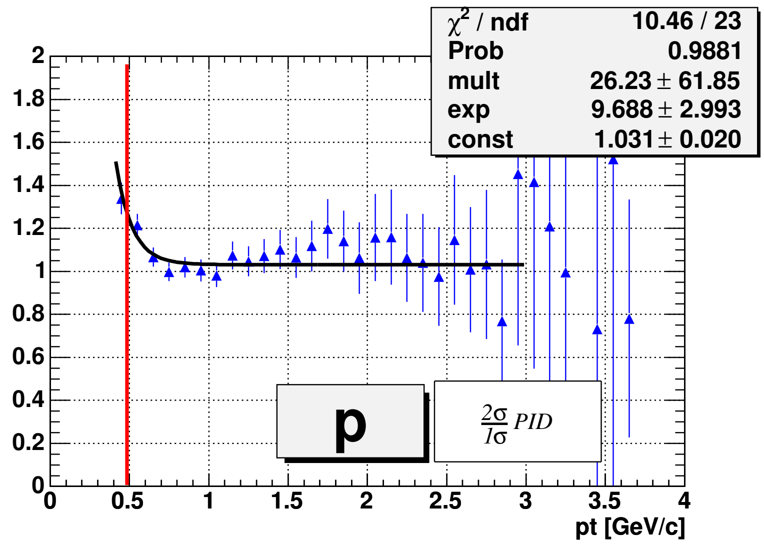

Figure 6.12: Ratio of corrected protons for 1σ and 2σ PID cuts.

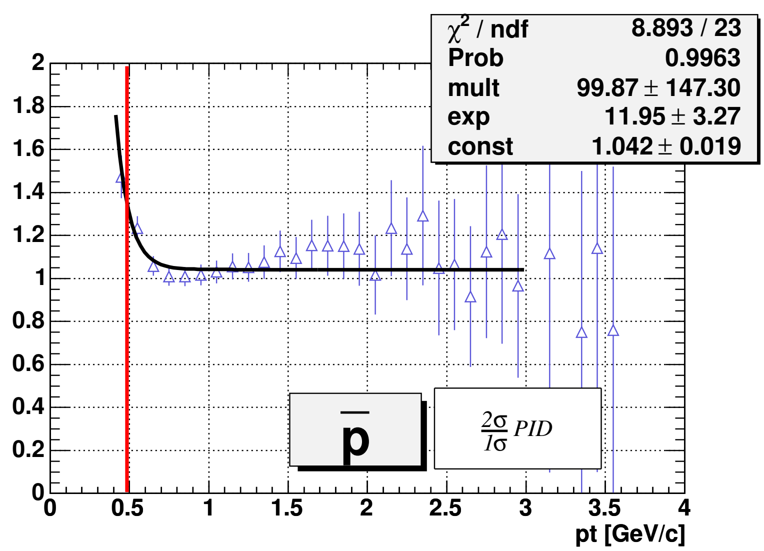

Figure 6.13: Ratio of corrected antiprotons for 1σ and 2σ PID cuts.

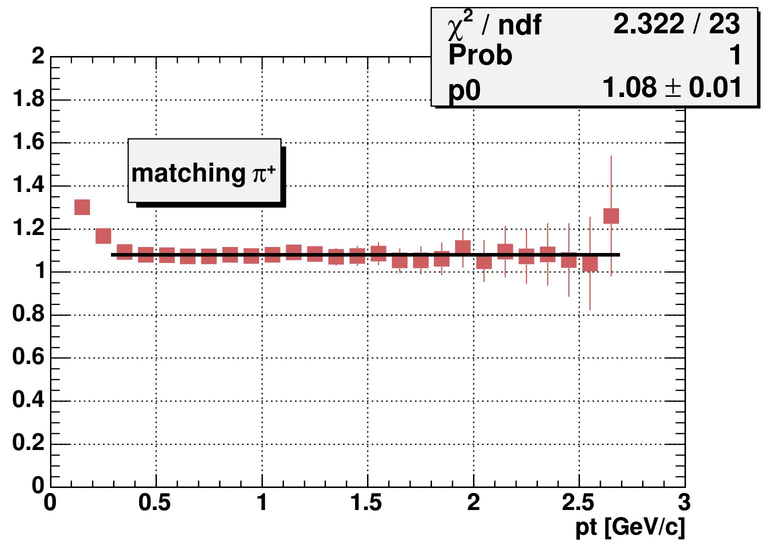

Figure 6.14: Ratio of corrected positive pion spectra for 2σ and 3σ matching cuts.

rameterization of this error at low p_T we refer the reader to the Summary section of this chapter.

6.1.4 Systematic Error on Matching Cuts

For the systematic error on the matching cuts we take the ratio of fully corrected spectra, on the numerator having applied a 3σ cut, while in the denominator a 2σ matching cut. The result for pion, kaon and proton spectra are shown in Figures 6.14, 6.15, 6.16.

We calculate a 9% error in the d+Au data set, and 8% for the p+p data.

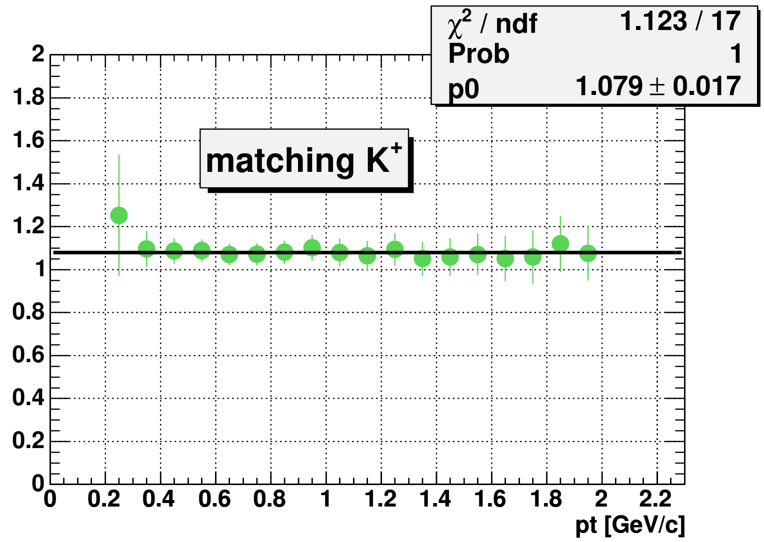

Figure 6.15: Ratio of corrected positive kaon spectra for 2σ and 3σ matching cuts.

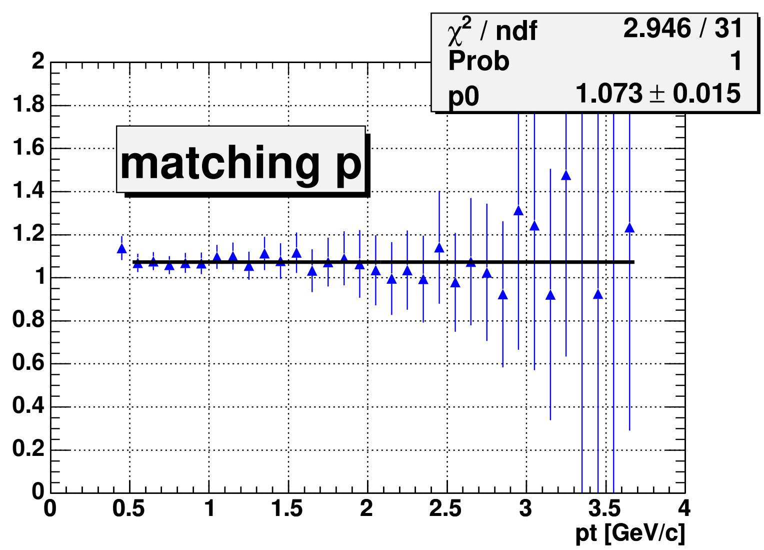

Figure 6.16: Ratio of corrected proton spectra for 2σ and 3σ matching cuts.

6.2 Summary of Systematic Errors

In this section we summarize all the systematic errors. We start with the momentum-independent type-C errors that are shown in Table 6.1 for the d+Au data set, and Table 6.2 for the p+p data set.

Table 6.1: Type-C systematic errors for the d+Au data set. Same for all particle species.

syst. error	eloss	acceptance	matching	run-by-run	efficiency
	1%	4%	9%	5%	3%

Table 6.2: Type-C systematic errors for the p+p data set. Same for all particle species.

syst. error	eloss	acceptance	match.	run-by-run	efficiency	BBC bias
	2%	4%	8%	5%	3%	4%

The average total systematic type-C error in p+p and d+Au is: 11.5%. The p+p data have an additional type-C error, arising from the BBC cross section uncertainty, which is 9.6%.

The type-B systematic errors for the p+p and d+Au data sets are common, but are species and charge dependent. The source of type-B errors are from the Particle Identification cuts. In addition, for the protons and antiprotons, we have a systematic error arising from the feed-down corrections. As will be shown in detail in the corresponding chapter, almost 30% of protons and antiprotons detected at the TOF are from weak decays of strange baryons. There is a 24% uncertainty on this number, which brings the total feed-down correction systematic error on the proton and antiproton spectra at the 10% level. Finally, the momentum resolution error is insignificant below p_T=4 GeV/c, and is not taken into account [80].

The PID systematic errors for Kaons and protons as a function of transverse momentum have been parameterized by the following functional form (shown in Fig. 6.10, 6.12):

$$syst - PID(p_T) = |[(A \cdot \exp -B \cdot p_T) + C] - 1.0|\% \tag{6.1}$$

We present the values of these parameters for kaons and (anti)protons in Table 6.3.

Table 6.3: Parameterization of the momentum dependent PID systematic error for Kaons and (anti)protons.

particle	A	B	C
K^+	6.00	9.61	1.027
K^-	3.99	7.82	1.027
p	26.23	9.68	1.031
$\overline{p}$	99.87	11.95	1.042

For protons and antiprotons, at low momentum the systematic PID error starts at ~8% and saturates at about 3% at high p_T. For kaons, at low momentum the systematic PID error starts at ~10% and saturates at about 3% at high p_T.

For pions, at low p_T, the systematic PID error is 4%, while for p_T>1.8 GeV/c, the kaon contamination introduces a momentum-dependent error, which reaches its maximum value of approximately 10-15% at p_T=2.6 GeV/c, as was shown in Figures 6.8 and 6.9. We parameterize the momentum-dependent

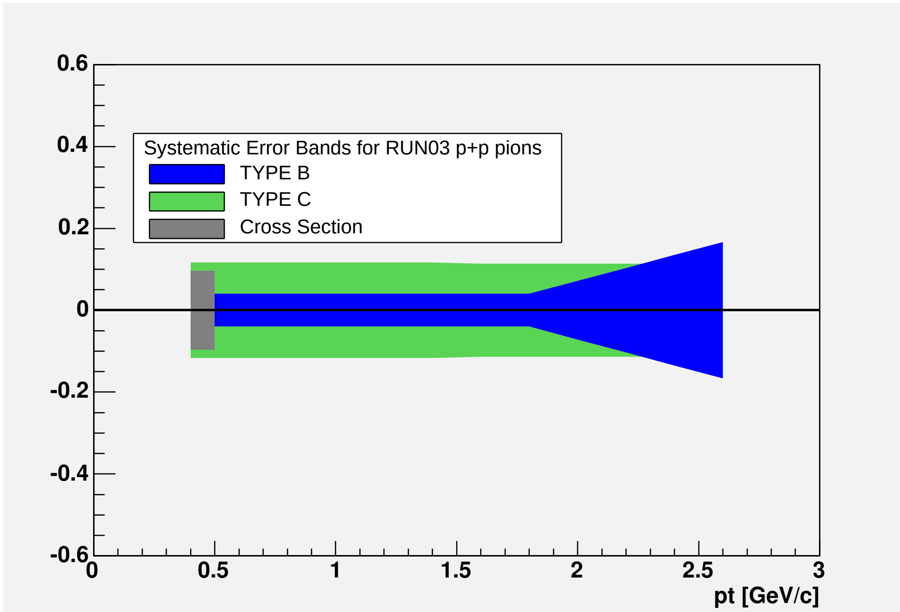

Figure 6.17: Total systematic errors for pions as a function of p_T.

part of this error with a linear function, with the following parameters:

$$SystError_{\pi}(p_T) = |((1.283 - 0.1574 \cdot p_T) - 1.0)|\% \tag{6.2}$$

We break-down and plot all systematic errors for the p+p data set in Figures 6.17, 6.18, 6.19, for positive pions, Kaons and protons. Notice that the type-B systematic error for the protons in Figure 6.19 does not include the 10% error from feed-down corrections.

Finally, the systematic errors on antimatter over matter ratios are shown in Table 6.4.

Table 6.4: Systematic errors on antimatter/matter ratios.

ratio	π^-/π^+	K^-/K^+	$\overline{p}/p$(includes feed-down error)
	6%	8%	12%

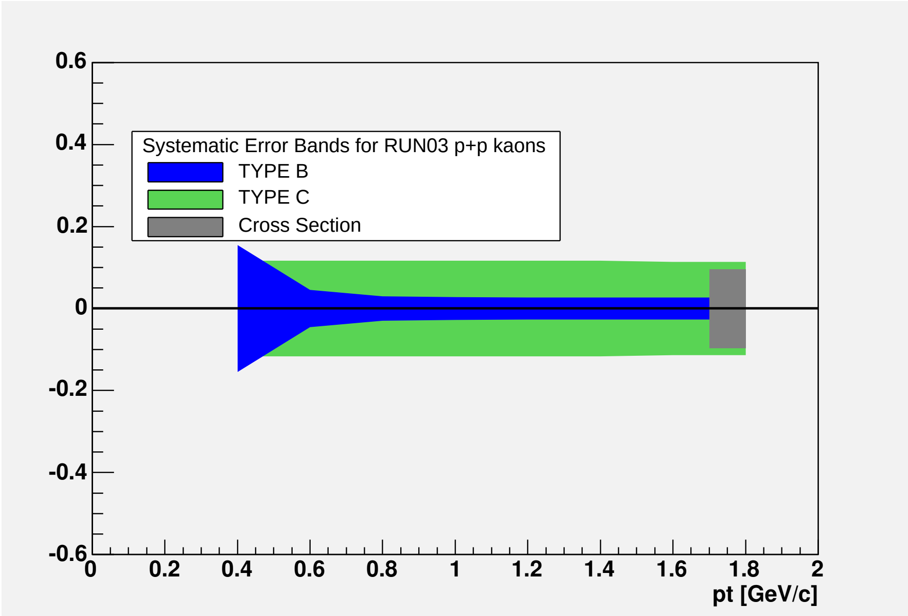

Figure 6.18: Total systematic errors for kaons as a function of p_T.

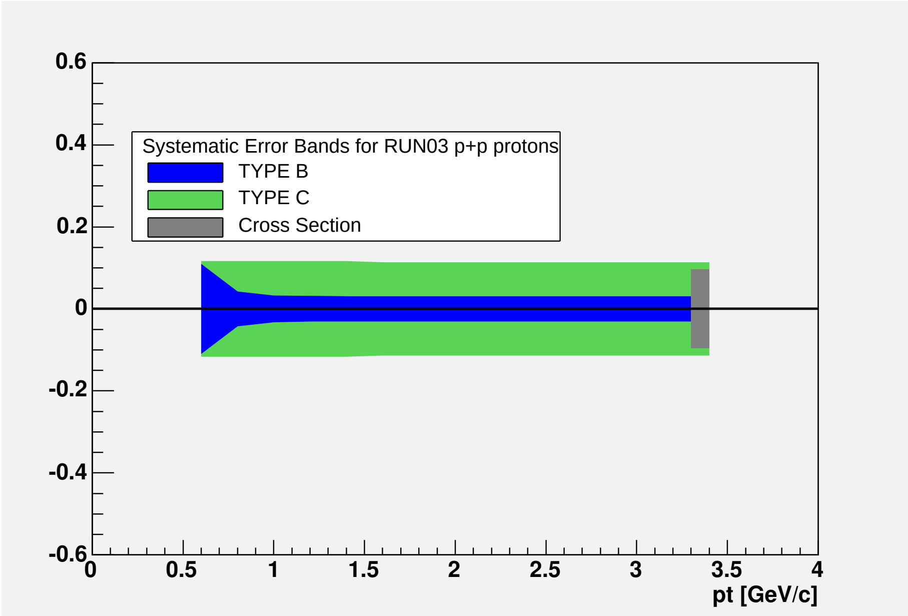

Figure 6.19: Total systematic errors for protons as a function of p_T. Feed-down correction error is about 10%, and is not shown in this plot.

The systematic errors on interspecies ratios are shown in Table 6.5.

Table 6.5: Systematic errors on interspecies particle ratios. Errors on ratios that involve protons and antiprotons, include the systematic error from feed-down corrections.

ratio	K^+/π^+	K^+/p	p/π^+	$\overline{p}/\pi^-$
	5.5%	12%	12%	15%

Chapter 7

Feed-down Corrections to Protons and Antiprotons

7.1 Protons and Antiprotons from Weak Decays

A significant fraction of the protons[1] detected by the PHENIX TOF originate from weak decays of hyperons $Y(qqs)$, $\overline{Y}(\bar{q}\bar{q}\bar{s})$, cascades $\Xi(qss)$, $\overline{\Xi}(\bar{q}\bar{s}\bar{s})$ and omegas $\Omega^-(sss)$, $\overline{\Omega^-}(\bar{s}\bar{s}\bar{s})$. These weak decay contributions to the measured proton spectra are usually called feed-down protons. The total number of protons detected can be written as: $p + 0.64(\Lambda + \Sigma^0 + \Xi^0 + \Xi^- + \Omega^-) + 0.52\Sigma^+$ [66], [67], where p denotes the primordial protons produced in the collision and 0.64 and 0.52 are the branching ratios for $\Lambda \to p\pi^-$ and $\Sigma^+ \to p\pi^0$ respectively. Based on mt-scaling assumptions for baryons, published data

[1] In this chapter the term protons also refers to antiprotons except when it is clearly stated otherwise.

by the UA5 collaboration and preliminary data from STAR on Λ production in p+p and d+Au collisions at $\sqrt{s} = 200$ GeV, we will attempt to estimate the fraction of feed-down protons with respect to the total number of protons measured by PHENIX. In this feed-down analysis we only refer to measured particle spectra and ratios, and, therefore, our results are model-independent although with a sizeable systematic error.

7.2 Hadrochemistry

There are three key ingredients in any attempt to estimate the number of feed-down protons. The first is a detailed knowledge of the particles that decay directly or indirectly to protons. Our source for that will be the Particle Data Group [45]. The second and most difficult to find ingredient is the average particle composition in a p+p or d+Au event. Our source for this information will be PHENIX data, published UA5 data [68] and preliminary Λ and $\overline{\Lambda}$ spectra from STAR [70], [71], [72]. Finally, someone needs to have a good simulation program that accurately defines the magnetic field and detector acceptances since the momentum dependence of the feed-down contribution is a strong function of these factors, originating from 2-body decays of strange baryons inside the magnetic field. For that we use the PHENIX standard $EXODUS \rightarrow PISA \rightarrow RECONSTRUCTION$ simulation chain.

In this section we do the hadrochemistry of strange baryons that decay directly to protons or to Λ, which then subsequently decays to protons and are of interest to this analysis. In the next section we will quote the relative abundance of these particles in a typical p+p event at 200 GeV.

Table 7.1: Strange baryons decaying to protons or Λ

particle	Mass [GeV]	$c\tau$	decay mode	Branching Ratio
Λ(uds)	1.115	7.89 cm	$\Lambda \to p\pi^-$	63.9%
Σ^0(uds)	1.192	$2.22x10^{-11}$ m	$\Sigma^0 \to \Lambda\gamma$	100%
Ξ^0(uss)	1.314	8.71 cm	$\Xi^0 \to \Lambda\pi^0$	99.5%
Ξ^-(dss)	1.321	4.91 cm	$\Xi^- \to \Lambda\pi^-$	99.89%
Ω^-(sss)	1.672	2.46 cm	$\Omega^- \to \Lambda K^-$	67.8%
Ω^-(sss)	1.672	2.46 cm	$\Omega^- \to \Xi^0\pi^-$	23.6%
Ω^-(sss)	1.672	2.46 cm	$\Omega^- \to \Xi^-\pi^0$	8.6%
Σ^+(uus)	1.189	2.39 cm	$\Sigma^+ \to p\pi^0$	51.57%

In Table 7.1 we gather all the strange baryons of interest that decay to protons or to Λ. We observe a few important things:

1. The Σ^0 which decays 100% to Λ is indistinguishable from the Λ in a tracking chamber due to its short decay length and also because one of the decay products is a photon. Frequently people forget that experiments that measure and quote Λ production in reality mean $\Lambda + \Sigma^0$.

2. Ξ^0 and Ξ^- decay 100% to Λ and therefore their entire yield contributes to feed-down protons through the branching ratio of the Λ. Ξ^0 is again hard to measure since it includes a neutral pion in its decay products. Ξ^- is measured by similar "V track" analysis as the Λ where one looks for a displaced "kink" with the invariant mass of Λ and 3 tracks in the final state.

3. Σ^+ makes a direct decay to protons with a branching ratio of 52% and should not be ignored in the feed-down hadrochemistry.

4. Ω^- also decays completely to products that contribute to protons. In

this analysis we ignore this contribution because the Ω^- yield is very small and there is no information on its production in the $p+p$ or $p+A$ literature at these energies. STAR has observed the Ω^- peak in $p+p$ but due to lack of statistics there is no further information other than the ratio of $\overline{\Omega}/\Omega = 0.9 \pm 0.1$ [74].

7.3 Average Particle Composition

The UA5 collaboration in [68] reports the average particle composition in non-single diffractive 200 GeV $p+\bar{p}$ collisions, Table 7.2 . Care must be exercised since some of these numbers are predictions by models and not real measurements. For further details on the UA5 model refer to [69]. Since PHENIX is also mostly sensitive to non-single diffractive p+p events we will use these multiplicities for our study. We also extrapolate the same relative fractions of strange baryons to the d+Au system.

Table 7.2: Particle composition at 200GeV $p+\bar{p}$ collisions from [68].

Particle	$< n >$
all charged	20.4 ± 0.4
$\pi^+ + \pi^-$	17.9 ± 0.5
$K^0 + \overline{K^0}$	1.50 ± 0.18
$K^+ + K^-$	1.50 ± 0.18
$p + \overline{p}$	0.5 ± 0.2
$n + \overline{n}$	0.5 ± 0.2
$\Lambda + \overline{\Lambda} + \Sigma^0 + \overline{\Sigma^0}$	0.46 ± 0.12
$\Sigma^+ + \overline{\Sigma^+} + \Sigma^- + \overline{\Sigma^-}$	0.23 ± 0.06
$\Xi^- + \overline{\Xi^-}$	$0.03^{+0.04}_{-0.02}$
$\Xi^0 + \overline{\Xi^0}$	$0.03^{+0.04}_{-0.02}$

The values quoted in Table 7.2 are mean multiplicities corrected to full phase space and not $< dn/dy >$ values in one unit of rapidity usually calculated by PHENIX. From this information we calculate three important ratios:

1. $(\Xi^0 + \Xi^-)/(\Lambda + \Sigma^0)$ is approximately 13%.

2. $(\Sigma^+ + \overline{\Sigma^+} + \Sigma^- + \overline{\Sigma^-})/(\Lambda + \overline{\Lambda} + \Sigma^0 + \overline{\Sigma^0})$ is approximately 50%. Because the Σ^- and $\overline{\Sigma^-}$ only decay to neutrons they don not contribute to feed-down protons. Assuming that the ratio of Σ^-/Σ^+ is very close to 1.0, we end up with: $(\Sigma^+ + \overline{\Sigma^+})/(\Lambda + \overline{\Lambda} + \Sigma^0 + \overline{\Sigma^0}) = 25\%$.

3. $(\Lambda + \overline{\Lambda} + \Sigma^0 + \overline{\Sigma^0})/(p + \overline{p}) = 0.92$ although with a very large systematic error that arises from the $p + \overline{p}$ measurement.

7.4 Effective $(\Lambda + \overline{\Lambda})/2$ Spectrum

From the previous section we know that the main contribution to feed-down protons are the Λ, Ξ that decays 100% to Λ and Σ that decays directly to protons. Armed with this information we produce an effective Λ spectrum with the following composition:

$$\Lambda^{Effective} = (\Lambda + 13\% \cdot \Lambda + 25\% \cdot 80\% \cdot \Lambda) \tag{7.1}$$

$$= (1 + 33\%) \cdot \Lambda \tag{7.2}$$

where Λ stands for $\Lambda + \overline{\Lambda} + \Sigma^0 + \overline{\Sigma^0}$ and the 80% in Equation 7.2 is the ratio of the branching ratios for

$$\frac{BR(\Sigma^+ \to p\pi^0)}{BR(\Lambda \to p\pi^-)} = \frac{51.57\%}{63.9\%} = 80\% \tag{7.3}$$

Given an initial Λ spectrum in p+p or d+Au collisions (discussed in the next section) , we can construct an effective Λ spectrum, let it decay in the PHENIX volume and finally measure the number of feed-down protons that arise from this effective distribution and hit the Time of Flight detector.

This effective method of producing the spectrum of feed-down protons is robust and uses published particle ratios from the literature instead of using any particular theoretical model. We construct an effective Λ spectrum that contains all the hyperon contributions to feed-down protons. This effective approach makes the implicit approximation that the Ξ and Σ have the same decay length as the Λ but this is a reasonable approximation given that the $c\tau$ values for these strange baryons are similar as can be seen in Table 7.1. The decay kinematics of the last decay to protons is almost identical for the Σ and Λ since their mass difference is of the order of 6%.

Care must be taken in the Λ spectrum used to produce the effective distribution. Namely it must be feed-down corrected for Ξ decays since we explicitly include the Ξ contribution in our method. In the next section we discuss the sources of the Λ spectra we used.

7.5 $(\Lambda + \overline{\Lambda})/2$ Production

The available Λ spectra available in the literature are shown in Figures 7.2 and 7.3 [68], [70], [72].

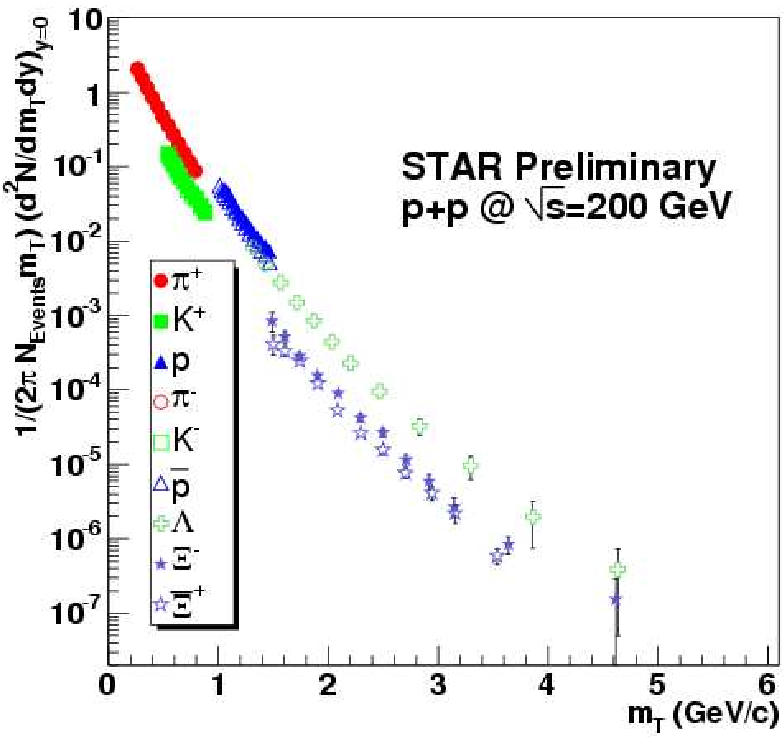

Figure 7.1: Transverse mass distributions for different particles in 200 GeV p+p collisions from [73].

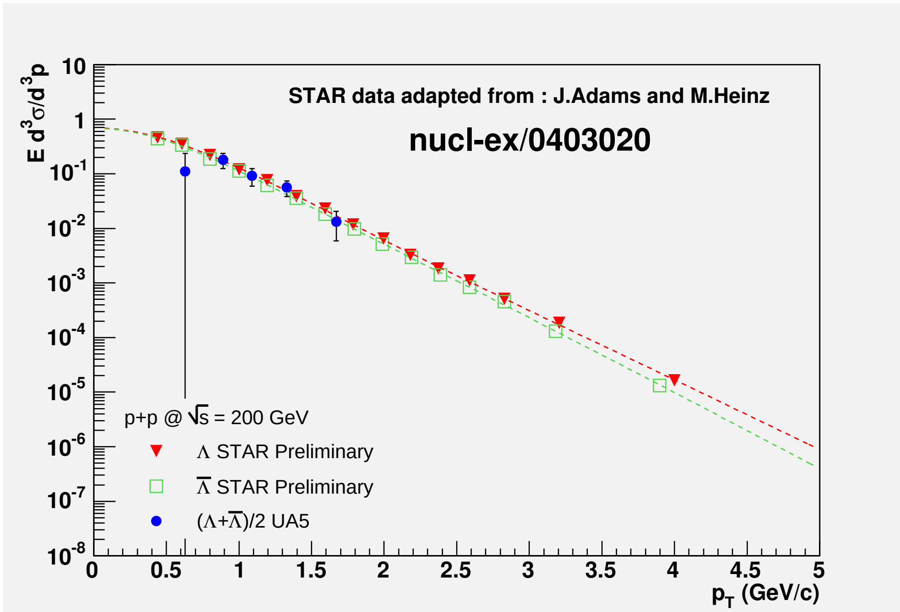

Figure 7.2: Published UA5 and preliminary STAR Λ spectra from [68], [70].

We follow two approaches with respect to the primordial Λ production in p+p and d+Au (the spectrum that will be upscaled to produce the effective Λ spectrum).

1. For p+p we assume absolute (shape and normalization) mt-scaling for protons and Λ. For p+p the UA5 $\Lambda+\overline{\Lambda}$ spectrum sets the absolute scales but fails to produce a usable shape since there are only 5 data points with large systematic errors. For that reason we assume absolute (shape and normalization) mt-scaling for protons and Λ and use the mt-scaled PHENIX proton spectra to get the shape of the Λ spectrum. Preliminary results from the STAR collaboration for mt-scaling in p+p validate this approximation as can be seen in Figure 7.1. We chose to use this method of mt-scaling since it is based on published UA5 data instead of using the STAR preliminary Λ spectrum in p+p that may change in the future.

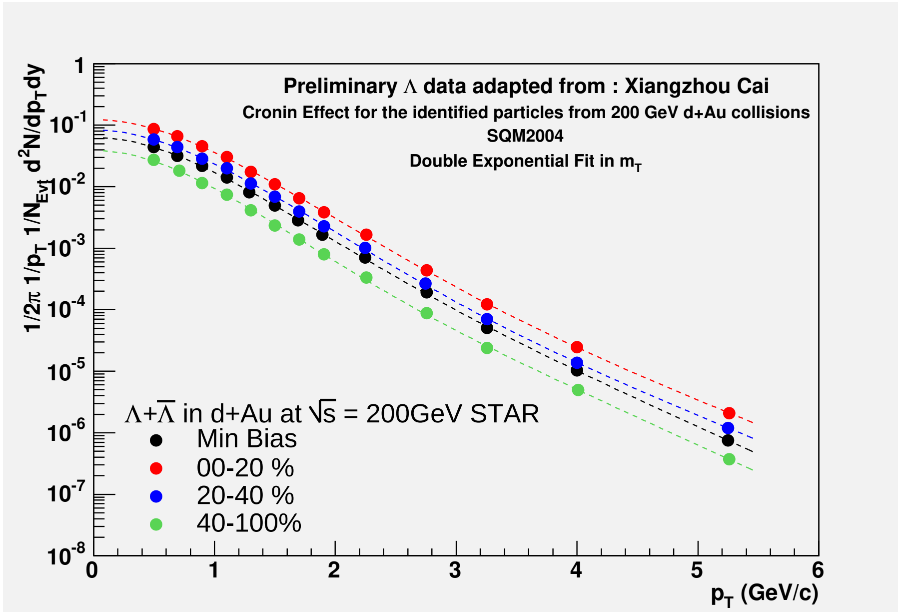

Figure 7.3: Preliminary d+Au STAR Λ spectra from [72].

2. For d+Au at 200 GeV there are no data in the literature besides STAR preliminary results on $\Lambda+\overline{\Lambda}$ which are feed-down corrected for Ξ decays [72] and are directly usable as an input in the effective method that we developed.

7.5.1 p+p

For the p+p Λ we use the PHENIX $(p+\overline{p})/2$ mt-spectrum and treat it as the Λ spectrum. As can be seen in Figure 7.4 the mt proton spectrum is nearly identical with the UA5 and STAR Λ spectra, a direct consequence of absolute mt-scaling for protons and Λ in p+p collisions at 200 GeV, although this scaling does not hold in general for all particles at these energies as can be seen in Figure 7.1. The slope for all particles appears to be very similar while the absolute scale is different , but for protons and Λ absolute mt-scaling is at

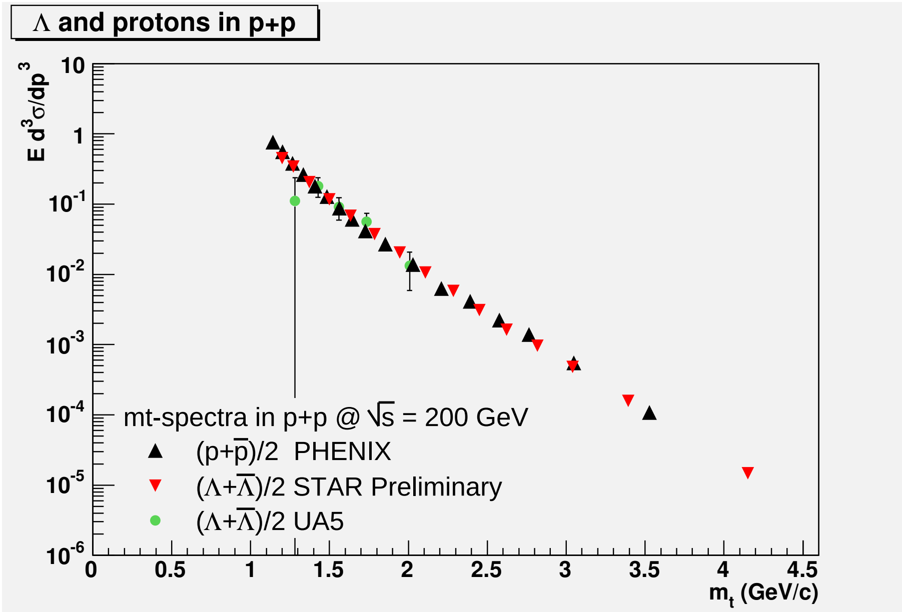

Figure 7.4: mt-scaled PHENIX proton spectra along with the $\Lambda + \overline{\Lambda}$ UA5 and STAR preliminary results.

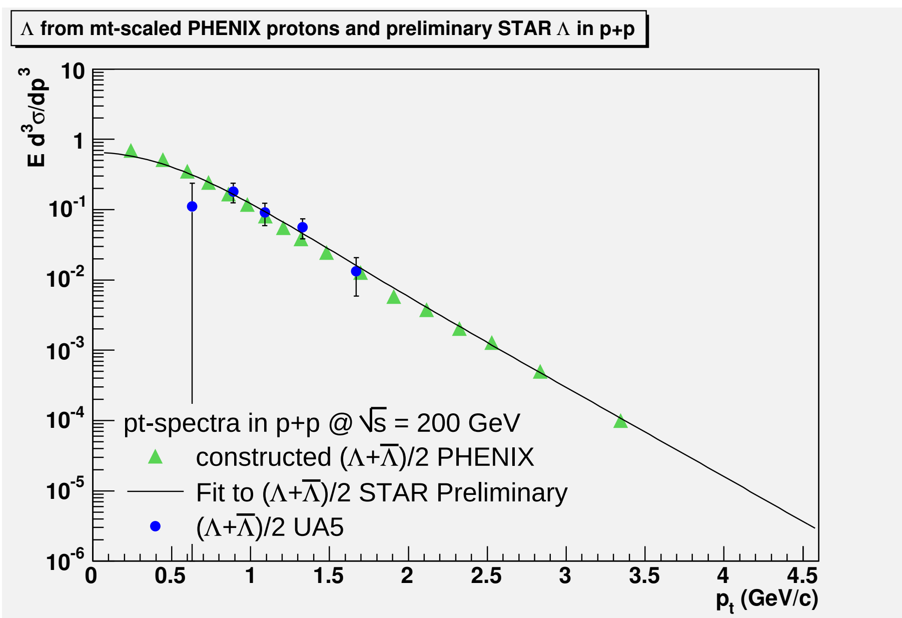

Figure 7.5: pt-spectra for the PHENIX constructed $\Lambda+\overline{\Lambda}$ along with the $\Lambda+\overline{\Lambda}$ UA5 data and a fit to the STAR preliminary results.

work.

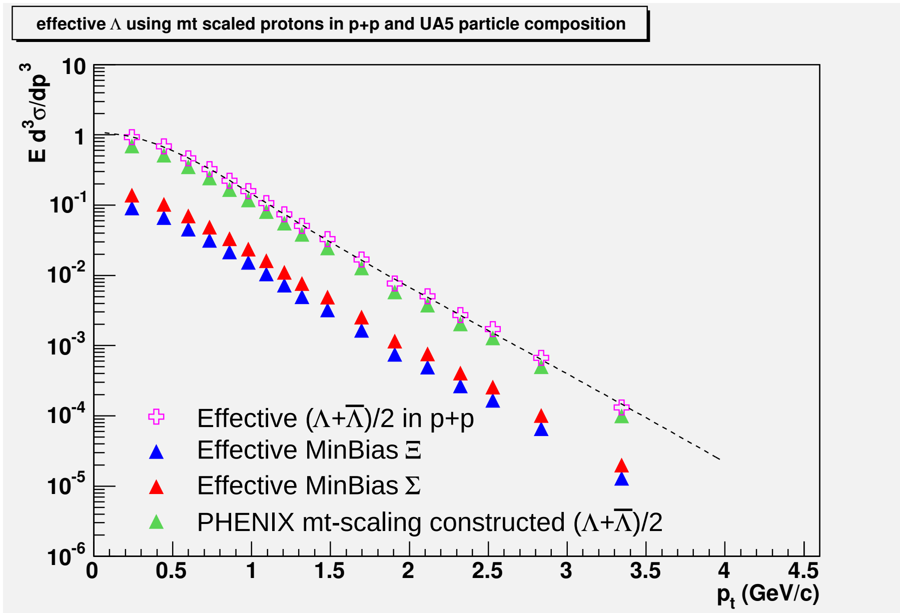

Figure 7.6: Effective Λ spectrum in p+p . The Ξ and Σ contributions are also shown, along with a fit to the effective spectrum.

Using the mass of the Λ we convert the mt proton spectrum back to a pt spectrum, ($p_t^2 = m_t^2 - m_\Lambda^2$), as can bee seen in Figure 7.5 where we also plot the fit to the preliminary STAR Λ spectrum along with the pt spectrum from UA5. We see that the PHENIX constructed Λ spectrum using absolute mt-scaling is in very good agreement with the “real” Λ spectra. In that way we do not need to reference any preliminary results for this part of the analysis. The PHENIX constructed Λ spectrum is then used to construct the effective Λ spectrum that will finally be used as an input to the simulation chain. The effective spectrum is shown in Figure 7.6.

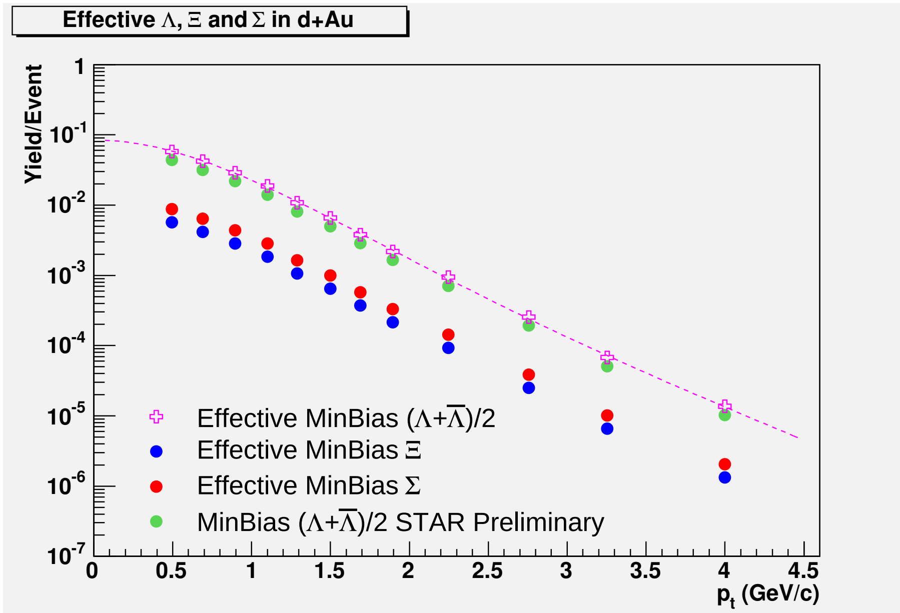

Figure 7.7: Effective Λ spectrum in d+Au. The preliminary d+Au minimum bias STAR Λ that was used as the basis spectrum is also shown.

7.5.2 d+Au

For the d+Au case we also produce an effective Λ distribution in the same way as was done for the p+p case, but this time we use as the initial Λ spectrum the STAR preliminary Minimum Bias spectrum in d+Au as shown in Figure 7.7. We follow this approach since there are no other available data in the literature and also because we want to examine if the two approaches converge.

Given the two effective Λ spectra in p+p and d+Au we now proceed to the next section were we describe how these spectra were used in simulation for the final stage of this analysis.

7.6 Λ Decay and Reconstruction with EXODUS, PISA and RECO

We generated 5 Million Λ events with the EXODUS generator, flat in pt, flat in 1.2 units of rapidity and isotropic in the ϕ direction covering 360 degrees. This phase space is a superset of the phase space seen by the TOF in order to account for the bending of decay products in the magnetic field and detector edge effects. This flat input distribution is then taken over by PISA which decays the Λ and propagates the decay products inside the PHENIX magnetic field and material. The detector signal is then reconstructed by the PHENIX reconstruction software as usual and the end product is a proton spectrum as reconstructed by the DCH+PC1+TOF.

The resulting decay proton spectrum has been derived from a flat pt Λ distribution and therefore must be weighted with the effective Λ distributions in p+p and d+Au as shown in Figures 7.6 and 7.7. Care must be taken in the application of this weight. Someone naively would apply a pt-dependent weight based on the pt of the detected decay proton but this is not correct since the proton does not take the entire momentum of the decayed Λ but only a fraction of it. Therefore for each proton in the simulation we trace back the pt of its parent and then apply the weight that corresponds to the parent pt. In that way the input pt distribution of the Λ is accurately reflected in the pt distribution of the decay protons. After that we apply the same cuts as were used in the real analysis, namely matching cuts, fiducial cuts, PID, energy loss etc. and then correct the protons with the same correction function that was used in the analysis of the real data. In this way it is guaranteed that the detection efficiency of the decay protons is the same with the one in the real data analysis.

We summarize the entire process of assembling the feed-down proton spectrum from the effective Λ input in the following equation:

$$\frac{\frac{1}{p_t}\frac{dN^{p_{\Lambda}^{TOF}}}{dp_t dy} \times corr(p_t) \times \left(\frac{1}{2\pi}\frac{1}{p_t^{parent}}\frac{d^2\sigma^{\Lambda}(p_t^{parent})}{dp_t dy}\right)}{\frac{1}{p_t^{parent}}\frac{dN^{\Lambda}_{simulation}}{dp_t dy}} \tag{7.4}$$

The resulting proton spectrum is an absolutely corrected and normalized feed-down spectrum since we started with absolutely normalized physical spectra for both p+p and d+Au .

7.7 From $(\Lambda + \overline{\Lambda})/2$ to Λ and $\overline{\Lambda}$

The effective Λ spectrum that was constructed in order to provide an input to our simulation chain was derived explicitly from UA5 (for p+p) and preliminary STAR (for d+Au) results on $\Lambda+\overline{\Lambda}$ production and therefore is an average effective spectrum that sets an average scale of the effect but there is one last step that needs to be applied before we apply the feed-down corrections to the PHENIX protons and antiprotons. Namely, given the average $\Lambda+\overline{\Lambda}$ correction we need to extrapolate to the individual Λ and $\overline{\Lambda}$ contributions.

This last step involves the $\overline{\Lambda}/\Lambda$ ratio. In the ideal case where the $\overline{\Lambda}/\Lambda$ ratio is equal to the $\overline{p}/p$ ratio or $\overline{\Lambda}/\Lambda = 1$ then the feed-down correction is the same for protons and antiprotons and the average correction that we already derived would be sufficient. It is known though that these two ratios have not achieved saturation even at RHIC energies and the net-baryon density is not zero even at $\sqrt{s} = 200$ GeV. Furthermore the $\overline{\Lambda}/\Lambda$ ratio is not equal to the $\overline{p}/p$ ratio, the former being larger at 200GeV. At $\sqrt{s}$ =200 GeV the only available data on the $\overline{\Lambda}/\Lambda$ comes from STAR preliminary results in p+p and Au+Au . From [74] and [75] we have:

$$\frac{\overline{\Lambda}}{\Lambda} = 0.8 \pm 15\% \ \text{ Au+Au} \tag{7.5}$$

and

$$\frac{\overline{\Lambda}}{\Lambda} = 0.89 \pm 15\% \ \text{ p+p} \tag{7.6}$$

None of these ratios are feed-down corrected for Ξ decays but this is a negligible effect on the ratio since from [74] we know that the Ξ has reached saturation at $\sqrt{s} = 200$ GeV, namely: $\overline{\Xi^-}/\Xi^- = 0.97$ and therefore the $\overline{\Lambda}/\Lambda$ stated above should be unchanged even after feed-down corrections.

In this analysis we adopt a $\overline{\Lambda}/\Lambda = 0.845 \pm 10\%$ ratio, which is the average of the preliminary p+p and Au+Au STAR result. We take then the effective Λ and $\overline{\Lambda}$ contributions to be:

$$\Lambda^{effective} = 1.084 \cdot (\frac{\Lambda + \overline{\Lambda}}{2})^{effective} \tag{7.7}$$

$$\overline{\Lambda}^{effective} = 0.916 \cdot (\frac{\Lambda + \overline{\Lambda}}{2})^{effective} \tag{7.8}$$

This assumption on the $\overline{\Lambda}/\Lambda$ ratio directly translates on the number of feed-down protons and antiprotons detected at the TOF:

$$p_{FD}^{\Lambda} = 1.084 \cdot p^{(\frac{\Lambda+\overline{\Lambda}}{2})^{effective}} \tag{7.9}$$

and

$$\overline{p}_{FD}^{\overline{\Lambda}} = 0.916 \cdot p^{(\frac{\Lambda+\overline{\Lambda}}{2})^{effective}} \tag{7.10}$$

Based on what was presented in this section it is obvious that the feed-down corrected $\overline{p}/p$ ratio that will be formed with the corrected protons and antiprotons, is very sensitive on the $\overline{\Lambda}/\Lambda$ ratio and its uncertainty. We will deal with this additional systematic uncertainty later on in this analysis.

7.8 Result

The resulting feed-down proton and antiproton spectra for both collision systems are shown in Figures 7.8 and 7.9 along with the total proton and antiproton spectra for comparison. This is the final result. The feed-down proton and antiproton spectra are then subtracted from the total spectra to produce the prompt proton and antiproton component in p+p and d+Au collisions.

In order to compare our result with the feed-down correction used in the RUN02 Au+Au analysis we construct the fractional feed-down correction f:

$$f = \frac{p_{feed-down}}{p_{total}} \tag{7.11}$$

and plot it along with the RUN02 result [78] as shown in Figures 7.10 and 7.11. The RUN02 result was constructed assuming mt-scaling of Λ and protons and using the Λ/p ratios from the 130 GeV data [76] due to lack of

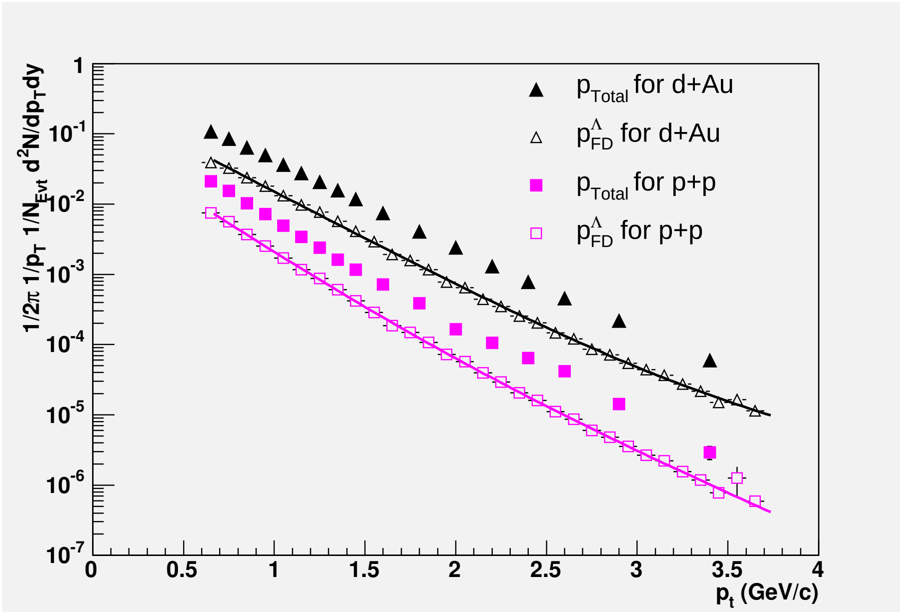

Figure 7.8: Inclusive PHENIX proton spectra in p+p and d+Au along with the proton spectra from feed-downs calculated in this analysis for the corresponding collision systems.

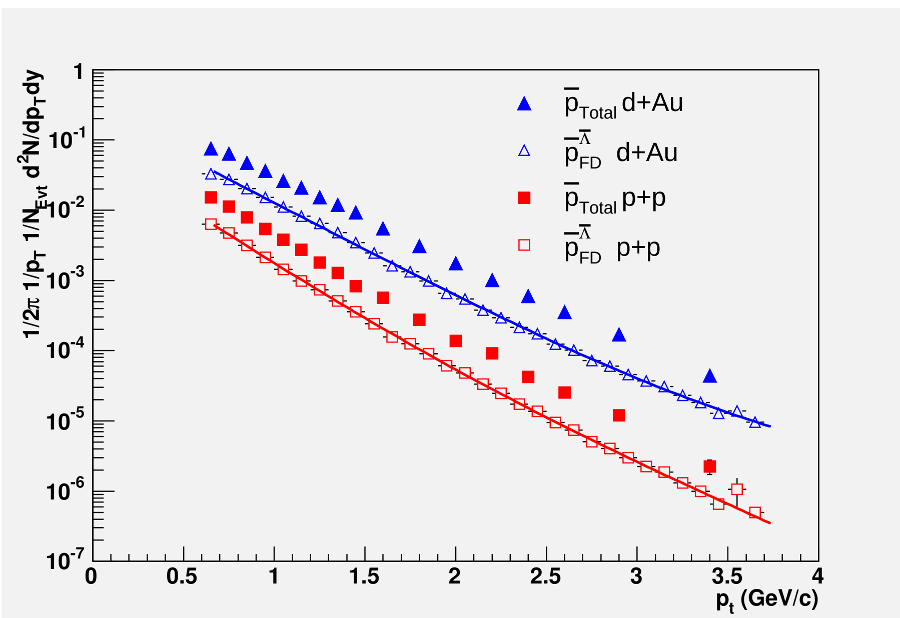

Figure 7.9: Inclusive PHENIX antiproton spectra in p+p and d+Au along with the antiproton spectra from feed-downs calculated in this analysis for the corresponding collision systems.

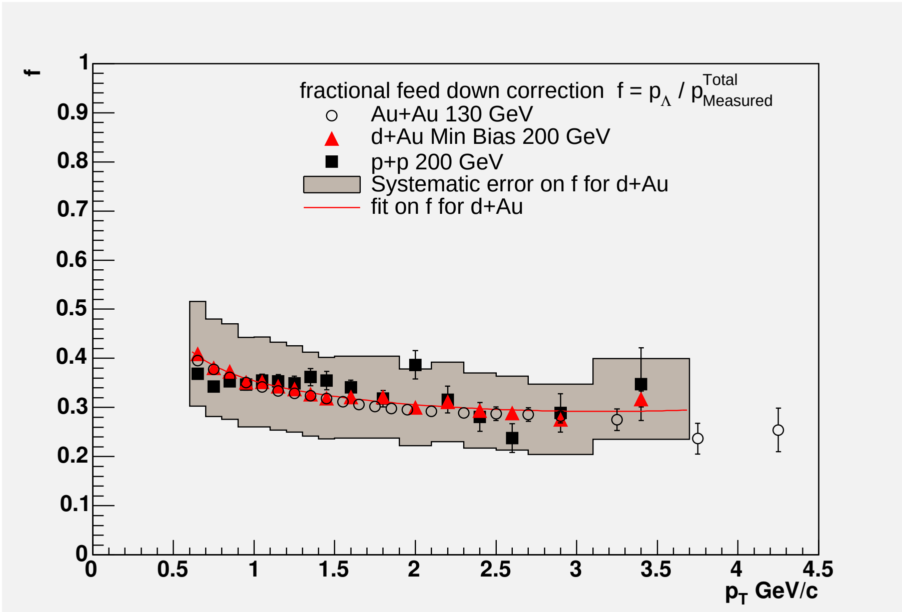

Figure 7.10: Fractional feed-down corrections for protons in p+p and d+Au. The feed-down correction for $Au + Au$ at 130 GeV is also shown.

data in the 200 GeV energy. We further comment on the relative size of the feed-down fraction in the Epilogue section.

In Figures 7.10 and 7.11 we also present fits to the f function that will be used for the feed-down correction:

$$f(p_t) = \sqrt{(\frac{p_0^2}{p_t^2} + p_1^2)} - p_2 \cdot p_t - p_3 \cdot p_t^2 \tag{7.12}$$

The parameters of the fit that will be used are as follows:

$$f(p_t): \quad p_0 = -0.1515, \quad p_1 = 0.3674, \quad p_2 = 0.05166, \quad p_3 = -0.008488 \tag{7.13}$$

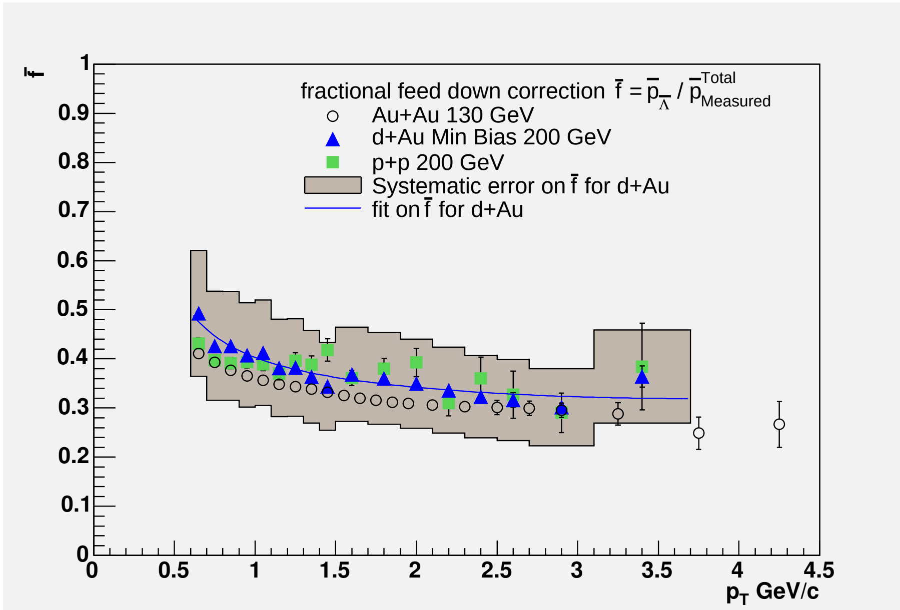

Figure 7.11: Fractional feed-down corrections for antiprotons in p+p and d+Au. The feed-down correction for $Au + Au$ at 130 GeV is also shown.

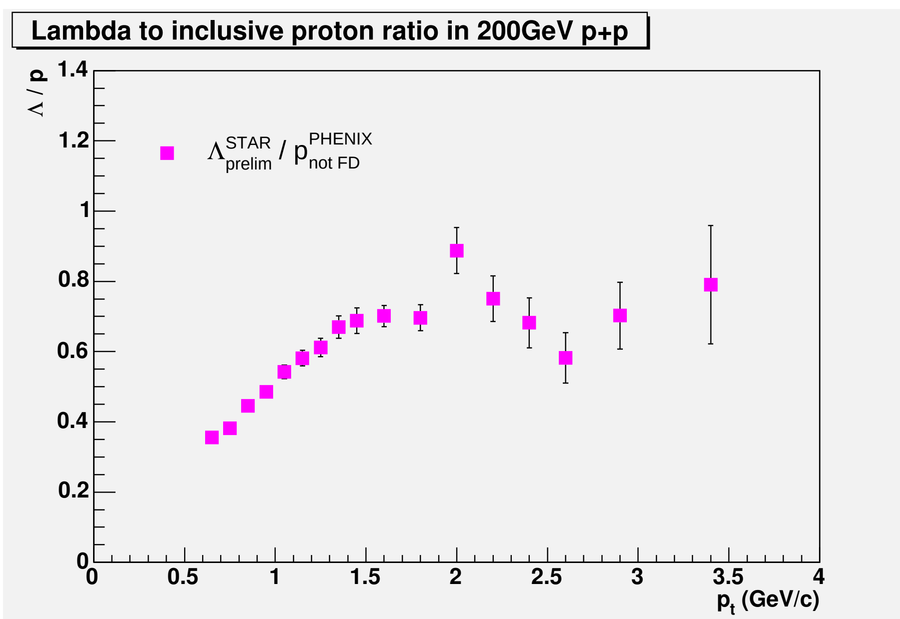

Figure 7.12: Λ/p ratio in p+p (protons here are not averaged with antiprotons). Both Λ and protons are not feed-down corrected. This ratio is only a crude approximation of the feed-down corrected ratio.

$$\overline{f}(p_t) = 1.135 \cdot f(pt) \tag{7.14}$$

The parameters of the fitting function $f(pt)$ were determined by fitting the positive feed-down correction f. For the negative $\overline{f}(p_t)$ correction, we used the same parameters and functional form as for the positive function, but introduced a normalization parameter and fitted the negative correction in order to determine it. This ensures that the shape of the correction for protons and antiprotons is the same, as it should, with only the size of the correction changing for positives and negatives.

The feed-down correction for the protons is applied as:

$$p_{corr} = p_{Total} - p_{\Lambda} = (1 - f) \cdot p_{Total} \tag{7.15}$$

and the systematic error is applied as:

$$\delta p_{corr} = \sqrt{(\sigma_{p_{Total}} \cdot p_{Total})^2 + (\sigma_{p_{\Lambda}} \cdot f \cdot p_{Total})^2} \tag{7.16}$$

where $\sigma_{p_{\Lambda}} = 24\%$, is the relative systematic error on $\Lambda^{effective}$ and subsequently on p_{Λ}, as explained in the next section, and $\sigma_{p_{Total}}$ is the relative TYPE-B systematic error on the total protons. The relative TYPE-B systematic error on the corrected protons then becomes:

$$\sigma_{p_{corr}}^{TYPE-B} = \frac{\delta p_{corr}}{p_{corr}} = \frac{\sqrt{\sigma_{p_{Total}}^2 + (f \cdot \sigma_{p_{\Lambda}})^2}}{(1 - f)} \tag{7.17}$$

The two methods applied , for p+p and d+Au although starting with different inputs for the initial Λ spectrum produced very similar results. This strengthens our confidence for the validity of the result. We chose to use the d+Au fits for both p+p and d+Au corrections since the statistics are better in this case.

7.9 Systematic Error Estimation

For the systematic error estimation we propagate the errors on the yields for all the particles involved in the construction of the effective Λ spectrum. The systematic errors are taken from UA5 as shown in Table 7.2. We add in quadrature:

$$\Lambda^{effective} \pm \delta\Lambda = ((0.46 \pm 0.12) + (0.06^{+0.08}_{-0.02}) + (\frac{0.23}{2} \pm 0.03) \cdot 0.8) \qquad (7.18)$$

and finally

$$\Lambda^{effective} = 0.612^{+0.146}_{-0.124} = 0.612^{+24\%}_{-20\%} \approx 0.612 \pm 24\% \qquad (7.19)$$

Our final systematic error on the feed-down protons is 24%. The error is rather large and reflects the poor systematic errors in the UA5 data. We take the same error for p+p and d+Au making the implicit assumption that the preliminary d+Au Λ spectrum has a systematic error of the same size as the Λ measurement by UA5, namely 26%. The systematic error on the fractional feed-down corrections f and $\overline{f}$ have approximately the same size, dominated by the large uncertainty in the effective Λ spectrum and are shown in Figures 7.10 and 7.11.

7.10 Systematic Error on $\overline{p}/p$

As discussed before, the systematic error on the preliminary $\overline{\Lambda}/\Lambda$ ratio that determines the relative difference for the feed-down protons and antiprotons must be propagated in the corrected $\overline{p}/p$ ratio. Before the feed-down corrections were applied , for the preliminary result, we calculated a not-feed-down corrected ratio $\overline{p}/p = 0.75 \pm 7\%(syst)$ where the systematic error was determined by varying the analysis cuts and recalculating the ratio. The systematic error on f is of course quite sizeable but it is the same for both protons and antiprotons and therefore should not be propagated in the corrected ratio. But the systematic uncertainty on $\overline{\Lambda}/\Lambda$ has a direct effect on the value and systematic error of the corrected $\overline{p}/p$ ratio that must be taken care of.

We write the corrected ratio as:

$$
\begin{aligned}
(\frac{\overline{p}}{p})_{FD-corr} &= \frac{\overline{p} - \overline{p}_{\overline{\Lambda}}}{p - p_{\Lambda}} && (7.20)\\
&= \frac{\overline{p} - (\frac{\overline{\Lambda}}{\Lambda}) \cdot p_{\Lambda}}{p - p_{\Lambda}} && (7.21)\\
&= \frac{\overline{p} - (\frac{\overline{\Lambda}}{\Lambda}) \cdot f \cdot p}{p - f \cdot p} && (7.22)\\
& && (7.23)
\end{aligned}
$$

and finally

$$(\frac{\overline{p}}{p})_{FD-corr} = \frac{(\frac{\overline{p}}{p})_{not-FD} - (\frac{\overline{\Lambda}}{\Lambda}) \cdot f}{1 - f} \qquad (7.24)$$

Taking an average $f = 0.3$ and the uncorrected ratio $\overline{p}/p = 0.75 \pm 7\%$ we propagate the error of the $\overline{\Lambda}/\Lambda$ and $\overline{p}/p$ and get:

$$(\frac{\overline{p}}{p})_{FD-corr} \approx 0.71 \pm 0.086(syst) = 0.71 \pm 12\%(syst) \tag{7.25}$$

The final value of the corrected $\overline{p}/p$ will be of course determined by fitting the ratio as a function of pt after we correct the proton and antiproton spectra, but the point is that the systematic error that will be applied to the fit result will be 12%.

7.11 Epilogue

Now that we know that the feed-down contribution to protons is of the order of 30% and that the Ξ contribution to the Λ is of the order of 15% we can take the not feed-down corrected Λ/p ratio seen in Figure 7.12 and quote an estimate of the corrected ratio at high pt where the uncorrected ratio becomes flat and saturates around 0.70 :

$$(\frac{\Lambda}{p})_{FD-corrected} \approx (\frac{\Lambda}{p})_{not-FD-corrected} \cdot \frac{0.85}{0.70} \approx 0.70 \cdot 1.20 = 0.84 \tag{7.26}$$

The corresponding corrected ratio at 130GeV Au+Au collisions is $0.89 \pm 0.07(syst)$ [76]. We therefore see that the reason that the 130GeV feed-down correction, shown in Figure 7.10, is so similar with our corrections for p+p and d+Au at 200 GeV can be attributed to a similar Λ/p ratio.

Also, the fact that we presently calculate a larger asymmetry between the proton and antiproton feed-down correction from the one calculated in the 130

GeV analysis, can be attributed to the fact that the $\frac{\overline{\Lambda}/\Lambda}{\overline{p}/p} = 0.98 \pm 0.09$ from [77] while in the 200 GeV data used in this analysis we have $\frac{\overline{\Lambda}/\Lambda}{\overline{p}/p} \approx 0.845/0.71 \approx 1.20$. There are relatively more anti-Lambdas than antiprotons with respect to their matter partners.

Chapter 8

Results

8.1 Identified Particle Spectra

We begin the presentation of our results with the 36 fully corrected identified particle spectra in p+p and d+Au collisions. All the corrections that have been mentioned previously, including geometrical corrections, efficiencies, feed-down corrections for the protons and antiprotons, trigger bias and centrality bin-shifting effects, have been applied to the data. In Fig. 8.1 we present the Minimum Bias d+Au invariant yields. Two clarifications are in order here:

- As was discussed extensively in Part 3, the d+Au spectra are differential yields per inelastic event. The p+p spectra, that will be presented shortly, are invariant differential cross sections. We will use the term "particle spectra" interchangeably to refer to these quantities.
- The units of momentum in both cases are in GeV/c. That makes the units of the invariant yields to be $[1/GeV^2]$. The units for the invariant

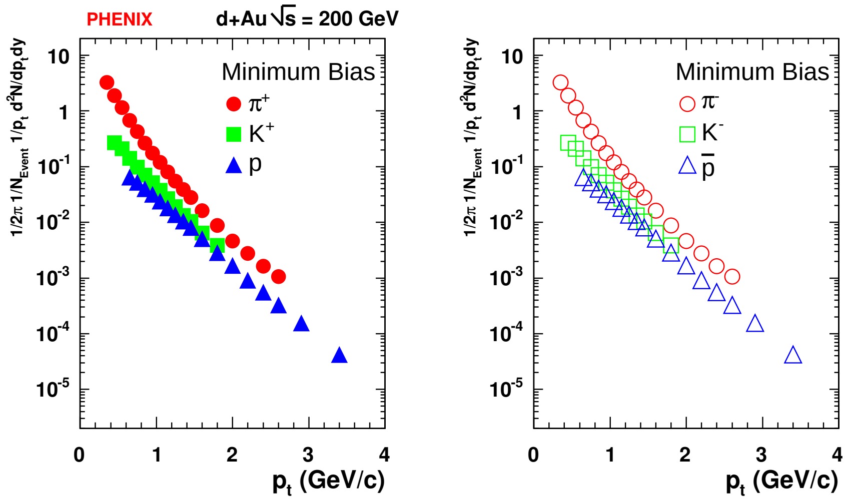

Figure 8.1: Transverse momentum spectra of identified particles in Minimum Bias d+Au collisions.

cross sections are $[mb/GeV^2]$.

The total number of events analyzed in the d+Au case is approximately 42M Minimum Bias Events. In the p+p case we analyzed approximately 25M events. Using the value of the RUN02 BBC cross section, $\sigma_{BBC} = 21.8$ mb, the 25M p+p events correspond to 1.146 nb^{-1} (inverse nanobarns).

In Figures 8.2-8.5 we present identified particle spectra in the four d+Au centrality bins defined in Section 3.5.

In Fig. 8.6 we present identified particle spectra (invariant cross sections) in p+p collisions.

Our results are in good agreement, within the stated errors, with identified particle spectra published by the STAR Collaboration [94].

We also present the same spectra in a different configuration. In Figures 8.7-8.9 we present particle spectra in p+p and d+Au for each species in a

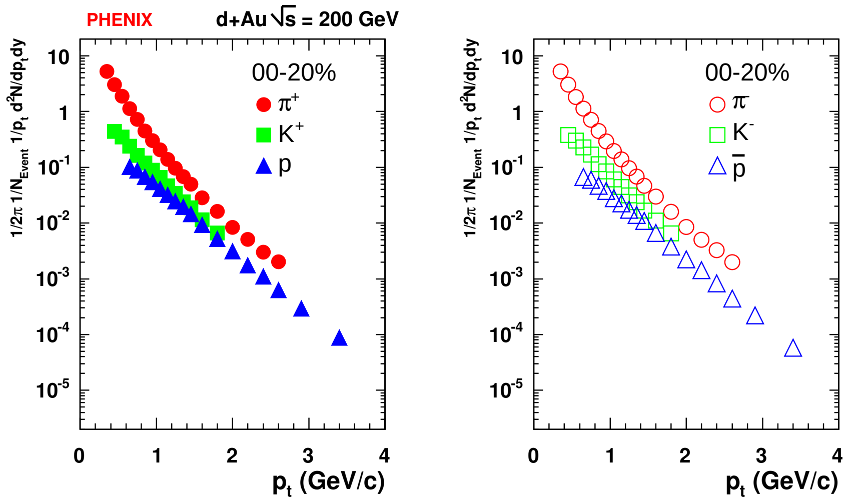

Figure 8.2: Transverse momentum spectra of identified particles in 00-20% d+Au collisions.

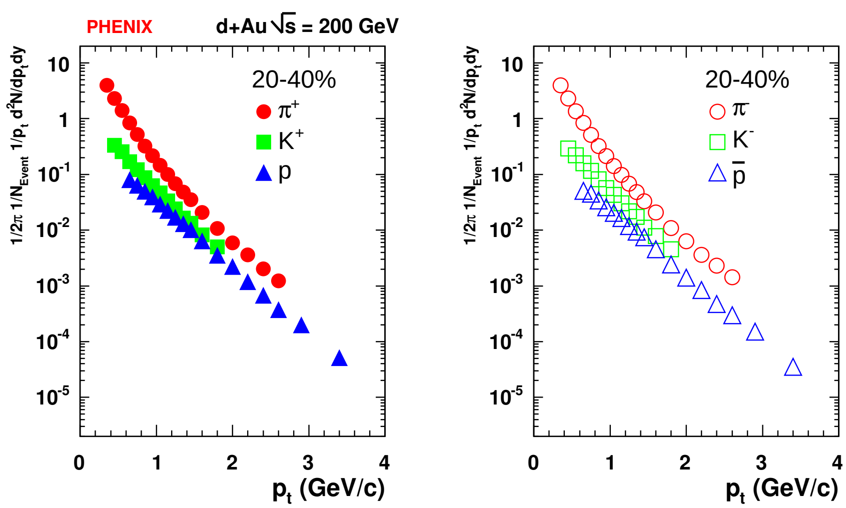

Figure 8.3: Transverse momentum spectra of identified particles in 20-40% d+Au collisions.

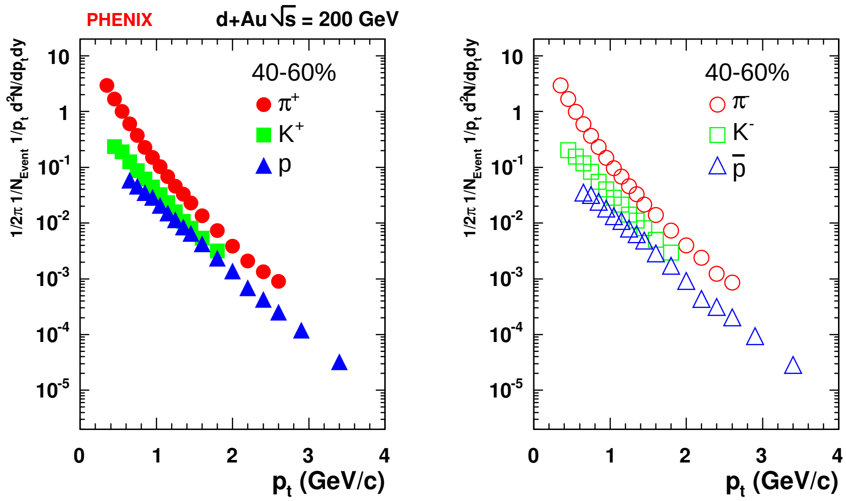

Figure 8.4: Transverse momentum spectra of identified particles in 40-60% d+Au collisions.

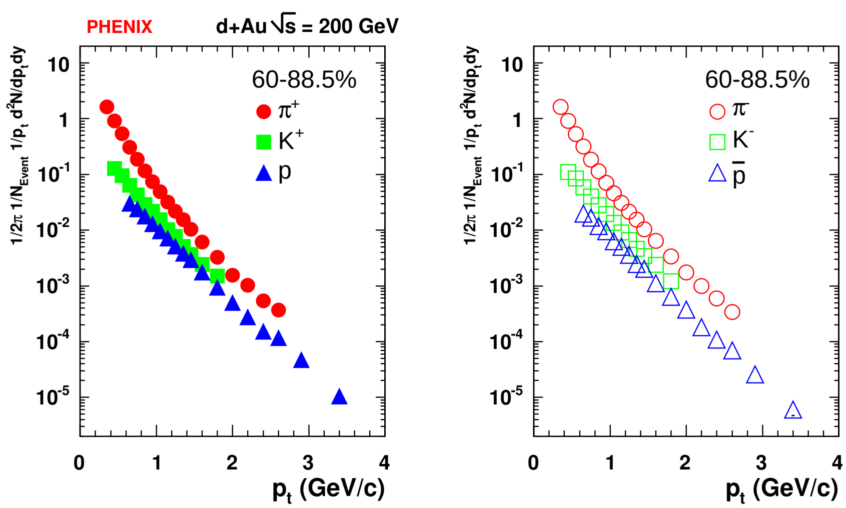

Figure 8.5: Transverse momentum spectra of identified particles in 60-90% d+Au collisions.

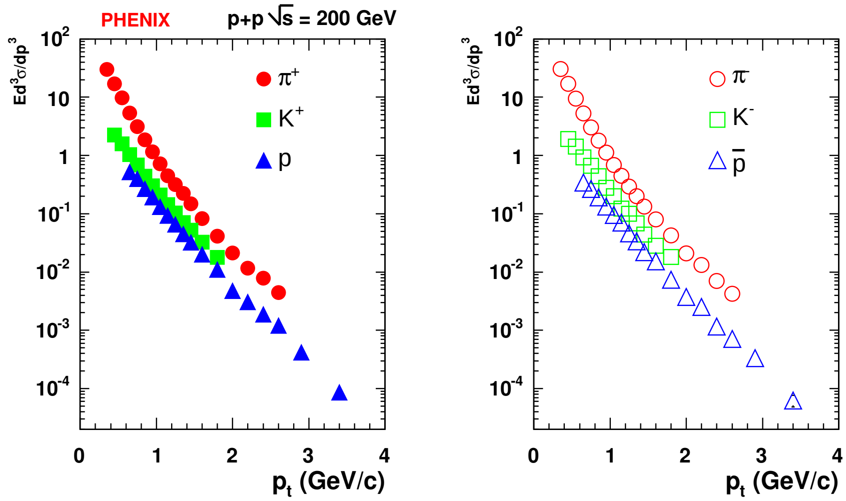

Figure 8.6: Differential cross section of identified particles in p+p collisions.

single plot. In that way we can examine the shape of each particle spectrum, in differing nuclear geometries, and make comparisons more easily. In these plots, the p+p data are presented as differential Yield/Event.

8.2 Nuclear Modification Factors

We now proceed to present one of the central results of this thesis, namely the nuclear modification factors for identified particles in d+Au and Au+Au collisions. As was mentioned previously these factors in the d+Au case reveal the size of cold nuclear matter effects, like Cronin, shadowing and possible parton saturation phenomena, which establish the initial conditions for the Au+Au system. In the Au+Au case the nuclear modification factors describe the effect of the hot and dense medium on identified particle production. We note that this is the first time that identified R_{AuAu} are presented, since the

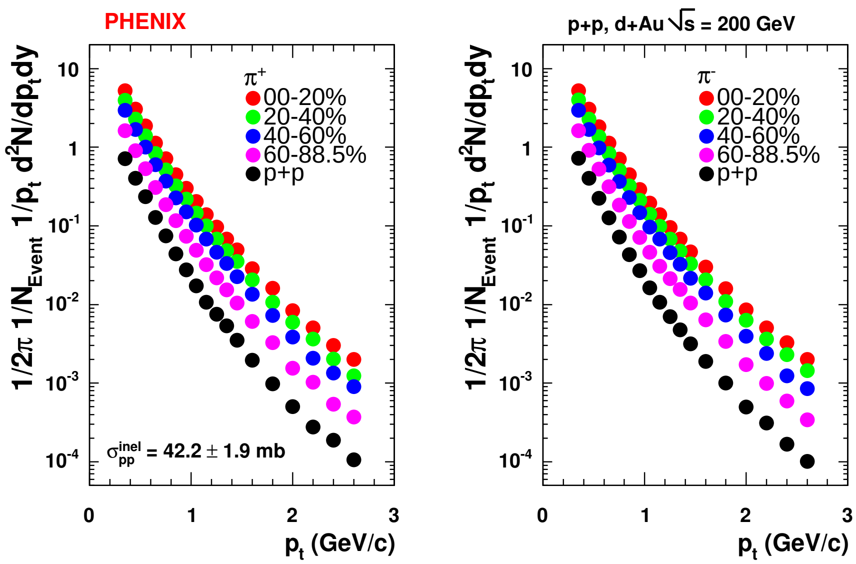

Figure 8.7: Transverse momentum spectra of pions in p+p and d+Au collisions.

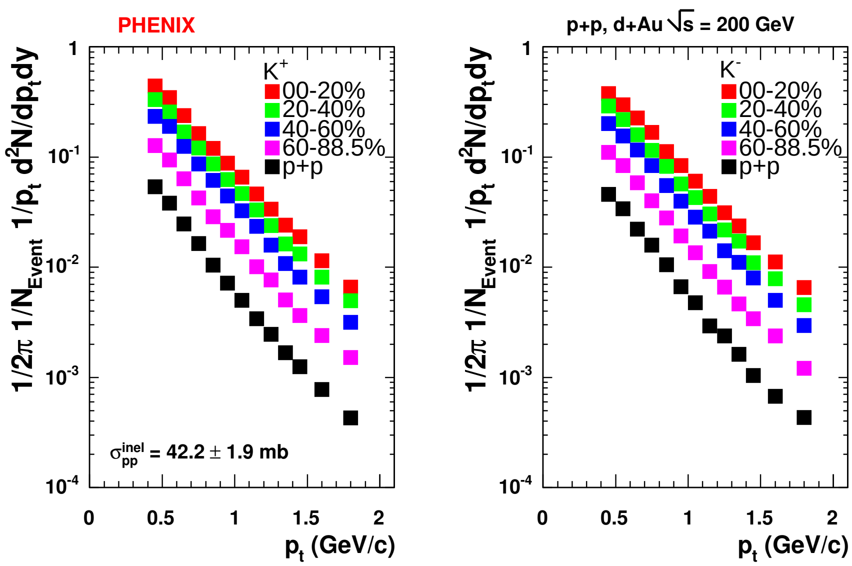

Figure 8.8: Transverse momentum spectra of Kaons in p+p and d+Au collisions.

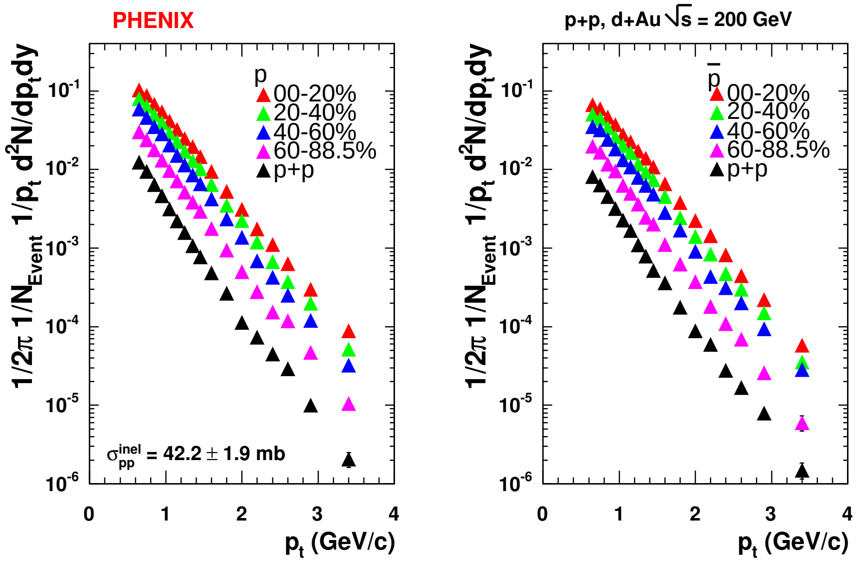

Figure 8.9: Transverse momentum spectra of protons and antiprotons in p+p and d+Au collisions.

key ingredient of these ratios, namely the p+p reference, is for the first time measured in this analysis. The nuclear modification factors are formed by using Equation 3.73, which we present again here for completeness:

$$R_{AB}(p_T) = \frac{\dfrac{1}{N^{Total\,Events}_{inelastic,AB}} \cdot \dfrac{d^2(N^{hard}_{AB})_{MB}}{dp_T dy}}{\dfrac{< N_{coll} >_{MB}}{\sigma_{NN}} \cdot \dfrac{d^2\sigma^{hard}_{NN}}{dp_T dy}} \tag{8.1}$$

The number of collisions in the d+Au case have been presented in Section 3.5. For Au+Au we take the number of collisions in the most central and the most peripheral bin from [48]. In this Glauber model calculations we have $N_{coll} = 1065.4 \pm 105.3$ for the most central Au+Au bin, while $N_{coll} = 14.5 \pm 4.0$ for the most peripheral bin.

In Fig. 8.10 we present identified R_{AuAu} for the most central Au+Au cen-

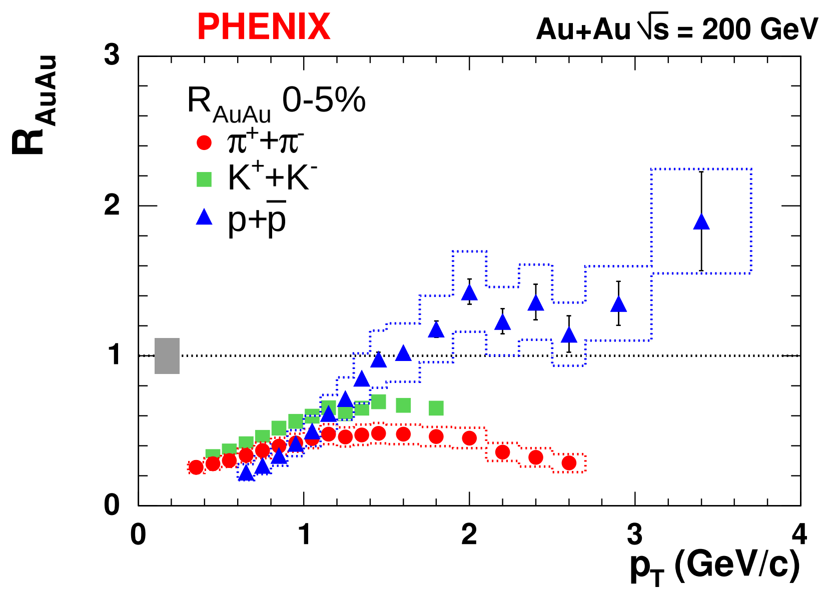

Figure 8.10: Nuclear modification factors for identified particles, R_{AuAu}, for the most central Au+Au centrality bin, 00-05%. Systematic error bars are shown for pions and protons. The vertical grey bar is the overall scale systematic error on the number of collisions from the Glauber model and the uncertainty in the BBC cross section in p+p collisions. The meaning of these error bars is the same in all R_{AuAu} figures.

trality bin, and in Fig. 8.11 we include the neutral pion R_{AuAu} from [26]. In Fig. 8.12 we present a zoomed-in version of Fig. 8.11, where the vertical axis goes up to 1.5, instead of 3.0 (the last proton point is outside the plotting range), for a better comparison of the nuclear modification factors. In this most central Au+Au bin we expect to see the full extent of the final state effects of the hot hadronic matter.

In Fig. 8.13 we present identified R_{AuAu} for the most peripheral Au+Au centrality bin, and in Fig. 8.14 we include the neutral pion result from [26].

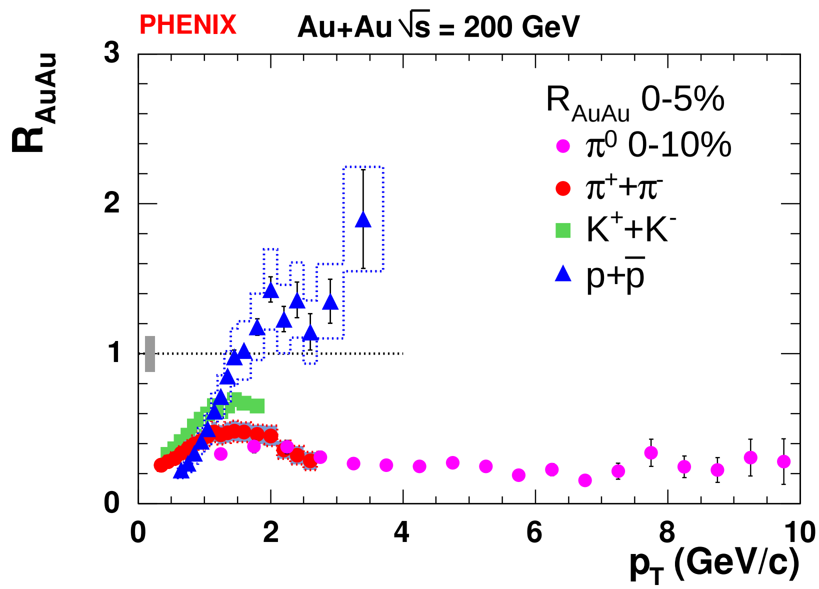

Figure 8.11: Nuclear modification factors for identified particles, R_{AuAu}, for the most central Au+Au centrality bin, 00-05%. Neutral pions are also shown from [26]. Note that the nuclear modification factor for the neutral pions is from the 00-10% bin.

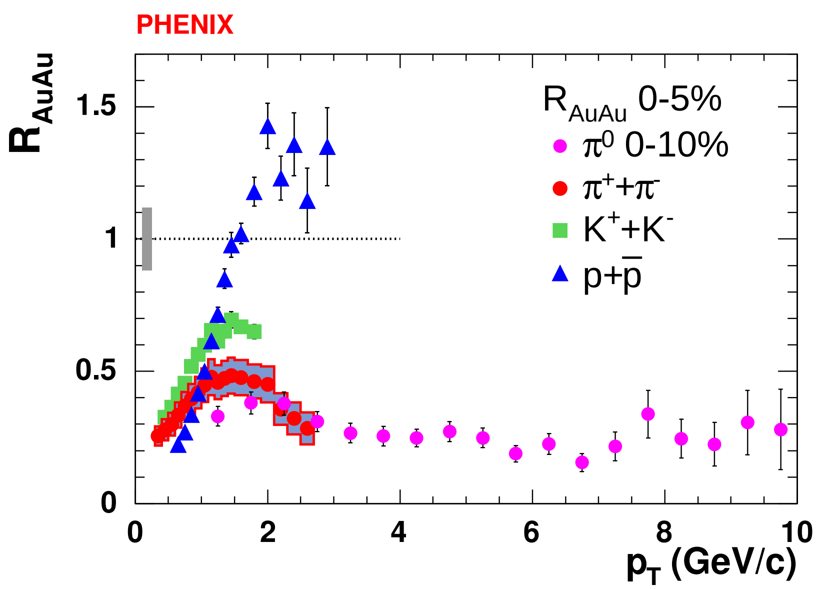

Figure 8.12: Nuclear modification factors for identified particles, R_{AuAu}, for the most central Au+Au centrality bin, 00-05%. Neutral pions are also shown. Note that the nuclear modification factor for the neutral pions is from the 00-10% bin.

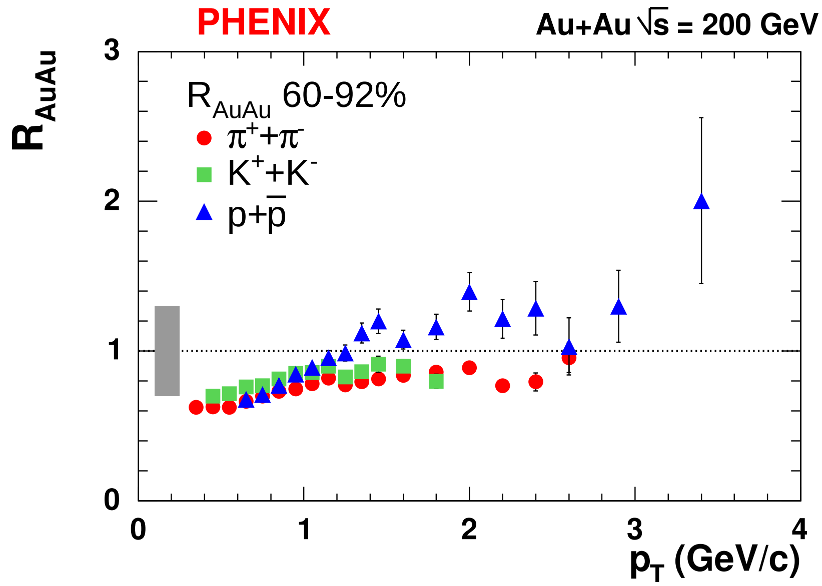

Figure 8.13: Nuclear modification factors for identified particles, R_{AuAu}, for the most peripheral Au+Au centrality bin, 60-92%.

8.2.1 Nuclear Modification Factors in d+Au.

We now turn to the nuclear modification factor R_{dAu} in d+Au for pions kaons and protons. As discussed earlier, R_{dAu} is a measure of particle production in d+Au collisions with respect to point-like scaled p+p particle production. It establishes the initial conditions for the Au+Au system and it quantitatively shows the effect of the cold nuclear matter on particle production. This can also be regarded as the effect of the Au wave function on particle production. In Fig. 8.15 we present the Minimum Bias R_{dAu} for pions kaons and protons.

In Figures 8.16-8.19 we present the d+Au nuclear modification factors in the four d+Au centrality bins. We start with the most central bin , where we fully probe the Au nucleus, and continue with more peripheral bins, where we expect any nuclear effects to decrease continuously, until the most peripheral

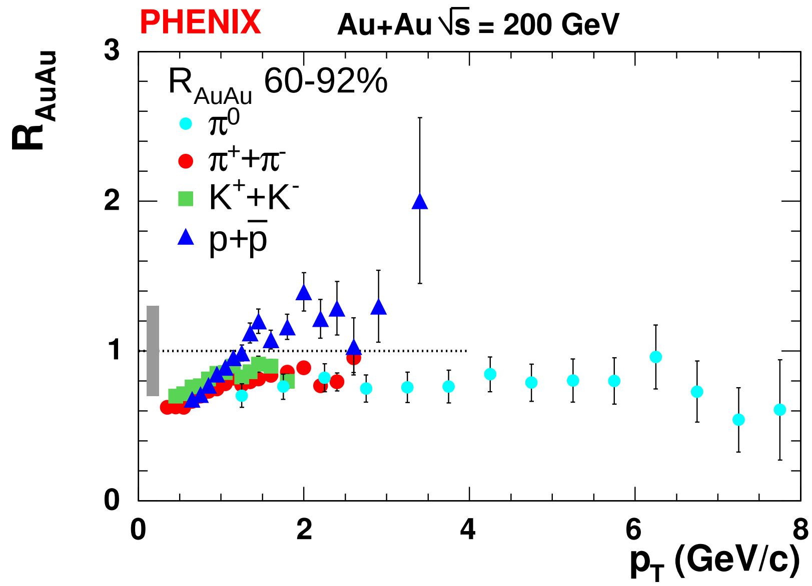

Figure 8.14: Nuclear modification factors for identified particles, R_{AuAu}, for the most peripheral Au+Au centrality bin, 60-92%.Neutral pions are also shown from [26].

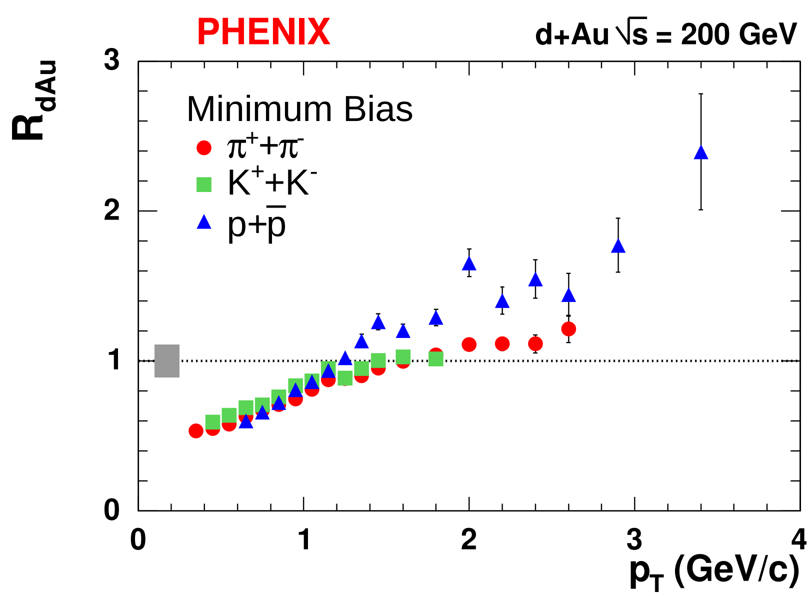

Figure 8.15: Nuclear modification factors for identified particles, R_{dAu}, in Minimum Bias d+Au collisions.

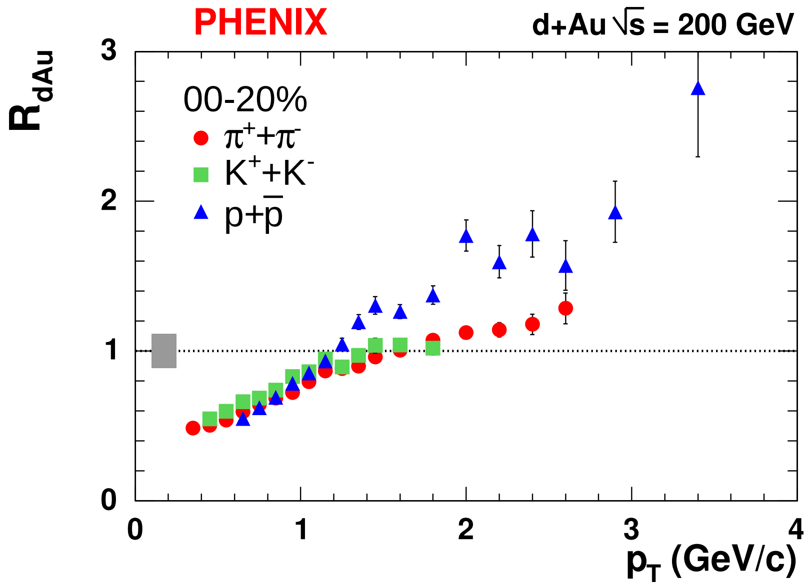

Figure 8.16: Nuclear modification factors for identified particles, R_{dAu}, in in 00-20% d+Au collisions.

bin where we recover point-like scaling at intermediate and high p_T.

Finally, in order to compare the centrality dependence of R_{dAu} in a single plot, for pions and protons, we present in Fig. 8.20 integrated R_{dAu} as a function of $\nu = N_{coll}/N^{d}_{part}$, the number of collisions suffered by each deuteron participant. We present two integrating regions. The low pt region is from $0.6 < pt < 1.5\, GeV/c$, which represents the suppression region where R_{dAu} is always below 1. The higher integration region in p_T, $1.5 < p_T < 2.7\, GeV/c$, represents the range of transverse momenta where we observe enhancement in the particle production relative to p+p and therefore the nuclear modification factors are all above or close to 1.

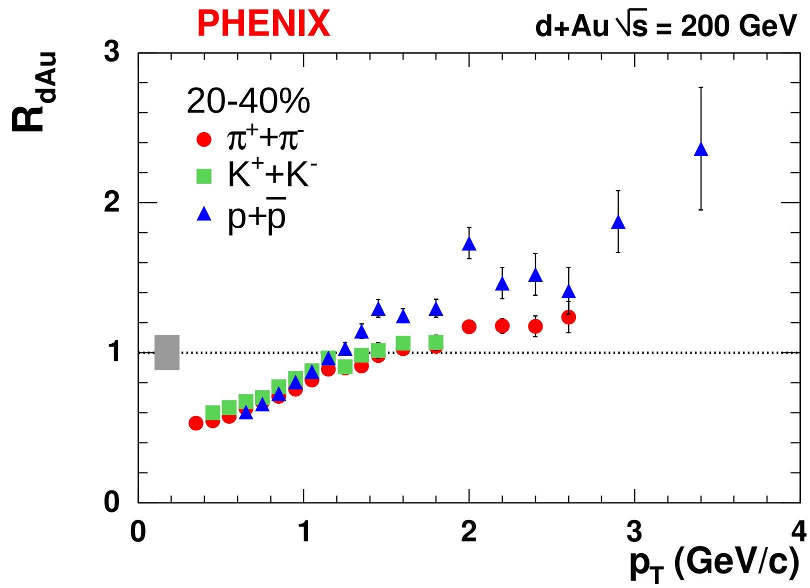

Figure 8.17: Nuclear modification factors for identified particles, R_{dAu}, in in 20-40% d+Au collisions.

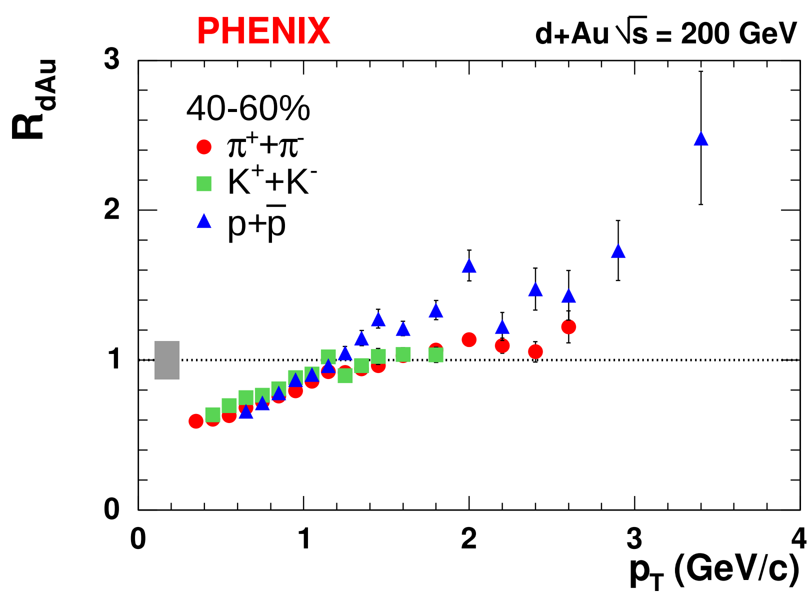

Figure 8.18: Nuclear modification factors for identified particles, R_{dAu}, in in 40-60% d+Au collisions.

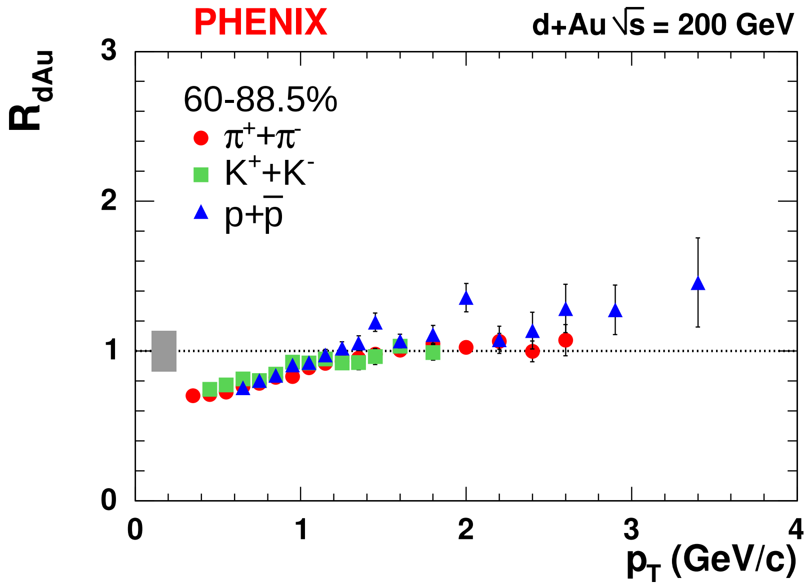

Figure 8.19: Nuclear modification factors for identified particles, R_{dAu}, in in 60-90% d+Au collisions.

8.2.2 Comparing R_{AuAu} and R_{dAu}.

We present now comparison plots for the nuclear modification factors in d+Au and Au+Au. We start with Fig. 8.21 where we show R_{AuAu} for the most central and the most peripheral Au+Au bin, along with the Minimum Bias nuclear modification factor R_{dAu}, from d+Au. In the same plot we also show the corresponding number of binary collisions in these three nuclear geometries.

In Fig. 8.22 we present the same R_{AuAu} that were shown in Fig. 8.21, but now we compare them with the most central R_{dAu}. In the most central d+Au bin, the number of binary collisions is almost the same with the number of collisions from the most peripheral Au+Au bin.

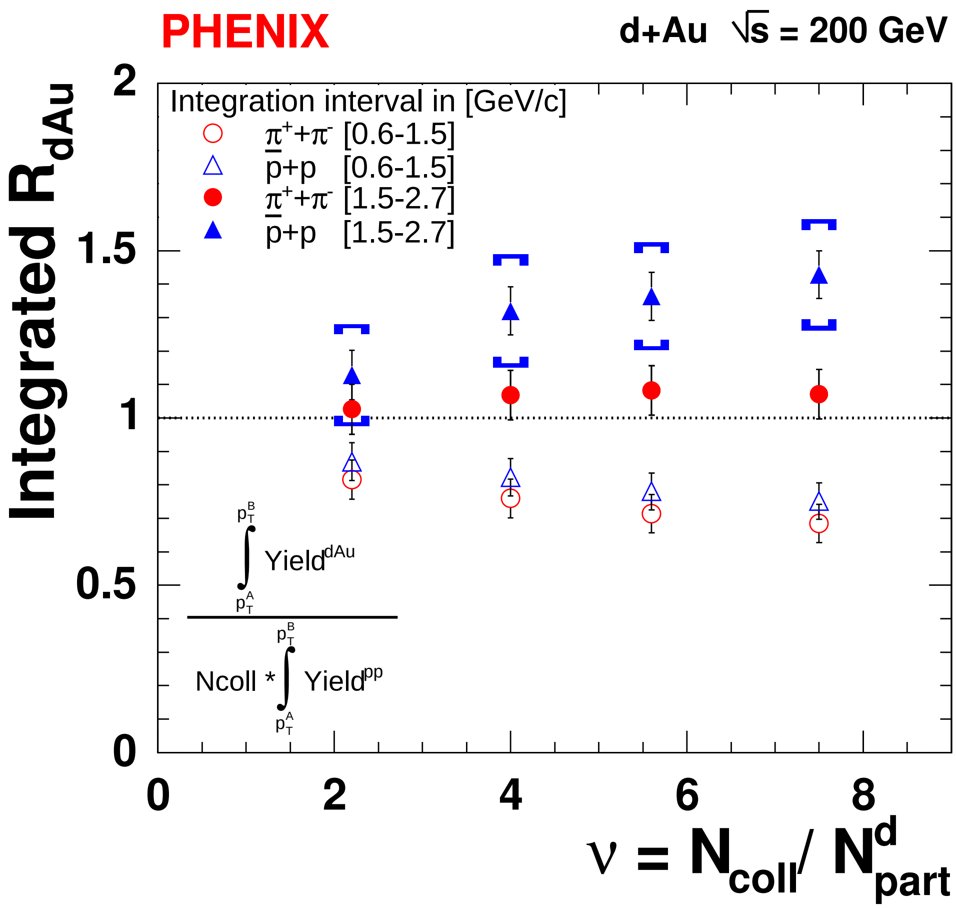

Figure 8.20: Integrated Nuclear modification factors for pions and protons as a function of the number of collisions per Deuteron participant in d+Au collisions.

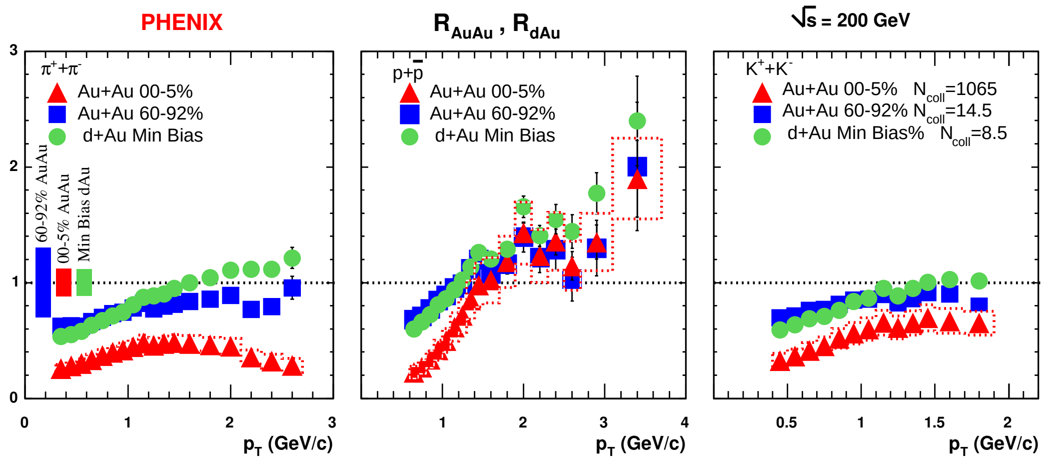

Figure 8.21: Nuclear modification factors for identified particles in Minimum Bias d+Au, and, central and peripheral Au+Au collisions.

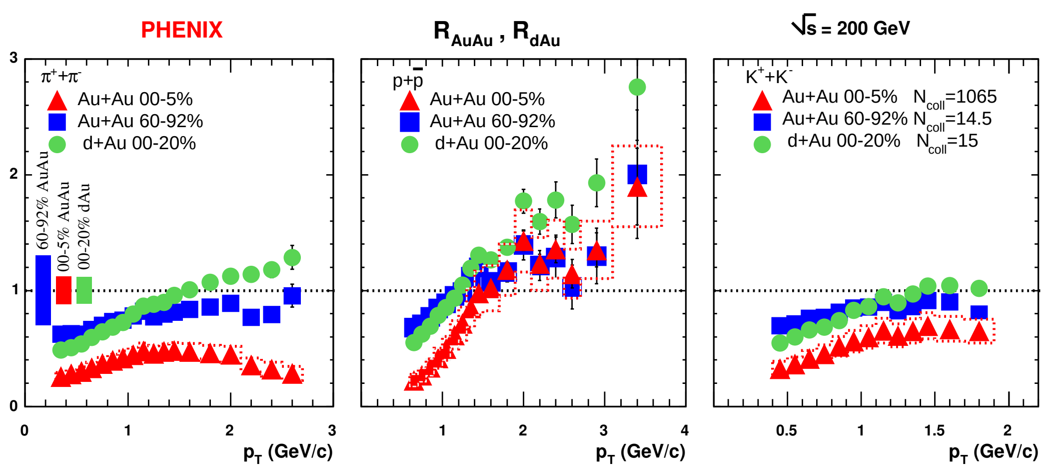

Figure 8.22: Nuclear modification factors for identified particles in 00-20% d+Au, and, central and peripheral Au+Au collisions.

8.3 Interspecies Ratios

Particle ratios between different species of particles are presented in this section. We begin with the p/π ratio, which , as was discussed in the Introduction, has an anomalously high value in central Au+Au collisions. From this analysis we can calculate the p/π ratio in p+p and in d+Au collisions, and therefore, for the first time at RHIC energies, we are in a position to compare the proton to pion ratio in all three colliding systems, p+p, d+Au, and Au+Au, at $\sqrt{s}$ = 200 GeV. In Fig. 8.23 we show the p/π in all three colliding systems. The Au+Au ratio is presented for central, mid-central and peripheral Au+Au collisions from [27] while the d+Au ratio is from Minimum Bias events.

In order to examine the centrality dependence of the p/π ratio in d+Au collisions, we present in Fig. 8.24 the p/π ratio in central and peripheral d+Au collisions, along with the p+p result. We see a moderate centrality dependence in d+Au. The departure of the central d+Au ratio from the p+p value is more prominent, and it is a result of the large Cronin effect of the protons in d+Au collisions.

A comparison of the K/π ratio in all three collision systems is shown in Fig. 8.25. The centrality dependence in d+Au of the same ratio, along with the p+p result is shown in Fig. 8.26. It is clear that the K/π ratio in these three systems does not exhibit the large variations that we show in the p/π ratio. Its centrality dependence in d+Au is virtually non existent, and it has the same value as in p+p collisions.

Finally, the p/K ratio is shown in Fig. 8.27 in the most central d+Au events and in p+p. The more copious production of protons with respect to

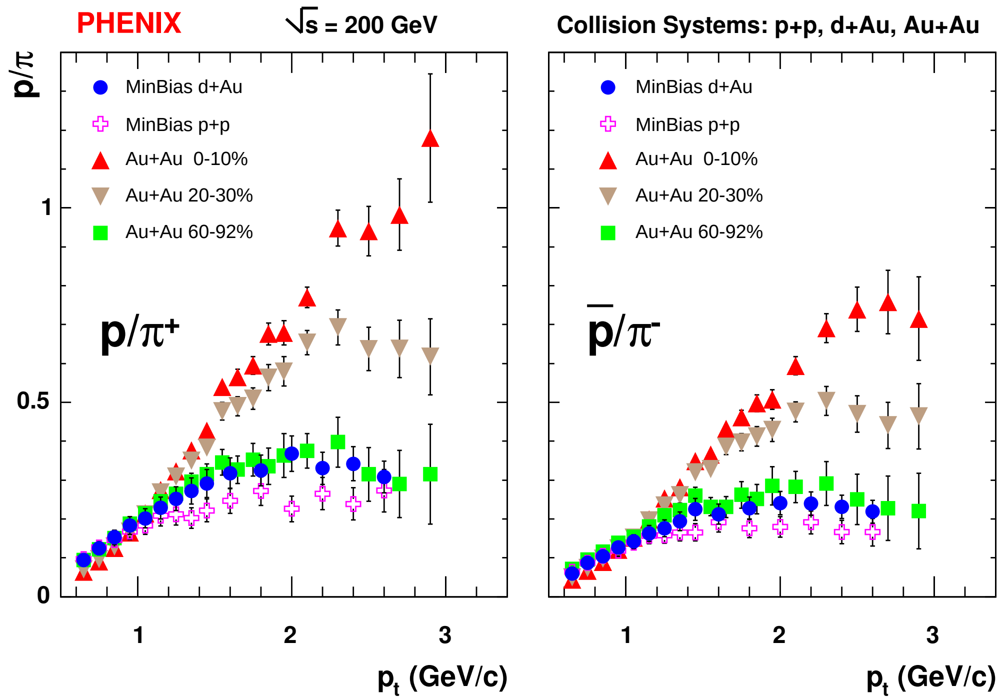

Figure 8.23: Proton to pion ratio in p+p d+Au, and Au+Au. The error bars represent combined statistical and systematic errors.The Au+Au results are from [27].

the kaons in the most central d+Au collisions is evident from this plot, at least for the positive charges.

Our results are in agreement, within the stated errors, with the ratios published by the STAR, PHOBOS and BRAHMS collaborations [94], [95], [96], [97].

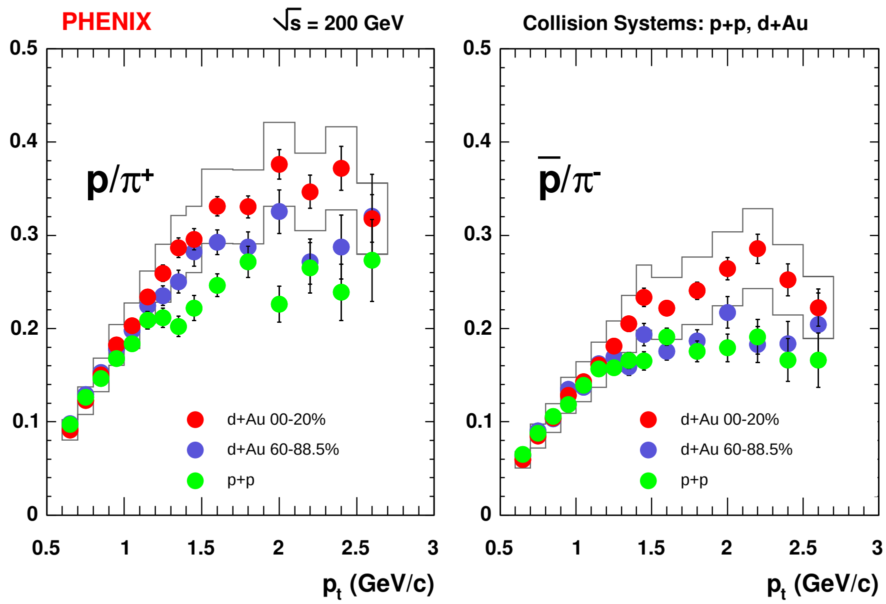

Figure 8.24: Proton to pion ratio in p+p and d+Au. Systematic errors for the most central d+Au ratio are also shown.

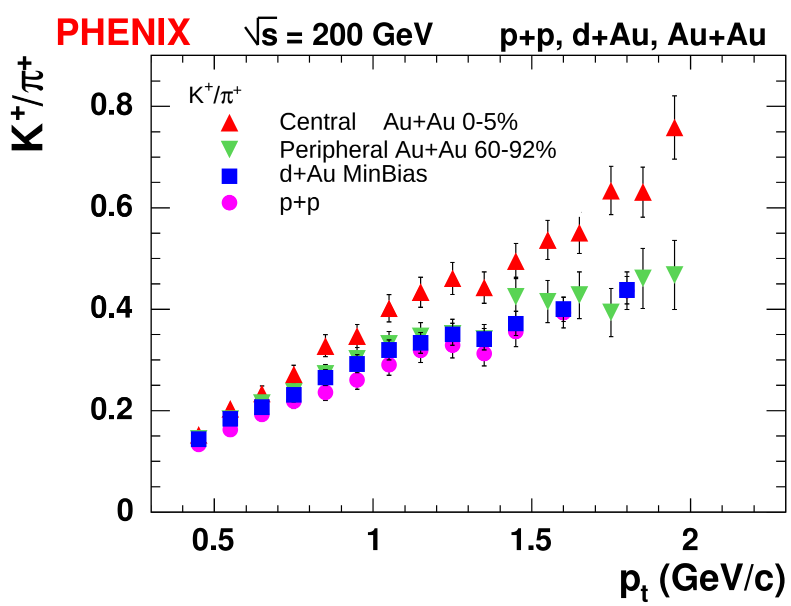

Figure 8.25: Kaon to pion ratio in p+p, d+Au, and Au+Au.

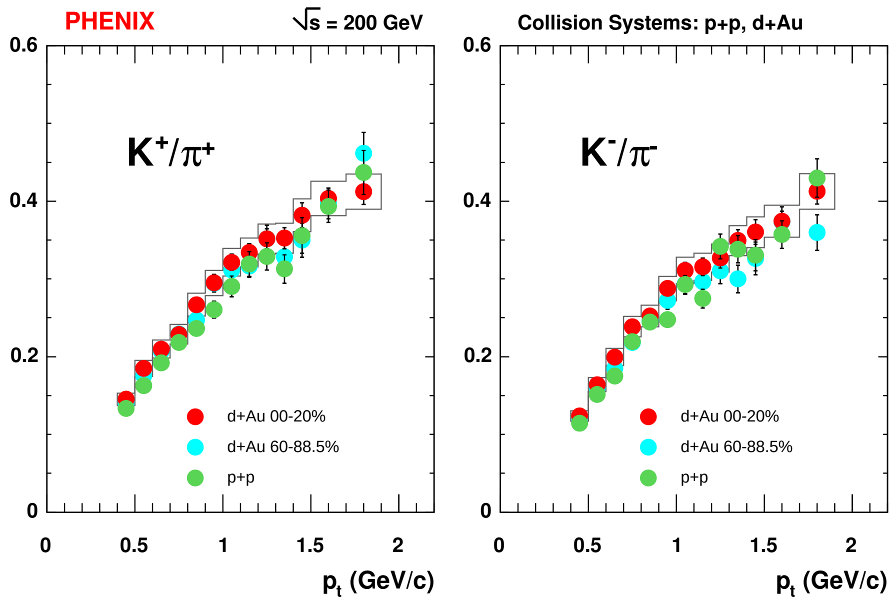

Figure 8.26: Kaon to pion ratio in p+p and d+Au.

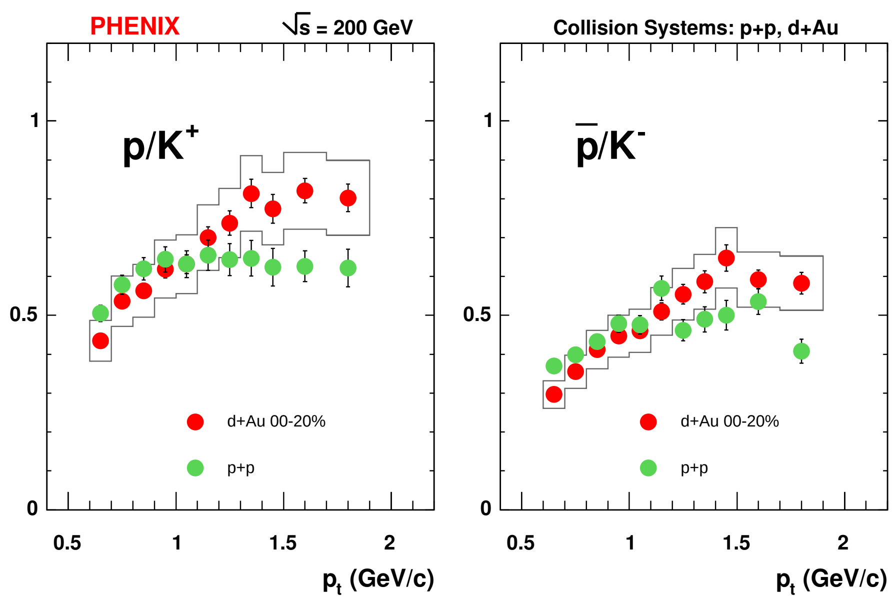

Figure 8.27: Proton to Kaon ratio in p+p and d+Au.

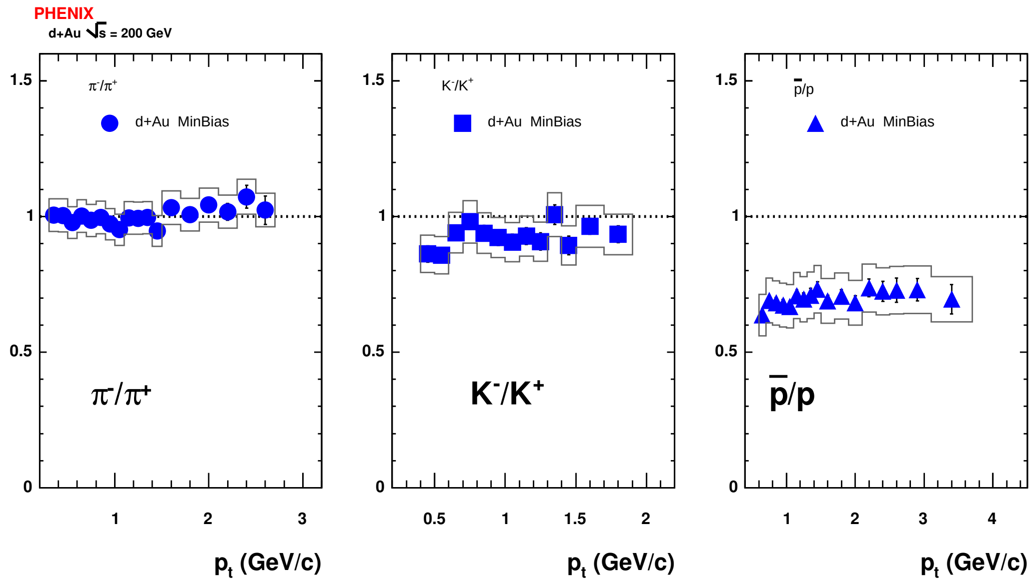

Figure 8.28: Antiparticle to particle ratios for pions, Kaons and protons, in Minimum Bias d+Au, with systematic error bars shown for all ratios.

8.4 Antiparticle to Particle Ratios

In this section we present the antiparticle to particle ratios. From the Au+Au analysis [27], we have seen that these ratios are virtually unchanged going from the most peripheral Au+Au collisions, involving only a handful of binary collisions, to the most central collisions, where the Glauber model calculates more than 1000 nucleon-nucleon collisions. Throughout this range, the antiparticle to particle ratios are flat in p_T, and have the same value, within the error bars.

We present the properties of these ratios now in p+p and d+Au collisions. In Fig. 8.28 we show the corresponding ratios for pions, Kaons and protons in Minimum Bias d+Au. The systematic error bars are also shown in this plot, while they will be suppressed in the following figures due to the clattering of many symbols. In Fig. 8.29 we plot the ratios for the most central and the

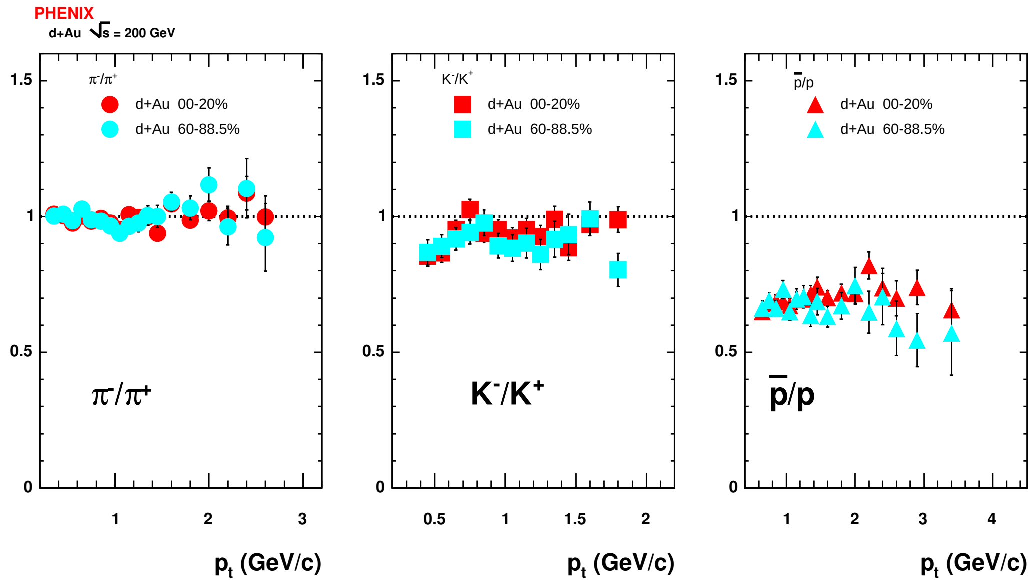

Figure 8.29: Antiparticle to particle ratios for pions, Kaons and protons, in central and peripheral d+Au.

most peripheral d+Au collisions. There is no centrality dependence of these ratios in the d+Au system, within the error bars.

In Fig. 8.30 we show the antiparticle to particle ratios in p+p, and in Fig. 8.31 we compare the p+p and d+Au results. The values of these ratios are shown in Table 8.1.

Table 8.1: Antiparticle to particle ratios in p+p and d+Au. The first error is statistical error, the second is systematic.

ratio	Minimum Bias d+Au	p+p
$\pi^-/\ \pi^+$	0.99±0.01 ±0.06	0.97±0.01±0.06
$K^-/\ K^+$	0.92±0.01±0.07	0.92±0.01±0.07
$\overline{p}/\ p$	0.70±0.01±0.08	0.71±0.01±0.08

In the next two Figures 8.32-8.33 we also include the corresponding Au+Au

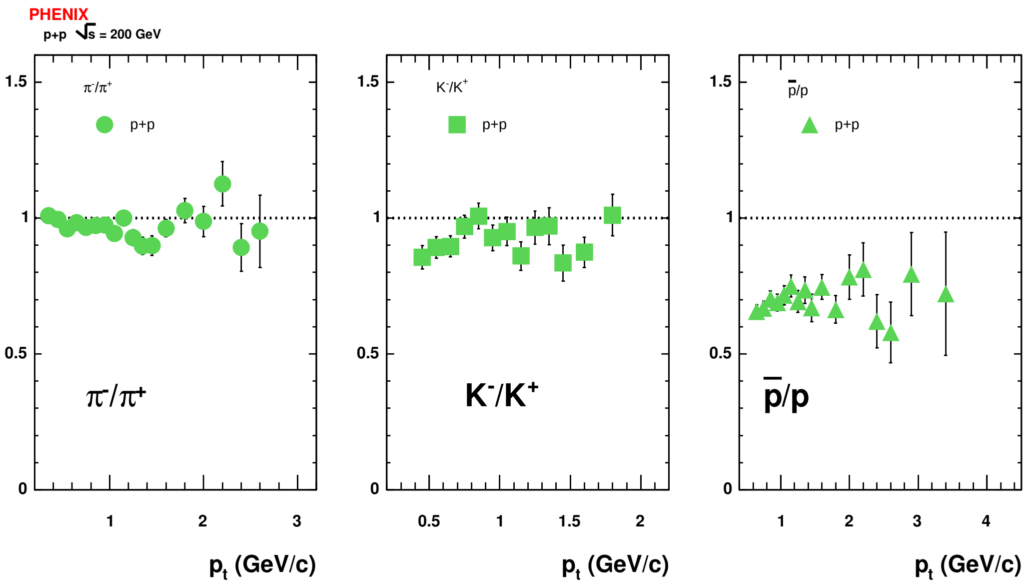

Figure 8.30: Antiparticle to particle ratios for pions, Kaons and protons, in p+p.

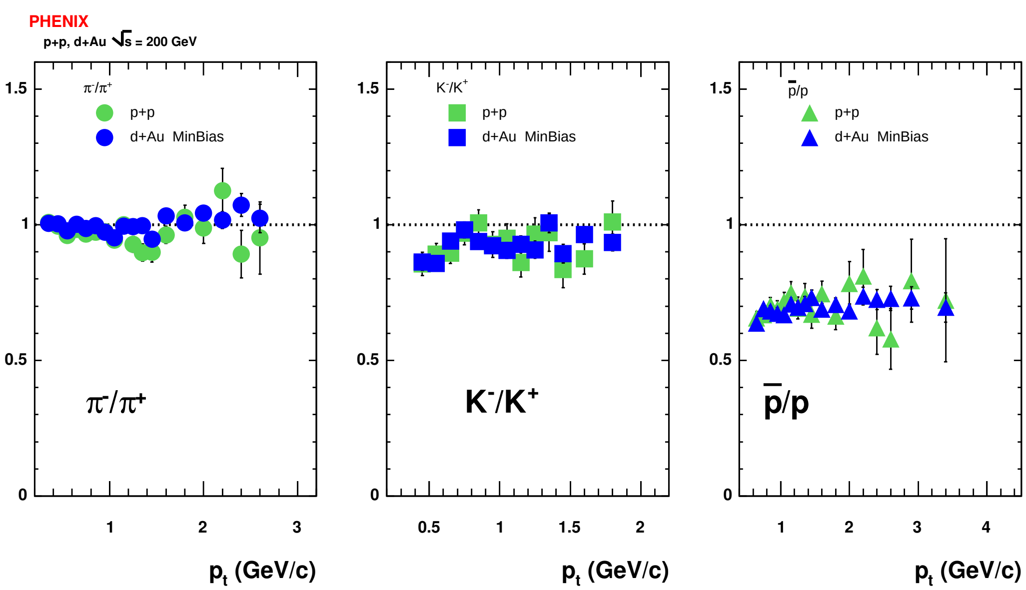

Figure 8.31: Antiparticle to particle ratios for pions, Kaons and protons, in p+p and Minimum Bias d+Au.

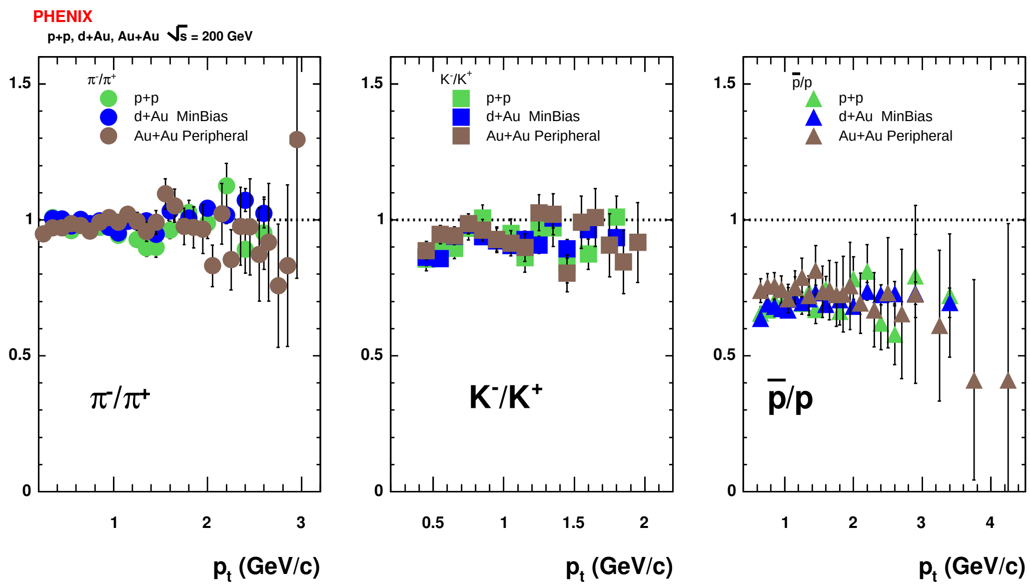

Figure 8.32: Antiparticle to particle ratios for pions, Kaons and protons, in p+p, Minimum Bias d+Au and peripheral Au+Au.

ratios, starting with the most peripheral, and concluding with the most central events.

8.5 Mean p_T and dN/dy

We now turn to particle yields, dN/dy, and average transverse momenta, $\langle p_T \rangle$, in p+p and d+Au collisions, along with a comparison with the Au+Au results from [27]. We plot these quantities as a function of participating nucleons, (N_{part}). In Fig. 8.34 we show the dN/dy values for p+p and d+Au. In Fig. 8.35 we show the dN/dy values for the same systems, divided by the number of participating nucleons, in order to test if the soft particle production scales with N_{part}.

We emphasize that, due to the nature of the steeply falling particle spectra,

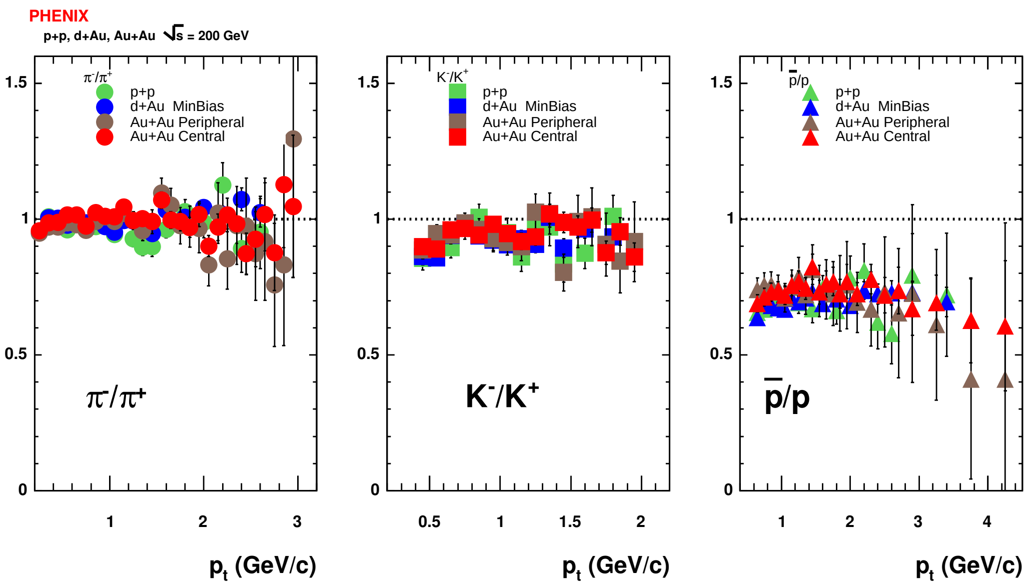

Figure 8.33: Antiparticle to particle ratios for pions, Kaons and protons, in p+p, Minimum Bias d+Au, and, central and peripheral Au+Au.

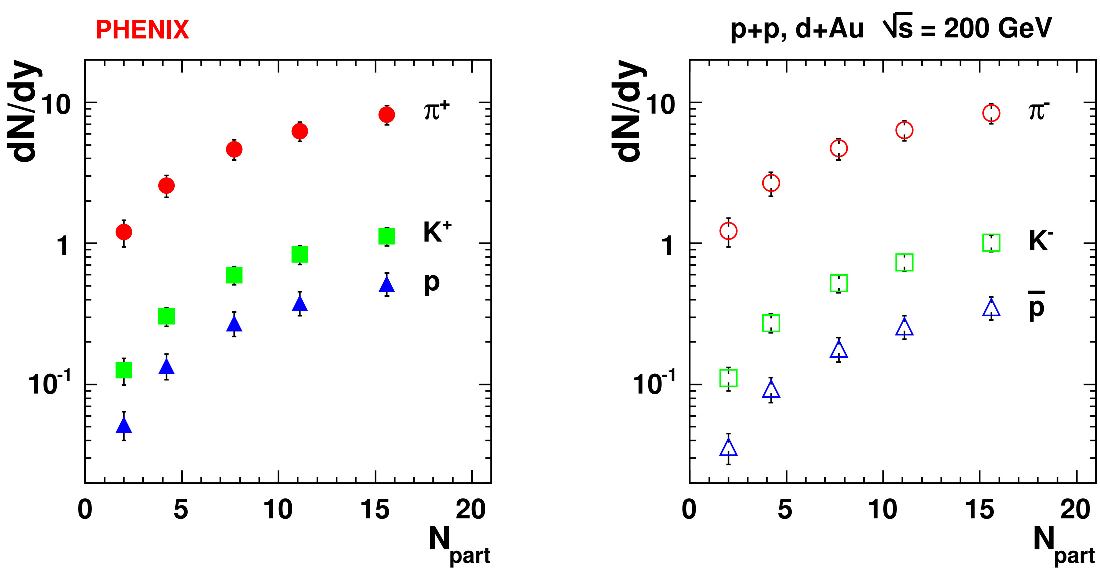

Figure 8.34: dN/dy as a function of the number of participating nucleons in p+p, and d+Au collisions.

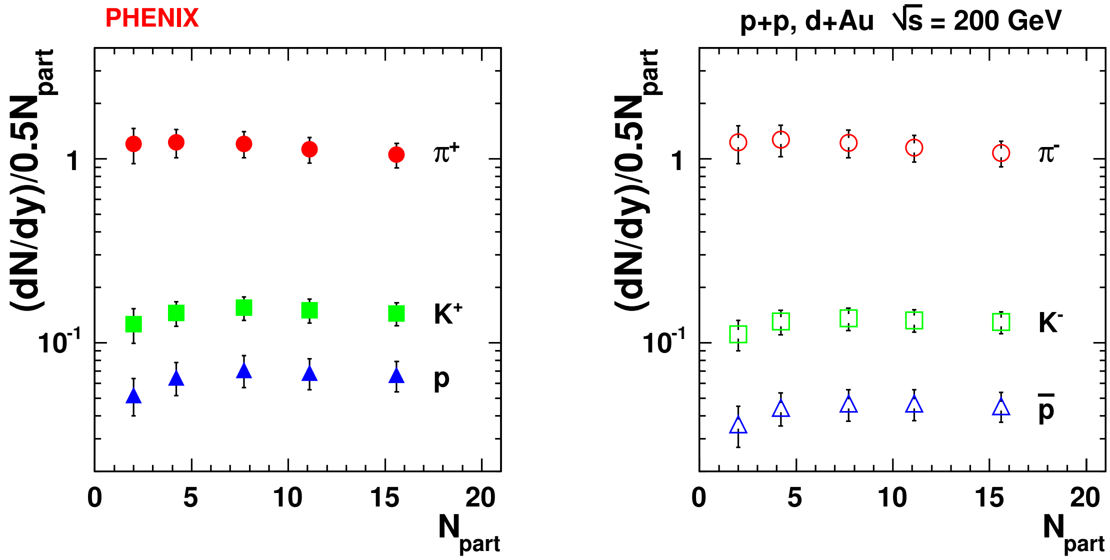

Figure 8.35: dN/dy per participating nucleon, as a function of the number of participating nucleons in p+p, and d+Au collisions.

most of the yield comes from soft particle production, below 1 GeV/c, so the apparent scaling of dN/dy with N_{part} is a property of soft particle production. For higher p_T we have already shown, with the nuclear modification factors, that point-like processes should scale with the number of binary collisions, in the absence of any nuclear effects.

In Fig. 8.36 we present $(dN/dy)/N_{part}$ results for all three colliding systems, and in Fig. 8.37 we plot a zoomed-in version of the previous figure, for a closer look at the limiting behavior of the Au+Au system towards more peripheral events, when the number of participating nucleons approaches the d+Au and p+p values.

In Fig. 8.38 we show the average transverse momenta in p+p and d+Au collisions. In Fig. 8.39 we also include the Au+Au result, and we also show a

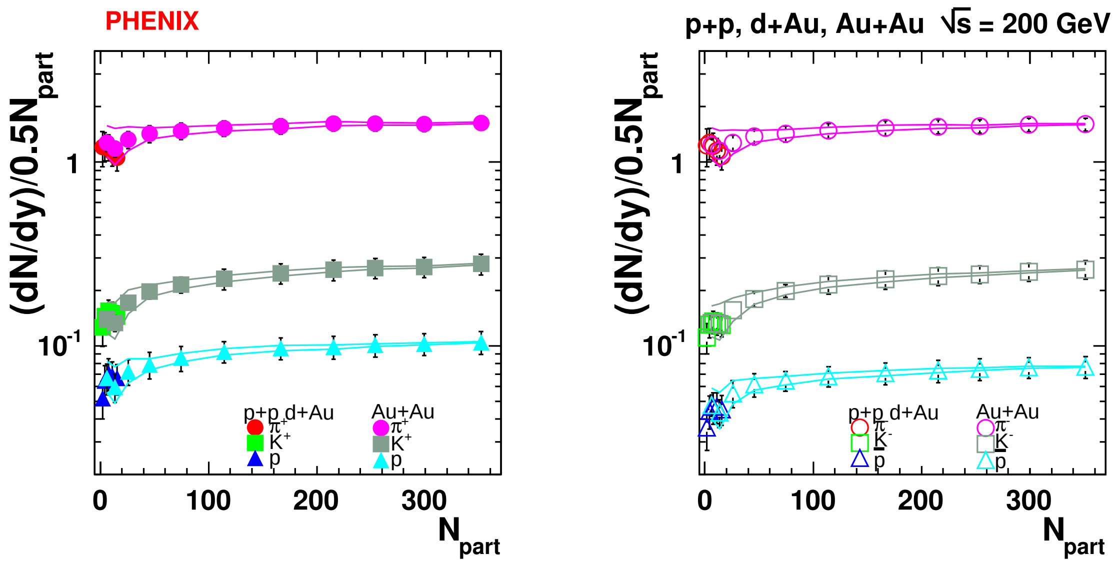

Figure 8.36: dN/dy per participating nucleon, as a function of the number of participating nucleons in p+p, d+Au, and Au+Au collisions.

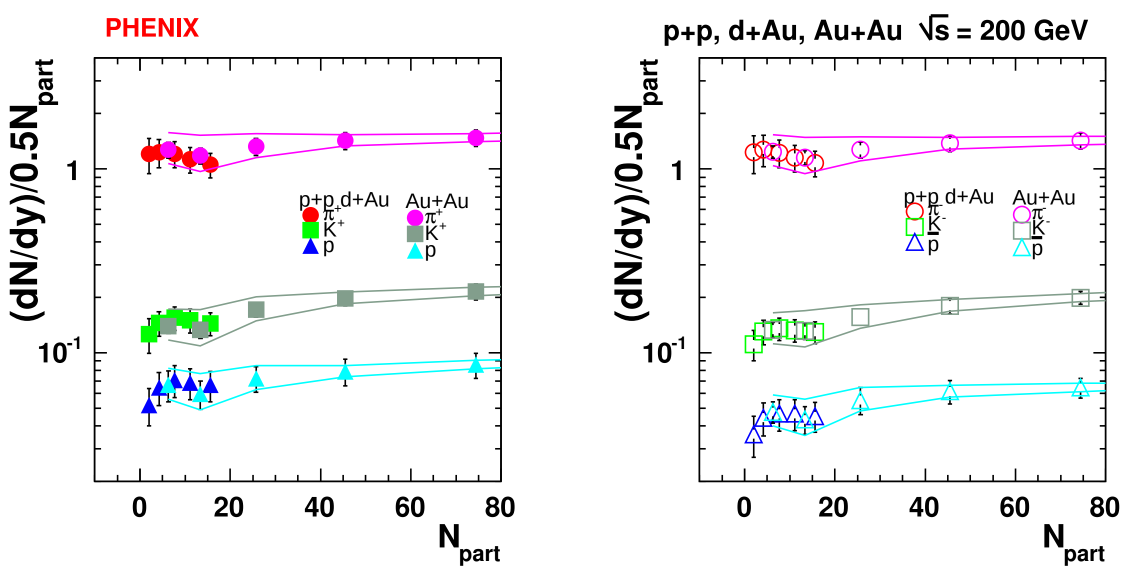

Figure 8.37: dN/dy per participating nucleon, as a function of the number of participating nucleons in p+p, d+Au, and Au+Au collisions. Only mid-peripheral to peripheral Au+Au centralities are shown.

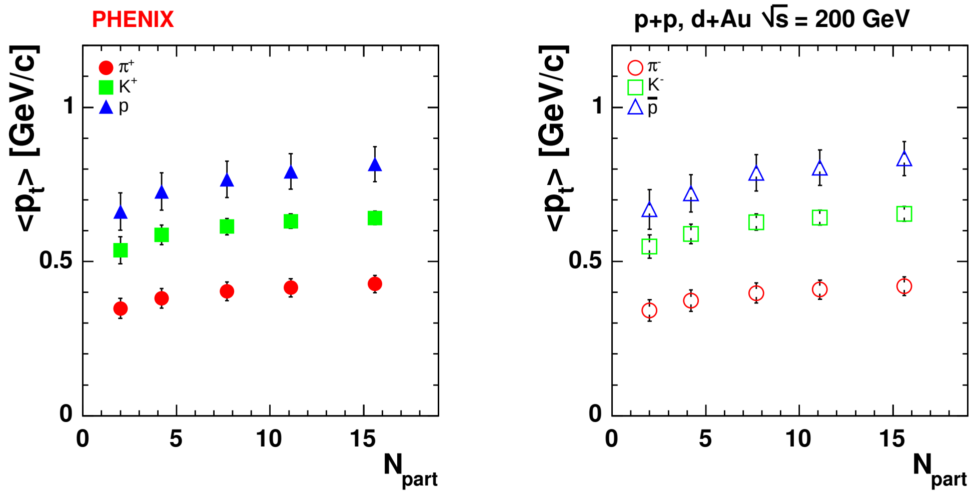

Figure 8.38: Mean p_T as a function of the number of participating nucleons in p+p and d+Au collisions. Combined statistical and systematic errors are shown.

zoomed-in version of this plot in Fig. 8.40. The p+p and d+Au values of $\langle p_T \rangle$ appear to be slightly higher than the most peripheral Au+Au values, but due to the large systematic errors we can not make a conclusive statement about this difference at the moment.

Finally we present in Fig.8.41 the $\langle p_T \rangle$ values for all three colliding systems and for all particle species, as a function of particle mass. A clear evolution from the p+p system to d+Au and then central Au+Au is clear from this figure, in particular for the heavier protons. The high average transverse momentum in the central Au+Au collisions is attributed to the radial flow of the system that affects heavier particles the most.

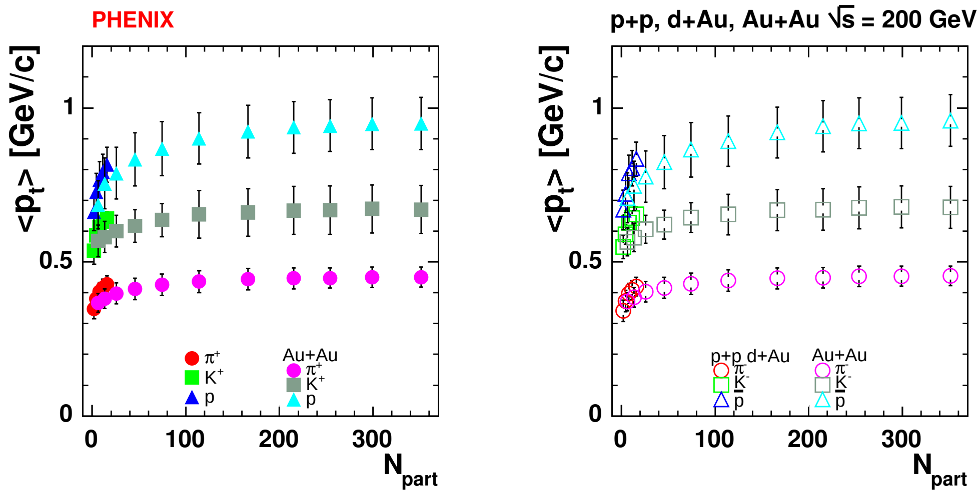

Figure 8.39: Mean p_T as a function of the number of participating nucleons in p+p d+Au and Au+Au collisions. Combined statistical and systematic errors are shown.

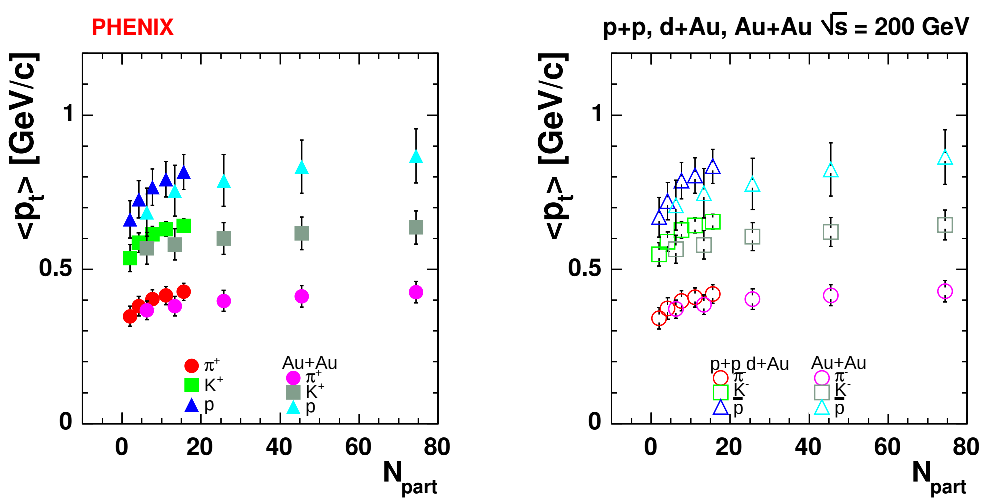

Figure 8.40: Mean p_T as a function of the number of participating nucleons in p+p d+Au and Au+Au collisions. Only mid-peripheral to peripheral Au+Au centralities are shown. Error bars are combined statistical and systematic errors.

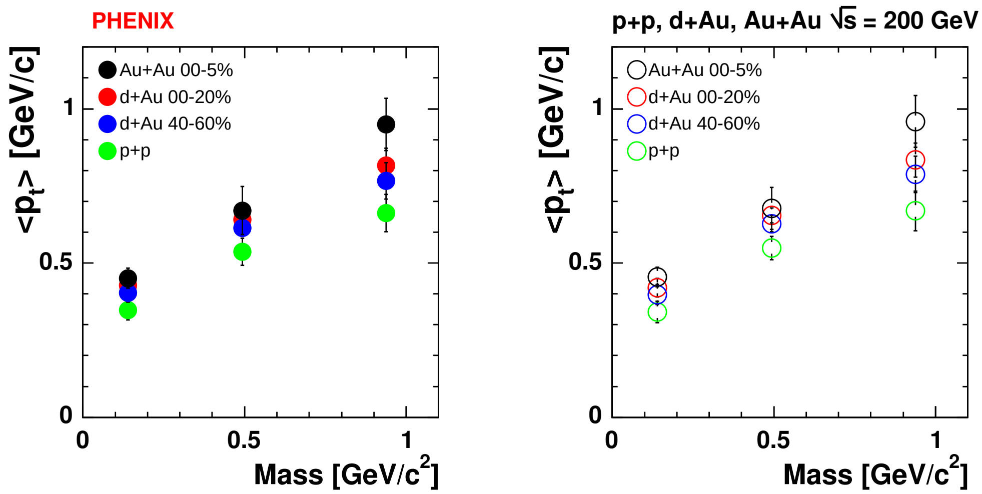

Figure 8.41: Mean p_T as a function of particle mass, in p+p d+Au and Au+Au collisions.

Chapter 9

Discussion and Conclusions

9.1 It's Good To Be The Experimentalist.

To paraphrase Mel Brooks in the "History of the World, Part I" [79], it's good to be an experimentalist in our field these days. The RHIC collider in its four years of operation has provided us with a wealth of data, as is evident from this thesis, that puts the experimentalists in a unique position. We are able to make significant statements about the behavior of nuclear matter, in the broadest range of conditions, based, for the large part, on the collected experimental data.

We are in a position to paint a cohesive picture of particle production in p+p, d+Au, and Au+Au collisions, and impose very strong boundaries for the theory that will integrate all these experimental observations. We proceed now in answering the questions that were put forth in the opening chapter of this thesis.

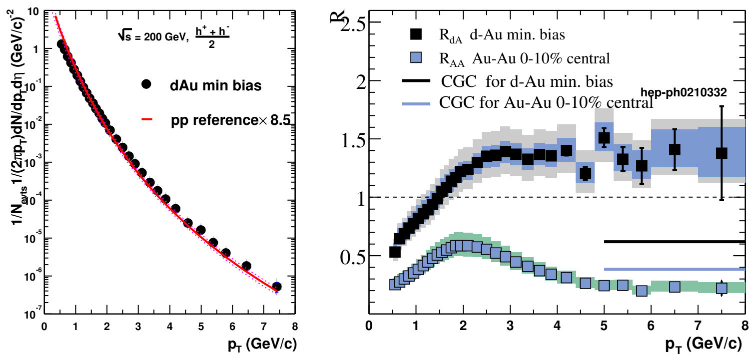

Figure 9.1: Nuclear modification factor for inclusive hadrons in d+Au collisions from [80]. Left panel shows the inclusive hadron spectrum along with the p+p reference.

9.1.1 Enhancement or Suppression in d+Au ?

Obviously we do not observe any suppression in d+Au collisions at intermediate and high p_T, at least at the central rapidity window that PHENIX is located, $|\eta| < 0.35$. The nuclear modification factors in d+Au, as shown in Fig. 8.15, are at, or above, 1, for all particle species, for all centralities. Saturation scenarios will have to be probed at more forward rapidities, where the x-values of the probed partons may perhaps reach the saturation scale (which is still a matter of theoretical investigation).

The observation of absence of suppression in d+Au collisions that we observe with the identified analysis in this thesis, Fig. 8.15, was first observed in the inclusive hadron and neutral pion measurements, in PHENIX [80] (Fig. 9.1), and the rest of the RHIC experiments [81–83] . The impact of this discovery was so important, that first publications of this topic from the RHIC experiments, made the cover of the Physical Review Letters. The identified analysis followed soon this remarkable result, that proved, without any doubt, that the suppression observed in central Au+Au collisions is not an ini-

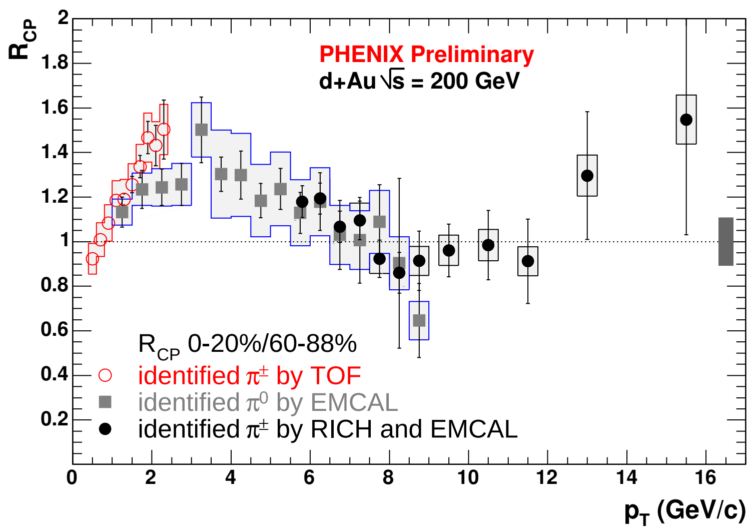

Figure 9.2: Central to peripheral nuclear modification factor for charged and neutral pions in d+Au collisions measured by three PHENIX subsystems from [84], [85] and [86].

tial state effect, but rather, a final state effect that originates from a genuine energy loss of fast partons inside the hot and dense nuclear medium [1].

Another demonstration on the absence of suppression, from very low p_T up to the highest p_T value obtained at any RHIC experiment thus far, is shown in Fig. 9.2. In this plot we present preliminary results for the central-to-peripheral nuclear modification factor, R_{CP}, of identified pions, made by three different PHENIX subsystems. Identified charged pions are from this analysis, using the TOF detector [84], neutral pions from the PHENIX EMCAL [85] , and charged pions at very high p_T from the Ring Imaging Cerenkov detector [86] (pions above 4.5 GeV/c in p_T exceed the $\gamma \sim 35$ threshold of the RICH detector). This plot was one of the highlights at the 17th International Con-

[1]The author of this thesis will always cherish the official announcement of this result, made jointly by all RHIC experiments, at the Large Seminar Room at Brookhaven. It was his adviser that was chosen to announce the discovery, on behalf of the PHENIX collaboration, to the physics community and the press.

ference on Ultra Relativistic Nucleus-Nucleus Collisions (Quark Matter 2004), due to the consistency of the result, measured by three completely independent analyses, with three different detectors, and due to its unprecedented p_T range.

9.1.2 Species Dependence of Cronin Effect in d+Au

As we have presented in Fig. 8.15, there is a clear species dependence on the size of the Cronin effect. For the Minimum Bias d+Au collisions, the nuclear modification factor for the Kaons seems to saturate around 1, while the pions seem to have around 10% enhancement relative to binary scaling, above p_T~1.5 GeV/c. More specifically, a fit to the Minimum Bias R_{dAu} for the pions gives $R_{dAu} = 1.13 \pm 0.03(stat)$, $p_T > 2.0\ GeV/c$, while for the most central bin we have: $R_{dAu} = 1.17 \pm 0.04(stat)$, $p_T > 2.0\ GeV/c$.

The protons and antiprotons though are clearly more enhanced. A fit to the Minimum Bias R_{dAu} for the combined protons and antiprotons gives $R_{dAu} = 1.43 \pm 0.04(stat)$, $p_T > 1.6\ GeV/c$, while for the most central bin we have: $R_{dAu} = 1.56 \pm 0.04(stat)$, $p_T > 1.6\ GeV/c$. This is a pattern that was known already from the lower energy data [6], and as we have shown, it is also present at $\sqrt{s}$ =200 GeV (we will the energy dependence of this asymmetry at a later section). This observation is of fundamental importance as we discuss in the next section.

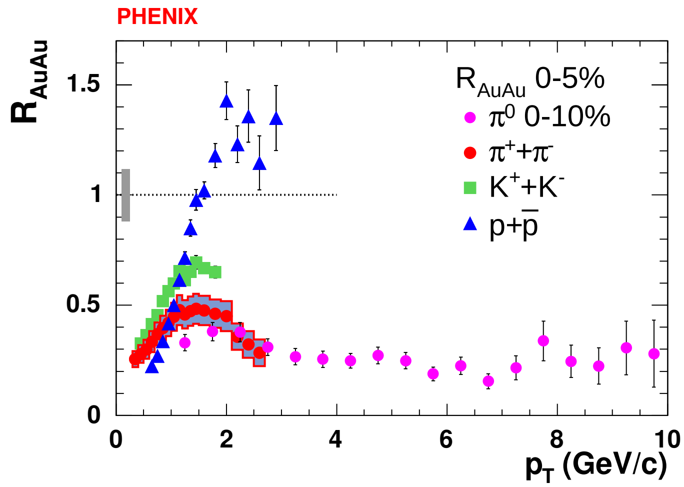

Figure 9.3: Nuclear modification factors for identified particles, R_{AuAu}, for the most central Au+Au centrality bin, 00-05%. Neutral pions are also shown from [26]. Note that the nuclear modification factor for the neutral pions is from the 00-10% bin.

9.1.3 Enhancement versus Suppression in Au+Au

Armed with this information we are now in a position to answer one of the fundamental questions posed by the identified Au+Au analysis [28], namely, can the observed asymmetry in the suppression of pions and protons in central Au+Au collisions be attributed to initial state conditions ? The answer is no. From Fig. 9.3, and, as was discussed in detail in [26], for the most central Au+Au events, the suppression factor for pions is ∼2.5 at p_T=2 GeV/c, and increases to ∼4-5 at p_T=4 GeV/c. Our identified p+p measurement provides for the first time the denominator for the proton and antiproton R_{AuAu}, and, as can be seen from Fig. 9.3, and from a fit to the data, we have $R_{AuAu} = 1.26 \pm 0.04(stat)$, $p_T > 1.6\ GeV/c$. We therefore see that the pions are suppressed relative to the protons almost by a factor of 6, at p_T∼3 GeV/c. On the other hand, from the d+Au data we measured an asymmetry between protons and pions of the order of $\sim 30\%$. We conclude therefore that initial state effects can not account for the large asymmetry between pions and protons in central Au+Au collisions. The origin of this fundamentally different behavior must be searched elsewhere.

Furthermore, we see from Fig. 9.4 that the proton R_{AuAu} for central and peripheral Au+Au collisions, have basically collapsed into a universal R_{AuAu} value , around 1.3 for $p_T > 1.6\ GeV/c$ as stated earlier. On the other hand, the Minimum Bias proton R_{dAu} appears to be higher, although, of course, not outside the systematic errors of the data. Nevertheless we can make a qualitative statement. It appears that the collisional scaling of the protons in Au+Au is accidental, in the sense that the Au+Au data do not saturate at the d+Au value, which is the result of the cold nuclear matter on proton production. It seems that there must be a novel microscopic mechanism for proton and antiproton production in Au+Au collisions that accidentally lands the nuclear modification factors at around 1.3, having nothing to do with the microscopic mechanism of the Cronin effect in d+Au. Why this novel mechanism appears to have an approximate collisional scaling at intermediate p_T is something that must be closely investigated by the theory.

9.1.4 The Return of Particle Ratios to Normal Values (some ratios always stayed normal though)

The anomalous proton to pion ratio in central Au+Au collisions took the community by surprise. It escaped every theoretical prediction of QGP signatures,

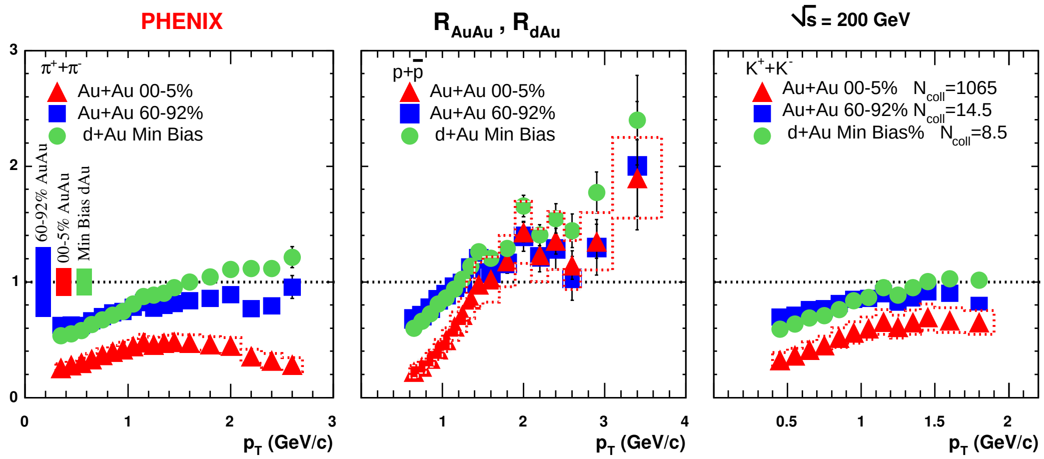

Figure 9.4: Nuclear modification factors for identified particles in Minimum Bias d+Au, and, central and peripheral Au+Au collisions.

and, if Isidor Rabi were around, he would have certainly repeated his famous question : "Who ordered that ?".

Certainly not the p+p nor the d+Au data. The proton to pion ratio smoothly decreases with centrality in Au+Au collisions as is shown in Fig. 9.5, and the corresponding d+Au ratio simply verified the result of the most peripheral Au+Au centrality bin. We conclude therefore that cold nuclear matter effects at these energies have nothing to do with the anomalous p/π ratio. On the other hand, the proton to pion ratio in p+p collisions seem to be somewhat lower, a manifestation of the larger Cronin effect of the protons compared to pions. The anomalous p/π ratio seems to indicate our poor understanding of the hadronization process. In the suppression scenarios for pions with p_T>2 GeV/c, the pions are treated as the result of fragmentation of hard scattered quarks and gluons. As was stated in [11], the explanation of this suppression in terms of partonic energy loss assumes that the hadronic wave-function

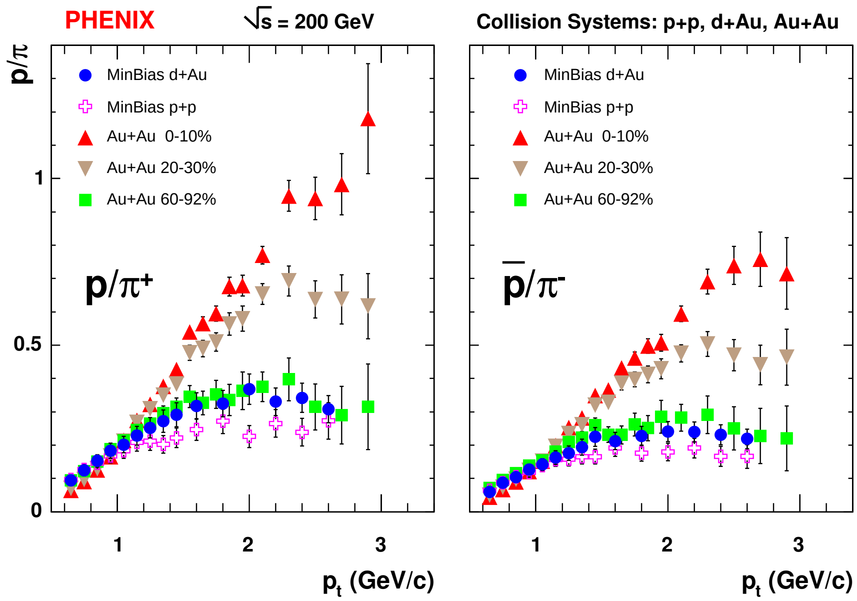

Figure 9.5: Proton to pion ratio in p+p d+Au, and Au+Au. The error bars represent combined statistical and systematic errors.The Au+Au results are from [27].

only becomes coherent outside the medium. It appears then that protons , with their larger mass and different hadronic structure, may have a different, shorter, time scale for coherence.

The formation time for a 2.5 GeV/c pion according to the uncertainty principle [102], is approximately 9-18 fm/c, well outside the medium, while for a proton of the same energy, the corresponding formation time is only 2.7 fm/c, suggesting that the hadronization process may begin inside the medium. Certainly, this is at the heart of recombination models [34] which seem to successfully explain the anomalous proton to pion ratio, but still lack a universal description of relativistic heavy ion collisions. It is possible that differing interactions with the medium may produce different scaling for proton and

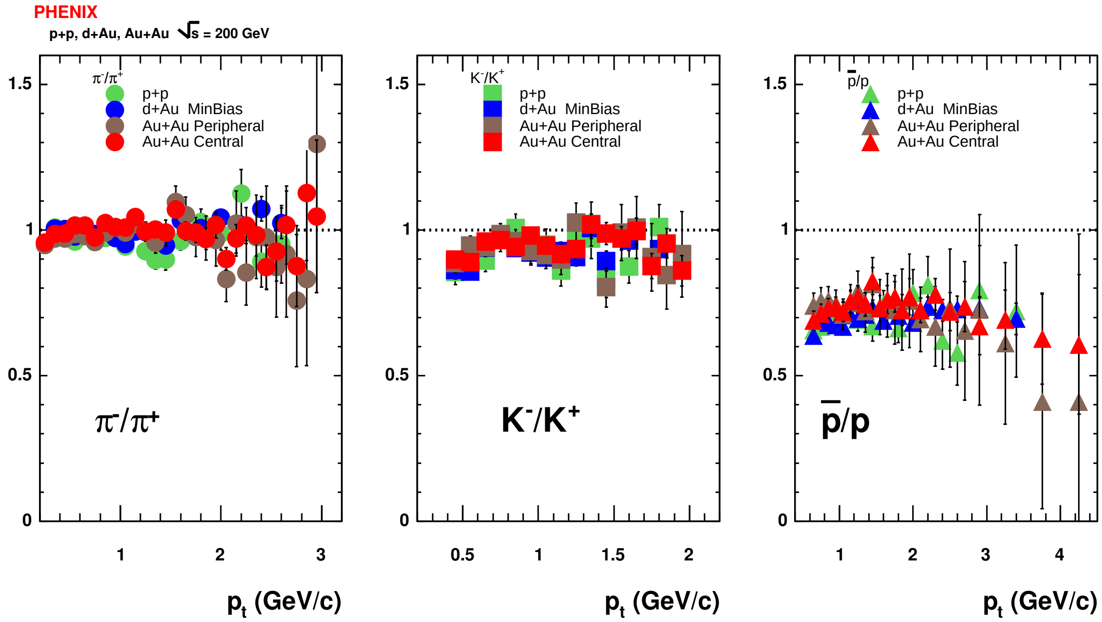

Figure 9.6: Antiparticle to particle ratios for pions, Kaons and protons, in p+p, Minimum Bias d+Au, and, central and peripheral Au+Au.

pion production, and, therefore, result in modified fragmentation functions for Au+Au collisions.

One of the most important results of this work will help enormously our input in the formulation of fragmentation scenarios, such as the above. As we presented in Fig. 9.6, the antimatter to matter ratios, for all species, in p+p and d+Au collisions have virtually the same value as in Au+Au collisions. Already from the Au+Au result it was known that there is little, if any, centrality dependence of these ratios, but now we are in a position to state that these ratios have the same value with the corresponding ratios arising from the most elementary hadronic collisions. This behavior remains a mystery. The fact that the antiproton to proton ratio measured in the hottest nuclear matter ever created in the laboratory, has the same value as in elementary p+p collisions is astonishing. Despite the fact that completely different microscopic mechanisms seem to be responsible for particle production in central Au+Au and p+p collisions, at the end of the day, they are all under the constraint of keeping these ratios constant.

In addition, these ratios are independent of p_T. Despite the fact that even at RHIC energies we do not have a baryon-free system at mid-rapidity, and hence a significant amount of protons is still being transported from the beam nuclei, still, the proton spectra have the exact same shape as the antiprotons. Perhaps, further re-scattering smooths out the created and transported spectra, but that remains to be proved.

9.1.5 Energy Dependence of the Cronin Effect

The power-law parameterization of proton-nucleus cross sections in the original papers by J.W. Cronin and collaborators [5], [6], enables us to calculate the p+Au cross section at lower energies. Furthermore, using some basic assumptions, we can calculate the per nucleon d+Au cross section at these energies, which is equivalent to the nuclear modification factors in d+Au from this work, at RHIC energies.

This is an important comparison. The heavy ion programme at the lower energy CERN-SPS ($\sqrt{s}$~20 GeV), which claimed, for the first time, the discovery of a new state of matter in heavy ion reactions, never observed any type of suppression, for any particle species. For a long time this was attributed to a large Cronin effect at these energies, and it therefore becomes important to have a handle of how different the size of the effect is at RHIC energies.

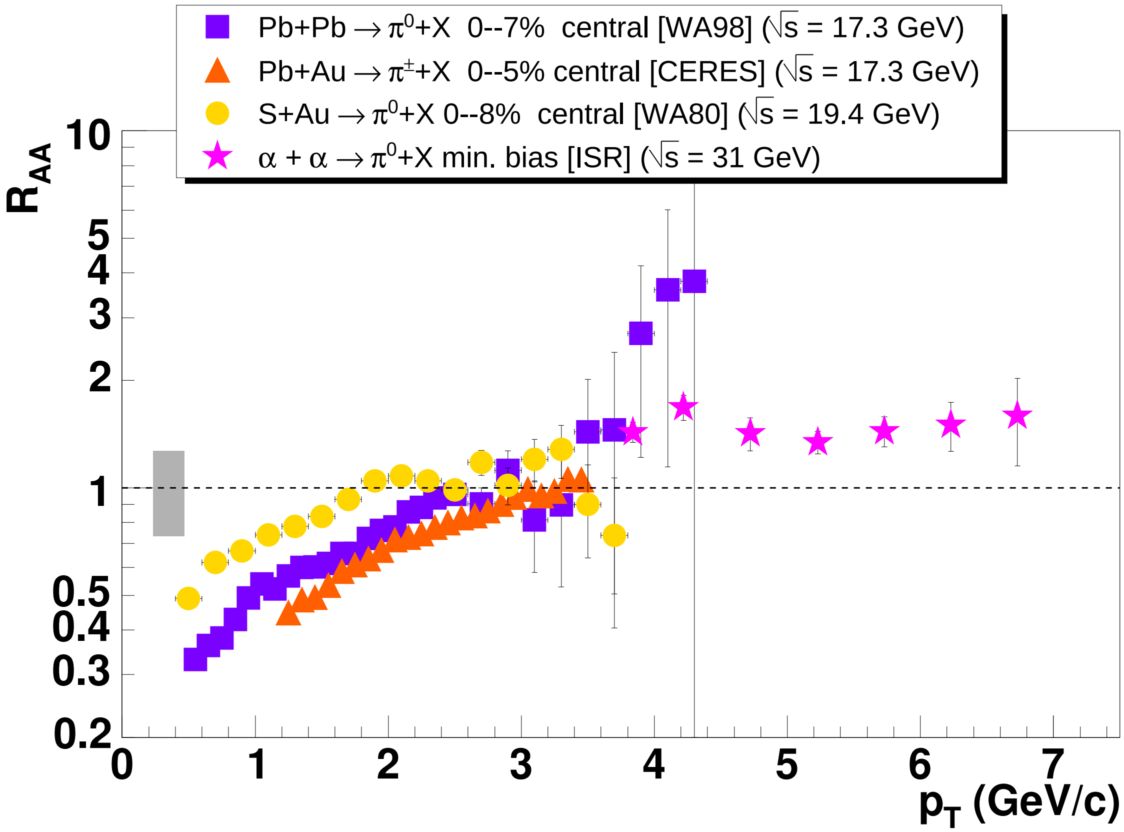

Figure 9.7: Nuclear modification factors for neutral pion production at the CERN-ISR in minimum-bias $\alpha+\alpha$ reactions at $\sqrt{s_{NN}} = 31$ GeV [107] and for pion production at the CERN-SPS in central Pb+Pb [105], Pb+Au [108], and S+Au [106] reactions at $\sqrt{s_{NN}} \approx 20$ GeV. The R_{AA} from SPS are obtained using the p+p parametrization proposed in [103]. The shaded band around $R_{AA} = 1$ represents the overall fractional uncertainty of the SPS data (including in quadrature the 25% uncertainty of the p+p reference and the 10% error of the Glauber calculation of N_{coll}). There is an additional overall uncertainty of $\pm 15\%$ for the CERES data not shown in the plot [108].

Recently, the absence of suppression in the CERN-SPS data has been revisited by D'Enterria [103]. In this paper the author claims that a poor knowledge of the baseline p+p spectra may have been the reason for missing the suppression at SPS. Even with the new reanalysis of the data, the effect appears to be marginal, but still, the old picture of a large enhancement appears not to be valid anymore, as seen in Fig 9.7.

Starting from the the power-law parameterization of proton-nucleus cross sections

$$I_i(p_T, A) = I_i(p_T, 1) \cdot A^{a_i(p_T)} \tag{9.1}$$

where I_i denotes the invariant cross section and the index i refers to the particle species produced, we can extrapolate the p+A cross section, for any nucleus, at lower energies, assuming that we know the $\alpha_i(p_T)$ factors for each particle species, at the energy of interest.

We can then write the ratio of any proton-nucleus cross sections, for example, pW-to-pBe, as

$$\frac{E\dfrac{d\sigma^{pW}}{dp^3}}{E\dfrac{d\sigma^{pBe}}{dp^3}} = \frac{A_W^{a_i(p_T)}}{A_{Be}^{a_i(p_T)}} \tag{9.2}$$

and then trivially, the per-nucleon cross section ratio, $R_{W/Be}$, becomes

$$\frac{E\dfrac{d\sigma^{pW}}{dp^3}/A_W}{E\dfrac{d\sigma^{pBe}}{dp^3}/A_{Be}} = (\frac{A_W}{A_{Be}})^{a_i(p_T)-1} = R_{W/Be} \tag{9.3}$$

We now turn to the $\alpha_i(p_T)$ factors. Antreasyan *et al* in [6], measured identified particle production in p+p and p+d, p+Be, p+Ti and p+W collisions, in three different energies, and, with a fitting procedure, calculated $\alpha(p_T)$ factors for pions, kaons, protons and antiprotons. The $\sqrt{s} = 27.4$ GeV measurement has high enough statistics, for all particle species, in a wide p_T range and for that reason we are going to compare our results with results at this energy. Similar comparisons were done by Straub *et al* [7], where they compare the $R_{W/Be}$ ratio that they measured at $\sqrt{s} = 38.8$ GeV with the Antreasyan *et al* result [6], through the use of α factors. We show this comparison in Fig. 9.8.

From this Fig. 9.8 we notice a few interesting things. First of all , for the first time, we see the experimental observation of the decrease of the Cronin effect as a function of energy. Second, we note the size of the species-dependence of the effect. The protons and antiprotons exhibit a "gigantic" enhancement at these low energies, almost by a factor of 3, and even more, at a peak p_T around 5 GeV/c.

We now turn to the d+Au case. Similar to the $R_{W/Be}$ ratio, we can define the per-nucleon cross section ratio for d and Au, $R_{Au/d}$, as:

$$\frac{E\dfrac{d\sigma^{pAu}}{dp^3}/A_{Au}}{E\dfrac{d\sigma^{pd}}{dp^3}/A_d} = (\frac{A_{Au}}{A_d})^{a_i(p_T)-1} = R_{Au/d} \tag{9.4}$$

From [6] we make an interesting observation: the p+d cross section is twice the size of the p+p cross section, $\sigma^{pd} \sim 2 \cdot \sigma^{pp}$, within the systematic errors (this is a measurement not an assumption). Inspired by this fact, we now make the assumption that the d+Au cross section is approximately twice the size of the p+Au cross section, and therefore, $R_{Au/d}$ can be rewritten as

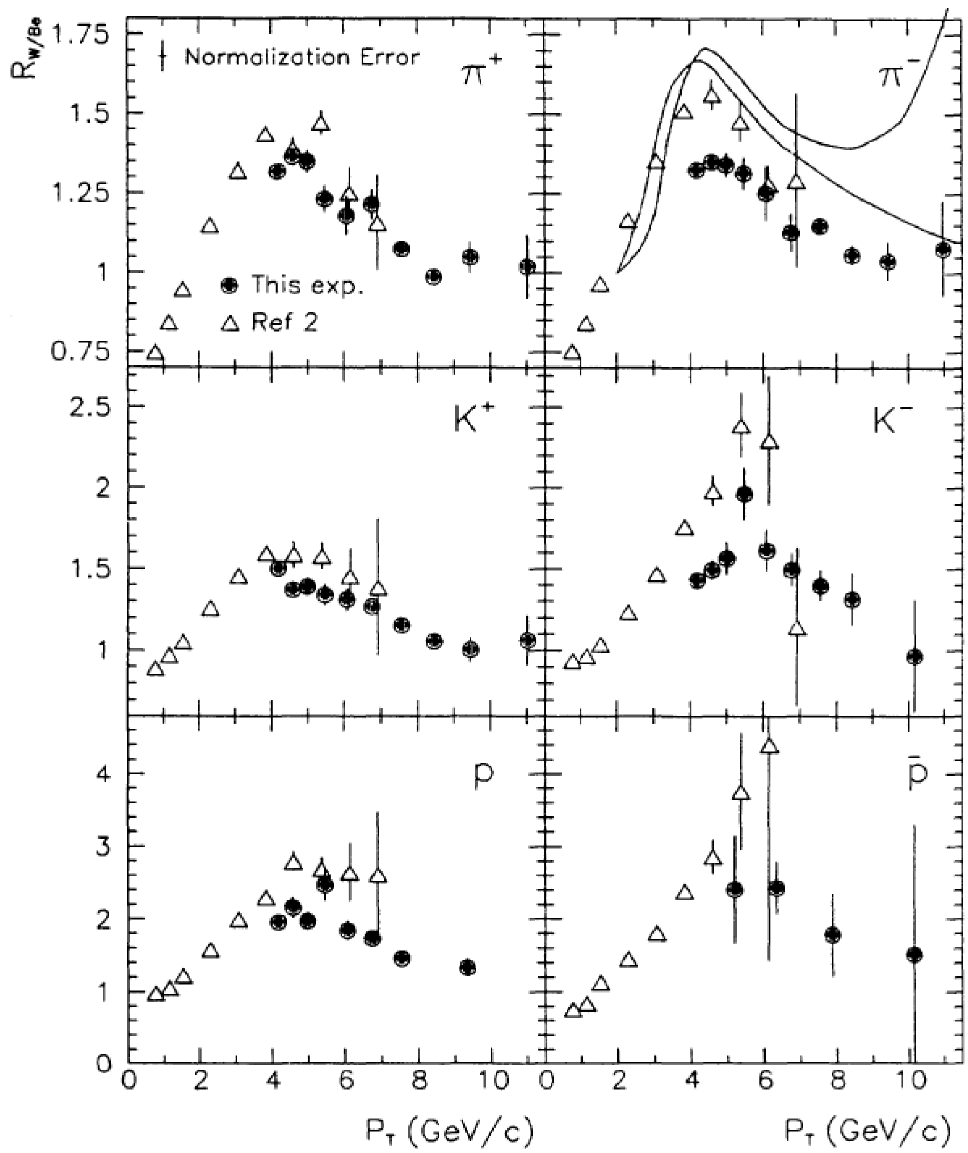

Figure 9.8: W-to-Be ratio of per-nucleon cross sections, $R_{W/Be}$ vs p_T for each hadron species at $\sqrt{s} = 38.8$ GeV from [7] . Also shown are results from [6] at $\sqrt{s} = 27.4$ GeV and model calculations [109] for π^- at $\sqrt{s} = 27.4$ GeV (upper curve) and $\sqrt{s} = 51.3$ GeV (lower curve).

$$
\begin{aligned}
R_{Au/d} &= \frac{E\dfrac{d\sigma^{pAu}}{dp^3}/A_{Au}}{E\dfrac{d\sigma^{pd}}{dp^3}/A_d} && (9.5)\\
&\simeq \frac{\dfrac{1}{2}\times E\dfrac{d\sigma^{dAu}}{dp^3}/A_{Au}}{2\times E\dfrac{d\sigma^{pp}}{dp^3}/A_d} && (9.6)\\
&= \frac{(\dfrac{d\sigma^{dAu}}{dp^3})}{4\cdot\dfrac{A_{Au}}{A_d}(\dfrac{d\sigma^{pp}}{dp^3})} && (9.7)\\
&= \frac{(\dfrac{d\sigma^{dAu}}{dp^3})}{A_{Au}\,A_d(\dfrac{d\sigma^{pp}}{dp^3})} && (9.8)\\
&\equiv R_{dAu} && (9.9)
\end{aligned}
$$

which is nothing more than the nuclear modification factor in d+Au. We finally have that under these assumptions,

$$
R_{dAu} \simeq R_{Au/d} = (\frac{A_{Au}}{A_d})^{a_i(p_T)-1} \tag{9.10}
$$

and therefore we can calculate the identified nuclear modification factors in d+Au collisions at $\sqrt{s} = 27.4$ GeV, by using the $\alpha(p_T)$ factors for pions, kaons, protons and antiprotons from [6], measured at this energy . We show our calculation in Fig. 9.9.

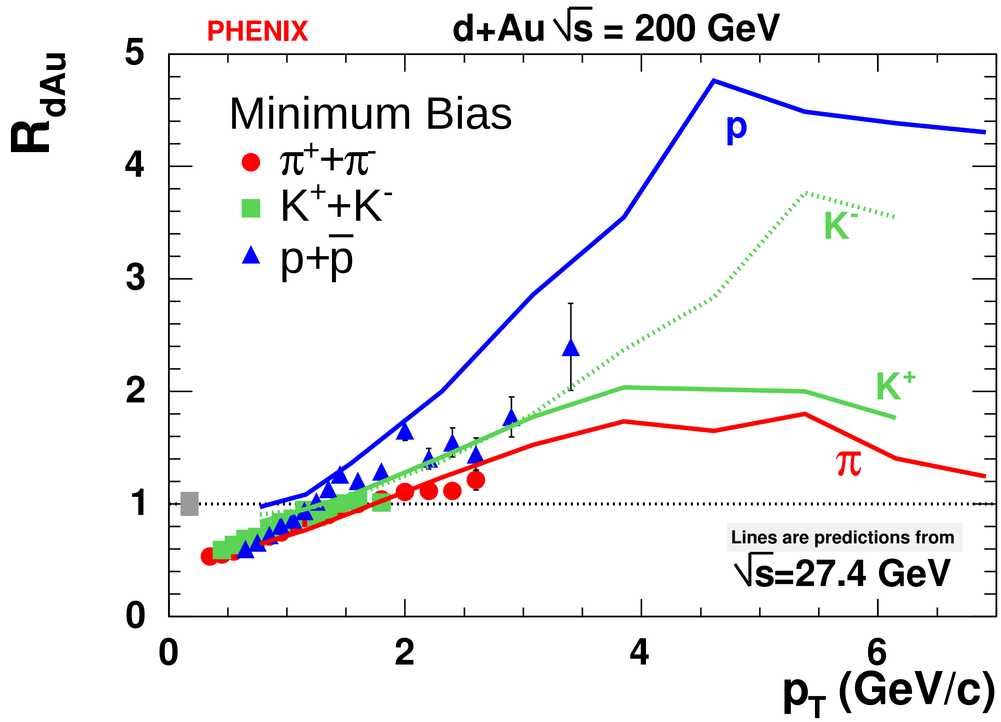

Figure 9.9: d+Au nuclear modification factors in $\sqrt{s}$ = 200 GeV collisions (this analysis), and α-extrapolated nuclear modification factors at $\sqrt{s}$ = 27.4 GeV, using data from [6].

A few qualitative comments are in place[2]. Up to the momentum that we can measure charged pions in this work, the Cronin effect is similar to the enhancement at lower energies. The same applies for the measured charged Kaons. On the other hand, the protons and antiprotons at $\sqrt{s} = 27.4$ GeV, although at low momentum show a similar enhancement to our measurement, at higher p_T they exhibit a very large Cronin effect. At low energies we see approximately a factor of 5 enhancement, at a peak value of $p_T \sim 4.5$ GeV/c, as opposed to the $\sim 45\%$ enhancement at $\sqrt{s} = 200$ GeV. Although we do not have proton data above 4 GeV/c, the nuclear modification factors for neutral pions and inclusive charged hadrons [80], [85], [110], at $\sqrt{s} = 200$ GeV strictly forbid such a huge enhancement for the protons and antiprotons at higher p_T. It is safe to state then that the Cronin effect for the protons and antiprotons at lower energies is dramatically larger than the enhancement observed at RHIC energies. It is also noteworthy how well the low energy slopes match the higher energy nuclear modification factor slopes at low p_T.

9.1.6 Theory Encounters Experiment: Radical and Conventional Explanations for the d+Au Data

We finally compare our data with two diametrically opposing scenarios. Accardi and Gyulassy have adapted multiple initial state interactions in d+Au collisions through a Glauber-Eikonal (GE) formalism [98]. The GE series is computed directly via numerical convolution of elementary parton-nucleon processes and unitarity is automatically conserved. In this model, the convo-

[2]Time constraints did not allow us to make a careful evaluation of the systematic error on the extrapolated $\sqrt{s} = 27.4$ GeV R_{dAu}, and we are only limited to qualitative comments.

lution of perturbative QCD parton-nucleon cross sections predicts naturally the competing pattern of low-p_T suppression due to geometrical shadowing, and a moderate-p_T Cronin enhancement of hadronic spectra.

The integrated parton-nucleon cross section depends on an infrared scale p_0, which is determined by fitting p+p data, along with the usual intrinsic transverse momentum $\langle k_t \rangle$, necessary to describe the p+p spectrum. After a fit to the PHENIX p+p neutral pion spectra at $\sqrt{s} = 200$GeV, p_0 was taken to be 1.0 ± 0.1 GeV, while $\langle k_t^2 \rangle = 0.52\ GeV^2$ also gave the best fit to the data. The K factor in this work is equal to 1. In the following, the theoretical errors are obtained by changing the p_0 mass regulator within the fit errors ($p_0 = 1.0 \pm 0.1$ GeV) (the theoretical result is shown as a band that corresponds to this variation of p_0) . The factorization, renormalization and fragmentation scales were chosen to be either $Q_p = Q_h = m_T$ or $Q_p = Q_h = m_T/2$. The latter choice is by far the best description of the data and was finally used in the theoretical curves that we will present shortly.

Before we show how the calculation compares to our measurement we first present, in Fig. 9.10, the result of the Accardi-Gyulassy calculation for the W-to-Be ratio of per-nucleon cross sections, $R_{W/Be}$, for pions, at $\sqrt{s} = 27.4$ GeV from [6], that was discussed at length in the previous section and was shown in Fig. 9.8. The p+p cross section at $\sqrt{s} = 27.4$ GeV, that was used to determine the mass regulator and intrinsic transverse momentum at this lower energy, is also taken from the same publication [6].

The agreement with the data, as can be seen in Fig. 9.10, is quite satisfactory, within the theoretical errors that we described above. We now turn to comparisons of the model with our charged pion measurement. In Fig. 9.11

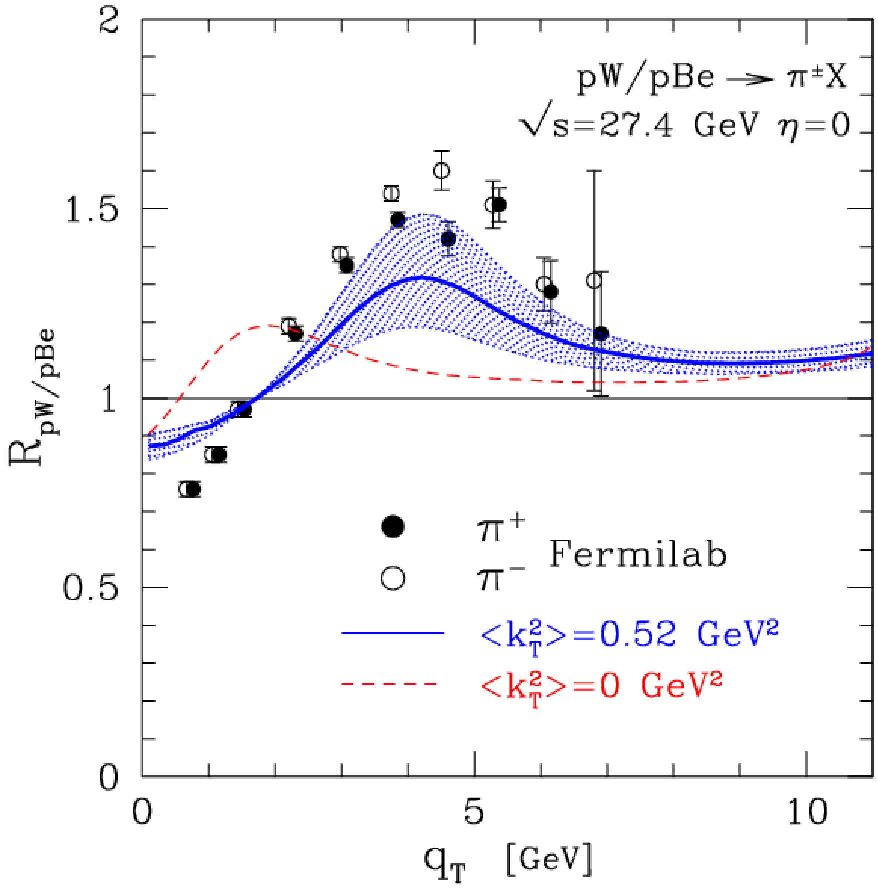

Figure 9.10: Comparison of the Accardi-Gyulassy model [98] with data from [6], for the W-to-Be ratio at $\sqrt{s} = 27.4$ GeV .

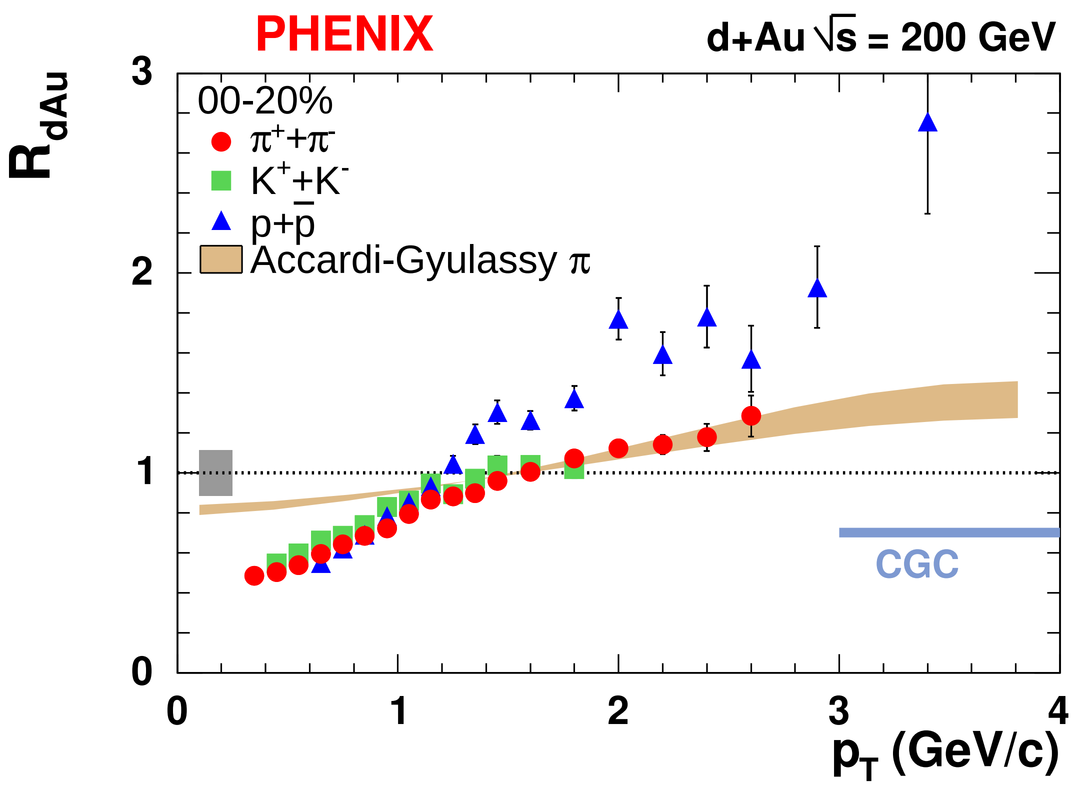

Figure 9.11: Identified R_{dAu} for 00-20% centrality, along with the calculation by Accardi and Gyulassy at $\sqrt{s} = 200$ GeV, [98]. The Color-Glass prediction from [104] is also shown.

we present the 00-20% nuclear modification factors for pions, kaons and protons, along with the calculation for pions by Accardi and Gyulassy. Obviously any comparisons below $p_T \sim 1$ GeV/c are not reliable, and are shown only for demonstration purposes. We also present in Fig. 9.12 the comparison of the model with the rest of the d+Au centrality bins.

One of the important aspects of this work is that geometrical shadowing is taken into account automatically in this model. Therefore, if the theoretical curve falls below the data, that leaves room for dynamical shadowing scenarios, or, in other words, a possible onset of parton saturation, although not of the magnitude that was originally proposed [104].

We see, though, from the comparison of the model to our data, that there is very little room for additional effects. The theoretical description is in quantitative agreement with our data, albeit at the limited p_T range available to the TOF analysis for the pions. Preliminary results from neutral pions that reach higher in p_T are also in good agreement with this model, within the stated systematic error bars [85].

We therefore conclude that a conventional , Glauber-Eikonal multiple scattering scenario is adequate to describe our data at $\sqrt{s} = 200$ GeV, without any further requirement for dynamical shadowing. The same mechanism can also describe the Cronin effect at lower energies. Unfortunately there is no prediction for the Kaon and proton spectra at this moment.

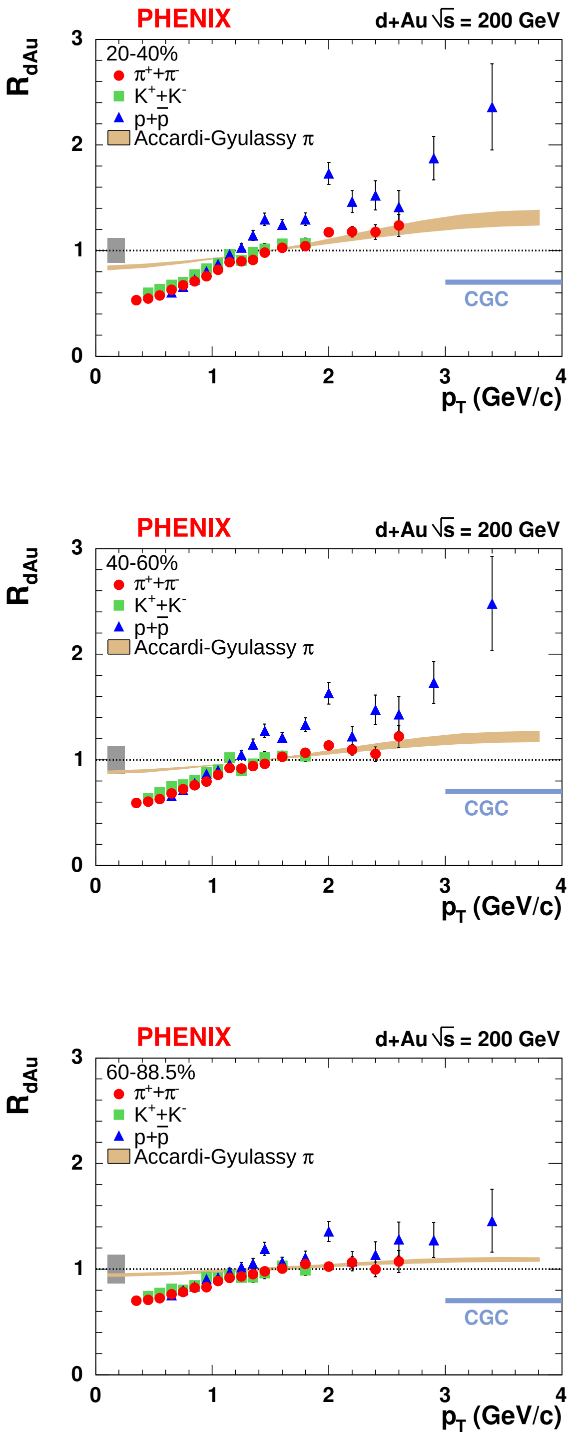

Figure 9.12: Identified R_{dAu} for various centralities, along with the calculation by Accardi and Gyulassy at $\sqrt{s} = 200$ GeV, [98]. The Color-Glass prediction from [104] is also shown.

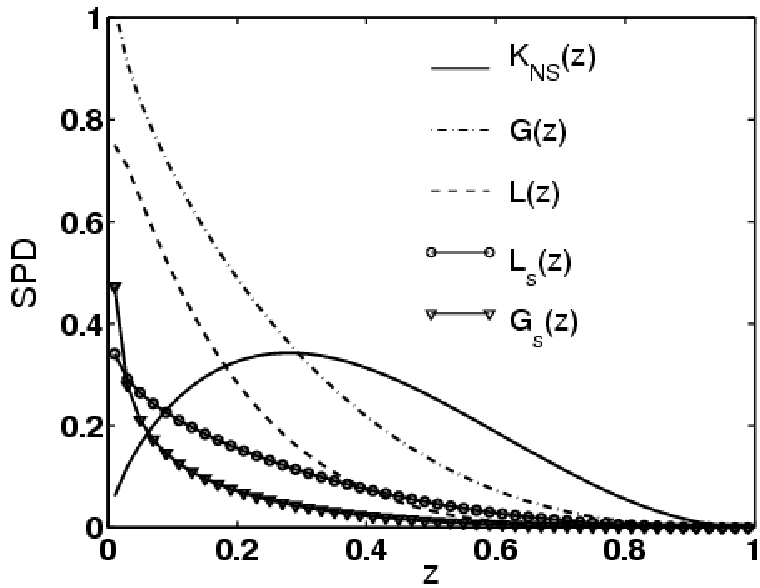

Figure 9.13: Shower parton distributions plotted as a function of their momentum fractions from [90].

Cronin Effect from Final-State Interactions ?

We now turn to the "radical" interpretation of our data by Hwa and Yang (Oregon Group) and the notorious thermal-shower (*TS*) term of this theory. In their approach they propose that the enhancement of hadron production at moderate p_T in d+Au collisions is due to the recombination of soft and shower partons in the final state. In this framework, the species-dependence of the nuclear modification factors is viewed as a manifestation of the dependence of the hadronization mechanism on the medium.

The central issue in these kind of models has always been the determination of the appropriate distributions of partons that recombine. Hwa and Yang in [90] have tackled this problem by formulating a recombination model for fragmentation and introducing the notion of shower parton distribution functions (SPDs). In this model, the generic formula for a hadronization process, or in other words, the fragmentation function (FF), is expressed as a convolution:

$$xD_i^M(z) = \int \frac{dx_1}{x_1}\frac{dx_2}{x_2} F^i_{q\overline{q}'}(x_1, x_2)\, R^M(x_1, x_2, z) \tag{9.11}$$

where M is the meson in a jet initiated by a hard parton i. $F^i_{q\overline{q}'}(x_1, x_2)$ is the joint distribution of the shower partons q and $\overline{q}'$ in the jet, which are to recombine to form M. The recombination function (RF) $R^M(x_1, x_2, z)$ for the formation of a meson is computed within the framework of the valon model [88], [89]. Assuming that $F^i_{q\overline{q}'}$ is factorisable into products of two SPDs, it can be written as:

$$F^i_{q\overline{q}'}(x_1, x_2) = S_i^q(x_1) S_i^{\overline{q}'}(x_2) \tag{9.12}$$

where $S_i^q(x_1)$ is the distribution of shower partons q with momentum fraction x_1 in a shower initiated by a hard parton i. The main idea in [90] is that the SPDs can be explicitly calculated from Equation 9.11 by solving this integral equation for $S_i^q(x_1)$, and using as an input the measured fragmentation functions from various processes. The solution of this equation for $S_i^q(x_1)$ is shown in Fig. 9.13, where the five shower parton distributions calculated are

- K_{NS} : distribution of valence quarks
- L: distribution of sea quarks
- L_S: distribution of strange quarks

- G: distribution of light quarks in gluon showers

- G_S: distribution of strange quarks in gluon showers

As Hwa and Yang argue in [90] , once the SPDs are known, their relevance to high-p_T hadron production at Au+Au and d+Au collisions at RHIC is unavoidable, since shower partons can recombine with thermal partons in the Au+Au environment, and soft partons in the d+Au environment (soft partons in d+Au are sometimes also called thermal partons for ease of language). In [91] the use of SPDs successfully reproduces the large proton to pion ratio, while in d+Au, as we shall explicitly show in the following [92], [93], they successfully describe the pion and proton spectra and, therefore, provide a natural explanation for the Cronin effect and the observation that protons show a significantly larger enhancement than pions.

We proceed now to the final steps of this calculation. The inclusive distribution for pions can be written as

$$p\frac{dN_\pi}{dp} = \int \frac{dp_1}{p_1}\,\frac{dp_2}{p_2}\,F_{q\overline{q}'}(p_1,p_2)\,R^\pi(p_1,p_2,p) \tag{9.13}$$

and, restricting the momentum to the transverse plane and averaging over the azimuthal angle ϕ, the pion distribution at mid-rapidity becomes

$$\frac{dN_\pi}{pdp} = \frac{1}{p^3}\int_0^p dp_1\,F_{q\overline{q}'}(p_1,p-p_1) \tag{9.14}$$

This equation is applicable to any of the p+p, d+Au, or Au+Au collision types, only $F^i_{q\overline{q}'}$ depends on the colliding hadron/nuclei. The equation for the inclusive distribution for protons is similarly given by

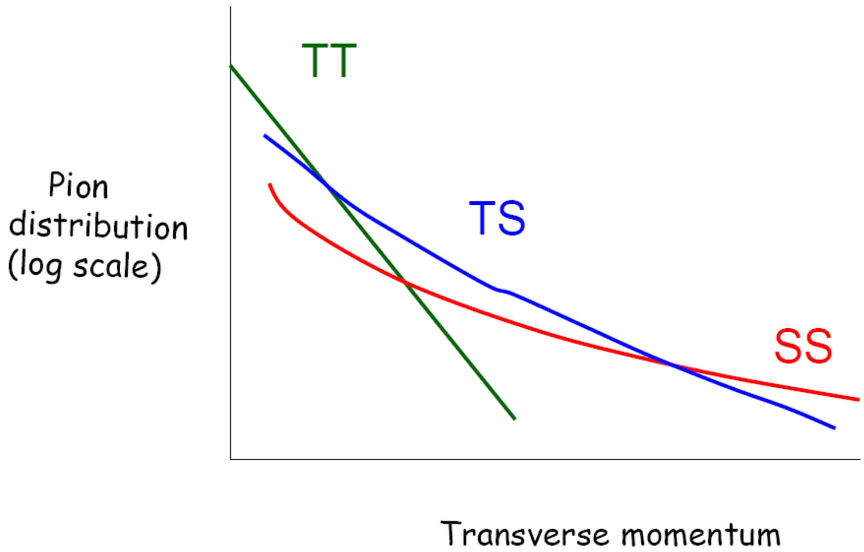

Figure 9.14: The turn-on of different terms, as a function of momentum, in the Hwa-Yang recombination model [92], [93].

$$p^0 \frac{dN_p}{dp} = \int \frac{dp_1}{p_1} \frac{dp_2}{p_2} F(p_1, p_2, p_3) R^p(p_1, p_2, p_3, p) \tag{9.15}$$

where all momentum variables p_i and p are transverse momenta and p^0 denotes the energy of the proton.

For pions , $F^i_{q\bar{q}'}$ is expressed as

$$F_{q\bar{q}'} = TT + TS + (SS)_1 + (SS)_2 \tag{9.16}$$

where T denotes the thermal (soft) distribution, while S denotes the shower distribution. The (SS) term denotes the soft component, dominant at low p_T as we shall see shortly, (TS) denotes the soft semi-hard component, responsible for the Cronin enhancement, and $(SS)_1$ can be trivially reduced to the fragmentation function, dominant at high-p_T, using Equation 9.11. The $(SS)_2$

term has to do with recombination of shower partons from two different jets and is small enough that can be ignored at RHIC energies. The size of each term as a function of momentum in this recombination model is shown in Fig 9.14.

The unique ability of the model to account for the species dependence of the Cronin effect can now be viewed as a result of the different number of quarks in the pion and proton. More specifically, the $F_{q\bar{q}'}$ part for the proton can be written as:

$$F_{q\bar{q}'} = TTT + TTS + T(SS)_1 + (SSS)_1 + T(SS)_2 + ((SS)_1 S)_2 + (SSS)_3 \quad (9.17)$$

and thus, we have a natural explanation of the apparent difference in the hadronization mechanism for pions and protons within the surroundings of cold nuclear matter, which manifests itself as a larger Cronin enhancement for protons as compared to the pion enhancement.

The thermal term in this calculation is taken by fitting the data at low momentum. The authors argue that this soft component is not the predictable part of their model. On the contrary, it is the uniqueness and magnitude of the (TS) term that is predicted by the model, which is at the heart of the recombination mechanism in both d+Au and Au+Au collisions.

In Fig. 9.15 we show the result of the calculation for pions, along with the preliminary data of this analysis, and in Fig. 9.16 the result for the proton production. In both cases, the Cronin enhancement is successfully described by the (TS) term. At high momentum, fragmentation takes over and dominates the spectrum.

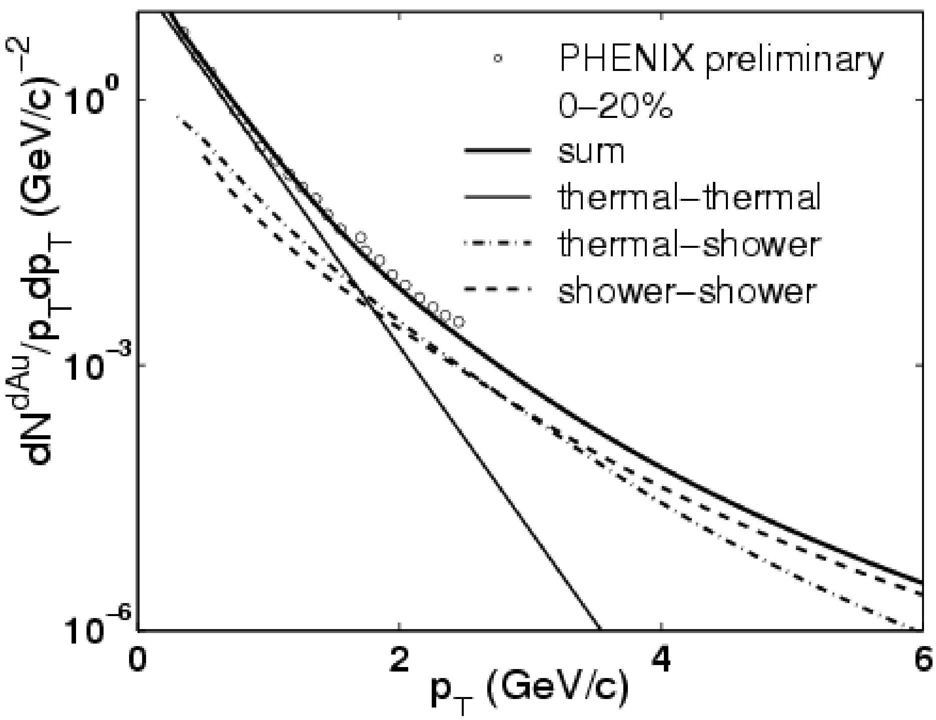

Figure 9.15: Preliminary pion spectra in the most central d+Au collisions along with the prediction from [92]. The contribution of each recombination term in this model is also shown.

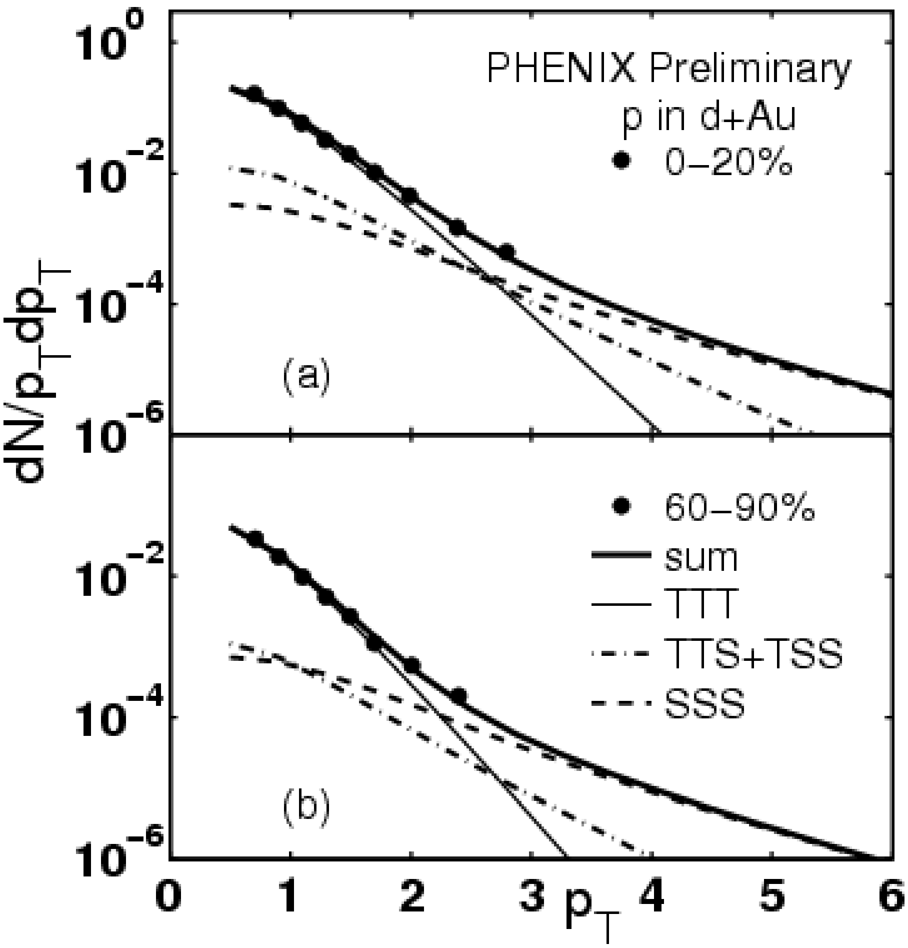

Figure 9.16: Preliminary proton spectra in the most central and most peripheral d+Au collisions. Theoretical curve is from [93]. The contribution of each recombination term in this model is also shown.

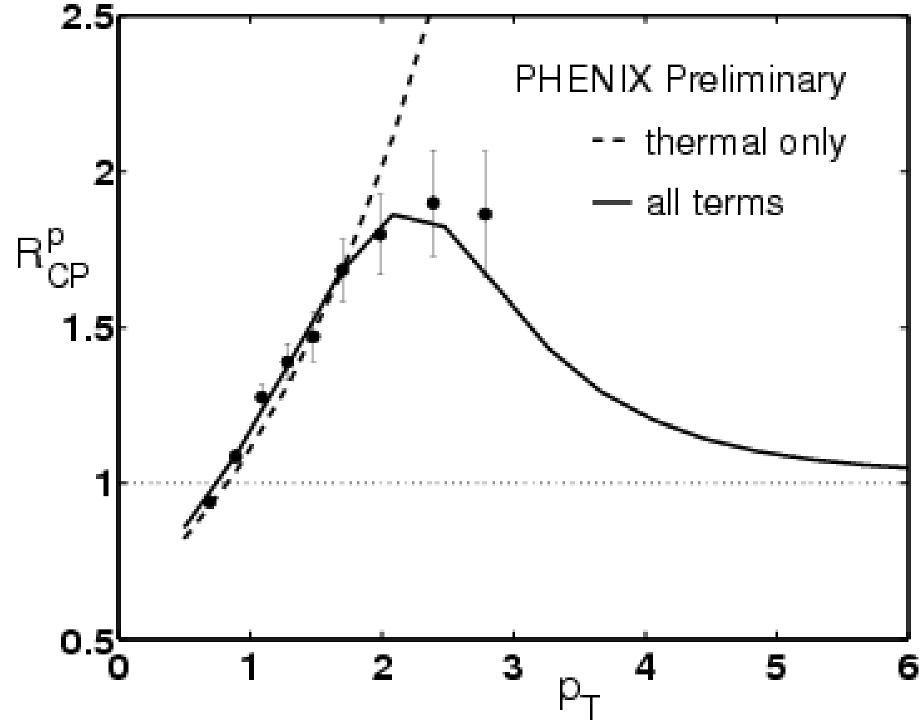

Figure 9.17: Central to peripheral nuclear modification factor for protons and antiprotons in d+Au collisions and theoretical prediction from [93].

Finally, the central-to-peripheral nuclear modification factor for protons is shown in Fig. 9.17. The Hwa and Yang calculation is in good agreement with the data.

We have now presented two diametrically opposing theoretical calculations that can successfully describe the Cronin effect. The first model by Accardi and Gyulassy incorporates a traditional initial multiple scattering of incoming partons with the nucleons in the nucleus. The second model by Hwa and Yang treats the Cronin effect as a final state interaction of thermal-shower recombination. We therefore conclude that the identified analysis by itself, does not have the discrimination power needed to show which mechanism is really at work. Could it be a combination of both ? The radical interpretation by Hwa and Yang introduces a reinterpretation of particle production with far reaching consequences. It means that the separation of partons into two noninteracting components, soft and hard, is an oversimplification [112].

The final judge of this model can not be the identified d+Au data alone as we have shown. The microscopic mechanism implied by this recombination scenario makes a dramatic prediction though. The dominance of the thermal-shower term implies that the jet structure in A+A and d+A collisions can not be the same as that in p+p collisions. According to this model, there should be more particles associated with a trigger particle in A+A collisions than in p+p collisions, for the simple reason that the abundance of soft thermal partons in the A+A case enhances the hadrons formed at moderate p_T through recombination. It is outside of the scope of this thesis to continue further on this topic, but as a final word we would like to mention that the experimental community at RHIC has dedicated tremendous amount of effort to investigate the jet structure of identified particles in d+Au and Au+Au collisions, in order to prove or disprove this fascinating scenario of recombination. For a recent result the viewer is referred to [111].

9.2 Final Remarks and Perspective

Tom Hemmick once told the author of this thesis that he would let him graduate as long as his work had a message. The author believes that this analysis carries an important message and will serve as a reference for future heavy ion measurements, like the upcoming Cu+Cu and Si+Si collisions, scheduled for the fifth year of RHIC running, at $\sqrt{s} = 200$GeV.

We have presented an exhaustive comparison between identified baseline p+p and d+Au spectra on one hand, and Au+Au particle production on the other. We have shown similarities and differences, and made clear which of the spectacular effects observed in central Au+Au collisions are already present in d+Au and p+p and which are completely novel effects that arise from the production of hot and dense matter in central Au+Au collisions.

We therefore have established the initial conditions for identified particle production at $\sqrt{s} = 200$ GeV. We also discussed at length the Cronin effect that we observe in d+Au collisions, its energy and species-dependence, and possible theoretical scenarios that can explain the data. The next generation analyses that are currently under way, investigate the jet structure of identified particle production, and we hope that through this channel the recombination question will be answered successfully in the near future.

The author of this thesis sincerely hopes that this work will serve as a comprehensive reference, in baseline particle production at RHIC energies, for both the theoretical and experimental community.

Bibliography

[1] THE PHENIX EXPERIMENT AT RHIC, Nucl. Phys. **A638**, 565 (1998), D.P. Morrison *et al.* , e-Print Archive: hep-ex/9804004

[2] "RHIC and Quark Matter : Proposal for a Relativistic Heavy Ion Collider at Brookhaven National Laboratory", BNL 51801 (August 1984)

[3] RHIC Design Manual, http://www.agsrhichome.bnl.gov/NT-share/rhicdm/index.html

[4] Established in 1947 on Long Island, Upton, New York, Brookhaven is a multi-program national laboratory operated by Brookhaven Science Associates for the U.S. Department of Energy (DOE). Six Nobel Prizes have been awarded for discoveries made at the Lab. http://www.bnl.gov

[5] J.W. Cronin *et al.*, Phys. Rev. D**11**, 3105 (1975)

[6] D. Antreasyan *et al.*, Phys. Rev. D**19**, 764 (1979)

[7] P.B. Straub *et al. Phys. Rev. Lett.* **68** 452, 1992

[8] M. Lev and B. Petersson, Z.Phys. **C** 21(1983)155.

[9] A .Krzywicki *et al.*, Phys. Lett. B**85**, 407 (1979)

[10] The QGP discovered at RHIC, M. Gyulassy, e-Print Archive: nucl-th/0403032

[11] K. Adcox *et al.*, PHENIX Collaboration, Oct 2004, e-Print Archive: nucl-ex/0410003 , Submitted to Nucl.Phys.A

[12] J.C. Collins and M.J. Perry, Phys. Rev. Lett. **34**, 1353 (1975)

[13] E.V. Shuryak, Phys. Repts. **61**, 71 (1980)

[14] F. Karsch, Lect. Notes Phys. **583**, 209 (2002), e-Print Archive: hep-lat/0106019

[15] J.W. Harris and B. Muller, Ann.Rev.Nucl.Part.Sci.**46**, 71-107 (1996), The search for the quark gluon plasma, e-Print Archive: hep-ph/9602235

[16] A. Kovner and U.A. Wiedemann, Gluon radiation and parton energy loss, 2003, e-Print Archive: hep-ph/0304151

[17] M. Gyulassy*et al.*, Jet quenching and radiative energy loss in dense nuclear matter, 2003, e-Print Archive: nucl-th/0302077

[18] M. Gyulassy et al. Nucl. Phys.A**538** 37c (1992)

[19] E. Wang and X. Wang , Phys. Rev. Lett. **89**, 162301 (2002) , e-Print Archive: hep-ph/0202105

[20] I. Vitev and M. Gyulassy, Phys. Rev. Lett. **89**, 252301 (2002) , e-Print Archive: hep-ph/0209161

[21] K. Adcox *et al.* , Phys. Rev. Lett. **88**, 022301 (2002) , e-Print Archive: nucl-ex/0109003

[22] K. Adcox *et al.* , Phys. Lett. B**561**, 82 (2003), e-Print Archive: nucl-ex/0207009

[23] K. Adcox *et al.* , Phys. Rev. Lett. **88**, 242301 (2002) , e-Print Archive: nucl-ex/0112006

[24] K. Adcox *et al.* , Phys. Rev. C**69**, 024904 (2004) , e-Print Archive: nucl-ex/0307010

[25] S.S. Adler *et al.* , Phys. Rev. C**69**, 034910 (2004) , e-Print Archive: nucl-ex/0308006

[26] S.S. Adler *et al.* , Phys. Rev. Lett. **91**, 072301 (2003) , e-Print Archive: nucl-ex/0304022

[27] S.S. Adler *et al.* , Phys. Rev. C**69**, 034909 (2004) , e-Print Archive: nucl-ex/0307022

[28] S.S. Adler *et al.* , Phys. Rev. Lett. **91**, 172301 (2003) , e-Print Archive: nucl-ex/0305036

[29] U. Heinz and P. Kolb, Nucl. Phys. *A*702, 269 (2002) , e-Print Archive: hep-ph/0111075

[30] P. Kolb and R. Rapp, Phys. Rev. C**67**, 044903 (2003) , e-Print Archive: hep-ph/0210222

[31] D. Teaney *et al.*, Phys. Rev. Lett. **86**, 4783 (2001); P. Kolb *et al.*, Nucl. Phys. **A696**, 197 (2001); P. Huovinen *et al.*, Phys. Lett. B**503**, 58 (2001).

[32] W. Broniowski and W. Florkowski, Phys. Rev. C**65**, 064905 (2002); Phys. Rev. Lett. **87**, 272302 (2001).

[33] P. Braun-Munzinger, D. Magestro, K. Redlich, J. Stachel, Phys. Lett. B**518**, 41 (2001).

[34] Hwa R C and Yang C B 2003 *Phys. Rev. C* **67** 034902; Fries R J *et al.* 2003 *Phys. Rev. Lett.* **90** 202303; Greco V *et al.* 2003 *Phys. Rev. Lett.* **90** 202302

[35] PHENIX Conceptional Design Report. Unpublished.

[36] A. Milov, Ph.D thesis, Weizmann Institute, Rohovot Israel, May 2002.

[37] A. Oskarsson, talk given in PHENIX RUN-2 focus seminar for the Pad Chamber Detectors.

[38] H. Masui, talk given in PHENIX RUN-2 focus seminar for the Time of Flight Detector..

[39] K. Adcox *et al.*, Nucl. Instrum. Methods **A499**, 469 (2003).

[40] S.H. Aronson *et al.*, NIM **A** 499 480-488 (2003)

[41] K. Adcox *et al.*, NIM **A** 499 489-507 (2003)

[42] M. Aizawa *et al.*, NIM **A** 499 508-520 (2003)

[43] J.T. Mitchell *et al.*, NIM **A** 482, 498 (2002) .

[44] M. Peskin , D. Schroeder, *An Introduction to Quantum Field Theory*, Addison-Wesley Publishing Company, 1995

[45] Particle Data Group, Phys. Rev. **D 66**, 2002

[46] TOTEM Collaboration, Letter of Intent, 1997, $http://totem.web.cern.ch/Totem/docs/tot_loi.pdff$, p.12

[47] D. Morrison, *Number of Binary Bollisions and Total Cross Section in d+Au at* $\sqrt{s_{NN}}$ *= 200 GeV* , PHENIX analysis note 165, 2002

[48] K. Reygers, *Glauber Monte-Carlo Calculations for Au+Au Collisions at* $\sqrt{s_{NN}}$ *= 200 GeV* , PHENIX analysis note 169, 2003

[49] D. Morrison, K. Reygers, D. d'Enterria , *Synthesis of Several Approaches to Determining* $\langle N_{coll} \rangle$ *in Minimum Bias d+Au Collisions at* $\sqrt{s_{NN}}$ *= 200 GeV* , PHENIX analysis note 216, 2003

[50] S. Belikov, G. Bunce, M. Chiu, K.A. Drees, B. Fox, Y. Goto, T. Kawabata, N. Saito, H. Sato, and M. J. Tannenbaum , *Determination of the Absolute Luminosity for the Proton-Proton Data at* $\sqrt{s}$ *= 200 GeV Recorded by PHENIX during RHIC Run-02* , PHENIX analysis note 184, 2003

[51] M. J. Tannenbaum, *Thickness Functions and Pointlike Scaling for Hard Scattering*, PHENIX analysis note 57, 2001

[52] M. J. Tannenbaum, *The centrality bias in high* p_T *particle production and how to correct it* , PHENIX analysis note 209, 2003

[53] K. Reygers, T_{AB} *or* N_{coll} *for Peripheral d+Au Collisions ?*, PHENIX private memo, 2004

[54] K. Okada, J. Jia, *Inclusive Charged Hadron Cross Section Measurement in Run2 p+p collisions*, PHENIX analysis note 276, 2004

[55] S. Bazilevsky, B. Fox, Y. Goto, K. Okada, H. Torii, *Updated Absolute Cross Section for π^0 Production in Proton-Proton Collisions at $\sqrt{s}$ = 200 GeV with the PbSc Calorimeter*, PHENIX analysis note 176, 2003

[56] K. Reygers, Ch. Klein-Bösing, T. Awes, S. Bathe, H. Büshing, M. Volkov, *Measurement of Neutral Pions in $\sqrt{s}$ = 200 GeV p+p Collisions with the PbGl Calorimeter* , PHENIX analysis note 175, 2003

[57] R.J. Glauber and G.Matthiae, Nucl.Phys.**B**21, 135 (1970)

[58] D. d'Enterria , *Hard Scattering Cross Sections at the LHC in the Glauber approach: from pp to pA and AA collisions*, Contribution to the CERN Yellow Report on Hard Probes in Heavy Ion Collisions at the LHC, nucl-ex/0302016

[59] Z. Conesa, G. Martinez, *Glauber calculation of Ncoll and Npart in d+Au collisions at $\sqrt{s}$ = 200 GeV. Evaluation of Centrality with Ncoll bias for the nuclear modification factor. Answer to AN275* , PHENIX analysis note 295, 2004

[60] C. Wong, *Introduction to High-Energy Heavy-Ion Collisions* , World Scientific Publishing Company, 1994

[61] J. Adams *et. al*, Phys. Rev. Lett. **91**, 172302 (2003), nucl-ex/0305015

[62] B. Kopeliovich, *Transparent Nuclei at RHIC*, 2003 Phys. Rev. **C 68**, 044906 (2003), nucl-th/0306044

[63] L. Hulthèn and M. Sagawara, Handbuch der Physics **39** (1957)

[64] Chun Zhang and Jamie Nagle, *Centrality Determination in Deuteron-Gold Reactions Using the Beam-Beam Counter*, PHENIX analysis note (not yet submitted) , October 2004

[65] Sasha Milov et al., *Centrality determination and pT centrality dependence in d-Au collisions*, PHENIX analysis note 210, June 2003

[66] STAR Collaboration, C. Adler *et al.* , Phys. Rev. Lett. **87**, 262302 (2001) , e-Print Archive: nucl-ex/0110009

[67] NA44 Collaboration, I.G. Bearden *et al.*, Phys. Rev. C **57**, 837 , (1998) , e-Print Archive: nucl-ex/9711004

[68] UA5 Collaboration, R.E. Ansorge *et al.*, Nucl.Phys.B**328**:36, 1989

[69] UA5 Collaboration, G.J. Alner *et al.*, Phys.Rept.**154**:247, 1987

[70] STAR Collaboration, J. Adams *et al.*, Mar 2004, e-Print Archive: nucl-ex/0403020

[71] STAR Collaboration, M. Heinz for the collaboration, Hot Quarks 2004, July 18-24, 2004 , Taos Valley, New Mexico

[72] STAR Collaboration, X. Cai for the collaboration, SQM2004, 8th International Conference on Strangeness in Quark Matter, Cape Town , South Africa, 15-20 September 2004

[73] STAR Collaboration, R. Witt for the collaboration, Poster paper presented at 17th International Conference on Ultra Relativistic Nucleus-Nucleus Collisions (Quark Matter 2004), Oakland, California, 11-17 Jan 2004. e-Print Archive: nucl-ex/0403021

[74] STAR Collaboration, A.E.M. Billmeier for the collaboration, SQM2003, 7th International Conference on Strangeness in Quark Matter, Atlantic Beach, North Carolina, 12-17 Mar 2003, Published in J.Phys.G30:S363-S368,2004

[75] STAR Collaboration, B. Hippolyte for the collaboration, To appear in the proceedings of 38th Rencontres de Moriond on QCD and High-Energy Hadronic Interactions, Les Arcs, Savoie, France, 22-29 Mar 2003 e-Print Archive: nucl-ex/0306017

[76] PHENIX Collaboration, K. Adcox *et al.*, Phys. Rev. Lett. **89**, 092302 (2002).

[77] STAR Collaboration, J. Adams *et al.* Phys. Lett. B567, 167 , (2003) , e-Print Archive: nucl-ex/0211024

[78] PHENIX Analysis Note 187, T. Chujo, A. Kiyomichi and J. Velkovska, April 2003

[79] Mel Brooks, writter and director, “History of the World: Part I”, 1981

[80] S.S. Adler *et al.* , Phys. Rev. Lett. **91**, 072303 (2003), e-Print Archive: nucl-ex/0306021

[81] J. Adams *et al.* , Phys. Rev. Lett. **91**, 072304 (2003)

[82] B.B. Back *et al.* , Phys. Rev. Lett. **91**, 072302 (2003)

[83] I. Arsene *et al.* , Phys. Rev. Lett. **91**, 072305 (2003)

[84] F. Matathias, "pi/K/p production and Cronin effect from p-p, d-Au and Au-Au at sqrts=200 GeV", J.Phys.**G30**:S1113-S1116, 2004 ,e-Print Archive: nucl-ex/0403029

[85] H. Buesching, "Centrality Dependence of Neutral Pion Production in d+Au Collisions at 200 GeV per Nucleon", Poster at the 17th International Conference on Ultra Relativistic Nucleus-Nucleus Collisions

[86] J. Jia, "High pT charged pions in PHENIX", Poster at the 17th International Conference on Ultra Relativistic Nucleus-Nucleus Collisions

[87] A. Accardi, "CRONIN EFFECT IN PROTON NUCLEUS COLLISIONS: A SURVEY OF THEORETICAL MODELS",Dec 2002, Contribution to CERN Yellow Report on Hard Probes in Heavy Ion Collisions at the LHC, e-Print Archive: hep-ph/0212148

[88] R.C. Hwa, Phys. Rev. D**22**, 1593 (1980)

[89] R.C. Hwa and C.B. Yang, Phys. Rev. C**66**, 025204 (2002), e-Print Archive: hep-ph/0202140

[90] R.C. Hwa and C.B. Yang, OITS-743, Dec 2003, e-Print Archive: hep-ph/0312271

[91] R.C. Hwa and C.B. Yang, Phys. Rev. C**70**, 024905 (2004), e-Print Archive: nucl-th/0401001

[92] R.C. Hwa and C.B. Yang, Phys. Rev. Lett. **93**, 082302 (2004), e-Print Archive: nucl-th/0403001

[93] R.C. Hwa and C.B. Yang, Phys. Rev. C**70**, 037901 (2004), e-Print Archive: nucl-th/0404066

[94] STAR Collaboration Adams J *et al.* 2003 Preprint nucl-ex/0309012

[95] PHOBOS Collaboration B.B. Back *et al.*, Phys. Rev. C**70**, 011901 (2004) e-Print Archive: nucl-ex/0309013

[96] PHOBOS Collaboration B.B. Back *et al.*, Sep 2004, Submitted to Phys.Rev.C , e-Print Archive: nucl-ex/0409003

[97] BRAHMS Collaboration I.G. Bearden *et al.*, Sep 2004, Submitted to Phys.Lett.B , e-Print Archive: nucl-ex/0409002

[98] A. Accardi and M. Gyulassy, Phys. Lett. B**586**, 244 (2004), e-Print Archive: nucl-th/0308029

[99] B.Z. Kopeliovich *et al.*, Phys. Rev. Lett. **88**, 232303 (2002)

[100] A. Accardi and D. Treleani, Phys. Rev. D**64**, 116004 (2001)

[101] X.-N. Wang, Phys. Rev. C**61**, 064910 (2000)

[102] X.-N. Wang, Phys. Lett. B**579**, 299 (2004)

[103] D. d'Enterria Phys. Lett. B**596**, 32 (2004) e-Print Archive: nucl-ex/0403055

[104] D. Kharzeev, E. Levin and L. McLerran, Phys. Lett. B**561**, 93 (2003) e-Print Archive: hep-ph/0210332

[105] M.M. Aggarwal *et al.*, Eur. Phys. J, **volume C23** , 225, 2002

[106] R. Albrecht *et al.*, Eur. Phys. J, **volume C5**, 255, 1998

[107] A.L.S. Angelis *et al.*, Phys. Lett. B**185**, 213 (1987)

[108] J. Slivova, Ph.D. thesis, Charles University, Prague, 2003, from the CERES experiment.

[109] T. Ochiai *et al.*, Prog. Theor. Phys. **75**, 288 (1986)

[110] S. Leckey, "Centrality Dependent Nuclear Modification in d-Au and what it teaches us about Au-Au suppression", Division of Nuclear Physics 2003 Fall Meeting, October 29 - November 1, 2003, Tucson, AZ.

[111] PHENIX Collaboration , "Jet Structure of Baryon Excess in $Au + Au$ Collisions at $sqrt(s_N N)$ = 200 GeV" , 2004 e-Print Archive: nucl-ex/0408007

[112] R.C. Hwa and C.B. Yang, J.Phys.**G**30:S1117-S1120, 2004 e-Print Archive: nucl-th/0403072